UNIVERSITY OF SOUTHAMPTON

Faculty of Engineering and the Environment

Wind Turbine Aerodynamics in Freestream Turbulence

by

Yusik Kim

Thesis for the degree of Doctor of Philosophy

October 2013

UNIVERSITY OF SOUTHAMPTON

ABSTRACT

FACULTY OF ENGINEERING AND THE ENVIRONMENT

Doctor of Philosophy

WIND TURBINE AERODYNAMICS IN FREESTREAM TURBULENCE

by Yusik Kim

Topics in wind turbine aerodynamics are reviewed. These include the effect of freestream turbulence on the flows over wind turbine blades; dynamic stall phenomenon; and rotational augmentation. The advantages of numerical studies on these topics are highlighted and large-eddy simulation (LES) is selected to overcome the defects for other numerical approaches, e.g. Reynolds Average Navier-Stokes (RANS), on such applications.

The atmospheric boundary layer in which wind turbines operate is almost always turbulent, and it has a strong influence on aerodynamic loads for wind turbines. To generate inflow turbulence in LES calculations, a new synthetic turbulence inflow condition is developed which is computationally efficient and satisfies the divergence-free condition. To investigate the effect of freestream turbulence on wind turbine blades, a flow over a static airfoil is simulated as a baseline case and the results (e.g. surface pressure and skin-friction) show good agreement with DNS data. The developed turbulent inflow condition is then applied in the upstream region of the airfoil and the unsteady surface pressure shows good agreement with the analytical solution by Amiet [2–4] at zero incidence. This provides a tool for aerodynamic predictions and unsteady surface pressure analysis of wind turbine flows subjected to freestream turbulence on which currently no reliable theory or prediction model exists in general situations. The capability of LES on highly separated and strong 3-D flows, e.g. dynamic stall is demonstrated. Details in the LES results can give a deep insight for developing wind turbine design tools. The turbulent inflow generated by the new inflow method is applied for the flow over a pitching airfoil and this is the first numerical study for the effect of freestream turbulence on dynamic stall to our knowledge. Aerodynamic hysteresis for the pitching airfoil subjected to freestream turbulence shows consistent results with those from wind tunnel measurements. The snapshots and the aerodynamic forces of the calculated flow fields explicitly reveal the influence of freestream turbulence on the flow over the pitching airfoil: the separated flow is suppressed resulting in the lift increase. The last part of the thesis is devoted to understanding the mechanism for the rotational effect of wind turbines, known as ‘rotational augmentation’. A sectional blade flow in a rotating reference frame is simulated and the Coriolis effect is exclusively identified as the primary mechanism for rotational augmentation.

Contents

List of Figures

List of Tables

Declaration of Authorship

I, Yusik Kim, declare that the thesis entitled *Wind Turbine Aerodynamics in Freestream Turbulence* and the work presented in the thesis are both my own, and have been generated by me as the result of my own original research. I confirm that:

1. This work was done wholly or mainly while in candidature for a research degree at this University;
2. Where any part of this thesis has previously been submitted for a degree or any other qualification at this University or any other institution, this has been clearly stated;
3. Where I have consulted the published work of others, this is always clearly attributed;
4. Where I have quoted from the work of others, the source is always given. With the exception of such quotations, this thesis is entirely my own work;
5. I have acknowledged all main sources of help;
6. Where the thesis is based on work done by myself jointly with others, I have made clear exactly what was done by others and what I have contributed myself;
7. Parts of this work have been published as: Kim et al. *6th Int. Conf. Fluid Mech., Guangzhou, China*, 2011, [71], Kim et al. *13th Int. Conf. Wind Eng., Amsterdam, Netherlands*, 2011, [72], Kim et al. *UK WES conf., Southampton, UK,* 2012, [68], Kim et al. *Comput. Fluids,* 2013, [69] and Kim et al. *Direct Large Eddy Simulation 9, Dresden, Germany,* 2013, [70].

Signed: _____

Date: _____

Acknowledgements

First of all, I highly acknowledge Dr. Zheng-Tong Xie's elaborate and relentless supervising throughout the Ph.D course. It would not be possible to complete the thesis without his support. With the oversight of supervisors, Dr. Zheng-Tong Xie and Prof. Ian Castro, editorial advice has been sought. No changes of intellectual content were made as a result of this advice.

I also acknowledge for valuable advice from Prof. Ian Castro, Prof. Richard Sandberg, Prof. Neil Sandham, Dr. Jae Wook Kim, Dr. Lloyd Jones, Prof. Timothy Lee and Mr. Ruggero Poletto. I especially appreciate Prof. Richard Sandberg, Dr. Lloyd Jones and Prof. Kenichi Rinoie who were willing to share their raw data, which provided critical reference data to my research. I am thankful to provision of a Ph.D studentship from Faculty of Engineering and the Environment, University of Southampton. All the computations were performed on supercomputers, IRIDIS3 and HECToR.

Last but the least, I deeply appreciate all my inspiring and amusing colleagues.

Nomenclature

Roman symbols

$\boldsymbol{A}$	surface area vector	[m^2]
A_P, A_l	coefficients in discretized equations, see Eq. 4.5	[.]
a_{ij}	amplitude tensor, Eq. 2.41	[m s^{-1}]
B	boundaries	[.]
b_j	digital filter coefficient, Eq. 2.50	[.]
c	chord length	[m]
C_f	skin-friction coefficient	[.]
C_p	pressure coefficient	[.]
C'_p	pressure fluctuation coefficient	[.]
C_D	drag coefficient	[.]
C_{DES}	model constant in DES model	[.]
C_L	lift coefficient	[.]
C_M	moment coefficient	[.]
C_{MTS}	model constant in MTS SGS model, Eq. 2.33	[.]
C_n	universal constant, Eq. 2.23	[.]
C_T	model constant in MTS SGS model, Eq. 2.35	[.]
C_{SGS}	constant in SGS model	[.]
C_s	Smagorinsky constant	[.]
C'_s	model constant in blending model, Eq. 2.69	[.]
C_{XC}	model constant, Eq. 2.51	[.]
C_ν	Eq. 2.36	[.]
$C(r)$	correlation function	[.]
D	drag	[kg m s^{-2}]
d	wall distance	[m]
dt	time step	[s]
dx	grid size	[m]
$E(\kappa)$	energy spectrum	[m^3 s^{-2}]
$\mathcal{E}$	Eq. 5.6	[.]
e	turbulent kinetic energy in Meteorology	[m^2 s^{-2}]
e, exp	exponential	[.]
$\boldsymbol{F}$	face flux vector	[.]

F_e	face-centre flux	[.]
F_s	sampling rate	[s^{-1}]
$\mathcal{F}$	Fourier transform	[.]
f	arbitrary function	[.]
f_I	shape function, Eq. 2.53	[.]
f'_r	additional term, Eq. 7.12	[m s^{-2}]
f_{SB}	separation bubble frequency	[s^{-1}]
f_s	shedding frequency	[s^{-1}]
f_*	normalized frequency	[s^{-1}]
G	filter function	[.]
G_{pp}	spectral density of pressure difference	[kg^2 m^{-2} s^{-4}]
g	transfer function, Eq. 5.5	[.]
H	mixed layer height	[m]
H	Heaviside function	[.]
I	integral length scale	[m]
K	turbulent kinetic energy	[m^2 s^{-2}]
K_{es}	estimated SGS kinetic energy, Eq. 2.34	[m^2 s^{-2}]
K_{SGS}	SGS kinetic energy	[m^2 s^{-2}]
k_{red}	reduced frequency	[.]
L	lift	[kg m s^{-2}]
L_x, L_y, L_z	computational domain length	[m]
$\mathcal{L}_{ij}$	resolved turbulence stress tensor	[m^2 s^{-2}]
log	logarithmic	[.]
l	cell centre distance	[m]
l_{DES}	length scale in DES model	[m]
l_{DDES}	length scale in DDES model	[m]
l_{hyb}	length scale in IDDES model	[m]
l_{LES}	length scale in LES model	[m]
l_{RANS}	length scale in RANS model	[m]
l_r	length for the refined region	[m]
l_0	largest length	[m]
l_{SB}	separation bubble thickness	[m]
M	Mach number	[.]
N	eddy points	[.]
N_{low}	number of grid points on the lower airfoil surface	[.]
N_R	number of grid points on R	[.]
N_W	number of grid points on W	[.]
N_{US}	number of grid points on US	[.]
N_{up}	number of grid points on the upper airfoil surface	[.]
N_s	number of sampling	[.]
N_x, N_y, N_z	number of grid points	[.]

N_z'	number of grid points after refinements	[.]
$\mathcal{N}$	normal distribution	[.]
$\mathcal{NS}$	Navier-Stokes operator	[.]
n	surface normal unit vector	[.]
P	cell centre point	[.]
p	pressure	[kg m^{-1} s^{-2}]
p_∞	reference/ambient pressure	[kg m^{-1} s^{-2}]
p^{**}, p^{***}	corrected pressure in PISO	[kg m^{-1} s^{-2}]
R	computational domain radius	[m]
R_{ij}	Reynolds stress tensor	[m^{2}s^{-2}]
Re	Reynolds number	[.]
Q	second invariant of the velocity gradient	[m^{-1}]
q	dynamic pressure	[kg m^{-1} s^2]
r	separation distance	[m]
r	random number	[.]
r_d	squared ratio of model length scale, Eq. 2.75	[.]
$\boldsymbol{S}$	rate of strain tensor	[s^{-1}]
S	surface area	[m^2]
S_ϕ	source term	[.]
s	surface tangential unit vector	[.]
St	Strouhal number	[.]
T	characteristic time	[s]
T_{ij}	SGS stress tensor at the test filter level	[m^2 s^{-2}]
t	time	[s]
t_*	normalized time	[.]
TI	turbulence intensity	[.]
TI_0	turbulence intensity at the inflow	[.]
U_b	prescribed bulk velocity	[m s^{-1}]
U_{eff}	effective velocity	[m s^{-1}]
U_{LEV}	LEV convection velocity	[m s^{-1}]
U_γ	yawed velocity	[m s^{-1}]
U_∞	freestream velocity	[m s^{-1}]
U_0	translational velocity	[m s^{-1}]
U, V	mean velocity	[m s^{-1}]
u, v, w	velocity components	[m s^{-1}]
u_θ, u_y, u_r	velocity components in cylindrical coordinate	[m s^{-1}]
U_{rot}	rotating velocity	[m s^{-1}]
$\boldsymbol{u}'$	fluctuation velocity vector	[m s^{-1}]
$\boldsymbol{u}_*$	intermediate velocity vector, Eq. 2.51	[m s^{-1}]
u^g	generated velocity, Fig. 4.6	[m s^{-1}]
u_τ	friction velocity	[m s^{-1}]

u^+	normalized velocity	[.]
u^*, u^{**}	intermediate velocity in PISO	[m s^{-1}]
US	computational domain upstream length	[m]
V_C	cell volume	[m^3]
W	computational domain wake length	[m]
W_*	convective velocity scale, see [165]	[m s^{-1}]
y_0	distance of the wall	[m]
y_1	distance of the first wall-off cell centre	[m]
y_1^+	normalized wall distance	[.]
x'	chord aligned coordinate	[m]

Greek symbols

α	angle of attack	[°]
α_{LEV}	mean angle of attack for LEVs	[°]
α_{eff}	effective angle of attack	[°]
β_m	limiter, Eq. 3.25	[.]
Γ	diffusivity coefficient	[.]
γ	yaw angle, Fig. 1.1	[°]
γ	diffusivity for the dynamic mesh, Eq. 6.2	[.]
Δ	mesh related length scale	[m]
$\Delta_{\|\|}$	wall parallel grid size	[m]
$\overline{\Delta}$	filter length scale	[m]
δ	half channel depth	[m]
δ_{ij}	Kronecker delta	[.]
δ_{99}	thickness for 99% freestream velocity	[m]
δ^*	displacement thickness	[m]
Δp	pressure difference	[kg m^{-1} s^{-2}]
$\Delta x^+, \Delta y^+, \Delta z^+$	normalized grid size	[.]
ε	turbulent kinetic energy dissipation rate	[m^2 s^{-3}]
ε^*	error for velocity, Eq. 4.21	[m s^{-1}]
ε_{SGS}	Eq. 2.38	[m^2 s^{-3}]
η	smallest scale	[m]
η^*	wall normal distance normalized by δ^*	[.]
κ	von Kármán constant	[.]
κ	wave number	[m$^-$1]
κ_c	cut-off wave number	[m$^-$1]
λ	tip speed ratio	[.]
ν	kinematic viscosity	[m^2 s^{-1}]
ν_{blend}	blended turbulent kinematic viscosity	[m^2 s^{-1}]
ν_t	turbulent kinematic viscosity	[m^2 s^{-1}]
ν_{SGS}	subgrid-scale kinematic viscosity	[m^2 s^{-1}]

$\tilde{\nu}$	modified eddy viscosity, Eq. 2.71	[m^2 s^{-1}]
ξ^*	error for pressure, Eq. 4.21	[kg m^{-1} s^{-2}]
ρ	fluid density	[kg m^{-3}]
τ_{ij}^{r}	residual (or SGS) stress tensor	[m^2 s^{-2}]
τ_w	wall shear stress	[m^2 s^{-2}]
Φ	turbulence spectrum	[m s^{-2}]
Φ	phase angle shift	[rad]
ϕ, ψ	general scalar property	[.]
ϕ_a	azimuth angle	[°]
$\boldsymbol{\phi}$, $\boldsymbol{\psi}$	intermediate velocity vector	[m s$^-$1]
ω	pitching frequency	[rad s^{-1}]
ω	specific dissipation rate	[s^{-1}]
Ω	angular velocity	[rad s^{-1}]

Oversymbols

$\bar{\phi}$	filtered
$\tilde{\phi}$	test or explicitly filtered
$\langle\phi\rangle$ or $\overline{\phi}$	assembly averaging operator
$\hat{\phi}$	property in spectral space

Abbreviations

ABL	**A**tmospheric **B**oundary **L**ayer
BEM	**B**lade **E**lement **M**omentum
BL	**B**oundary **L**ayer
CD	**C**entral **D**ifferencing
CFD	**C**omputational **F**luid **D**ynamics
CFL	**C**ourant **F**riedrichs **L**ewy
DDES	**D**elayed **D**etached **E**ddy **S**imulation
DES	**D**etached **E**ddy **S**imulation
FSM	**F**orward **S**tepwise **M**ethod
FVM	**F**inite **V**olume **M**ethod
HAWT	**H**orizontal **A**xis **W**ind **T**urbine
HIT	**H**omogeneous **I**sotropic **T**urbulence
IDDES	**I**mproved **D**elayed **D**etached **E**ddy **S**imulation
LES	**L**arge **E**ddy **S**imulation
LEV	**L**eading **E**dge **V**ortex
LLM	**L**ogarithmic **L**ayer **M**ismatch
LSB	**L**aminar **S**eparation **B**ubble
NVL	**N**ormalized **V**ariable **A**pproach
MTS	**M**ixed **T**ime **S**cale
MSD	**M**odelled **S**tress **D**depletion

PBC	**P**eriodic **B**oundary **C**ondition
PC	**P**it**C**hing
PDE	**P**artial **D**ifferential **E**quation
PIMPLE	**PI**so + si**MPLE**
PISO	**P**ressure **I**mplicit with **S**plitting of **O**peratprs
PSD	**P**ower **S**pectral **D**ensity
RANS	**R**eynolds **A**veraged **N**avier **S**tokes
SGS	**S**ub **G**rid **S**cale
SIMPLE	**S**emi-**I**mplicit **M**ethod for **P**ressure-**L**inked **E**quation
ST	**ST**atic
TI	**T**urbulence **I**ntensity
TKE	**T**urbulent **K**inetic **E**nergy
TSR	**T**ip **S**peed **R**atio
UD	**U**pwind **D**ifferencing
WT	**W**ind **T**urbine
XC	**X**ie and **C**astro [183]
XCMC	**XC** **M**ass **C**orrection
XCDF	**XC** **D**ivergence **F**ree

Chapter 1

Introduction

1.1 Background

According to the models used by the Intergovernmental panel on climate change, the global carbon emission will have to be cut to half of their 1990 levels by 2050 to keep the global temperature from increasing more than $2°C$ above the pre-industrial levels. For rich countries that means an 80% cut in their emissions which is the consensus of the G8 group of nations in 2008, by that date. This is a reduction of two tonnes of CO2 equivalent per head per year [28]. Due to the carbon emission regulation, interest in renewable energy which generates zero or near-zero carbon has increased these days but the portion of power from renewable energy sources is still less than 1% of the overall power generation in the world. Wind energy is one of the most successful renewable energy sources. Therefore the need to improve competitiveness of wind energy through cost reduction and new innovative aerodynamic design [155] is increasing.

Generating electricity using wind turbines has a long history. The first electricity generation from a wind turbine was in 1887 [155]. Despite the long history of the wind turbines, wind turbine designers still rely on safety factors and empiricism due to the inaccurate prediction of wind loads on the blade. Also, physical understanding of wind turbine aerodynamics is far from complete. Over-designed wind turbines are less cost-effective and a poor prediction model weakens reliability of wind energy. Simms et al. (2001) [149] reported that turbine power predictions ranged from 25% to 175% of that measured under the simplest situation, i.e. no-yaw (see Fig. 1.1), steady-state and no-stall conditions. These differences are not desirable considering the increase of the modern wind turbine size because the cost of wind turbine installments grows with the size of the wind turbine [153].

In this chapter, topics of wind turbine aerodynamics are explained. Literature on each topic is reviewed and the objectives of the research are clarified towards the end

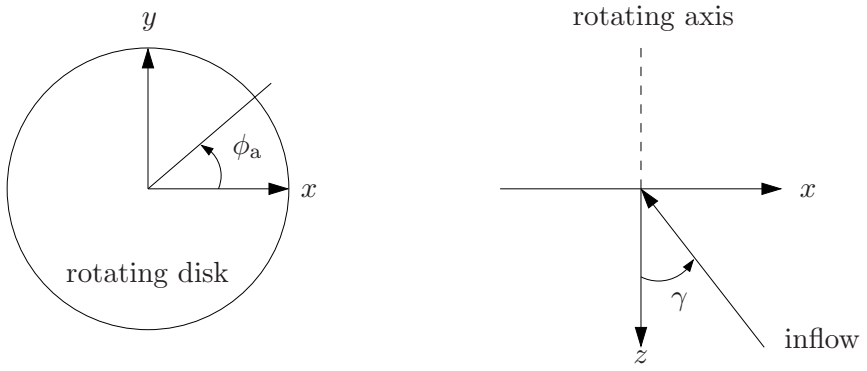

FIGURE 1.1: A sketch of the azimuth angle, ϕ_a (left) and the yaw angle, γ (right) in wind turbine aerodynamics.

of this chapter which attempt to unveil the complexity of wind turbine aerodynamics. More comprehensive reviews on wind turbine aerodynamics can be found in [44, 45, 155].

1.2 Topics in wind turbine aerodynamics

The aerodynamics of wind turbines include various topics from static airfoil characteristics to geographical wind assessments. Fig. 1.2 shows some major topics in wind turbine aerodynamics.

1.2.1 2-D airfoil database

One may think that there is a huge difference between a 2-D airfoil and a 3-D rotating blade and one may also wonder whether the 2-D airfoil data is useful to wind turbine aerodynamics. We can recognize why the 2-D airfoil database is required once we understand the prediction methods of wind turbines. Many of the prediction methods for the wind turbine performance, such as blade element-momentum (BEM) technique, require 2-D airfoil data as an input parameter (prediction methods for the wind turbine performance are well summarized by Hansen et al. (2006) [45]). A substantial number of airfoil characteristics in the aerospace engineering industry have been accumulated but the data on high angles of attack and thick airfoils are relatively sparse. These data are necessary for assessing wind turbine aerodynamics. Thus building a reliable 2-D airfoil database with various angles of attack and airfoils would serve, as the backbone of modelling and prediction for wind turbine aerodynamics.

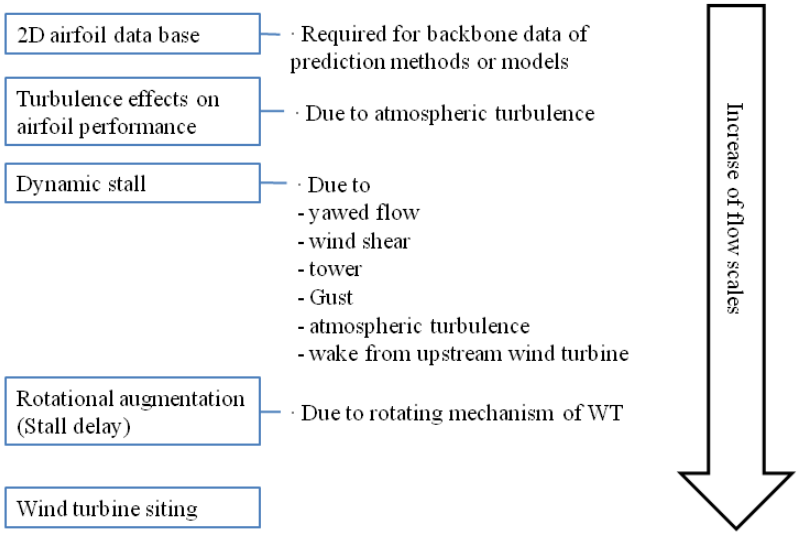

FIGURE 1.2: Topics in wind turbine aerodynamics (in boxes): their reasons of study and/or causes

1.2.2 The effect of turbulence on wind turbine aerodynamics

From the windmill to modern commercial wind turbines, all such devices are placed on the earth's surface. The surface is covered with the atmosphere and the lowest part is the atmospheric boundary layer (ABL) which is almost always turbulent. Consequentially, turbulence is an unavoidable factor in wind turbine aerodynamics and different turbulence levels lead to different aerodynamic characteristics for the blade. Therefore the turbulence effects on the airfoil characteristics are important issues in wind turbine aerodynamics. For realistic prediction methods for the wind turbine performance, the structure and characteristics of the atmospheric boundary layer need to be understood. Before literature for the effects of turbulence on airfoil flows is reviewed, the characteristics of the atmospheric boundary layer are summarized.

Atmospheric boundary layer

Stull (1988) [165] defined the atmospheric boundary layer as, "*part of troposphere that is directly influenced by the presence of the earth's surface, and responds to surface forcings with a timescale of about an hour or less*". The thickness of the atmospheric boundary layer (order of 1km) varies depending on the pressure, latitude and temperature. Above the atmospheric boundary layer, there is a free atmosphere which is of the order of 11km thick as shown in Fig. 1.3(a). Even the largest modern wind turbine, up to 200m height, lies within the atmospheric boundary layer, thus the atmospheric boundary layer directly affects the wind turbines' performance. The characteristics of the boundary layer compared with the free atmosphere are listed as [165],

- Almost continuously turbulent over its whole depth.

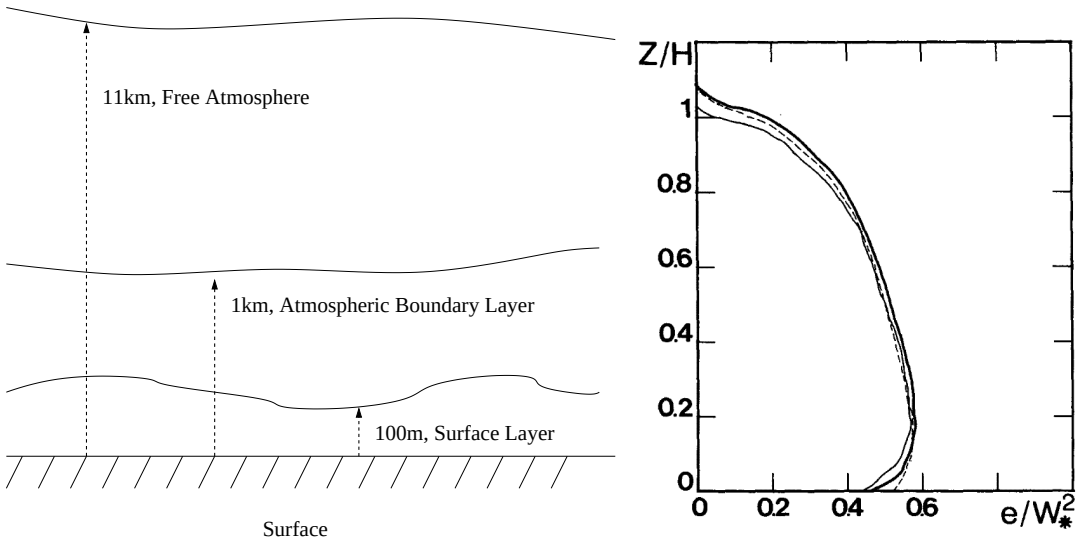

(a) (b)

FIGURE 1.3: (a) The structure of the atmosphere (not to scale) and (b) the vertical profile of normalized turbulence kinetic energy in the daytime at 1200 (dashed line), 1400 (thick solid line) and 1600 (thin solid line) [10].

- Strong drag against the earth's surface. Large energy dissipation.
- Rapid turbulence mixing in the vertical and horizontal direction.
- Near logarithmic wind speed profile in the surface layer.

The bottom 10% (50-100m) of the atmospheric boundary layer is the surface layer, see Fig. 1.3(a), and this layer has approximately constant shearing stress (in the vertical direction), where the flow is insensitive to the earth's rotation. The wind structure of the surface layer is determined primarily by the surface friction and vertical gradient of temperature. The rest of the atmospheric boundary layer has a variable shearing stress and its wind structure is influenced by the surface friction, temperature gradient and also the earth's rotation. Fig. 1.3(b) shows the vertical profile of turbulent kinetic energy (TKE) in the atmospheric boundary layer. H is approximated to the thickness of the atmospheric boundary layer during the daytime. e denotes the TKE and W_* is the convective velocity scale (see Stull (1988) [165] for the definition) which reaches $1-2$m/s in the daytime with vigorous heating at the ground.

The effect of turbulence on the flow over an airfoil

Wind turbines are operated in the atmospheric boundary layer and are subjected to complicated environments. To simplify the problem, the effect of freestream (isotropic and shear-free) turbulence on airfoil aerodynamics was investigated. This topic was initiated to detect the discrepancies of airfoil measurements in different wind tunnels in the 1930s [164]. Stack (1931) [164] measured the effects of different turbulence intensities on aerodynamic performances for five different airfoils including NACA 0006 and NACA

0021. The objective of this study was to identify discrepancies in the test results from different wind tunnels. It showed the maximum lift increased as the turbulence level increased.

Hoffmann (1991) [49] tested a NACA 0015 airfoil to observe effects of freestream turbulence. The Reynolds number in his experiment was $250,000$, freestream turbulence intensity varied from 0.25% to 12% and aspect ratio of the test wing was 2.9. He reported that the maximum lift coefficient increased with increasing freestream turbulence up to 9% without a significant increase of the drag coefficient. Oil flow visualizations showed that the laminar separation bubble disappeared in high freestream turbulence and the stall angle was delayed to a higher point.

Huang and Lee (1999) [52] tested the effects of turbulence on the surface flow characteristics and aerodynamic forces on a NACA 0012 airfoil. They tested various Reynolds numbers, $Re = 30,000 - 120,000$, with various angles of attack up to 20°. They reported that separation points are delayed towards the trailing edge as the turbulence intensity increases. However, the freestream turbulence effect was not obvious at the high Reynolds number. This might be due to too low turbulence intensities ($TI < 0.65\%$) in their work. In addition, they found that the bubble length reduced significantly when the turbulence intensity increased. The lift-to-drag ratio decreased and stall was delayed as the turbulence intensity increased.

A sectional blade of wind turbines experiences wide angles of attack, more than 90° in extreme cases. The lower layer of the atmosphere and the wake from wind turbines in a wind farm are in the high turbulence regions. Thus a wide range of different angles of attack and turbulence intensities have to be considered for wind turbine aerodynamics. Devinant et al. (2002) [23] measured the flow over a NACA 64_4-421 airfoil for varying turbulence intensities, $0.5\% < TI < 16\%$, angles of attack, $-10° < \alpha < 90°$ and Reynolds numbers, $100,000 < Re < 700,000$. They reported that the freestream turbulence intensity affected aerodynamic characteristics for the airfoil and these effects were also a function of Reynolds number. Increases of the turbulence level decreased the lift gradient in the linear region (before stall) and also delayed the separation point. The maximum lift coefficients tended to increase as Reynolds number increased but the Reynolds number effects were not significant in high turbulence.

A numerical study on the effect of turbulence on the flow over an airfoil was conducted by Gilling (2009) [37], but he reported that the turbulence effects on the stall angle could not be predicted by the method that he applied. He used the detached eddy simulation for the turbulence model and a synthetic turbulence inflow to generate freestream turbulence. An advanced approach, such as LES, might be needed to capture the effect of freestream turbulence over the flow over an airfoil.

1.2.3 Dynamic stall

Operating conditions for wind turbines provide the situation in which dynamic stall can occur. Dynamic stall is a phenomenon associated with an unsteady airfoil motion that presents large hysteresis on the lift and pitching moments while the time varying incidence is beyond its static stall angle [15]. On a pitching airfoil, stall appears at a higher angle of attack than the static stall angle. Also the lift and moment reveal large hysteresis with respect to angle of attack [98]. Yawed flow (when wind is not normal to the rotating plane of a turbine), wind shear, tower shadow, gust, atmospheric turbulence and wake from the upstream turbine in a wind farm, all generate an unsteady inflow condition which can lead to dynamic stall.

Fig. 1.4 shows the chronological events of dynamic stall for a pitching NACA 0012 airfoil at $k_{\mathrm{red}} = 0.15$, $Re = 2.5 \times 10^6$ and $\alpha = 15^\circ + 10^\circ \sin(\omega t)$ (see Eq. 1.1 for k_{red}). Carr et al. (1977) [15] reported that virtually all airfoils experienced a fully developed dynamic stall. They presented an illustrative description of the dynamic stall events as shown in Fig. 1.4. Dynamic stall is initiated as the pitching airfoil passes its static stall angle at (a) in Fig. 1.4. The boundary layer is thin and there is no discernible flow reversal within the viscous layer, i.e. stall is delayed. The reversed flow emerges from the trailing edge and proceeds towards the leading edge as incidence increases while the inviscid flow is still attached at (b) in Fig. 1.4. When the viscous flow can no longer remain attached, an energetic vortex develops at the leading edge ((e) in Fig. 1.4). The generated vortex which is called the leading edge vortex (LEV), grows fast and convects downstream rapidly. The LEV creates a low pressure region over the airfoil resulting in an increase in the lift slope (see (e) - (h) in Fig. 1.4) while the LEV resides on the upper airfoil surface. As the LEV passes the pitching pivot point, the pitching moment starts to drop, referred as the moment-stall [15] at (f) in Fig. 1.4, and the flow is fully separated after the LEV sheds from the trailing edge. The flow is attached again as incidence passes the lowest angle of attack.

Many experimental studies were conducted on dynamic stall. Carr et al. (1977) [15] performed the experiments to examine the effects of the leading edge shape, camber and variable parameters based on a NACA 0012 airfoil. They summarized that airfoil geometry, frequency of pitching, amplitude of pitching and Reynolds number were the parameters affecting dynamic stall, in order of decreasing importance. They also reported that locations of the flow reversal and flow separation were distinctively different on a pitching airfoil while they occurred at almost the same point on a static airfoil. For the purpose of helicopter rotor design, extensive studies on dynamic stall of oscillating airfoils were performed [15, 95, 98, 99]. Their interests were, however, on relatively small amplitudes of oscillation and small mean angles of attack because helicopters were designed to avoid deep stall conditions [12].

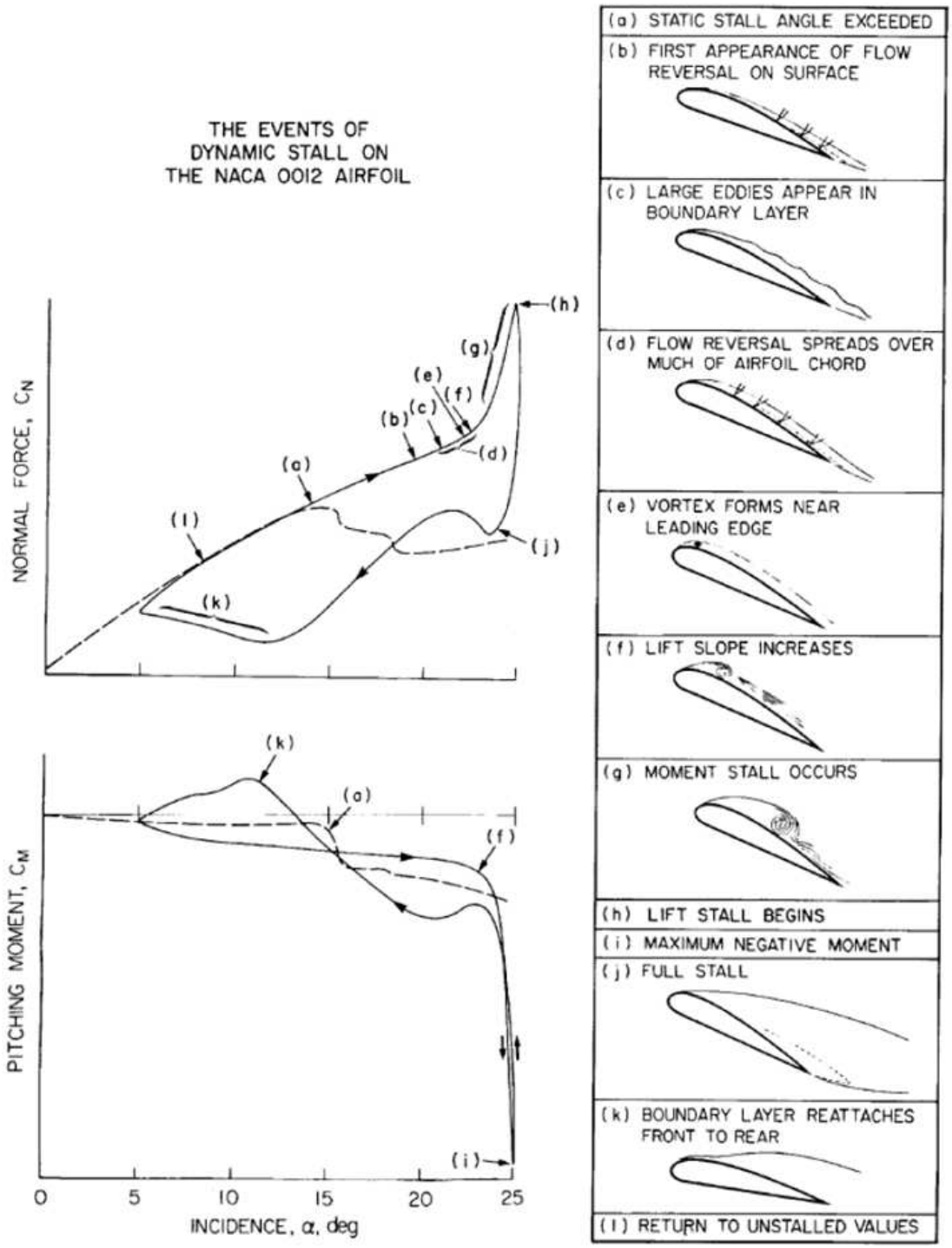

FIGURE 1.4: The events of dynamic stall on a NACA 0012 airfoil [15].

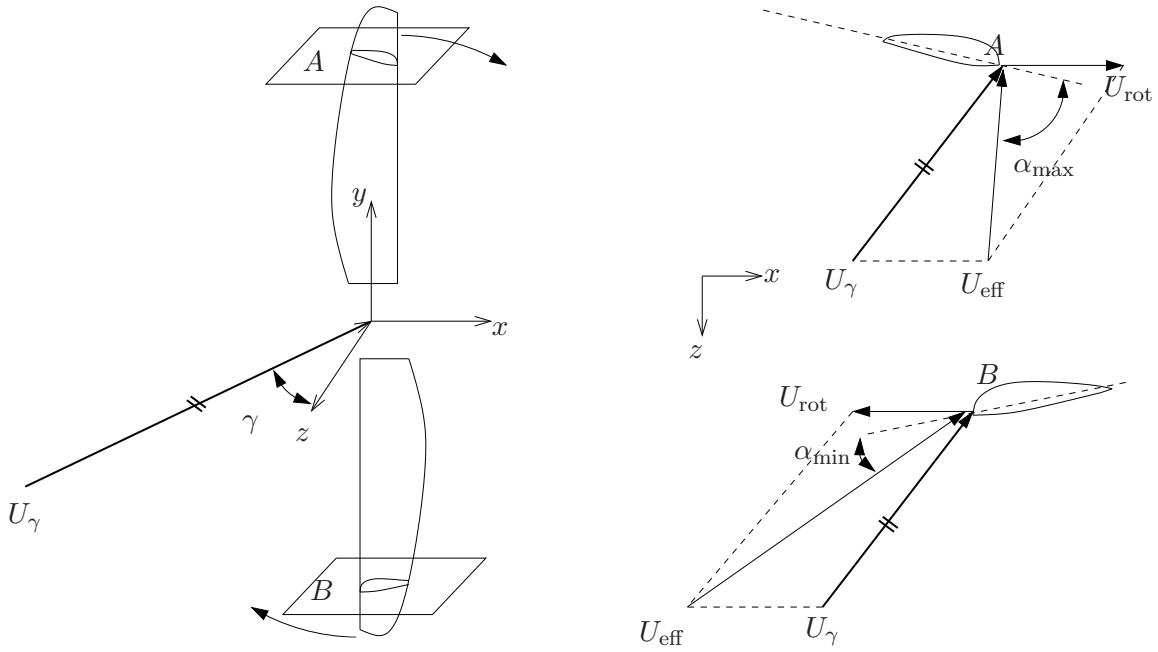

FIGURE 1.5: A local angle of attack of the wind turbine blade under the yawed flow. z is the axis of rotation, U_γ is the yawed flow velocity, $U_{\rm rot}$ is the rotating speed, α is the local angle of attack and $U_{\rm eff}$ is the effective velocity.

Does dynamic stall occur on wind turbines?

In wind turbine aerodynamics, dynamic stall is characterized by the rotating frequency of wind turbines. As the upstream wind is not normal to the rotating plane, the sectional blade operates in a periodically oscillating condition at the frequency of the turbine rotation. Fig. 1.5 shows the sectional changes of angle of attack under yawed flow. Note that dynamic stall can also occur due to a dynamic inflow and atmospheric turbulence etc. but the mechanism for dynamic stall is the same in principle.

One may argue whether dynamic stall occurs on a wind turbine or not because, at a glance, the blade does not seem to rotate fast enough to go through such a dramatic unsteady phenomenon. To understand this question, we need to consider the relation between the period (time unit) for the rotation and the time scale for the flow over each section of blades. This relation leads us to the reduced frequency,

$$k_{\rm red} = \frac{\omega c}{2U_\infty}, \tag{1.1}$$

where ω is the pitching frequency, c is the chord length and U_∞ is the freestream velocity. In wind turbine aerodynamics, ω is characterized by the rotating frequency of the blade and U_∞ is determined by the upstream velocity and the radius distance from the hub, see Eq. 1.2. A considerable number of works were conducted on dynamic stall for variable reduced frequencies both on pitching airfoils [15, 85, 98, 99, 120] and rotating blades

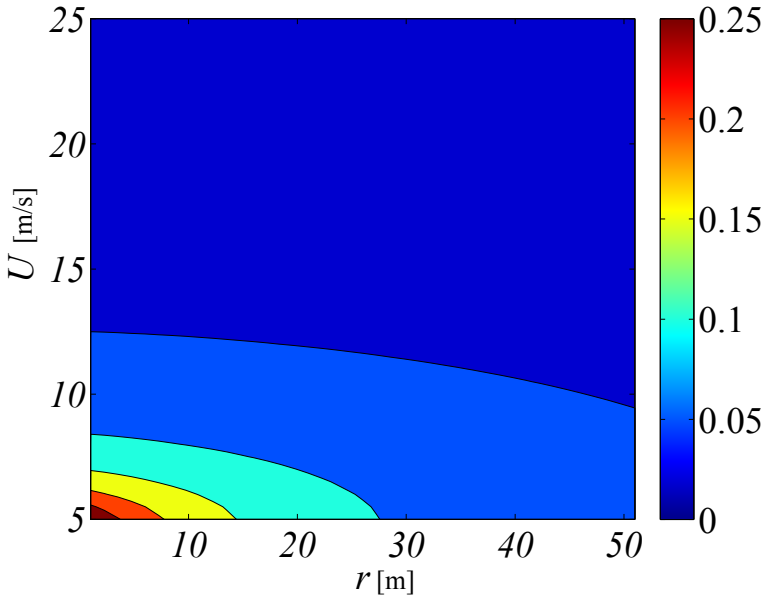

FIGURE 1.6: A reduced frequency (k_{red}) contour for various freestream velocities (U_∞) at different radial positions (r). It is assumed that the angular frequency is 15 rpm and constant chord is 2m.

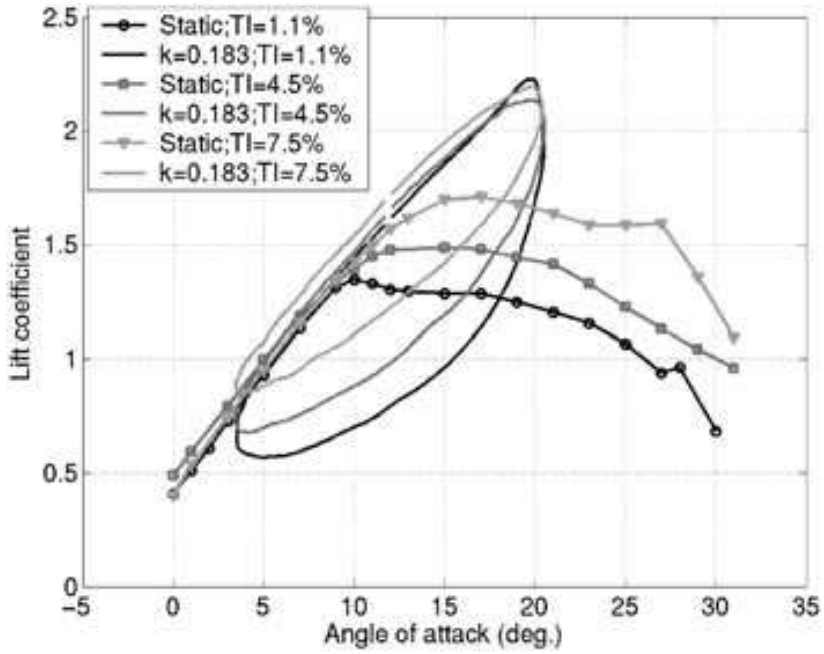

FIGURE 1.7: Experimental data [1] for the effect of freestream turbulence on the lift coefficients for a pitching airfoil. A NACA 64_4-421 airfoil was used and the conditions were $Re_c \approx 10^6$, $\alpha = 8° + 12°\sin(\omega t)$ and $k_{\text{red}} = 0.183$.

TABLE 1.1: Summary of literature on dynamic stall. α_0 and α_1 are the mean angle and pitching amplitude. The tip speed ratio (TSR) is $\mathrm{TSR} = r\Omega/U_\infty$ and k_{red} from the rotating blades are based on U_{eff} in Eq. 1.2

	Authors	Method	Re $[10^6]$	k_{red}	Airfoils	α_0 [°]	α_1 [°]
Oscillating airfoil	Carr et al. [15]	Experiment	$1.3-3.5$	$0.02-0.25$	NACA0012, cambered airfoils	$6-15$	$6-14$
	McCroskey et al. [99], McCalister et al. [97]	Experiment	$0.5-4$	$0.05-0.25$	NACA0012, 7 more types	$6-15$	$6-14$
	Piziali [120]	Experiment	2	$0.04-0.2$	NACA0015	$4-17$	$2-5$
	Ekaterinaris and Menter [29]	CFD	$2-4$	0.1	NACA0012, NACA0015	$4-15$	$4.2-5$
	Raffel et al. [123]	Experiment	0.373	0.15	NACA0012	15	10
	Ramsay et al. [126]	Experiment	$0.75-1.4$	$0.025-0.1$	S809	$8-20$	$5.5-10$
	Barakos and Drikakis [5]	CFD	$1-4.6$	$0.1-0.25$	NACA0012, NACA0015	$2.8-17$	$2.4-10$
	Lee and Gerontakos [85]	Experiment	0.135	$0.025-0.1$	NACA0012	$0-10$	$5-15$
	Amandolèse and Széchényl [1]	Experiment	1	$0.018-0.18$	NACA 64_4-421	12	$2-8$
	Wang et al. [177]	CFD	$0.135-0.373$	$0.1-0.15$	NACA0012	$10-15$	$10-15$

	Authors	Method	TSR	k_{red}	Airfoils
Rotating blade	Butterfield et al. [12]	Experiment	2.82	$0.04-0.12$	S809
	Shipley et al. [145]	Experiment	$1.7-6.3$	$0.04-0.21$	S809
	Schreck and Robinson [141]	Experiment	$2.5-4.2$	$0.03-0.26$	S809

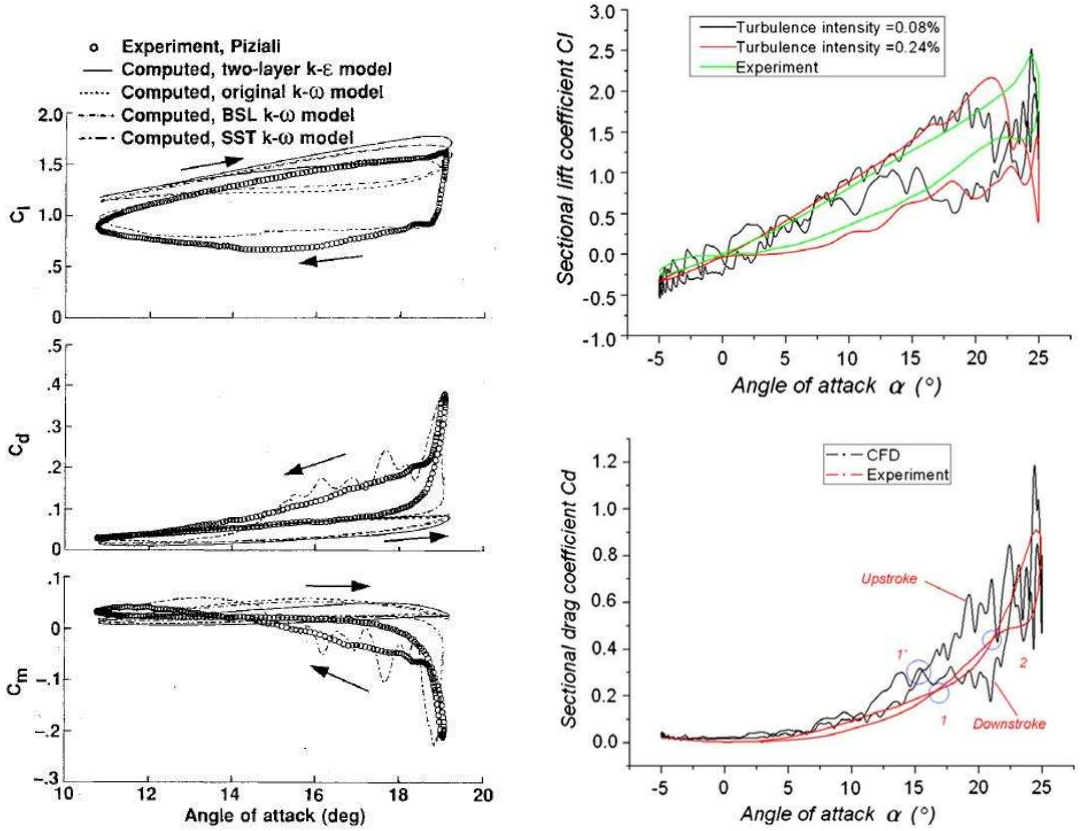

(a) Ekaterinaris and Menter (1994) [29]

(b) Wang et al. (2010) [177]

FIGURE 1.8: Hysteresis of the aerodynamic forces: (a) NACA 0015 airfoil, $\alpha(t) = 15° + 10° \sin(\omega t)$, $k_{\text{red}} = 0.1$, $Re = 2 \times 10^6$; (b) NACA 0012 airfoil, $\alpha(t) = 10° + 15° \sin(\omega t)$, $k_{\text{red}} = 0.1$, $Re = 1.35 \times 10^5$.

[12, 126, 145]. Previous studies are summarized in Table 1.1. To estimate the reduced frequency for the rotating blades, the effective velocity, U_{eff}, is used instead of U_∞ in Eq. 1.1 and it is defined as,

$$U_{\text{eff}} = \sqrt{(U_\infty)^2 + (r\Omega)^2}, \tag{1.2}$$

where Ω is the angular velocity of turbines. Modern large wind turbines have a 100m (or even larger) blade diameter and the cut-in and cut-out wind speeds are generally 5m/s and 25m/s respectively. With these conditions, reduced frequencies at each radial position (r) are shown in Fig. 1.6. The reduced frequencies based on the operating conditions of a modern large wind turbine as shown in Fig. 1.6, are mostly placed within the range at which dynamic stall was reported in literature (see Table 1.1). Thus dynamic stall does occur on wind turbines.

Numerical studies on dynamic stall

As computing power has increased, dynamic stall on a pitching airfoil has been investigated by calculating the Reynolds Averaged Navier-Stokes (RANS) equations. Ekaterinaris and Menter (1994) [29], Barakos and Drikakis (2000) [5] and Wang et al. (2010) [177] presented numerical studies on dynamic stall and these showed good agreement with the measurements for some cases. Ekaterianris and Platzer (1997) [30] presented a comprehensive review on the prediction methods for dynamic stall. They pointed out that RANS approaches were not adequate to predict the aerodynamic hysteresis for the complex flows, such as the flow reattachment during the downstroke and deep stall.

Fig. 1.8(a) shows the hysteresis of aerodynamic forces on a NACA 0012 airfoil by using RANS turbulence models. The drag and pitching moment coefficients reveal oscillatory behaviours due to strong 3-D effects during the downstroke. Wang et al. [177] confirmed that 2-D RANS models were limited where the flow was fully detached, e.g. at a high angle of attack (see Fig. 1.8(b)). They reported that advanced CFD methods such as large-eddy simulations or detached-eddy simulations had to be adopted to capture the hysteresis more accurately.

The effect of freestream turbulence on dynamic stall

As mentioned earlier in Sec. 1.2.2, the wind turbine's operating condition is always turbulent. Thus it is of great interest to investigate the effect of turbulence on dynamic loads on wind turbines but there is little work on this subject. Amandolèse and Széchényi (2004) [1] tested the effects of the mean angle of attack, reduced frequency, pitching amplitude and turbulence intensity on dynamic stall of a pitching airfoil. They reported that the lift overshoot and time delay of the maximum lift in dynamic stall decreased as the turbulence intensity decreased. There is no numerical work on this subject to our knowledge.

1.2.4 Rotational augmentation

Rotational augmentation is the phenomenon that stall occurs at a higher angle of attack on a rotating blade than that on a static airfoil. Rotational augmentation is generally known as stall delay but the term, rotational augmentation, is used in this study to avoid the confusion with the stall delay in dynamic stall. Fig. 1.9 shows the rotational augmentation on a rotating blade. In many prediction models for the wind turbine performance, 2-D airfoil data are used as input parameters. Understanding and identifying the exact mechanism for rotational augmentation is necessary in extrapolating the 2-D airfoil data to the prediction models.

Rotational augmentation was observed for the first time by Himmelskamp (1945) [47]. Through analytical, experimental, numerical approaches and their cross validations, rotational augmentation was characterized, measured and quantified. Some of

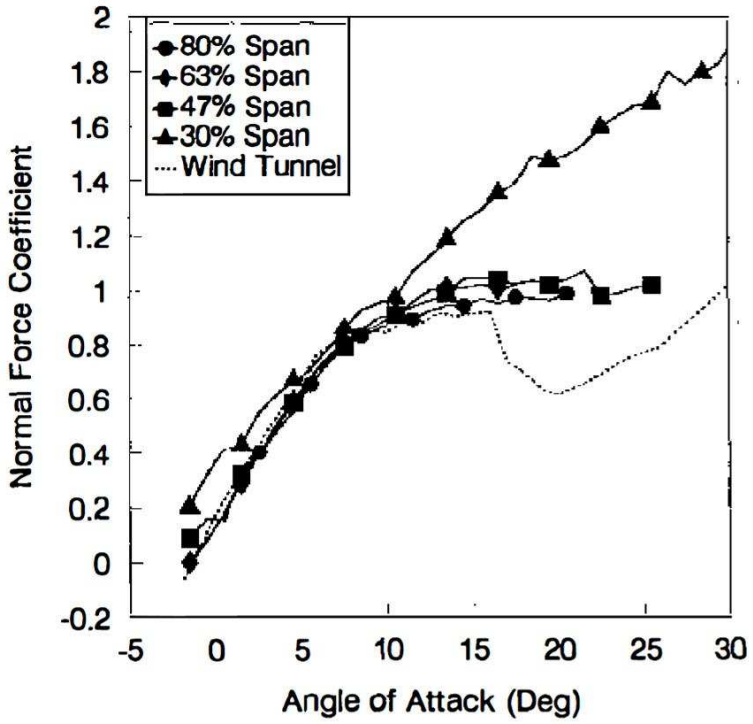

FIGURE 1.9: Normal force coefficients measured on a rotating blade and a static airfoil ($\cdots$, wind tunnel). Data was taken from an S809 airfoil with a constant 0.5m chord, zero twist, 5m blade, 72RPM rotating speed [44].

these works simply observed the phenomena and some explained the mechanisms for rotational augmentation.

An analytical solution for the 3-D laminar boundary layer on a rotating flat plate was suggested by Fogarty (1951) [33]. He presented the radial velocity profile on the rotating laminar boundary layer and reported that the separation line was unaffected by the rotation. Fogarty's [33] solution was further developed by different research groups [50, 106, 131, 168] for general cases such as the flow in a rotating helical coordinate system. Lakshminarayana et al. (1972) [80] derived the momentum integral equations for the turbulent boundary layer on a rotating helical blade and showed reasonable agreement for the skin-friction with the measurement.

In experiments, comparisons for the aerodynamic forces between a rotating blade and static airfoil were conducted by [13, 129, 138] and they all showed the lift enhancement especially at the inner section of the rotating blade. Schreck and Robinson (2002) [138] reported the relations between the spanwise pressure gradient and normal force amplification on the rotating blade surface. Their following works [137, 139, 140] characterized rotational augmentation further. McCroskey and Yaggy (1968) [100] reported that the cross flow on a helicopter blade tended to delay the separation on the retreating side of the rotor. The cross validation between measurements and calculations were also reported in [51, 142].

Sicot et al. (2008) [148] measured effects of grid turbulence and rotation on the separation point of the rotating blade. They reported that the separation points showed little differences between rotating and non-rotating blades at the given turbulence intensity ($TI \approx 9\%$). The separation points, however, were delayed towards the trailing edge as the turbulence intensity increased for both rotating or non-rotating blades.

Several numerical approaches with the simplified boundary layer equations were used to predict the lift enhancement for a wind turbine blade [11, 18, 26, 154]. Snel et al. (1994) [154] modified the boundary layer equations based on an order-of-magnitude analysis so that the rotational effects were taken into account in the 2-D modified boundary layer equations. They reported that higher lift coefficients were predicted near the rotating axis (i.e. near the hub). Corten (2001) [18] took into account the contribution of the radial velocity in Snel et al.'s equations. Wood (1991) [181], Tangler and Selig (1997) [169] confirmed that the rotational effects (e.g. higher lift near the hub) were small for attached flows. They noted that the local solidity (c/r) was an important parameter in the rotational effects. This was because c/r determined the local angle of attack based on the relation, $U_{\mathrm{rot}} = r\Omega$. As r decreased (closer to the hub), U_{rot} decreased and the effective angle of attack increased resulting in flow separations (see Fig. 1.5). Thus the solidity was equivalent to the radial position on the rotating blade. Sørensen et al. (2002) [156] simulated a full scale blade flow in a rotating reference frame with a RANS model and the result showed good agreement with measurement. Quasi-3D Navier-Stokes equations were derived by Chaviaropoulos and Hansen (2000) [17], Shen and Sørensen (1999) [144] and it was confirmed that the rotational effects depended on the radius to chord ratio (r/c). Gross et al. (2012) [39] computed a sectional blade in a rotating reference frame and they reported that the radial flow destabilized the flow and thus delayed separation.

The mechanism for rotational augmentation were explained in several ways [17, 39, 44, 46, 154, 156, 170] but perhaps they are all related. The mechanisms which have been introduced in literature can be summarized mainly in two groups. Firstly, the centrifugal force pushes the air on the blade to the tip and the mass depletion due to the radial flow thins the boundary layer thickness leading to a low pressure on the suction side. This mechanism is called centrifugal (or spanwise, radial) pumping. Secondly, the radial flow to the blade tip provides the Coriolis acceleration toward the trailing edge. This acceleration acts as a favourable pressure gradient and thus increases the lift. Gross et al. [39] further scrutinized the mechanisms for rotational augmentation. They argued that the spanwise flow provided the cross-flow instability which triggered early transition, and then it delayed separation and increased lift. They excluded the mass depletion effect by adopting a periodic boundary condition in the spanwise direction for the sectional blade simulation. However, they did not differentiate the contribution of the Coriolis effect on rotational augmentation from the cross-flow instability.

The mechanism for rotational augmentation is not fully understood yet and it is important to understand this to design prediction models.

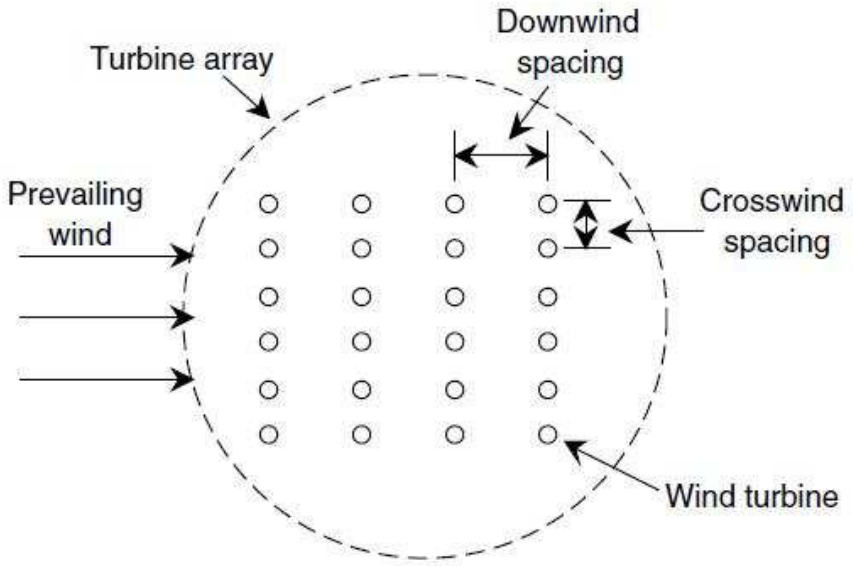

FIGURE 1.10: A sketch for a wind farm array from Manwell et al. (2002) [93].

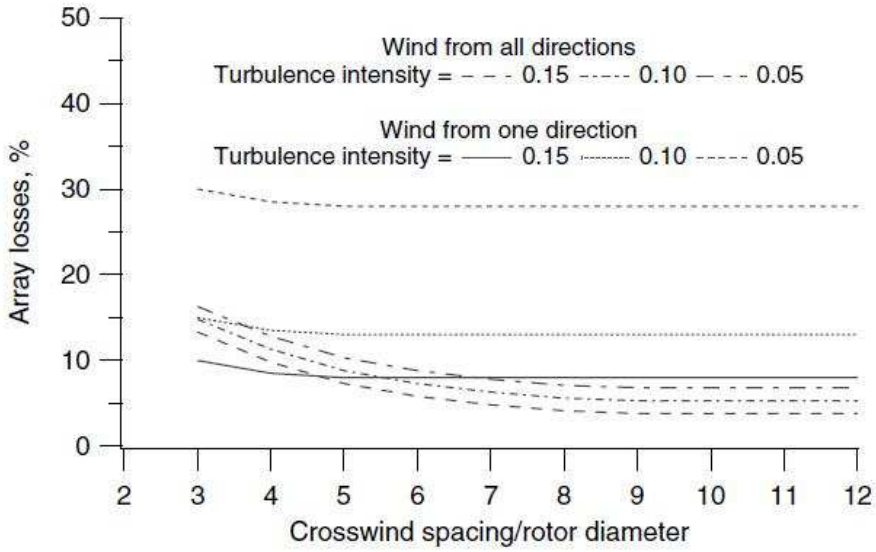

FIGURE 1.11: A wind farm array loss from Manwell et al. (2002) [93].

1.2.5 Wind turbine siting and turbine wake

Once a wind turbine is designed, a single or a group of wind turbines has to be placed at a certain site with a certain configuration. Depending on the place and the configuration,

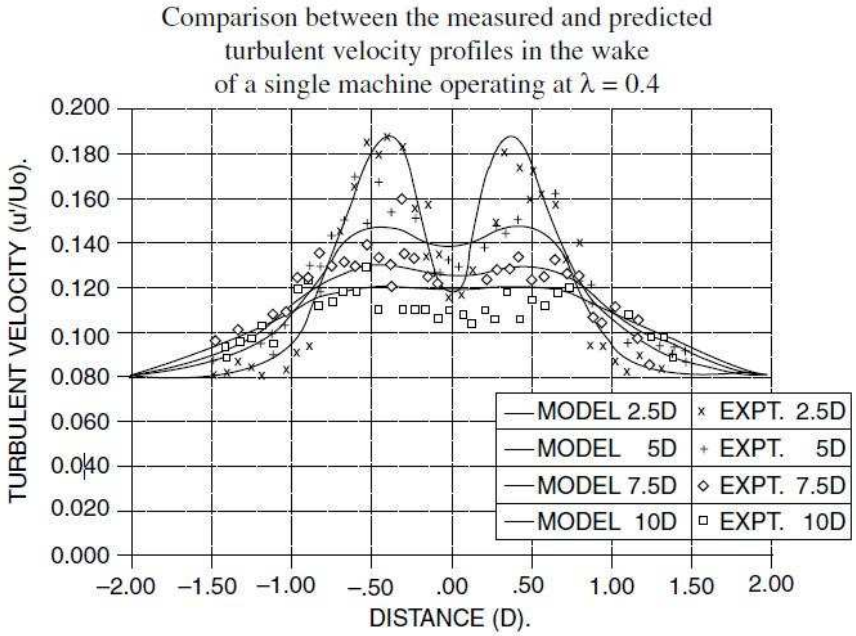

FIGURE 1.12: The *root-mean-square* of the turbulence fluctuations downwind of a wind turbine where λ is the tip speed ratio from Manwell et al. (2002) [93].

total energy generation varies, thus the wind turbine siting is also a critical issue in wind turbine aerodynamics.

The major objective of siting studies is to allocate wind turbine(s) to maximize the power output and to minimize noise emissions and visual effects [93]. The scope of the siting study has a very wide range, from the resource assessments of a geographical scale to decision making of a single wind turbine placement on a site or in a wind farm. Placing of an individual wind turbine is called micrositing [93]. Due to this wide scope of range, the wind turbine siting study has to consider many other factors apart from the aerodynamic or meteorological aspects, such as ecological impact, safety, public acceptance and infrastructure costs etc. Most of these factors are beyond the scope of the current study but some aspects of siting study are summarized which are directly related to aerodynamics such as the effects of wind shear, atmospheric turbulence and wake interaction.

Kinetic energy in the wind is extracted by wind turbines, thus the downstream wind (wake) has a lower wind speed and higher turbulence level than the prevailing wind. The power output of wind turbines placed in the downstream wake, decreases due to the low wind speed and the wake-induced fatigue of these turbines increases due to the high turbulence level.

Array loss

The energy production from a wind farm is not the same as the sum of the energy outputs from a stand-alone wind turbine under the same wind conditions, i.e. mean

wind velocity, turbulence intensity etc. This difference is referred as the array loss and defined as,

$$\text{Array loss} = 1 - \frac{\text{Annual energy of whole array}}{(\text{Annual energy of one isolated turbine})(\text{total no. of turbines})}. \quad (1.3)$$

The downwind, cross flow spacing (see Fig. 1.10 for the definitions) and the turbulence intensity are the main parameters of the array loss. Fig. 1.11 shows the array loss from a 6 by 6 hypothetical wind farm that has 8 turbine blade diameter of a downwind spacing among individual turbines. It illustrates that the effects of the cross spacing and turbulence intensity on the array loss are significant.

Turbine wake
The turbine wake affects the inflow conditions for the downstream turbines thus it affects the performance of them. Fig. 1.12 shows the *root-mean-square* of the turbulence fluctuations at different downstream (unit of rotor diameter) locations at a given tip velocity ratio and 0.08 turbulence intensity. Tip vortices induce a higher turbulence level at the annular region of the blade tips and wake turbulence gradually recovered to the level of the ambient turbulence intensity as it is convected to the downstream region.

1.2.6 Summary on the issues raised in the topics

Some of the major topics in wind turbine aerodynamics are reviewed and key points for each topic are introduced. Among these topics, the effect of turbulence on the flow over an airfoil, dynamic stall and rotational augmentation are directly related to the wind turbine aerodynamics in atmospheric turbulence and its rotating mechanism.

The effects of turbulence on the flow over an airfoil were measured in the wind tunnel and quantified with variable parameters, e.g. airfoil geometry, turbulence intensity etc. There are still issues to be addressed in this subject such as the effect of the turbulence length scale. Also numerical studies on this subject were not successful to date. Due to advantages in the numerical study, it is important to develop a reliable framework of numerical approaches for turbulence effects on wind turbine blades. For example, it is relatively easy to reproduce realistic turbulence (e.g. inhomogeneous and shear stress containing) in numerical simulations.

In literature, many measurements and simulations showed that **dynamic stall** occurs on a wind turbine blade when it is subjected to various operating conditions such as yawed flow, wind shear etc. Predictions for the dynamic loads on the blade are important as they determine the expected service life. An accurate prediction for stall delay

and dynamic stall is still challenging with a conventional approach such as RANS, thus an advanced approach, e.g. LES, is required for the reliable prediction for dynamic loads on wind turbines and perhaps for improving RANS models. In addition, the effects of freestream turbulence need to be taken into account because they are intrinsic parts of the wind turbines' operating conditions.

Previous studies on **rotational augmentation** have contributed to characterizing and understanding this phenomenon but it is not fully clarified yet what are the causes of the rotational augmentation and their significance. Numerical simulations can elucidate physical aspects of these questions in a manner which is difficult to achieve in a wind tunnel experiment. The radial flow due to the centrifugal acceleration and Coriolis effects in the chordwise direction can be dealt with separately in numerical simulations. Therefore individual and combined roles of these factors on rotational augmentation can be understood by an appropriate numerical approach.

1.3 Thesis outline

Most of the existing numerical prediction methods for wind turbine performance such as blade element momentum (BEM), lifting line or surface methods and their applications, require 2-D airfoil data as input parameters. Errors in these predictions are mainly attributed to different behaviours of the boundary layer between a 2-D airfoil and 3-D rotating blade. Note that the boundary layer in this context means the flow adjacent to the blade, not the atmospheric boundary layer. For deeper understanding of wind turbine aerodynamics and better prediction models, an alternative approach is desirable which does not depend on 2-D airfoil data sets.

Thanks to ever growing computing power, details of the boundary layer on wind turbine blades can nowadays be resolved by numerical methods. Wind turbine designers can be free from many empirical models, if the crucial details of the boundary layer on the blade are available. Thus boundary layer resolving CFD is adopted for this study in order to understand the wind turbine aerodynamics and to improve the aerodynamic load predictions. Although the boundary layer can be resolved with the enhanced computing power, turbulence in the wind turbine flow still needs to be modelled (or partially modelled) due to its wide range of scales. Among different types of turbulence models, a RANS approach adopts an averaging concept in which the velocity can be decomposed into the mean and the fluctuations. The turbulence model in the RANS approach should represent all turbulence fluctuations. Wind turbine blades experience a wide range of angles of attack due to the atmospheric boundary layer and their rotation. Under this wide range of angles of attack, stall is frequent over the blade. To estimate the peak power and dynamic loads under deep stall, unsteady effects have to be considered. The unsteady RANS (URANS) can provide a time dependent solution but the separation

of time scales between unsteady flows and turbulence is ambiguous. Especially, when the time scale of the atmospheric turbulence is comparable with that of rotation, the URANS approach is debatable. To avoid this ambiguity, large-eddy simulation (LES) is adopted for the current study. Details of the main concept and related techniques for LES are presented in Ch. 2. The discretization practices which are important for the current research are reviewed in Ch. 3.

To investigate the effects of turbulence on wind turbine aerodynamics, a time dependent turbulent inflow boundary condition is used for LES calculations. Two conditions need to be satisfied for the turbulent inflow boundary condition in the present study. Firstly, the turbulence generation technique should be substantially more efficient compared with the computational time required for developing turbulence naturally from the laminar state. Secondly, the turbulent inflow technique should not produce unphysical pressure fluctuations as the instantaneous pressure is important for dynamic load predictions and aeroacoustic analysis on wind turbines. To achieve the second condition, the turbulent inflow has to satisfy the divergence-free condition. Therefore, a new turbulent inflow for LES which is computationally efficient and satisfies the divergence-free condition is developed in that regard. This new model is presented in Ch. 4 with the assessment of the performance on a plane channel flow.

The new turbulent inflow is then applied to the flow over a static airfoil to provide a reliable framework that is applicable to the flow over wind turbines subjected to freestream turbulence. Details of the methodology and results are presented in Ch. 5. A pitching airfoil is simulated in Ch. 6 to demonstrate the capability of LES on capturing the dynamic stall characteristics. The developed turbulent inflow is used to investigate the impact of freestream turbulence on the dynamic stall characteristics in the same chapter.

The mechanism for rotational augmentation has been explained mainly in two groups; the mass depletion by the centrifugal pumping and Coriolis acceleration toward the trailing edge. However, it has so far not been attempted to identify their contributions separately. In Ch. 7, an attempt is made to isolate the Coriolis effect on rotational augmentation. A sectional blade is simulated in a rotating reference frame. In this simulation, the mass depletion due to the centrifugal pumping and cross-flow instability due to the radial flow are excluded. Therefore the Coriolis effect is identified as the primary mechanism for rotational augmentation. The conclusions and suggestions follow in Ch. 8.

Finally, the novel aspects of the thesis are listed,

- A new turbulent inflow condition is developed which is computationally efficient and satisfies the divergence-free condition. (Chapter 4, the major part is published in Kim, Castro, Xie. *Comput. Fluids*, 2013 [69])

- A reliable framework is suggested for a numerical study regarding the effects of freestream turbulence on aerodynamics and unsteady surface pressure analysis of wind turbine flows. (Chapter 5, part of the work is reported in Kim, Castro, Xie. *UK WES conference, Southampton, UK*, 2012 [68])

- The LES capability is demonstrated for highly separated and strong 3-D flows, e.g. dynamic stall. (Chapter 6, part of the work is reported in Kim, Castro, Xie. *DLES9, Dresden, Germany*, 2013 [70])

- The first attempt is made to investigate the effect of freestream turbulence on dynamic stall *via* numerical approaches. (Chapter 6, part of the work is reported in Kim, Castro, Xie. *DLES9, Dresden, Germany*, 2013 [70])

- The role of the Coriolis effect on rotational augmentation is demonstrated through numerical tests. (Chapter 7, part of the work is reported in Kim, Castro, Xie. *DLES9, Dresden, Germany*, 2013 [70])

Chapter 2

Large-eddy simulations : concepts, modelling and boundary conditions

2.1 Scale separation and governing equations

Turbulence has a wide range of spatial and temporal scales, with the disparity of scales increasing with Reynolds number. The ratio between the largest (l_0) and smallest (η), but yet dynamically active, scales in homogeneous isotropic turbulence is [133],

$$\frac{l_0}{\eta} = O\left(Re^{3/4}\right). \tag{2.1}$$

This means that the number of grid points scales as $O(Re^{9/4})$ for a 3-D turbulent flow to resolve all dynamics of motion in the numerical solution. In the fields of aeronautics and wind energy aerodynamics, Reynolds number reaches $O(10^8)$ [133]. Thus resolving all scales of turbulence at a practical Reynolds number is not possible even with today's largest super computers. Due to this limit, turbulence needs to be modelled; here the term 'modelling' is interpreted in different ways depending on which decomposing method is used. For instance, if one decomposes the flow into mean and fluctuating parts through an ensemble averaging operation, this modelling is called the Reynolds Averaged Navier-Stokes (RANS) approach. If one decomposes the flow into large and small eddies through a filtering operation then it is called large-eddy simulation (LES). The scale separation between the large and small motions through the filtering operation is a critical concept in LES calculations. The terms '*large*' and '*small*' are interchangeably used with '$large \leftrightarrows filtered \leftrightarrows resolved$' and '$small \leftrightarrows residual \leftrightarrows unresolved \leftrightarrows subgrid$ '.

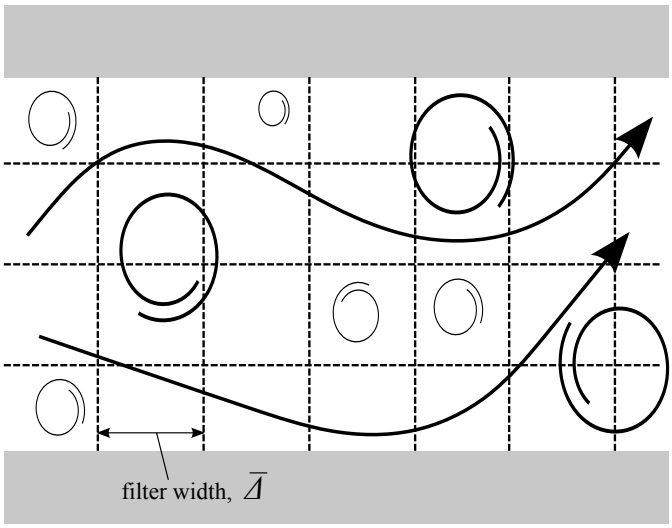

(a)

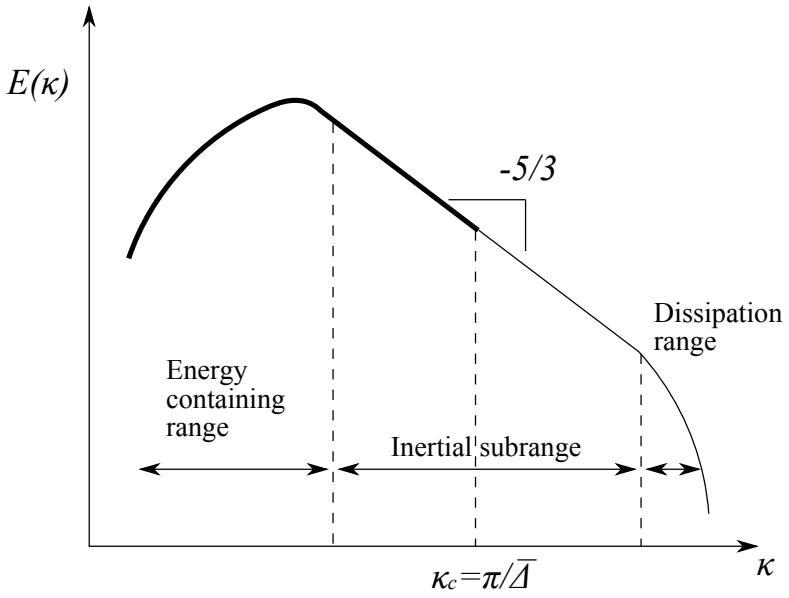

(b)

FIGURE 2.1: The concept of the filtering operation in a (a) physical space and (b) spectral space (in log-scale) where $E(\kappa)$ is the energy spectrum and κ is a wavenumber. The thick and thin lines represent filtered and residual motions respectively. The sketch is taken from Ferziger and Perić (2002) [32], Sagaut (2006) [133].

Typical filtering operations are explained in Sec. 2.1.1.

2.1.1 Spatial filtering

Fig. 2.1 shows the concept of the decomposition between the filtered and residual motions. The cut-off wavenumber, κ_c, is related with the filter width, $\overline{\Delta}$, as $\kappa_c = \frac{\pi}{\overline{\Delta}}$. The cut-off wavenumber needs to be placed at higher than the energy containing range

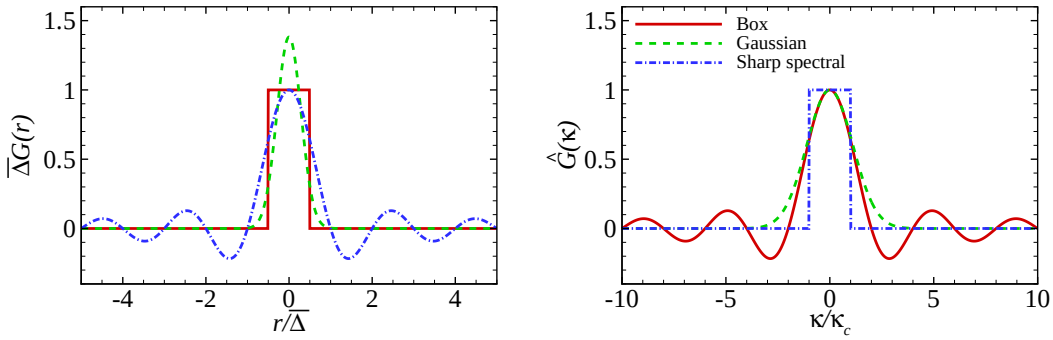

FIGURE 2.2: Filter functions in (a) physical space and (b) spectral space [122].

for LES, see Fig. 2.1(b). To separate the large and small scales, Leonard (1974) [87] introduced a filter operator and it can be applied to the velocity vector fields $\boldsymbol{U}$ as,

$$\overline{\boldsymbol{U}}(\boldsymbol{x}) = \int G(\boldsymbol{r})\boldsymbol{U}(\boldsymbol{x}-\boldsymbol{r})\mathrm{d}\boldsymbol{r}, \tag{2.2}$$

where $\overline{\boldsymbol{U}}$ is a filtered velocity vector and $(\bar{})$ indicates the filtered property. The filter function, G, is associated with the filter width and it is defined in spectral space by using Fourier transform, $\mathcal{F}$,

$$\begin{aligned} \hat{\overline{\boldsymbol{U}}}(\kappa) &= \mathcal{F}\{\overline{\boldsymbol{U}}\}, \\ &= \hat{G}(\kappa)\hat{\boldsymbol{U}}(\kappa), \end{aligned} \tag{2.3}$$

where the filter function in spectral space is defined as [122],

$$\hat{G}(\kappa) = \int_{-\infty}^{\infty} G(r)e^{-i\kappa r}dr = 2\pi\mathcal{F}\{G(r)\} \tag{2.4}$$

and $(\hat{})$ indicates properties in spectral space. There are three classical filter functions and they are shown below in a one-dimensional form.

- Box (top-hat) filter:

$$G(r) = \frac{1}{\overline{\Delta}}H(\frac{1}{2}\overline{\Delta} - r), \tag{2.5}$$

$$\hat{G}(\kappa) = \frac{\sin\frac{1}{2}\kappa\overline{\Delta}}{\frac{1}{2}\kappa\overline{\Delta}}. \tag{2.6}$$

- Gaussian filter:

$$G(r) = \left(\frac{6}{\pi\overline{\Delta}^2}\right)^{1/2}\exp\left(\frac{-6r^2}{\overline{\Delta}^2}\right), \tag{2.7}$$

$$\hat{G}(\kappa) = \exp\left(-\frac{\kappa^2\overline{\Delta}^2}{24}\right). \tag{2.8}$$

- Sharp spectral filter:

$$G(r) = \left(\frac{\sin(\pi r/\overline{\Delta})}{\pi r}\right), \tag{2.9}$$

$$\hat{G}(\kappa) = H(\kappa_c - |\kappa|), \tag{2.10}$$

where H is the Heaviside function. Fig. 2.2 shows the filter functions above, in both physical and spectral space. The box filter has a sharp cut (local) in physical space but it does not in spectral space while the opposite is true for the sharp spectral filter. The Gaussian filter is non-local both in physical and spectral space [133]. Piomelli (1999) [116] applied the three filtering operations on the test function E as shown in Fig. 2.3. The top hat and Gaussian filters smooth both large and small structures while the sharp spectral filter only affects the scale beyond the cut-off wavenumber.

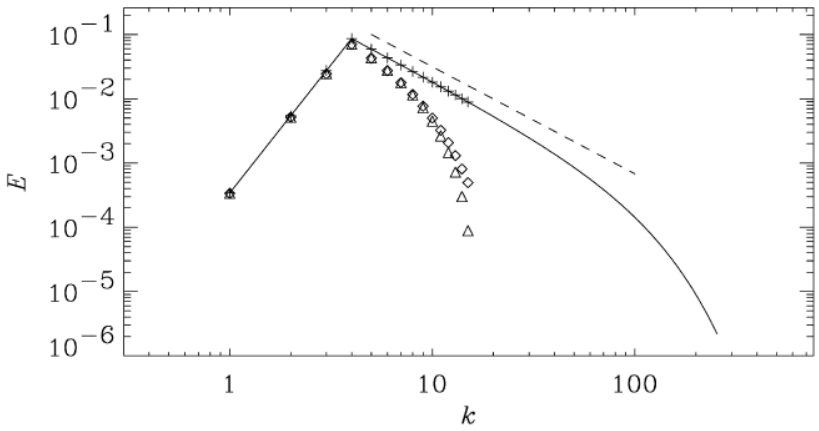

FIGURE 2.3: Filtering of a test function, E, —— unfiltered, + sharp spectral, ◊ Gaussian, △ top hat, - - $\kappa^{-5/3}$ [116].

2.1.2 Unsteady filtered Navier-Stokes equation

By using the filtering methods introduced in the preceding section, the filtered Navier-Stokes equations can be derived. To show the filtering procedure on the Navier-Stokes equations, three filter properties are introduced [133] first,

1. Conservation of constant

$$\overline{a} = a \Leftrightarrow \int_{-\infty}^{\infty} G(r)dr = 1. \tag{2.11}$$

2. Linearity

$$\overline{\phi + \psi} = \overline{\phi} + \overline{\psi}, \tag{2.12}$$

where ϕ and ψ are general scalar properties.

3. Commutation with derivation

$$\overline{\frac{\partial \phi}{\partial \boldsymbol{x}}} = \frac{\partial \overline{\phi}}{\partial \boldsymbol{x}}. \tag{2.13}$$

The commutation property is valid with constant filter width, i.e. isotropic filter. When the flow is inhomogeneous, such as a wall-bounded flow, it would be desirable to use a spatially varying filter, i.e. $G(r, \boldsymbol{x})$. When the filter operator is a function of space, Eq. 2.14 shows that $G(r, \boldsymbol{x})$ does not commute with the derivative by using simple differential algebra,

$$\begin{aligned} \overline{\frac{\partial \phi}{\partial \boldsymbol{x}}} &= \int G(r, \boldsymbol{x}) \frac{\partial \phi}{\partial \boldsymbol{x}} dr \\ &= \int \frac{\partial}{\partial \boldsymbol{x}} \left[G(r, \boldsymbol{x}) \phi \right] dr - \int \phi \frac{\partial}{\partial \boldsymbol{x}} G(r, \boldsymbol{x}) dr \\ &= \frac{\partial \overline{\phi}}{\partial \boldsymbol{x}} - \int \phi \frac{\partial}{\partial \boldsymbol{x}} G(r, \boldsymbol{x}) dr. \end{aligned} \tag{2.14}$$

The second term in the right-hand side of Eq. 2.14 appears due to the non-uniform filter size, which is desirable for many applications. This additional term is referred to as the commutation error. It would be small with a gradually changing filter width since $\frac{\partial}{\partial \boldsymbol{x}} G(r, \boldsymbol{x}) \approx 0$, and thus the commutation errors are not considered in the current study. Further discussions and demonstrations on the commutation error can be found in [36, 89].

The incompressible unsteady Navier-Stokes equations in Cartesian coordinates are,

$$\frac{\partial u_i}{\partial x_i} = 0, \tag{2.15}$$

$$\frac{\partial u_i}{\partial t} + \frac{\partial u_i u_j}{\partial x_j} = -\frac{1}{\rho} \frac{\partial p}{\partial x_i} + \frac{\partial}{\partial x_j} \left(\nu \frac{\partial u_i}{\partial x_j} \right), \tag{2.16}$$

where ρ is the fluid density and ν is the kinematic viscosity. Using the filtering operator, Eq. 2.2, throughout the whole domain, the unsteady filtered Navier-Stokes equations can be obtained,

$$\overline{\mathcal{NS}(\boldsymbol{u})} = \int G(\boldsymbol{r})\,[\mathcal{NS}(\boldsymbol{u})]\,\mathrm{d}\boldsymbol{r}, \tag{2.17}$$

where $\mathcal{NS}$ is the Navier-Stokes operator. By applying the filter properties in Eqs. 2.11 - 2.13, the unsteady filtered Navier-Stokes equations become,

$$\frac{\partial \bar{u}_i}{\partial x_i} = 0, \tag{2.18}$$

$$\frac{\partial \bar{u}_i}{\partial t} + \frac{\partial \overline{u_i u_j}}{\partial x_j} = -\frac{1}{\rho}\frac{\partial \bar{p}}{\partial x_i} + \frac{\partial}{\partial x_j}\left(\nu \frac{\partial \bar{u}_i}{\partial x_j}\right). \tag{2.19}$$

Filtering the Navier-Stokes equations introduces an unknown term, which originates from the second term on the left-hand side (convective term) due to its nonlinearity. This term can be decomposed into the product of the filtered velocities and the contributions of the residual parts.

$$\overline{u_i u_j} = \overline{(\overline{u}_i + u_i'')(\overline{u}_j + u_j'')} = \overline{u}_i \overline{u}_j + \tau_{ij}^{\mathrm{r}}, \tag{2.20}$$

where u_i'' is the residual fluctuation and τ_{ij}^{r} is the residual-stress tensor or subgrid-scale (SGS) stress tensor. Note that $\overline{\overline{u}}_i = \overline{u}_i$. To close the filtered Navier-Stokes equations, this term has to be modelled. τ_{ij}^{r} in Eq. 2.20 represents the contribution of the residual motions. Conventionally it is written in the form of a diffusion term on the right-hand side of the filtered Navier-Stokes equations, see Eq. 2.21.

$$\frac{\partial \bar{u}_i}{\partial t} + \frac{\partial \bar{u}_i \bar{u}_j}{\partial x_j} = -\frac{1}{\rho}\frac{\partial \bar{p}}{\partial x_i} + \frac{\partial}{\partial x_j}\left(\nu \frac{\partial \bar{u}_i}{\partial x_j} - \tau_{ij}^{\mathrm{r}}\right). \tag{2.21}$$

For clarification of the velocity scale notations in large-eddy simulations, the relation among the instantaneous velocity (u_i), resolved (filtered) velocity ($\bar{u}_i$), residual fluctuation (u_i''), mean resolved velocity (U_i) and resolved fluctuation (u_i') are defined as,

$$\begin{aligned} u_i &= \bar{u}_i + u_i'' \\ &= U_i + u_i' + u_i''. \end{aligned} \tag{2.22}$$

2.2 Subgrid scale modelling

The principle of LES is to separate the scales into large (filtered) and small (residual) scales through the filtering operation. The filtered scale is resolved explicitly by the

governing equations, Eq. 2.21, and the residual part is modelled by subgrid-scale (SGS) modelling. The most important idea behind the SGS modelling is the scale invariance property. The Smagorinsky model [151] which is a simple and widely used SGS model is introduced in the following section. Some other SGS models which are important for the current study are reviewed as well. A complete review on LES modelling was presented by Sagaut (2006) [133].

The scale invariance property in turbulent flows was implied by Kolmogorov (1941) [74]. Kolmogorov hypothesized that a range of scales exists in which the length scales are much smaller than the large and energy containing scales but is much larger than the viscous length scale. In this range, the velocity field is 'statistically isotropic' and the energy transfer from the large to small scales (energy cascade) is an inviscid process, since the viscous scale is too small to act at this range, i.e. inertial subrange in Fig. 2.1(b). Then the only important quantity is the energy transfer rate from the large to small scales through the cascade process. When the energy injection and transport from the large scale to the next scale level are balanced, i.e. in equilibrium, then the velocity in the inertial subrange only depends on the energy dissipation rate, ε, and the local length scale, r. Further details on the Kolmogorov hypothesis can be found in Hinze (1975) [48] and Pope (2000) [122]. In spite of the success of the Kolmogorov hypotheses, the notions of 'local isotropy' and 'scale independence' between large and small scales are constantly under revision [14, 186] and details on this discussion would be out of the scope for the current study.

The scale invariance property implies that the normalized velocity increment on dimensional grounds is $\Delta u_r/(r\varepsilon)^{(1/3)}$ where $\Delta u_r = u(x+r) - u(x)$ [163]. Then the longitudinal structure function is defined as,

$$\langle \Delta u_r^n \rangle = C_n \, (r\varepsilon)^{n/3} \,, \tag{2.23}$$

where the integer n is the moment of velocity increments and C_n is a universal constant [163]. The SGS stress tensor τ^{r} in Eq. 2.21 is also scaled with the velocity increment Δu_r on dimensional grounds as,

$$\tau^{\mathrm{r}} \sim \langle \Delta u_r^2 \rangle. \tag{2.24}$$

Using Eqs. 2.23 and 2.24, the moment of velocity increments for the SGS stress contribution is determined, i.e. $n = 2$. Then the SGS stress contribution is scaled as $\tau^{\mathrm{r}}(r) \sim (r\varepsilon)^{2/3}$ for r in the inertial subrange. It implies that $\tau^{\mathrm{r}}(r)$ is scale invariant which means that $\mathcal{C}^{-2/3}\tau^{\mathrm{r}}(\mathcal{C}r)$ is unchanged with the scale transform $r \to \mathcal{C}r$ where $\mathcal{C}$ is a positive constant [102]. Eqs. 2.23 and 2.24 are the most important properties of the scale invariance for the SGS modelling and some models which are based on these properties are introduced.

2.2.1 Smagorinsky model

Viscous stresses are proportional to the strain rate of the velocity in Newton's law of viscosity. This relation is extended to model turbulence stresses in many RANS approaches, which is called the turbulent viscosity hypothesis introduced by Boussinesq (1877). Smagorinsky [151] applied the turbulent viscosity hypothesis on the deviatoric part of the SGS stress as,

$$\tau_{ij}^{\mathrm{r}} = -2\nu_{SGS}\bar{S}_{ij} + \frac{1}{3}\tau_{kk}\delta_{ij}, \tag{2.25}$$

where the Kronecker delta $\delta_{ij} = 1$ for $i = j$, otherwise $\delta_{ij} = 0$. The SGS eddy viscosity, ν_{SGS}, is local and instantaneous. The Smagorinsky model is analogous to the Prandtl's mixing length model but the filter length, $\overline{\Delta}$, is used as the characteristic length scale. In general, the grid size, Δ, is used for the filter length and the cube root of the control volume is used for the grid size, i.e. $\Delta = (\Delta_1\Delta_2\Delta_3)^{1/3}$. Based on the scale invariance property, the eddy viscosity in the Smagorinsky model is proportional to the product of a length scale, Δ, and velocity scale, $\Delta|\overline{S}|$,

$$\nu_{SGS} = (C_s\Delta)^2|\bar{S}|, \tag{2.26}$$

where C_s is the Smagorinsky constant and $|\bar{S}| = \sqrt{2\bar{S}_{ij}\bar{S}_{ij}}$. Though the Smagorinsky model is simple and does not produce numerical instability, it has disadvantages. The model constant in the Smagorinsky model depends on a specific type of flow such as $C_s = 0.17$ for homogeneous turbulence [101] and $C_s = 0.065$ for a plane channel flow [107]. The Smagorinsky model needs a wall damping function such as the van Driest damping to reduce the eddy viscosity in the viscous layer and also ν_{SGS} does not vanish in a laminar flow as long as the strain rate is non-zero as Eq. 2.26.

2.2.2 Dynamic Smagorinsky model

As the coefficient in the Smagroinsky model is not universal and one needs to know C_s in Eq. 2.26 *a priori* for different types of flow. Germano et al. (1991) [35] suggested a new approach which dynamically determined the model constant by comparing subgrid-scale stresses at two different filtered levels. For this purpose, the test filter was introduced and the test filer length, $\widetilde{\overline{\Delta}}$, was assumed to be larger than the filter length, $\overline{\Delta}$. The SGS stresses at these two filter levels are defined as (cf. Eq. 2.20)

$$T_{ij} = \widetilde{\overline{u_iu_j}} - \widetilde{\overline{u}}_i\widetilde{\overline{u}}_j, \tag{2.27}$$

$$\tau_{ij}^{\mathrm{r}} = \overline{u_iu_j} - \overline{u}_i\overline{u}_j. \tag{2.28}$$

Using Eqs. 2.27 and 2.28, the resolved turbulence stress, $\mathcal{L}_{ij}$, is defined as,

$$\begin{aligned}\mathcal{L}_{ij} &= T_{ij} - \widetilde{\tau^{\mathrm{r}}_{ij}} \\ &= \widetilde{\overline{u}_i\overline{u}_j} - \widetilde{\overline{u}}_i\widetilde{\overline{u}}_j.\end{aligned} \tag{2.29}$$

It is noted that $\mathcal{L}_{ij}$ is presented with all known terms in Eq. 2.29. Then the deviatoric part of the SGS stresses at the two filtered levels are modelled in Eqs. 2.30 and 2.31 as in the Smagorinsky model (Eqs. 2.25 and 2.26),

$$T_{ij} - \frac{1}{3}T_{kk}\delta_{ij} = -2C'_s\widetilde{\overline{\Delta}}^2|\widetilde{\overline{S}}|\widetilde{\overline{S}}_{ij}, \tag{2.30}$$

$$\tau^{\mathrm{r}}_{ij} - \frac{1}{3}\tau^{\mathrm{r}}_{kk}\delta_{ij} = -2C'_s\overline{\Delta}^2|\overline{S}|\overline{S}_{ij}., \tag{2.31}$$

where C'_s is the model constant which would be determined dynamically. By substituting Eqs. 2.30 and 2.31 into Eq. 2.29, the deviatoric part of the resolved turbulence stress is written as

$$\mathcal{L}_{ij} - \frac{1}{3}\mathcal{L}_{kk}\delta_{ij} = 2C'_s\left(\overline{\Delta}^2\widetilde{|\overline{S}|\overline{S}_{ij}} - \widetilde{\overline{\Delta}}^2|\widetilde{\overline{S}}|\widetilde{\overline{S}}_{ij}\right), \tag{2.32}$$

where $\mathcal{L}_{kk} = T_{kk} - \widetilde{\tau}^{\mathrm{r}}{}_{kk}$. The model coefficient in the dynamic Smagorinsky model can be calculated at each grid point and time step because all terms are known in Eq. 2.32 except C'_s. As the model constant can be negative number depending on the solution of flow, this model is capable of taking into account for backscatter, i.e. energy transfer from small scales to large scales. However, a large negative coefficient induces instability and thus an averaging operation in time and space was adopted to remedy this issue [122].

2.2.3 Mixed-time-scale model (MTS)

Inagaki et al. (2005) [54] suggested the mixed-time scale model. This model is based on the scale similarity hypothesis proposed by Bardina (1983) [6]. The scale similarity hypothesis assumes that the statistical structure of a tensor based on the subgrid scale is similar to that based on the smallest (yet larger than SGS) resolved scale. The SGS tensor is approximated by scaling an analogous tensor from the highest resolved frequency through a frequency extrapolation [133].

$$\nu_{SGS} = C_{MTS}K_{es}T_S, \tag{2.33}$$

$$K_{es} = |\bar{u}_i - \tilde{\bar{u}}_i|^2, \tag{2.34}$$

$$T_S^{-1} = \left(\frac{\Delta}{\sqrt{K_{es}}}\right)^{-1} + \left(\frac{C_T}{|\overline{S}|}\right)^{-1}, \tag{2.35}$$

where C_{MTS} and C_T are 0.05 and 10 respectively and ($\tilde{}$) in Eq. 2.34 is the explicit filter operator. K_{es} is the estimated SGS kinetic energy by using the explicitly filtered scale, $\widetilde{\overline{\Delta}}$, and the ratio between the explicit and cut-off filter sizes is $\widetilde{\overline{\Delta}}/\overline{\Delta} = 2$, in general. The estimated SGS kinetic energy guarantees that ν_{SGS} is close to zero in laminar flows as $\tilde{\bar{u}}_i = \bar{u}_i$. T_S in Eq. 2.35 is a harmonic average of the characteristic time scales between the cut-off ($\Delta/\sqrt{K_{es}}$) and large ($1/|\overline{S}|$) scales [54].

The dynamic Smagorinsky model by Germano et al. (1991) [35] does not need a wall damping function because the model constant is dynamically estimated but it suffers from a numerical instability due to the possibility of negative eddy viscosity in the model. To remedy this issue, a spatial average in the homogeneous direction or clipping the negative eddy viscosity to zero have been used. However there is no universal averaging strategy for general flows and some applications do not have homogeneity. Also clipping the eddy viscosity can lead to a poor result [54]. The MTS model does not require a wall damping function nor any type of a temporal or spatial averaging procedure. It is also suitable for transitional flow due to the estimated SGS kinetic energy in Eq. 2.34. Note that the MTS model was implemented in OpenFOAM and tested in the channel and airfoil flows.

2.2.4 Transport-equation SGS model

The idea of the transport-equation SGS model is that it estimates the velocity scale from the SGS kinetic energy ($\sqrt{K_{SGS}}$), rather than the velocity scale from the product of the resolved velocity gradient and the length scale as in the Smagorinsky model, i.e. $\Delta|\bar{S}|$ [174]. An additional transport equation is used to calculate K_{SGS} and the SGS eddy viscosity is defined as,

$$\nu_{SGS} = C_\nu \Delta \sqrt{K_{SGS}}. \tag{2.36}$$

This model is flexible to solve ν_{SGS} under a dynamic flow field and the transport equation for $K_{_{SGS}}$ is,

$$\frac{\partial K_{SGS}}{\partial t} + \frac{\partial \bar{u}_j K_{SGS}}{\partial x_j} = \frac{\partial}{\partial x_j}\left[\frac{\nu_{SGS}}{\sigma_K}\frac{\partial K_{SGS}}{\partial x_j}\right] + \nu_{SGS}|\bar{S}|^2 - \epsilon_{SGS} \tag{2.37}$$

$$\text{with } \epsilon_{SGS} = C_\epsilon \frac{K_{SGS}^{3/2}}{\Delta} , \tag{2.38}$$

where $C_\nu = 0.094$ and $C_\epsilon = 0.93$ [122]. Performance for the transport equation model has been demonstrated on homogeneous isotropic turbulence [174] and a turbulent boundary layer [136].

2.3 Inflow boundary conditions

Partial differential equations cannot be solved without imposing proper boundary conditions (BCs). In aerodynamics, especially for convective flows, inflow conditions strongly influence the results. Direct numerical simulation (DNS) and large-eddy simulation (LES) all resolve the unsteady, three-dimensional and energy-containing eddies. For a laminar inflow, 'smooth' velocity profiles naturally provide sufficient inlet conditions, whereas appropriate details of the fluctuating motions are required for a turbulent inflow. For wind engineering applications, turbulent inflow conditions are important for generating atmospheric turbulence. Thus a physically reasonable and computationally efficient turbulent inflow method is critical in determining the effects of turbulence on, for example, wind turbine aerodynamics and also other associated applications such as prediction of peak loads on buildings and bridges.

The simplest way to develop turbulence is to use a long enough upstream region to develop the flow. Jarrin et al. (2006) [58] mentioned that a theoretical distance of adjustment for the distance of developing the turbulent flow from a laminar flow is 110 δ for the plane channel flow (δ is the half depth of the channel). It is impractical to use such a long upstream region to develop the turbulent flow. The computational cost for the upstream region would far exceed that of the part in which one is interested. Temporally developing flows (e.g. homogeneous isotropic turbulence) allow one to use periodic boundary conditions (PBC) as inflow conditions. However, spatially developing flows such as boundary layers cannot adopt the PBC in the streamwise direction as an inflow boundary condition.

Present inflow methods so far fall mainly in two categories. The first is the recycle/rescale method (Sec. 2.3.1) in which inflow data is collected either from a certain point downstream of the same simulation or from an auxiliary simulation. The second is the synthetic approach (Sec. 2.3.2), in which artificially generated turbulence fluctuations are provided, using random sequences. Usually, statistical information required for representing the inflow turbulence includes first and second moments, space and time correlations and spectra. Comprehensive reviews according to these categories can be found in, for example, Keating et al. (2004) [66], Jarrin (2008) [57] and Tabor and Baba-Ahmadi (2010) [167].

2.3.1 Recycling methods

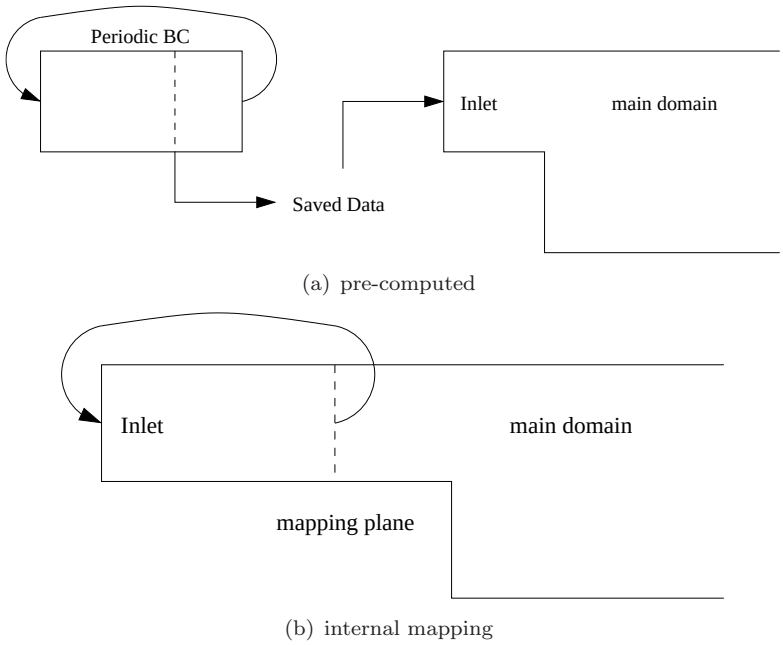

FIGURE 2.4: Sketches for recycling methods; (a) pre-computed method, (b) internal mapping method.

There are three major recycling methods: periodic boundary condition, pre-computed method and internal mapping methods (see Fig. 2.4). A canonical way to reach the fully developed flow for simple flows such as channel and pipe flows is applying periodic boundary conditions in the axial-direction. This method uses outlet data and introduces them at the inlet thus it can only be applied for the repeated geometry.

The pre-computed method separately calculates a fully developed flow field using a periodic channel flow and the data in time and space is saved. Then it is introduced at the inlet of the main domain. This method is computationally demanding due to a huge storage space requirement for the pre-computed data.

The internal mapping method merges the pre-calculated domain with the main domain. At a certain upstream point, data is collected on a plane and reintroduced at the inlet. This method is more economical than the pre-computed method but once an error is reintroduced, it can be intensified as it circulates between the inlet and the collecting plane [58, 113].

Lund et al. (1998) [92] suggested a recycling method to tackle the turbulent inflow condition of spatially developing flow on a flat plate. This method was a simplification of Spalart and Leonard's (1987) [160] method. At a few boundary layer thickness distances downstream, data was collected. The data was separately rescaled in the inner and outer layers and reintroduced at the inlet. Pamies et al. (2009) [113] pointed out that Lund et al.'s [92] method was accurate and inexpensive; only 5δ was required to reach the desired

data [161]. However there were a few drawbacks of this method [58, 113]. One of the major drawbacks was that the recycling procedure introduced a spurious periodicity in the streamwise direction due to a repeating inflow condition.

2.3.2 Synthetic methods

A synthetic method as a turbulent inflow condition means that turbulence is generated by superimposing artificially generated fluctuations on the statistically averaged properties. Synthetic methods do not use the recycling process, thus they are free from the drawbacks in the recycling methods [113]. This is because an ideal random sequence does not allow periodicity. The most straightforward way to generate turbulence fluctuation is to use a set of random numbers, $r_i = \mathcal{N}(0,1)$, where $\mathcal{N}(0,1)$ indicates the normal distribution with zero mean and unit variance, see Eq. 2.39.

$$u_i = U_i + r_i\sqrt{\frac{2}{3}K}, \tag{2.39}$$

where K is the turbulent kinetic energy. r_i should be a different set of random number on each velocity component i. However, Klein et al. (2003) [73] reported that turbulence by Eq. 2.39 decayed quickly and had no clear difference with the laminar inflow. If the signal consists of a pure random number as in Eq. 2.39, then it does not have any coherent structure; there are no energy containing (large) scales of motions. Thus the simple random signal becomes laminar as soon as it convects downstream.

To impose coherent structures on a random sequence, a usual relation for the inlet velocities for synthetic turbulence can be shown as

$$u_i = U_i + a_{ij}u_{*,j}, \tag{2.40}$$

where $i, j = 1, 2, 3$. u_i is an instantaneous velocity which is imposed at the inlet boundary, U_i is a mean velocity, a_{ij} is an amplitude tensor and $u_{*,j}$ is an unscaled fluctuation with a zero mean and unit variance. Lund et al. [92] suggested a form for a_{ij}, using Cholesky decomposition of the Reynolds stress tensor, R_{ij},

$$a_{ij} = \begin{pmatrix} \sqrt{R_{11}} & 0 & 0 \\ R_{21}/a_{11} & \sqrt{R_{22} - a_{21}^2} & 0 \\ R_{31}/a_{11} & (R_{32} - a_{21}a_{31})/a_{22} & \sqrt{R_{33} - a_{31}^2 - a_{32}^2} \end{pmatrix}. \tag{2.41}$$

This provides scaling and cross-correlations for $u_{*,j}$ in Eq. 2.40. Here, the scaling means that once the Reynolds stress tensor is available from DNS or experiments as input data, random numbers with a zero mean and a unit variance can be scaled as *root-mean-square* of the Reynolds stress by Eq. 2.41. To impose spatial and temporal

correlations, several approaches were suggested for the synthetic methods and they can be categorized into two groups: one is the spectral method in which superimposing is executed in spectral space. The other is the algebraic method in which the superimposing is executed in physical space [57].

Spectral methods

Kraichnan (1969) [77] decomposed the signal into Fourier modes to investigate scalar diffusion in homogeneous isotropic turbulence. The unscaled fluctuation velocity, u_*, in Eq. 2.40 is synthesized in a spectral space as,

$$u_*(x) = \sum_{\kappa} \hat{u}_\kappa e^{-i\kappa \cdot x}, \tag{2.42}$$

where κ is a wavenumber, $\hat{u}_\kappa = |\hat{u}_\kappa| e^{i\Phi_\kappa}$ is a complex number and Φ_κ is a random phase angle, $\Phi \in [0, 2\pi]$. $\hat{u}_\kappa$ can be calculated from the prescribed energy spectrum, i.e. $|\hat{u}_\kappa| \approx E(\kappa)^{1/2}$. Then Eq. 2.42 can be written as,

$$u_*(x) = \sum_{\kappa} \sqrt{E(|\kappa|)} e^{-i\kappa \cdot x + \Phi_\kappa}. \tag{2.43}$$

This method is widely used to initialize homogeneous isotropic turbulence. Lee et al. (1992) [84] applied this inverse Fourier transform for a prescribed spectral density function to provide temporal correlations of the velocity fluctuations. They tested it for isotropic turbulence. Rai and Moin (1993) [124] and Le et al. (1997) [83] used a similar method to test a spatially developing boundary layer and a backward-facing step flow respectively. Le et al. [83] reported that ten step heights were required for the recovery of turbulence characteristics due to the randomized phase angle in Lee et al.'s [84] approach.

Another spectral synthetic method was proposed by Smirnov et al. (2001) [152] for inhomogeneous and anisotropic turbulence. This model was simplified by Batten et al. (2004) [7] and they applied their model on the hybrid RANS/LES channel flow. Keating et al. (2004) [66] tested Batten et al.'s [7] method on a plane channel flow and reported that 20δ is required to recover the desired properties (e.g. skin friction and Reynolds stresses).

Algebraic methods

Klein et al. (2003) [73] proposed another synthetic method by using a Gaussian window to provide spatial correlations. They described this as a digital filter. The spatial correlations are imposed on a random number sequence, $r_m = \mathcal{N}(0, 1)$, by using the digital filter method. The intermediate velocity signal ψ_m in 1-D is,

$$\psi_m = \sum_{j=-N}^{N} b_j r_{m+j}, \tag{2.44}$$

where N is associated with the integral length scale and b_j is the filter coefficient. Note that the subscripts, m, j are the position indices. To estimate the filter coefficient b_j, Klein et al. [73] adopted the Gaussian autocorrelation function with the separation distance r and the integral length scale I,

$$C(r) = \exp\left(-\frac{\pi r^2}{4I^2}\right). \tag{2.45}$$

The autocorrelation $C(r = i\Delta x)$ on the discretized grid points with the size of Δx was calculated by using ψ_m,

$$\frac{\langle \psi_m \psi_{m+i} \rangle}{\langle \psi_m \psi_m \rangle} = C(r) = \exp\left(-\frac{\pi(i\Delta x)^2}{4(n\Delta x)^2}\right) = \exp\left(-\frac{\pi i^2}{4n^2}\right), \tag{2.46}$$

where $I = n\Delta x$. The filter coefficient b_j was approximated by using Eqs. 2.44 and 2.46 with some properties of the normal distribution on the random number, i.e. $\langle r_m r_l \rangle = 0$ and $\langle r_m r_m \rangle = 1$ where $l \neq m$,

$$b_j = \frac{b'_j}{\left(\sum_{l=-N}^{N} b'^2_l\right)^{1/2}} \quad \text{with} \quad b'_j = \exp\left(-\frac{\pi j^2}{2n^2}\right). \tag{2.47}$$

It was shown that $N = 2n = 2\frac{I}{\Delta x}$ in Eqs. 2.44 and 2.47 was enough to capture twice the length scale. Based on Eq. 2.44, it is straightforward to generate spatial correlations for a 2-D space as in Eq. 2.48,

$$\psi_{m,l} = \sum_{j=-N}^{N} \sum_{k=-N}^{N} b_j b_k r_{m+j,l+k}, \tag{2.48}$$

and similarly for a 3-D space. After generating a spatially correlated signal, the cross correlation is implemented by Cholesky decomposition (Eq. 2.41). Klein et al.'s method can be applied to inhomogeneous turbulence with arbitrary inlet geometry, but it becomes very expensive with a high resolution [58]. Xie and Castro (2008) [183] improved Klein et al.'s [73] method. They argued that the autocorrelation is close to an exponential function [109] rather than Gaussian, especially when the separation r is large which corresponds to large structures. So they used the exponential function for the autocorrelation as in Eq. 2.49 (cf. Eq. 2.45),

$$C(r) = \exp\left(-\frac{\pi r}{2I}\right), \tag{2.49}$$

and the filter coefficient was re-estimated as,

$$b_j = \frac{b'_j}{\left(\sum_{l=-N}^{N} b'^2_l\right)^{1/2}} \text{ with } b'_j = \exp\left(-\frac{\pi|j|}{n}\right) . \tag{2.50}$$

Xie and Castro [183] generated only one slice of a 2-D signal (Eq. 2.48) by using the filter coefficient in Eq. 2.50 at each time and correlated it with the 2-D signal from the previous time level. They used an exponential function for the correlation in time,

$$u_{*,i}(t+\Delta t) = u_{*,i}(t)\exp\left(-\frac{C_{XC}\Delta t}{T}\right) + \psi_i(t)\left[1-\exp\left(-\frac{2C_{XC}\Delta t}{T}\right)\right]^{0.5} , \tag{2.51}$$

where the model constant $C_{XC} = \pi/2$ and T is the Lagrangian time scale which is estimated by using $T = I/U$. Again, I is a turbulence integral length scale and U is a mean convective velocity. This exponential correlation function was originally suggested by Hanna et al. (2002) [43]. Note that the subscript i is a vector index, i.e. $i = 1, 2, 3$. The process in Eq. 2.51 effectively imposes an exponential correlation in the streamwise direction. In general, the integral length scales, I, depend on each velocity component and direction, see Eq. 2.52.

$$I_{ij} = \int_0^{r_{ij,0.1}} C_i(r\hat{e}_j)dr, \tag{2.52}$$

where $C_i(r\hat{e}_j)$ is the correlation function. i and j correspond to the components of the velocity vector and directions respectively, and $r_{ij,0.1}$ is the separation distance for $C_i(r\hat{e}_j) = 0.1$.

Kim, Xie, Castro (2011) [71] applied the exponential correlation procedure in Eq. 2.51 to all three directions. So it was expected to be less expensive than the Xie and Castro model [183] and more flexible, in that it allowed spatially varying length scales. In addition, the new model was easier to implement than the Xie and Castro model. This approach was called the forward stepwise method (FSM). Details of this method and the assessment of performance on a turbulent channel flow are presented in Appendix A.

Jarrin et al. (2006) [58] proposed another algebraic synthetic method. Turbulence spots were randomly distributed within the specified region and correlations were provided by a spatial integration of the shape function, $f_I(x)$. The integration interval

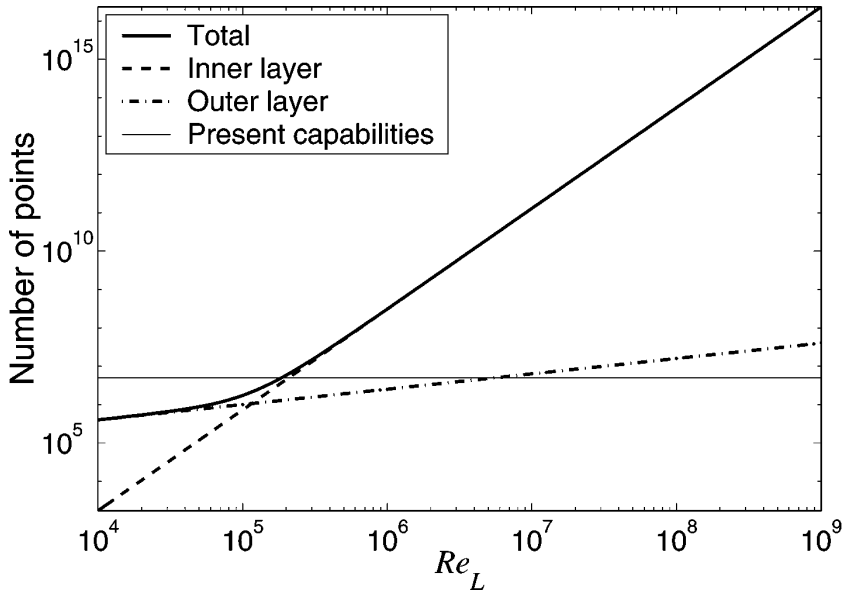

FIGURE 2.5: The number of grid points to resolve the boundary layer. Present capabilities is by the time when Piomelli and Balaras (2002) [117] is published.

was based on turbulence length scales. They used the shape function over randomly distributed eddy points. When the velocity signal is generated on the interval, $[a, b]$, the shape function satisfies the normalization condition,

$$\frac{1}{\Delta}\int_{-\Delta}^{+\Delta} f_{\boldsymbol{I}}^2(x)\mathrm{d}x = 1, \tag{2.53}$$

where $\Delta = b - a + 2I$. For simplicity, a one-dimensional spatially correlated signal is,

$$u_*(x) = \frac{1}{\sqrt{N}}\sum_{i=1}^{N} \epsilon_i f_I(x - x_i), \tag{2.54}$$

where N is the number of eddy points, ϵ_i is either $+1$ or -1 which are random variables with a zero mean and unit variance, $f_I(x - x_i)$ is the velocity distribution of the eddy located at x_i (shape function) and I is the length scale. For the two-point correlation, the shape function, f_I, satisfies,

$$C(r) = \frac{1}{\Delta}\int_{-\Delta/2}^{\Delta/2} f_I(x) f_I(x + r)\mathrm{d}x. \tag{2.55}$$

2.4 Wall boundary conditions

There are two main reasons why wall models are desirable in LES calculations. The first reason is that resolving all near wall structures in high Reynolds number flow is

impractical. To capture the near wall dynamics, a very fine mesh is needed. Fig. 2.5 is the estimation of the number of grid points required to resolve inner layer of flat plate boundary layer flow, given by Piomelli and Balaras (2002) [117]. Based on this relation the number of grid points to resolve the inner layer of wall-bounded flows at Reynolds number 5×10^6 is over 10^{10} which is 99% of total grid points. Considering modern large horizontal axis wind turbines (HAWT), the Reynolds number of the blade is approximately 10^6 to 10^7 at a windy area where the wind velocity is $10 - 15$ m/s. At these Reynolds numbers, resolving all the scales of motions in the inner layer using LES is not feasible. This is the primary reason that one needs wall models which present acceptable first and second moments.

The second reason for wall modelling is that the SGS model error increases as flow approaches the wall. The slow fluid pocket in the viscous sub-layer bursts out to the inner layer through the buffer layer and this event introduces fast fluid pockets to the viscous sub-layer. This intermittent process is highly anisotropic and induces backward energy cascades which undermines not only the SGS model but also eddy viscosity assumptions. Ideally, a perfect wall model can dispose of the SGS model errors near the wall [117]. Many wall modelling methodologies for LES can be found in Piomelli and Balaras (2002) [117], Fröhlich and von Terzi (2008) [34], Leschziner and Tessicini (2009) [90]. Some popular methods are introduced briefly in this section.

2.4.1 Wall stress models

The wall stress models aim to provide the estimated wall shear stress on a coarse grid where the mesh is incapable of resolving a sharp gradient in the boundary layer near the wall, i.e. the no-slip condition is not used. The wall stress model provides a locally averaged shear stress on the wall boundary while the nature of LES is unsteady and instantaneous. The concept of this approach, however, is applied in advanced hybrid RANS/LES methods, such as the segregate scheme in Sec. 2.4.2.2, therefore it is worth exploring its principles. The basic idea is that the sum of molecular and SGS viscosity at the first off-the-wall grid point is provided by using the statistical relation such as the law of the wall.

Schumann Model

Schumann (1975) [143] suggested a wall model which works for channel flow. It is,

$$\tau_{w,12} = \left(\frac{\bar{u}_1(y_1)}{\langle \bar{u}_1(y_1) \rangle} \right) \langle \tau_w \rangle \, , \tag{2.56}$$

$$\bar{u}_2 = 0, \tag{2.57}$$

$$\tau_{w,32} = \frac{2}{Re_\tau} \left(\frac{\bar{u}_2(y_1)}{y_1} \right), \tag{2.58}$$

where $\langle\ \rangle$ is a statistical average operator and subscript $1, 2, 3$ denotes the streamwise (x), wall normal (y) and spanwise (z) directions, respectively, and y_1 is the distance of the first off-the-wall grid point. The mean velocity profile can be obtained from the law of the wall and the mean shear stress is derived from the driving pressure gradient in the plane channel.

Grötzbach Model

Grötzbach (1987) [40] improved Schumann's wall model. This model follows the same method to calculate the wall shear stress as Schumann's wall model, but it does not need $\langle\tau_w\rangle$ *a priori*. This is calculated from the friction velocity, u_τ, from the law of the wall,

$$u_1^+ = \frac{\langle U_1(y_1)\rangle}{u_\tau} = \frac{1}{\kappa}\log(y_1 u_\tau/\nu) + 5.5 \pm 0.1. \tag{2.59}$$

Shifted correlations Model

Rajagopalan and Antonia (1979) [125] showed that the correlation between velocity and wall shear stress increases when the relaxation time is considered. This is because there is an inclined structure between the velocity fluctuation and the wall shear stress.

$$\tau_{w,12} = \left(\frac{\bar{u}_1(x+\Delta_s, y_1, z)}{\langle\bar{u}_1(x, y_1, z)\rangle}\right)\langle\tau_w\rangle\ , \tag{2.60}$$

$$\bar{u}_2 = 0 \tag{2.61}$$

$$\text{and}\ \ \tau_{w,32} = \frac{2}{Re_\tau}\left(\frac{\bar{u}_2(x+\Delta_s, y_1, z)}{\langle\bar{u}_1(x, y_1, z)\rangle}\right)\ , \tag{2.62}$$

where Δ_s is

$$\Delta_s = \begin{cases} (1-y_1)\cot(8^\circ) & \text{for } 30 \le {y_1}^+ \le 50-60 \\ (1-y_1)\cot(15^\circ) & \text{for } {y_1}^+ \ge 60 \end{cases}. \tag{2.63}$$

Ejection Model

Piomelli et al. (1989) [119] explained that the wall shear stress is highly dependent on whether the fluid motion is towards the wall or away from the wall. When the fluid pocket moves toward to the wall, it spins up the longitudinal and the lateral vortex tube. These spins induce the vortex stretching which intensifies the velocity fluctuations resulting in an increase of the wall shear stresses. When the fluid pocket moves away from the wall, reversal mechanisms weaken the wall shear stress.

$$\tau_{w,12} = \langle\tau_w\rangle - C u_\tau \bar{u}_2(x+\Delta_s, y_1, z), \tag{2.64}$$

$$\bar{u}_2 = 0 \tag{2.65}$$

$$\text{and } \tau_{w,32} = \frac{\tau_w}{\bar{u}_1(y_1)}\bar{u}_3(x+\Delta_s, y_1, z), \tag{2.66}$$

where C is the model constant. $\langle\tau_w\rangle$ can be computed from the law of the wall and Δ_s is identical to Eq. 2.63.

2.4.2 Hybrid RANS/LES

A hybrid RANS/LES type wall model uses RANS (mostly unsteady RANS) or a RANS based equation near the wall and uses LES away from the wall. The Reynolds stress in RANS (this is different from the SGS stress) is responsible for representing all scales of fluctuations. The resolved velocity from the RANS simulation is an ensemble averaged value while that from LES is from large scale motions. In general, the rate of change of the resolved velocity in the RANS region is much slower than that in the LES region in wall-bounded turbulence. This makes it possible for RANS to adopt much higher mesh aspect ratios, e.g. $\Delta x/\Delta y$ or $\Delta z/\Delta y$, near the wall compared with those required for LES. The gain of the hybrid RANS/LES comes from the more generous requirement of the near wall meshing strategy for the RANS calculations. Hybrid RANS/LES as a wall model for LES can be categorized in several branches depending on what governing equations are used and how the models define the interface between RANS and LES.

2.4.2.1 Unified scheme

The unified scheme is also known as a global scheme, which is the counter part of a segregated (or zonal) scheme described in Sec. 2.4.2.2. Thus it is also called a non-zonal scheme. The classification of these schemes is explained well by Fröhlich and von Terzi (2008) [34]. The governing equations for RANS and LES, as presented in Eqs. 2.67 and 2.68 respectively, are similar in form. Thus it is possible to use only one governing equation for two different turbulent viscosities, i.e. ν_t and ν_{SGS}, by using a weighting function.

$$\frac{\partial\langle u_i\rangle}{\partial t} + \frac{\partial\langle u_i\rangle\langle u_j\rangle}{\partial x_j} = -\frac{1}{\rho}\frac{\partial\langle p\rangle}{\partial x_i} + \frac{\partial}{\partial x_j}\left((\nu+\nu_t)\frac{\partial\langle u_i\rangle}{\partial x_j}\right), \tag{2.67}$$

$$\frac{\partial\bar{u}_i}{\partial t} + \frac{\partial\bar{u}_i\bar{u}_j}{\partial x_j} = -\frac{1}{\rho}\frac{\partial\bar{p}}{\partial x_i} + \frac{\partial}{\partial x_j}\left((\nu+\nu_{SGS})\frac{\partial\bar{u}_i}{\partial x_j}\right), \tag{2.68}$$

where $\langle\ \rangle$ is an ensemble average operator for RANS and $(\bar{})$ is a filtered operator for LES.

Blending model

The blending model is one of the simplest models of the unified schemes. This model has a blended viscosity, which is a sum of fractions of the RANS and SGS viscosities.

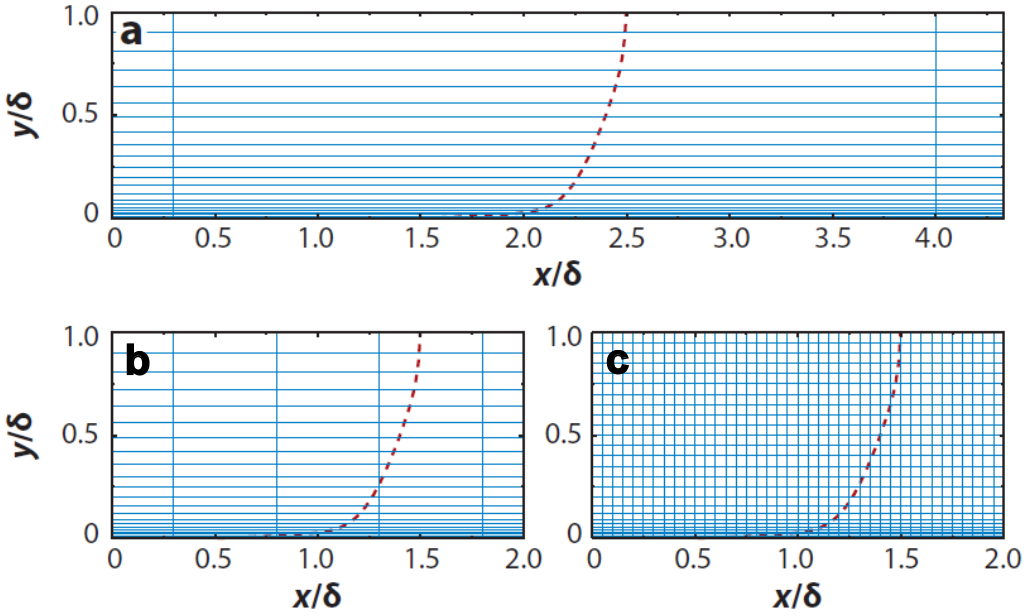

FIGURE 2.6: Different types of the mesh for boundary layers. The dashed line represents the velocity profile [157]. Mesh strategy: (a) the wall parallel grid size is larger than the boundary layer thickness; (c) the grid is fine enough to capture all eddies for LES calculations; (b) a mesh is in-between the strategies (a) and (c).

Fan et al. (2001) [31] modified the shear-stress transport (SST) turbulence model in a blending model. The original SST turbulence model by Menter (1994) [103] used the $K-\omega$ model for the near wall region and used the $K-\epsilon$ model away from the wall. Fan et al. [31] adopted LES for the outer region instead of the $K-\epsilon$ model. The blending model can be written as,

$$\nu_{blend} = f\nu_t + (1-f)\nu_{_{SGS}} = f\frac{K}{\omega} + (1-f)C_s'\sqrt{K}\Delta, \tag{2.69}$$

where C_s' is 0.01 and,

$$f = \tanh(\eta^4) \;\text{ with }\; \eta = \frac{1}{\omega}\max\left\{\frac{500\nu}{d^2}; \frac{\sqrt{K}}{C_{SGS}d}\right\}, \tag{2.70}$$

where C_{SGS} is constant in the SGS model and d is the wall distance. Turbulence properties such as the length scale and turbulent viscosity in the model are switched at the sharp interface between the RANS and LES regions. The velocity and pressure fields do not present discontinuities at the interface.

Detached eddy simulation

Detached eddy simulation (DES) is one of the most widely known hybrid RANS/LES

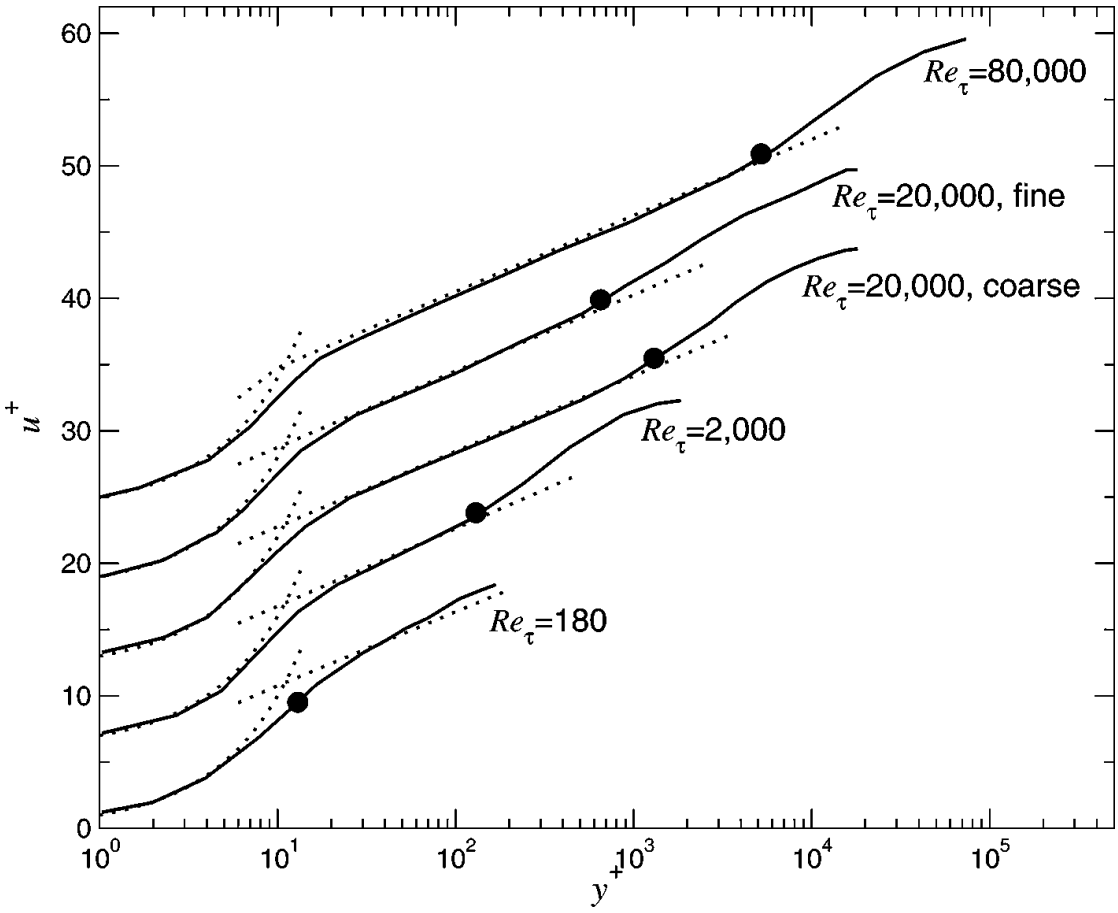

FIGURE 2.7: Profiles for the mean velocity profiles in the plane channel flow by using DES model [117]. Each profile is shifted by six u^+ units in vertical direction and the bullet points indicate the interface between the RANS and LES regions.

models. Spalart et al. (1997) [159] introduced a new Spalart-Allmaras model by modifying the dissipation term in the eddy viscosity transport equation, which is underlined in Eq. 2.71. The length scales for the RANS and LES regions are defined separately, i.e. the wall-normal distance for RANS and the grid size for LES.

$$\frac{\partial \tilde{\nu}}{\partial t} + \langle u_j \rangle \frac{\partial \tilde{\nu}}{\partial x_j} = c_{b1}(1 - f_{t2})\tilde{S}\tilde{\nu} - \frac{1}{\sigma}\left[\frac{\partial}{\partial x_j}\left((\nu + \tilde{\nu})\frac{\partial \tilde{\nu}}{\partial x_j}\right) + c_{b2}\frac{\partial \tilde{\nu}}{\partial x_i}\frac{\partial \tilde{\nu}}{\partial x_i}\right] - \underline{\left[c_{w1} f_w - \frac{c_{b1}}{k^2} f_{t2}\right]\left(\frac{\tilde{\nu}}{l_{DES}}\right)}. \tag{2.71}$$

The coefficients and closure functions can be found in a report from Langley Research Center, NASA [132]. l_{DES} is given by,

$$l_{DES} = \min(d; C_{DES}\Delta), \tag{2.72}$$

where d is the wall distance, $\Delta = \max(\Delta_x; \Delta_y; \Delta_z)$ and Δ_i is the grid size in the direction i. The original intention for the DES model was to use the RANS model for the entire boundary layer and to use LES model where the flow was separated. For this purpose, the effective wall parallel grid size, $C_{DES}\Delta_{||}$, should be larger than the thickness of the boundary layer so that l_{DES} is equal to d in Eq. 2.72 for the entire boundary layer (see Fig. 2.6(a)). However, it can be problematic when the mesh is fine, so that the length scale transition occurs within the boundary layer but the mesh is still too coarse to resolve the eddies within it (see Fig. 2.6(b)). In such a case, the modelled Reynolds stress is diminished due to excessive dissipation in Eq. 2.71 and unsteady fluctuations are under-predicted due to the coarse mesh. In consequence, the total turbulence level decreases in the boundary layer. Spalart et al. (2006) [158] referred to this reduced modelled Reynolds stress as the modelled-stress depletion (MSD). Menter and Kuntz (2004) [104] showed that the flow separation over an airfoil occured earlier with DES model than that with the RANS model due to the MSD. They called this phenomenon the "grid-induced separation". Note that Fig. 2.6(c) shows a mesh which is suitable for pure LES. Nikitin et al. (2000) [111] attempted to use DES on a plane channel flow with different Reynolds numbers. They observed that the mean velocity profiles were mismatched near the RANS and LES interfaces as shown in Fig. 2.7. This is called the log-layer mismatch (LLM).

Two papers followed to remedy the modelled-stress depletion and log-layer mismatch [146, 158]. Spalart et al. (2006) [158] suggested delayed detached eddy simulation (DDES) to improve the DES model. The model length scale for DDES is,

$$l_{DDES} = l_{RANS} - f_d \max(0; l_{RANS} - l_{LES}), \tag{2.73}$$

where

$$f_d = 1 - \tanh[(8r_d)^3], \tag{2.74}$$

$$r_d = \frac{\nu_t + \nu}{\sqrt{\frac{\partial u_i}{\partial x_j}\frac{\partial u_j}{\partial x_i}}\kappa^2 d^2} \left(\cong \frac{(\text{model length scale})^2}{(\text{wall distance})^2} \right), \tag{2.75}$$

where κ is the Kármán constant. The length scale for the RANS region is the wall distance as in the original DES model [159], i.e. $l_{RANS} = d$. The length scale in the LES region is $l_{LES} = \Psi C_{DES}\Delta$ where Ψ is a low-Reynolds number correction, see Spalart et al. (2006) [158]. The limiter function, r_d, is a square of the ratio between the model length scale and wall distance as shown in Eq. 2.75. The aim of the limiter is to 'preserve RANS' or 'delay LES' in the boundary layer. The limiter equals to one (leading to $f_d = 0$) in a logarithmic layer and gradually approaches zero near the boundary layer edge. The original idea was suggested by Menter and Kuntz (2004) [104]. These parameters ensure that the boundary layer remains in the RANS region

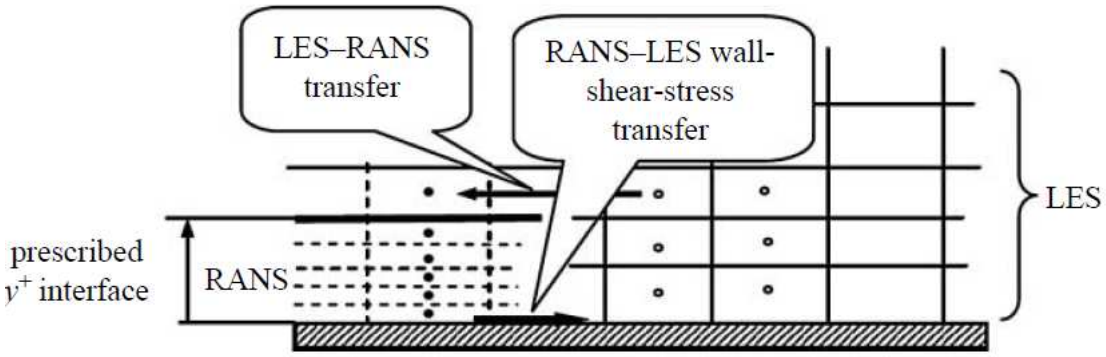

FIGURE 2.8: A sketch of the segregated scheme [90]. LES-RANS transfer: the resolved velocity and pressure in the LES region provide the boundary conditions to the RANS equation. RANS-LES wall-shear-stress transfer: the unsteady wall-shear-stress is estimated in the RANS region based on the resolved velocity and pressure from LES and it provides the wall boundary condition to LES.

independent of the mesh and wall distance. Thus these parameters can prevent the grid-induced separation which is the consequence of the modelled-stress depletion (MSD).

Shur et al. (2008) [146] improved the DDES model further which was called IDDES. The length scale for IDDES is,

$$l_{hyb} = \tilde{f}_d(1 + f_e)l_{RANS} + (1 - \tilde{f}_d)l_{LES}, \tag{2.76}$$

where,

$$\tilde{f}_d = \max\{(1 - f_{dt}), f_B\}. \tag{2.77}$$

The details of the blending functions can be found in the original paper [146]. If the inflow is laminar, $\tilde{f}_d = 1 - f_{dt}$ and $f_e = 0$, i.e. IDDES becomes DDES. If the inflow is turbulent, however, $\tilde{f}_d = f_B$ and f_e is non-zero. f_B is a function of the wall-distance d and maximum cell size $\Delta_{\max}$. It ensures that the length scale changes rapidly from l_{RANS} to l_{LES} at the interface. The elevating function, f_e, prevents the excessive reduction of the Reynolds stress near the RANS-LES interface.

2.4.2.2 Segregated scheme

This scheme is also called a zonal scheme because the RANS and LES regions are divided at a prescribed interface and an independent governing equation is needed for each region. The gain from such a scheme is that two-way coupling is possible between RANS and LES without degrading their compatibility. Two-way coupling means that the LES provides the temporal velocity and pressure fields to RANS, then RANS can provide the wall shear stress to LES as a boundary condition in an iterative way, see

Fig. 2.8. A fine wall-normal mesh ($y_1^+ \approx 1$) for the RANS equation is overlapped over the coarse mesh for the LES equation. The velocity and pressure are calculated in the global (coarse) mesh for LES by using Eq. 2.68. At the first cell-centre point of the LES mesh, the wall shear stress is provided from the RANS equation. Generally the RANS equation is solved with a simple algebraic turbulence model such as a mixing-length model [90],

$$\frac{\nu_t}{\nu} = \kappa y_w^+ \left(1 - \mathrm{e}^{-y_w^+/A}\right)^2, \tag{2.78}$$

where κ is von Kármán constant and y_w^+ is the normalized wall distance. Wang and Moin (2002) [176] used a simple mixed-length eddy viscosity model for the RANS equation and they reported that the trailing-edge separation was accurately predicted by using their model.

2.5 Employment of the methods

The filtering concepts, subgrid scale modelling, inflow and wall boundary conditions for LES have been reviewed. The specific methods which are employed in the later chapters are listed. The Smagorinsky SGS model in Sec. 2.2.1 is used for plane channel flows in Ch. 4 and the mixed-time scale SGS model in Sec. 2.2.3 is employed for all airfoil flow simulations in Chapters 5, 6 and 7. An explicit filtering operation is needed for the mixed-time scale SGS model, so the top-hat filter (Eq. 2.5) in Sec. 2.1.1 is adopted for that purpose. There is little difference between the Smagorinsky and MTS models in applying them to a channel flow. However, laminar-turbulent transition over an airfoil is poorly captured by the Smagorinsky model, while the MTS model presents a good prediction of the skin-friction compared with DNS data. (see Ch. 5).

For the turbulent inflow condition, Xie and Castro's [183] method in Sec. 2.3.2 is used to assess the performance of the new inflow technique in Ch. 4. No specific wall modelling strategy is employed in the thesis but the potential for the wall boundary conditions in Sec. 2.4 to overcome the limit of LES for wall-bounded high Reynolds number flows are discussed in Sec. 8.2.

Chapter 3

Finite volume discretization

3.1 Introduction

Analytical solutions for partial differential equations (PDE) provide continuously varying values for dependent variables within the domain as long as they exist explicitly. Apart from some specific cases, most of the PDEs' solutions are not known, such as for the Navier-Stokes equations, and they can be approximated numerically through discretization methods. The purpose of the discretization is to transform the partial differential equations into a corresponding system of algebraic equations [59], such that the solution for the PDE can be approximated on discrete grid points in the domain.

The open-source CFD code, OpenFOAM [112], is used for the present study. It is a finite-volume based solver in which the domain is subdivided into arbitrary unstructured control (or cell) volumes. The solution for the finite-volume method is calculated and stored at the cell-centroid on each control volume, unlike in finite-difference or finite-element methods. Some approximations arise to deal with the finite-volume method and different approximations are adopted for the sake of boundedness and accuracy of the solution. Basic principles for the finite-volume discretization are introduced in this chapter and some of the approximations which are used in the current study are also explained. Details on the finite-volume method are found in many textbooks and literature. Therefore a complete overview of this method is avoided.

3.2 Generic transport equation

The transport equation for a general scalar, ϕ, is,

$$\frac{\partial \phi}{\partial t} + \boldsymbol{\nabla} \cdot (\mathbf{u}\phi) = \boldsymbol{\nabla} \cdot (\Gamma \boldsymbol{\nabla} \phi) + S_\phi, \tag{3.1}$$

where Γ is the diffusivity coefficient and S_ϕ is the source term. It is assumed that all velocity fields and fluid properties are known. For the finite-volume method, the transport equation in Eq. 3.1 is integrated over the control volume V_C and the integral form of the conservation equation is then,

$$\frac{\partial}{\partial t}\int_{V_C}\phi dV_C + \int_{V_C}\boldsymbol{\nabla}\cdot(\boldsymbol{u}\phi)dV_C = \int_{V_C}\boldsymbol{\nabla}\cdot(\Gamma\boldsymbol{\nabla}\phi)dV_C + \int_{V_C}S_\phi dV_C. \tag{3.2}$$

The integral conservation equation is valid on an individual control volume and so it is on the entire domain [32]. Gauss' divergence theorem is used to transform some of the volume integrals in Eq. 3.2 to surface integrals [21].

$$\underbrace{\frac{\partial}{\partial t}\int_{V_C}\phi dV_C}_{\text{Temporal derivative}} + \underbrace{\int_A d\boldsymbol{A}\cdot(\boldsymbol{u}\phi)}_{\text{Convection}} = \underbrace{\int_A d\boldsymbol{A}\cdot(\Gamma\boldsymbol{\nabla}\phi)}_{\text{diffusion}} + \underbrace{\int_{V_C}S_\phi dV_C}_{\text{Source}}, \tag{3.3}$$

where $\boldsymbol{A}$ is the outward pointing surface area vector of a control volume. Each term in Eq. 3.2 has its own physical meaning as explained in Versteeg and Malalasekera (2007) [174]

- Temporal derivative : rate of change of the total amount of ϕ in the control volume.
- Convection : net rate of decrease (outward flux) of ϕ due to convection.
- Diffusion : net rate of increase (negative outward flux) of ϕ due to diffusion.
- Source : rate of creation of ϕ due to sources.

The surface and volume integrals in Eq. 3.3 require a certain level of approximations in actual calculations. These are explained in the following sections.

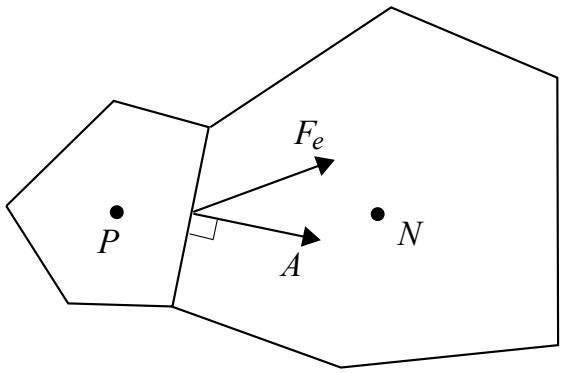

FIGURE 3.1: A sketch for neighbouring control volumes.

3.2.1 Surface integrations

Fig. 3.1 shows a sketch of two cell-volumes adjacent to each other where the point P is the cell-centre for the cell and the point N is the cell-centre for the neighbour. The surface integrations over the cell-volume (e.g. convection and diffusion terms in Eq. 3.3) are the sum of each cell-face value which leads to,

$$\int_A d\boldsymbol{A} \cdot \boldsymbol{F} = \sum_k \left[\int_A d\boldsymbol{A} \cdot \boldsymbol{F} \right]_k = \sum_k \left[\boldsymbol{A} \cdot \langle \boldsymbol{F} \rangle \right]_k , \tag{3.4}$$

where $\boldsymbol{F}$ is the face flux vector, which can be $(\boldsymbol{u}\phi)$ for the convection term or $(\Gamma \boldsymbol{\nabla} \phi)$ for the diffusion term, see Eq. 3.3. Note that k is the cell-face index. To calculate the surface integration, the face flux vector, $\boldsymbol{F}$, should be known everywhere on the surface area, $\boldsymbol{A}$, so that the mean face flux at the k_{th} face, $\langle \boldsymbol{F} \rangle$, can be calculated. However, the face flux value is generally not known for the finite-volume method as the solution is stored only at the cell-centroid [32]. Therefore an approximation must be introduced for the integration in Eq. 3.4. The simplest way is the mid-point rule: the mean face flux is approximated as the face-centre flux, $\boldsymbol{F}_e$, see Fig. 3.1.

$$\sum_k \left[\boldsymbol{A} \cdot \langle \boldsymbol{F} \rangle \right]_k \approx \sum_k \left[\boldsymbol{A} \cdot \boldsymbol{F}_e \right]_k . \tag{3.5}$$

This approximation becomes exact as $|\boldsymbol{A}| \to 0$, i.e. infinite grid points. A higher order of approximation is possible but this would be difficult to be implemented in 3-D domains [32]. The face flux at the cell-face centre, $\boldsymbol{F}_e$, in Eq. 3.5 needs to be interpolated from cell-centre values around the cell-face. Different interpolation schemes are desirable for the convection and diffusion terms, depending on the flow conditions. Some interpolation schemes which are particularly useful for the current study are introduced in Sec. 3.3. Using Eq. 3.5, the convection and diffusion terms in Eq. 3.3 are written, respectively,

$$\int_A d\boldsymbol{A} \cdot (\boldsymbol{u}\phi) = \sum_k \left[\boldsymbol{A} \cdot (\boldsymbol{u}\phi) \right]_k , \tag{3.6}$$

$$\int_A d\boldsymbol{A} \cdot (\Gamma \boldsymbol{\nabla} \phi) = \sum_k \left[\boldsymbol{A} \cdot (\Gamma \boldsymbol{\nabla} \phi) \right]_k . \tag{3.7}$$

3.2.2 Volume integrations

The temporal derivative and source terms in Eq. 3.3 require integrations over the cell-volume. This can be achieved by a simple approximation that the mean value of a cell is approximated as the cell-centre value as shown in Eqs. 3.8 and 3.9.

$$\frac{\partial}{\partial t}\int_{V_C}\phi dV_C = \frac{\partial}{\partial t}\langle\phi\rangle V_C \approx \frac{\partial}{\partial t}\phi_P V_C, \tag{3.8}$$

$$\int_{V_C} S_\phi dV_C = \langle S_\phi\rangle V_C \approx S_{\phi,P} V_C, \tag{3.9}$$

where the subscript P indicates the variables at the cell-centre point. The volume integrals are easy to calculate since all variables are available on the cell-centre point, P, for the finite-volume calculations, therefore, no interpolation is needed [32]. This approximation becomes exact when the integrands (i.e. ϕ, S_ϕ) are constant or linearly varying across the cell-volume. A higher order approximation would be possible with polynomial shape functions, but it is rarely used.

3.2.3 Time discretization

The spatially discretized transport equations are written by combining Eqs. 3.3 - 3.9,

$$\frac{d}{dt}\phi_P V_C + \sum \boldsymbol{A}\cdot(\boldsymbol{u}\phi) = \sum \boldsymbol{A}\cdot(\Gamma\boldsymbol{\nabla}\phi) + S_{\phi,P}V_C. \tag{3.10}$$

The cell-face index k in the convection and diffusion terms is omitted for brevity. Time can be discretized by using a marching manner which means that information propagates only forward in time. This is similar to the initial value problem of an ordinary differential equation [32] and Eq. 3.10 is re-written as,

$$\frac{d\phi_P(t)}{dt} = f(t,\phi(t)), \tag{3.11}$$

where

$$f(t,\phi(t)) = \frac{1}{V_C}\left[-\sum \boldsymbol{A}\cdot(\boldsymbol{u}\phi) + \sum \boldsymbol{A}\cdot(\Gamma\boldsymbol{\nabla}\phi) + S_{\phi,P}V_C\right]. \tag{3.12}$$

The right-hand side of Eq. 3.11 also contains the dependent variable, ϕ, of which the value can be chosen either from the current or previous time levels. One way of doing it is that the dependent variables in $f(t,\phi(t))$ are only taken from the previous time step. This is called an explicit method [32]. When the time indices are $t+\Delta t \to n+1$, $t \to n$ and $t-\Delta t \to n-1$, the explicit Euler (first-order) method is,

$$\frac{\phi_P^{n+1}-\phi_P^n}{\Delta t} = f(t^n,\phi(t^n)). \tag{3.13}$$

This method is easy to implement and solve but create a restriction on the time step due to a stability issue. The Runge-Kutta method is an another explicit approach

but has a higher accuracy than Euler method. It is a weighted average of increments between time levels $n+1$ and n. The fourth order accuracy is generally adopted [166],

$$\frac{\phi_P^{n+1} - \phi_P^n}{\Delta t} = \frac{1}{6}(k_1 + 2k_2 + 2k_3 + k_4), \tag{3.14}$$

where

$$\begin{aligned} k_1 &= f(t^n, \phi(t^n)), \\ k_2 &= f(t^n + \frac{\Delta t}{2}, \phi(t^n) + \frac{\Delta t}{2} k_1), \\ k_3 &= f(t^n + \frac{\Delta t}{2}, \phi(t^n) + \frac{\Delta t}{2} k_2), \\ k_4 &= f(t^n + \Delta t, \phi(t^n) + \Delta t k_3). \end{aligned} \tag{3.15}$$

Implicit methods are unconditionally stable and thus a much larger time step can be adopted. The implicit Euler method is,

$$\frac{\phi_P^{n+1} - \phi_P^n}{\Delta t} = f(t^{n+1}, \phi(t^{n+1})). \tag{3.16}$$

The second order accuracy of this implicit method, see Eq. 3.17, is called the backward differencing scheme and it is used for all simulations in following chapters.

$$\frac{3\phi_P^{n+1} - 4\phi_P^n + \phi_P^{n-1}}{2\Delta t} = f(t^{n+1}, \phi(t^{n+1})). \tag{3.17}$$

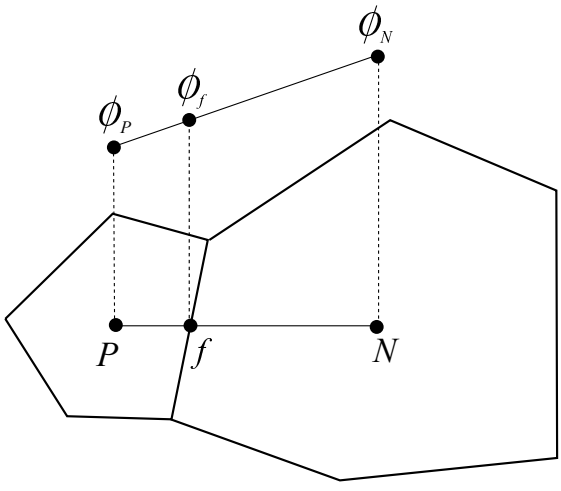

FIGURE 3.2: Face interpolation.

3.3 Interpolation practices

To discretize the finite-volume based transport equation such as Eq. 3.3, interpolations are needed because some surface or volume integrals need the cell-face value of dependent variables as presented in Sec 3.2. Specifically, the integrands in the convection term $\boldsymbol{A}\cdot(\boldsymbol{u}\phi)$ in Eq. 3.6 and diffusion term $\boldsymbol{A}\cdot(\Gamma\boldsymbol{\nabla}\phi)$ in Eq. 3.7 are calculated by interpolating the cell-centre values. Some interpolation schemes are briefly introduced in this section. More complete descriptions can be found in Ferziger and Perić (2002) [32] and Jasak (1996) [59].

Fig. 3.2 shows a sketch for the face value interpolation. P and N are the nodal points neighbouring the face f. The face variable, ϕ_f, can be calculated by interpolating the neighbouring points,

$$\phi_f = f_x\phi_P + (1 - f_x)\phi_N. \tag{3.18}$$

In general, f_x is defined as the distance ratio between neighbouring points,

$$f_x = \frac{\overline{fN}}{\overline{fP}}. \tag{3.19}$$

This scheme is called the central differencing (CD) scheme and is desirable for LES calculations. It should be noted, however, that the central differencing scheme presents numerical oscillations and it does not guarantee convergence (boundedness) [174] unless the mesh is sufficiently fine. A discretization scheme which guarantees the boundedness is the upwind differencing (UD) scheme which is defined as,

$$\phi_f = \begin{cases} \phi_P & \text{for } \boldsymbol{A}\cdot\boldsymbol{u} \geq 0 \\ \phi_N & \text{for } \boldsymbol{A}\cdot\boldsymbol{u} < 0 \end{cases}. \tag{3.20}$$

The upwind differencing scheme satisfies the boundedness but is diffusive and dissipative. In LES calculations, a diffusive scheme can be problematic because the SGS contribution is relatively small and the excessive diffusivity in the upwind differencing scheme can overwhelm the SGS contribution [21].

To overcome the boundedness issue in the central differencing and the excessive diffusivity issue in the upwind differencing, the normalized variable approach (NVA) was introduced by Leonard (1988) [88]. The normalized variable is defined as,

$$\tilde{\phi} = \frac{\phi - \phi_U}{\phi_D - \phi_U}, \tag{3.21}$$

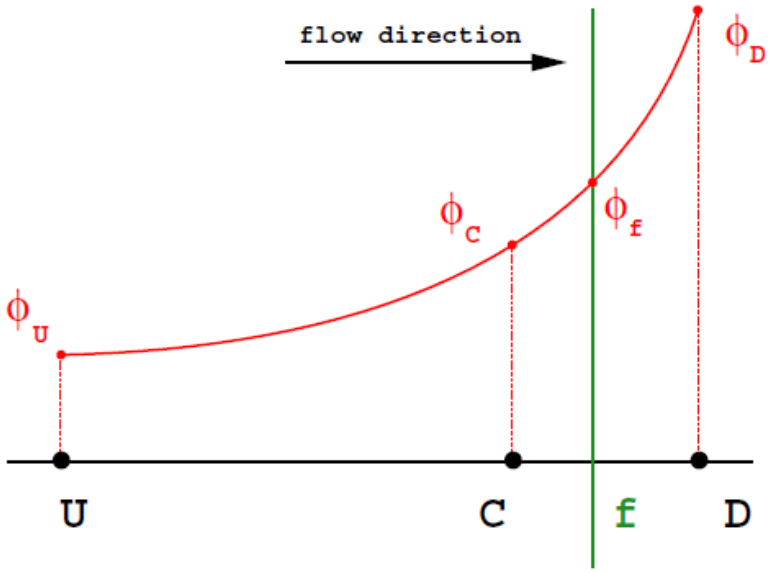

FIGURE 3.3: Variation of ϕ around face f [59]. C is the cell-centre point. U and D are the cell-centre points at the upstream and downstream cells respectively.

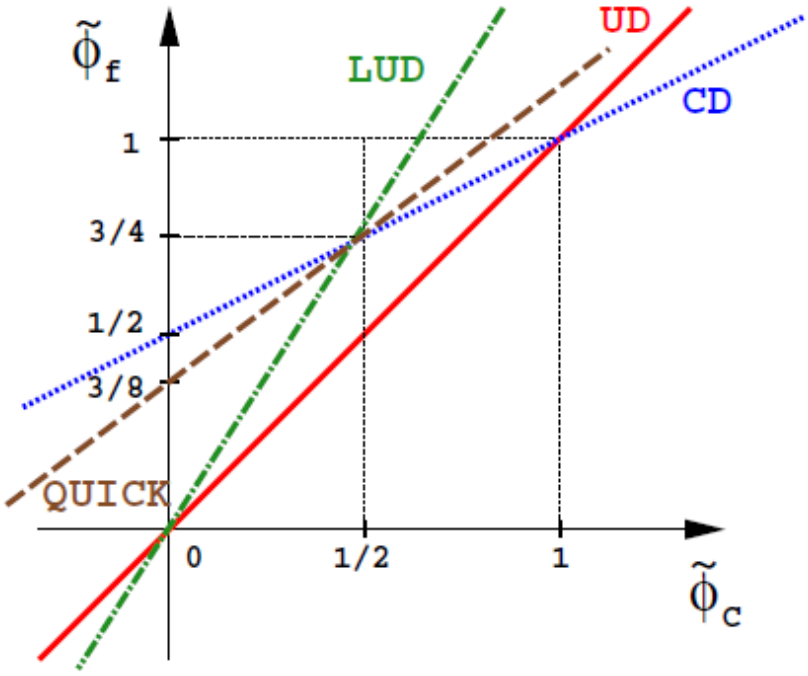

FIGURE 3.4: Differencing schemes in the normalized variable diagram [59].

where ϕ_U and ϕ_D are depicted in Fig. 3.3. Normalized variables at C and f are also defined in the same manner,

$$\tilde{\phi}_C = \frac{\phi_C - \phi_U}{\phi_D - \phi_U}, \tag{3.22}$$

$$\tilde{\phi}_f = \frac{\phi_f - \phi_U}{\phi_D - \phi_U}. \tag{3.23}$$

The relation between $\tilde{\phi}_C$ and $\tilde{\phi}_f$ depends on the differencing scheme and these relations are shown in Fig. 3.4. In NVA, the differencing scheme is switched depending on $\tilde{\phi}_C$ to maintain both the boundedness and accuracy. Jasak (1996) [59] proposed a blending function (called the Gamma scheme) for a smooth transition between upwind and central differencing schemes which is defined as,

- $\tilde{\phi}_C \leq 0$ or $\tilde{\phi}_C \geq 1$ then use the upwind differencing scheme :

$$\tilde{\phi}_f = \tilde{\phi}_C, \tag{3.24}$$

- $0 < \tilde{\phi}_C < \beta_m$ then use the blending function :

$$\tilde{\phi}_f = -\frac{\tilde{\phi}_C^2}{\beta_m} + \left(1 + \frac{1}{2\beta_m}\right)\tilde{\phi}_C, \tag{3.25}$$

- $\beta_m \leq \tilde{\phi}_C < 1$ than use the central differencing scheme :

$$\tilde{\phi}_f = \frac{1}{2} + \frac{1}{2}\tilde{\phi}_C, \tag{3.26}$$

where β_m is the 'limiter' which is $\frac{1}{10} \leq \beta_m \leq \frac{1}{2}$. The Gamma scheme maintains the central differencing scheme predominantly throughout the domain and the upwind differencing scheme is partially applied to avoid numerical oscillations. There is a smooth transition between central differencing and upwind differencing schemes through the blending function.

3.4 Employment of the methods

The finite-volume method and some approximations for the discretization on the generic transport equation have been briefly reviewed. The specific schemes which are employed in the later chapters are listed. The second-order backward differencing scheme for the temporal discretization, Eq. 3.17, is used for all turbulent flow simulations in Chs. 4 - 7. For the convection term, the second-order central differencing interpolation scheme in Sec. 3.3 is adopted for the plane channel flow in Ch. 4 and airfoil flow in Ch. 5. To avoid numerical oscillations near the strong shear layer at deep stall, the second-order bounded (Gamma, [59]) interpolation scheme in Sec. 3.3 is adopted for the pitching and rotating airfoil simulations in Chs. 6 and 7.

Chapter 4

Divergence-free turbulence inflow conditions on a plane channel flow

4.1 Introduction

Several turbulent inflow conditions for LES are reviewed in Sec. 2.3. Only very few papers in literature, however, introduce synthetic inlet turbulence satisfying the divergence-free condition. Smirnov et al. (2001) [152] considered the divergence-free condition using a superimposition of harmonic functions to provide synthetic turbulence. Huang et al. (2010) [53] improved the Smirnov method by imposing von Kármán spectra rather than a Gaussian model. Kornev and Hassel (2007) [76] derived the velocity potential which satisfies the divergence-free condition and then numerically calculated the solution. Poletto et al. (2011) [121] recently proposed a similar method and showed a significant decrease of pressure fluctuations in a turbulent channel flow using their new method.

Nevertheless, none of these authors analysed in any depth the impact of the inflow condition on pressure fluctuations, such as variance and spectra. For many applications the pressure fluctuation field is of primary interest. The major objective in the present work was therefore to develop a more satisfactory method in this regard. A divergence-free inflow generation method is proposed here, which is based on Xie and Castro's method [183] (hereafter, XC) with a slight, but crucial, modification of the incompressible flow solvers. This is described in Sec. 4.2, followed by a simple accuracy analysis. Results of simulations of a plane channel flow and comparisons between these and those obtained using the original method [183] and periodic inlet-outlet boundary conditions, as well as direct numerical simulation (DNS) data for the same flow [110], are presented in Sec. 4.3. The summary and concluding remarks follow in Sec. 4.4. The results in the chapter were reported in the journal paper by Kim, Castro, Xie. *Comput. Fluids*, 2013 [69].

4.2 Methodology

4.2.1 A length scale reconsideration in the XC model

The XC model is a synthetic turbulence generation method and imposes correlations using an exponential function to satisfy the prescribed space and time correlations. This model is reviewed in Sec. 2.3. It is noted that the correlation functions in XC were modelled as $C(r) = \exp(-\frac{\pi r}{2I})$. Based on DNS data [56, 110] of turbulent channel flows, the exponential model for the correlations was examined carefully at different wall-normal distances. If the integral length scale is defined as the enclosed area of the correlation function (see Eq. 2.52), the function $C(r) = \exp(-\frac{\pi r}{4I})$ gives a better fit compared to $C(r) = \exp(-\frac{\pi r}{2I})$ for the XC model. Therefore the filter coefficient was revised as,

$$b_j = \frac{b'_j}{\left(\sum_{l=-N}^{N} b'^2_l\right)^{1/2}} \quad \text{with} \quad b'_j = \exp\left(-\frac{\pi|j|}{2n}\right), \tag{4.1}$$

(cf. Eq. 2.50) and the model constant in Eq. 2.51 was set to $C_{XC} = \pi/4$ for the present study.

4.2.2 Inlet mass flux correction

Ideally the 2-D plane of velocity fluctuations generated from Eq. 2.51 has a zero mean. However usually the mean is not strictly zero because the size of the inlet area is finite in practice. Thus the instantaneous mass flux at the inlet by using the XC model changes very slightly in time. A small fractional difference in the mass flux may lead to significant modifications on the global pressure because of the nature of incompressible flow. Other types of inflow generators might have a similar issue due to the finite number of sampling points or interpolation errors, rather than the specific way of producing the synthetic inflow turbulence. Effects of the non-constant mass flux on the pressure fluctuations were reported in Poletto et al. (2001) [121] through numerical studies. Artificial pressure fluctuations due to the time dependent mass flux were observed in Gungor et al. (2012) [41] using a recycling/rescaling inflow method.

A simple correction is introduced to maintain a constant mass flux [121]. The instantaneous velocity at the inlet boundary is corrected as,

$$u_i = \frac{U_b}{U_{b,T}} u_{i,T}, \qquad \text{where, } U_{b,T} = \frac{\int_S u_{n,T} dS}{S}, \tag{4.2}$$

where $u_{i,T}$ is the generated velocity from the XC model and $u_{n,T}$ is the component of $u_{i,T}$ normal to the inlet boundary. S is the surface area of the inlet, U_b is the prescribed bulk velocity and $U_{b,T}$ is the instantaneous bulk velocity calculated from the uncorrected velocities. Simulations which use the corrected velocity in Eq. 4.2 will be denoted by XCMC. The effects of the mass flux correction on the pressure and velocity fields are reported in Sec. 4.3.

4.2.3 Divergence-free modification

To satisfy the divergence-free condition, first the generated synthetic turbulence is inserted on a plane near the inlet after having solved the momentum equations. The velocities are then adjusted by the velocity-pressure coupling procedure. This means that, on application of the pressure-correction step, the imposed velocities on the plane where the synthetic turbulence is introduced only act as intermediate velocities. Applying synthetic turbulence on the inlet boundary itself, in contrast, fixes those velocities as final velocities throughout one time step.

Once the synthetic turbulence goes through the velocity-pressure coupling procedure, the velocities are adjusted and are not generally exactly the same as the original. Nevertheless the changes are expected to be small [75]. The important feature of the method presented here is that it does not require any additional computational cost. A brief description of the standard sequence of velocity-pressure coupling procedure with incompressible flow solvers is presented to show the modification for the divergence-free method.

4.2.3.1 Velocity and pressure coupling procedure

The non-dimensionalised incompressible Navier-Stokes equations without any source term, in Cartesian coordinates, are

$$\frac{\partial u_i}{\partial t} + u_j \frac{\partial u_i}{\partial x_j} = -\frac{\partial p}{\partial x_i} + \frac{1}{Re} \frac{\partial \tau_{ij}}{\partial x_j}, \tag{4.3}$$

$$\frac{\partial u_i}{\partial x_i} = 0, \tag{4.4}$$

where i, j are vector indices and Re is the Reynolds number. Eq. 4.3 can be written in a semi-discretized form at each node (suffix P) as [32],

$$A_P u_{i,P}^{n+1} + \sum_l A_l u_{i,l}^{n+1} = -\left(\frac{\partial p^{n+1}}{\partial x_i}\right)_P + Q_i, \tag{4.5}$$

where n is the time index and l denotes the neighbouring points around node P, whose choice depends on the discretization schemes. Q_i is a sum of boundary conditions and quantities at previous time levels. Eq. 4.5 can be re-written as,

$$u_{i,P}^{n+1} = \frac{Q_i - \sum_l A_l u_{i,l}^{n+1}}{A_P} - \frac{1}{A_P}\left(\frac{\partial p^{n+1}}{\partial x_i}\right)_P. \tag{4.6}$$

The first term on the right-hand side can be written in a brief form as,

$$\tilde{u}_{i,P}^{n+1} = \frac{Q_i - \sum_l A_l u_{i,l}^{n+1}}{A_P}, \tag{4.7}$$

so that

$$u_{i,P}^{n+1} = \tilde{u}_{i,P}^{n+1} - \frac{1}{A_P}\left(\frac{\partial p^{n+1}}{\partial x_i}\right)_P. \tag{4.8}$$

Requiring $u_{i,P}^{n+1}$ to be divergence free and applying the divergence operator on Eq. 4.8 leads to,

$$\frac{\partial}{\partial x_i}\left[\frac{1}{A_P}\frac{\partial p^{n+1}}{\partial x_i}\right]_P = \left[\frac{\partial \tilde{u}_i^{n+1}}{\partial x_i}\right]_P. \tag{4.9}$$

Eqs. 4.8 and 4.9 are essentially discretized forms of the momentum and continuity equations respectively and now the pressure field is directly solved by using the velocity field in Eq. 4.9. Both u^{n+1} and p^{n+1} are unknown so they need to be solved for simultaneously; there are several methods for this calculation. The PISO algorithm by Issa (1985) [55] is one of the most widely used method for a transient solver thus it is introduced here. See Appendix B for other coupling algorithms. The PISO algorithm comprises one predictor and multiple, generally two, corrector steps. In the predictor step, an intermediate velocity u_i^* is calculated based on p, A_l and A_P at the previous time level,

$$u_{i,P}^{*} = \tilde{u}_{i,P}^{*} - \frac{1}{A_P}\left(\frac{\partial p^{n}}{\partial x_i}\right)_P, \tag{4.10}$$

where u_i^* generally does not satisfy the divergence-free condition. To satisfy this requirement, corrections are introduced for both velocity and pressure, $u_i^{**} = u_i^* + u_i'$, $p^* = p^n + p'$. Then the first corrector step is,

$$u_{i,P}^{**} = \tilde{u}_{i,P}^{*} + \tilde{u}_{i,P}' - \frac{1}{A_P}\left(\frac{\partial p^*}{\partial x_i}\right)_P, \tag{4.11}$$

with

$$\tilde{u}_{i,P}' = -\frac{\sum_l A_l u_{i,l}'}{A_P}. \tag{4.12}$$

$\tilde{u}_i'$ is neglected at the first corrector step and applying the divergence operator to Eq. 4.11 to calculate p^* yields

$$\frac{\partial}{\partial x_i}\left[\frac{1}{A_P}\frac{\partial p^*}{\partial x_i}\right]_P = \left[\frac{\partial \tilde{u}_i^*}{\partial x_i}\right]_P. \tag{4.13}$$

Note that the corrected velocities u_i^{**} satisfy the divergence-free condition. The neglected term $\tilde{u}_i'$ in Eq. 4.11 can be approximated via introducing one further correction, $u_i^{***} = u_i^{**} + u_i''$, $p^{**} = p^* + p''$. This leads to the second corrector step,

$$\begin{aligned} u_{i,P}^{***} &= \tilde{u}_{i,P}^{*} + \tilde{u}_{i,P}' - \frac{1}{A_P}\left(\frac{\partial p^{**}}{\partial x_i}\right)_P \\ &= \tilde{u}_{i,P}^{**} - \frac{1}{A_P}\left(\frac{\partial p^{**}}{\partial x_i}\right)_P. \end{aligned} \tag{4.14}$$

The corrected pressure p^{**} can be calculated requiring that the further corrected velocities u_i^{***} are divergence free,

$$\frac{\partial}{\partial x_i}\left[\frac{1}{A_P}\frac{\partial p^{**}}{\partial x_i}\right]_P = \left[\frac{\partial \tilde{u}_i^{**}}{\partial x_i}\right]_P. \tag{4.15}$$

More corrector steps are possible but it has been shown that further corrections are superfluous for most practical purposes [55]. u_i^{***} and p^{**} are considered to be accurate approximations of the exact solutions, u_i^{n+1} and p^{n+1}, and they are ready to be used for the next time step. The equations used here are consistent with those in the source code in OpenFOAM v1.7.1 [112] and literature [e.g. 32] as shown in Appendix C.

4.2.3.2 Divergence-free inflow condition method

Based on the XC method, a new method with the divergence-free condition satisfied is suggested and is denoted by XCDF. In Eq. 4.10, $\tilde{u}_i^*$ can be considered as the velocity excluding contributions of the pressure gradient [32]. The idea of the divergence-free turbulence method is to let $\tilde{u}_i^*$ on one 2-D transverse plane near the inlet contain turbulence and then correct them with appropriate pressure contributions to satisfy the divergence-free condition. The velocity fluctuations generated from the XC model are imposed appropriately on the 2-D plane at $x = x_0$ (see Sec. 4.3), rather than at the inlet as in Xie and Castro (2008) [183]. After the predictor step, Eqs. 4.11 and 4.13 at $x = x_0$ are modified as,

$$u_{i,P}^{**} = \tilde{u}_{i,P}^{g*} - \frac{1}{A_P}\left(\frac{\partial p^*}{\partial x_i}\right)_P, \tag{4.16}$$

$$\frac{\partial}{\partial x_i}\left[\frac{1}{A_P}\frac{\partial p^*}{\partial x_i}\right]_P = \left[\frac{\partial \tilde{u}_i^{g*}}{\partial x_i}\right]_P, \tag{4.17}$$

where $\tilde{u}_i^{g*}$ is defined in the same way as in Eq. 4.12; Eqs. 4.11 and 4.13 are not changed in the rest of the domain. $u_i^{g*}(x_0)$ is the generated velocity using the XC model. Note that $\tilde{u}_i'$ in Eq. 4.16 is neglected as in the standard PISO algorithm.

Now the first corrected velocity u_i^{**} in Eq. 4.16 satisfies the divergence-free condition and contains turbulence motions. Substituting the generated velocity u_i^{g*} for the predicted velocity u_i^* at $x = x_0$ is rather analogous to imposing momentum sources in the computational domain or, perhaps, to placing 'shark teeth' shape 2-D elements in a wind tunnel near the inlet to produce a 'simulated' atmospheric boundary layer [19].

A similar modification is introduced in the second corrector step. Eqs. 4.14 and 4.15 at $x = x_0$ thus become

$$u_{i,P}^{***} = \tilde{u}_{i,P}^{g**} - \frac{1}{A_P}\left(\frac{\partial p^{**}}{\partial x_i}\right)_P, \tag{4.18}$$

$$\frac{\partial}{\partial x_i}\left[\frac{1}{A_P}\frac{\partial p^{**}}{\partial x_i}\right]_P = \left[\frac{\partial \tilde{u}_i^{g**}}{\partial x_i}\right]_P. \tag{4.19}$$

The same generated velocities as in Eq. 4.16 are imposed at $x = x_0$, i.e. $u_i^{g**}(x_0) = u_i^{g*}(x_0)$. Further correction steps are possible but simulations showed no further improvement in terms of the development distance of wall skin friction and pressure fluctuations. Thus u_i^{***} and p^{**} are considered to be the solution for the next time level. Note that the corrected velocities u_i^{***}, in Eq. 4.18 are not used to calculate $u_{*,i}(t + \Delta t)$ in Eq.

2.51, so that the velocity correction in Eq. 4.18 would not affect the correlations which are imposed in Eqs. 2.44 - 2.51. Further analysis and remarks are presented below in subsections 4.2.3.3 and 4.3.4.1.

4.2.3.3 Accuracy analysis for the XCDF model

The PISO algorithm is a non-iterative method in the sense that the momentum equation is solved only once within one time step. Once the velocity is predicted based on the pressure and flux at the previous time level then it is adjusted through several corrector steps. Thus it is important to show that the final corrected velocities are a reasonable approximation. Comprehensive studies by Issa [55] on the accuracy and stability for the PISO algorithm showed that the errors induced in each predictor and corrector step decay with some power of the time step, i.e. dt^n.

Synthetic turbulence is substituted only on one transverse 2-D plane (near the inlet); the velocity-pressure coupling procedure in the rest of the whole domain remains unchanged. We would therefore not expect the modification to lead to solution divergence. It is nonetheless desirable to consider accuracy and consistency for the sake of reliability of the overall model. The decay of errors can be estimated in terms of dt both analytically and numerically. The analysis presented below, however, should be considered only as a guideline since, like that in Issa [55], it is based on *linear* partial differential equations. It must be tested in actual computations. Thus the full effects of the modification for the XCDF model is analysed and validated in Sec. 4.3.

Euler time discretization is adopted for the accuracy analysis but other discretization methods should, in principle, provide the same conclusion. As in Issa (1985) [55], A_P in Eq. 4.5 is decomposed into two parts, one is for the temporally discretized term and the other is for the rest,

$$A_P = \frac{1}{dt} + A'_P, \tag{4.20}$$

For the accuracy analysis, new error terms for velocity and pressure are introduced,

$$\begin{aligned} \varepsilon_i^k &= u_i^{n+1} - u_i^k, \\ \xi^l &= p^{n+1} - p^l, \end{aligned} \tag{4.21}$$

where $k = *, **, ***$ and $l = n, *, **$. Subtracting Eq. 4.10 from Eq. 4.8 gives,

$$A_P \varepsilon_{i,P}^* = -\sum_l A_l \varepsilon_{i,l}^* - \left(\frac{\partial \xi^n}{\partial x_i}\right)_P, \tag{4.22}$$

where ξ^n is $O(dt)$ via Taylor series expansion under the Euler discretization scheme, i.e. $\xi^n = p^{n+1} - p^n = O(dt)$.

Rewriting Eq. 4.22,

$$\frac{\varepsilon^*_{i,P}}{dt} = -A'_P \varepsilon^*_{i,P} - \sum_l A_l \varepsilon^*_{i,l} - \left(\frac{\partial \xi^n}{\partial x_i}\right)_P, \tag{4.23}$$

yields $\varepsilon^*_i = O(dt^2)$.

In a similar way, we subtract Eqs. 4.16, 4.17 from Eqs. 4.8, 4.9 and get the error equations on the 2-D plane where synthetic turbulence is imposed,

$$A_P \varepsilon^{**}_{i,P} = -\sum_l A_l \varepsilon^{g*}_{i,l} - \left(\frac{\partial \xi^*}{\partial x_i}\right)_P, \tag{4.24}$$

and

$$\frac{\partial}{\partial x_i}\left[\frac{1}{A_P}\frac{\partial \xi^*}{\partial x_i}\right]_P = \frac{\partial}{\partial x_i}\left[-\frac{1}{A_P}\left(\sum_l A_l \varepsilon^{g*}_{i,l}\right)\right]_P, \tag{4.25}$$

where $\varepsilon^{g*}_i = u^{n+1}_i - u^{g*}_i$. It is difficult to accurately estimate ε^{g*}_i at this stage. Nevertheless it is inherently no greater than the full difference of the generated (uncorrected) velocities between the time steps $n+1$ and n. When the time indices are $t+\Delta t \to n+1$ and $t \to n$ in Eq. 2.51, the full difference of the generated velocity, ε^g_i, can be estimated by combining Eqs. 2.40 and 2.51,

$$\begin{aligned}\varepsilon^g_i &= a_{ij}\left(u^{n+1}_{*,i} - u^n_{*,i}\right) \\ &= a_{ij}\left[-u^n_{*,i}\underbrace{\left(1 - e^{(-\frac{C_{XT}}{T}dt)}\right)}_{\sim O(dt)} + \psi^n_i \underbrace{\left(1 - e^{(-2\frac{C_{XT}}{T}dt)}\right)^{0.5}}_{\sim O(dt)}\right].\end{aligned} \tag{4.26}$$

Then it is estimated that $\varepsilon^g_i = O(dt)$ and $\varepsilon^{g*}_i = O(dt)$. We assume $\varepsilon^*_i{=}O(dt^2)$ is still valid for the pressure in the rest of the domain (i.e. except for $x = x_0$). Then the velocity error along the streamwise direction, i.e. $\varepsilon^*_i{=}O(dt^2)$ (for $x \neq x_0$) and ε^{g*}_i (for $x = x_0$) is in a Dirac delta function form. Note in Eq. 4.25, the left-hand side term is a second order spatial derivative, whereas the right-hand side term is a first order spatial derivative. As usual for simpler analyses, we start by considering a 1-D form of Eq. 4.25 in which synthetic velocity fluctuations are imposed only at $x = x_0$. Given that non-dimensional equations are being used and the CFL number $dt \times u/dx \sim 1$, integrating Eq. 4.25 in space leads to $\xi^*{=}O(dx\varepsilon^{g*}){=}O(dt\varepsilon^{g*})$. Nevertheless, our real problem is 3-D and thus it is difficult to give an accurate estimation for ξ^* in terms of ε^{g*}. If we agree that neither $\xi^* = O(\varepsilon^{g*}_i)$ nor $\xi^* = O(dt\varepsilon^{g*}_i)$ is an accurate estimation, perhaps $\xi^* = O(dt^\beta \varepsilon^{g*}_i) = O(dt^{1+\beta})$ is a slightly better one, where $0 < \beta < 1$.

Using Eq. 4.24 and following the same procedure as for the estimation for ε_i^*, we obtain $\varepsilon_i^{**} = O(dt^2)$. It is to be noted that $\xi^* = O(dt^{1+\beta})$ and $\varepsilon_i^{**} = O(dt^2)$ are the largest possible errors at $x = x_0$; further downstream the errors reduce to the levels suggested in Issa [55].

The errors in the second corrector step are calculated by subtracting Eqs. 4.18 and 4.19 from Eqs. 4.8 and 4.9. The magnitudes of the errors from this step are the same as those in the first corrector step because the same generated velocity is imposed at the second corrector too. Thus the maximum errors are $\xi^{**} = O(dt^{1+\beta})$ and ε_i^{***}=$O(dt^2)$ on the transverse plane $x = x_0$.

This analysis has revealed that the maximum velocity error (i.e. at $x = x_0$) is one order higher than the truncation error (i.e. $\sim O(dt)$ for the Euler discretization). However, the maximum pressure error is less than one order higher than the truncation error $O(dt)$. As discussed earlier, the modification is applied only on one 2-D plane. Again it is expected that the errors are not significant near the plane and decay downstream to the levels suggested in Issa [55].

In order to get more confidence in the error analysis, the decay of the errors are numerically calculated for plane channel flows and are compared with those using periodic in-outlet boundary conditions (PBC). The computational details for the two cases are identical except for the inflow conditions. Details of the numerical settings are presented in Sec. 4.3. The spanwise- and time-averaged profiles of the errors for velocity and pressure are presented in Fig. 4.1. Note that the velocity error from case XCDF is based on the generated velocity field on the plane at $x = x_0$, i.e. $|\varepsilon^*| = |u_1^{n+1} - u_1^{g*}|$, and the pressure error ξ^* is that defined in Eqs. 4.21 and 4.25. Note also that we are not able to get exact solutions u_i^{n+1} and p^{n+1} as in Eq.4.21, thus the final numerical solutions are used instead. Statistics for $|\varepsilon^*|$ and ξ^* obtained from using the XC model would be, in principle, the same as those from PBC as no velocity-pressure coupling modification was made in the XC model. Therefore, a comparison between cases PBC and XCDF is presented.

It is not surprising that the absolute magnitudes of the velocity errors for case XCDF are significantly greater than those for case PBC in Fig. 4.1(a). However, the error decay with time step for case XCDF is similar to that for case PBC shown in the inset at the upper corner of the figure. Both cases clearly show that as $dt \to 0$, the velocity errors decay towards zero at a rate close to dt^{-1}, confirming the $\varepsilon_i^{g*} = O(dt)$ behaviour estimated analytically. Again, the errors at $x = x_0$ shown here are the worst possible for case XCDF, whereas in the regions downstream (i.e. $x/\delta > 5$), they are close to those for case PBC. This confirms that the errors decays downstream to the levels suggested in Issa [55].

The pressure errors for cases PBC and XCDF in Fig. 4.1(b) show rather similar magnitude as that of the velocity errors. However the decay rate of the pressure errors

for case XCDF seems significantly slower than that of the velocity errors. This is because the pressure errors are also affected by the spatial discretization error as in Eq. 4.25. In these tests the mesh size was fixed in order to check the error decay rates in terms of time step, and also to save computational cost. It is expected that varying the grid size with the time step and keeping the CFL number $dt \times u/dx$ unchanged would lead to a faster decay rate of the pressure errors for case XCDF. Because it is impossible to get the exact solutions, the numerical procedure for the error estimation is not identical to the analytic procedure discussed earlier. Nevertheless, the former in general confirms those suggested by the latter. Again the numerical procedure shows that the errors in velocities and pressure decrease with decreasing time step dt. This suggests that our modification with the PISO procedure is self-consistent.

4.3 Validations of turbulent inflow conditions on a plane channel flow

The XC, XCMC (see, Sec. 4.2.2) and XCDF methods are used as inflow conditions to simulate a plane channel flow. These models are assessed through a validation against using periodic in-outlet boundary conditions (PBC) for the plane channel flow. The purpose of using periodic simulation data (as done in a number of previous papers - e.g. [7, 58, 66, 73, 173, 183]) is simply to provide a straightforward validation for the inflow method without the other uncertainties which would inevitably arise when using non-periodic test cases. Once the method is validated on a channel flow, it can be used for both free and wall-bounded flows. The input parameters, such as Reynolds stresses and integral length scales, can be obtained from the available experimental data and/or appropriate empirical stress ratios [e.g. 184].

TABLE 4.1: Summary of boundary conditions for different cases. U_i is the mean velocity and d/dn is a normal derivative to the boundary. The transverse plane is placed at x_0 where the synthetic turbulence is imposed for XCDF.

Case	Inlet	Outlet	$x_0/\delta = 1$
PBC	PBC	PBC	n/a
XC	XC	$du_i/dn = 0$, $p = p_\infty$	n/a
XCMC	XCMC	$du_i/dn = 0$, $p = p_\infty$	n/a
XCDF	$u_i = U_i$, $dp/dn = 0$	$du_i/dn = 0$, $p = p_\infty$	XCDF

4.3.1 Numerical description

The Reynolds number of the channel flow based on the friction velocity, u_τ and the half depth of the channel, δ, was $Re_\tau = 395$. The domain size was $60\delta \times 2\delta \times 3.5\delta$ in the streamwise (x), wall-normal (y) and spanwise (z) directions respectively (see Fig. 4.2).

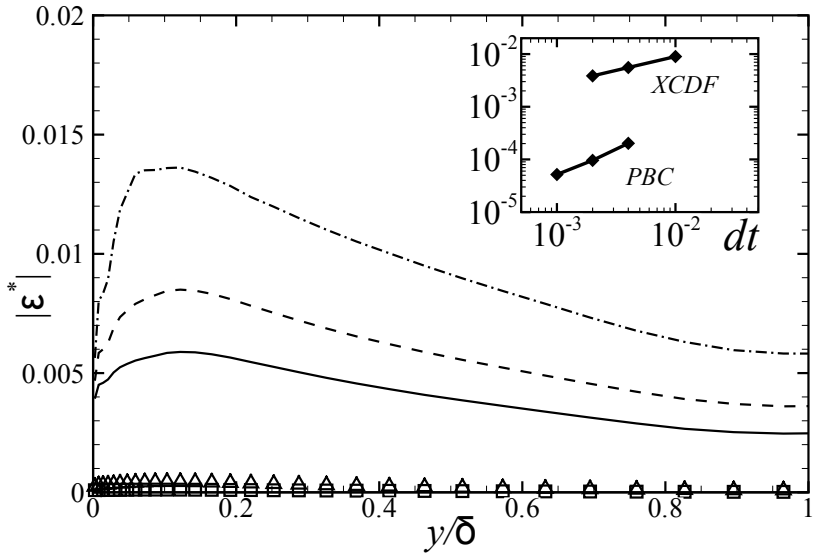

(a)

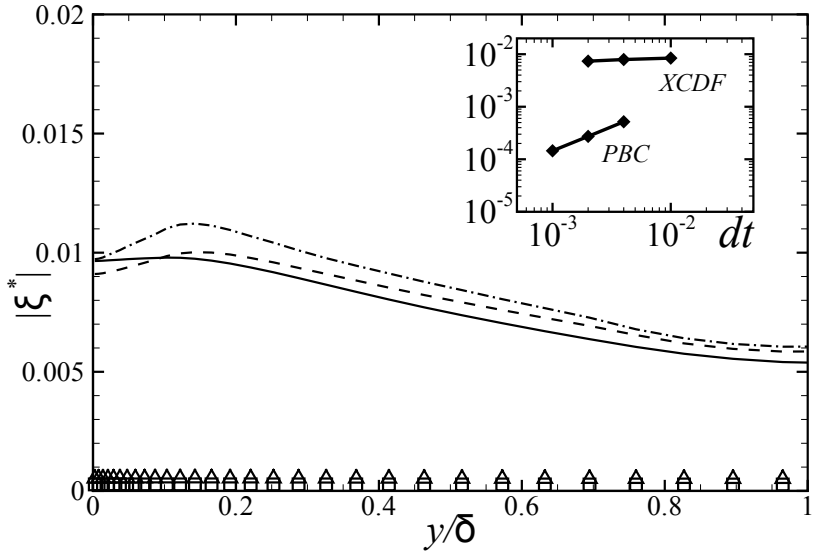

(b)

FIGURE 4.1: Profiles of error of (a) the streamwise velocity component, $|\varepsilon^*|$, and (b) pressure, $|\xi^*|$, with different time steps at the plane where synthetic turbulence is imposed, see Eq. 4.21 for definition. Case PBC: $dt_* = 0.002$ □, $dt_* = 0.004$ Δ; XCDF: $dt_* = 0.002$ −, $dt_* = 0.004$ −−, $dt_* = 0.01$ −· where $dt_* = dt \times u_\tau/\delta$. The insets show the errors against the time step dt_* at $y = 0.5\delta$. The errors are normalized by the bulk mean velocity and density.

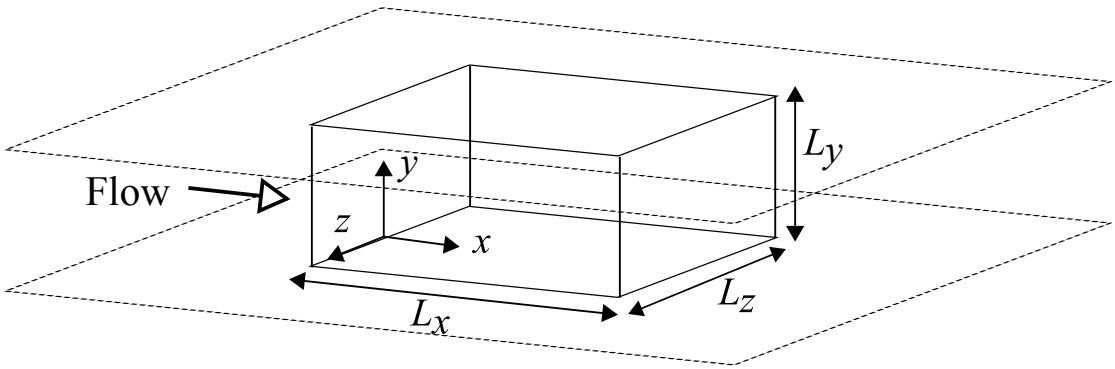

FIGURE 4.2: A sketch of the computational domain (not to scale) for a channel flow.

A uniform mesh was used in the streamwise and spanwise directions and a stretched mesh in the wall-normal direction for which $y_1^+ \leq 1$ was satisfied at the first cell centre.

All statistics were averaged over $40t_*$, where $t_* = tu_\tau/\delta$, and the averaging started after an initialization period of $20t_*$. The Smagorinsky subgrid-scale model with van-Driest damping [172] was adopted with the constant $C_s = 0.065$ [107]. The time step was chosen such that the CFL number was less than unity, corresponding to $\Delta t_* = \Delta t \times u_\tau/\delta = 0.002$. A second order, implicit scheme was used for time discretization, with a second order central difference scheme for spatial discretization. The transient incompressible flow solver in OpenFOAM 1.7.1 [112] was used and the PISO algorithm was adopted for the velocity-pressure coupling. The number of pressure correctors was set to two. We noticed that increasing the number of correctors did not improve the results.

A periodic boundary condition was applied in the spanwise direction and no-slip wall boundary conditions were applied on the bottom and top walls for all cases. Other boundary conditions are summarized in Table 4.1. For the XCDF model, generated synthetic turbulence from Eq. 2.40 by using the XC model was imposed at the cell centres of a yz plane which was placed in the domain near the domain inlet, e.g. at $x = x_0 = \delta$ rather than at the inlet boundary (i.e. $x = 0$). Meanwhile, the mean velocity profile was specified at the domain inlet to fix the mass flow rate to a constant. Ideally, the shifted inflow plane is to be placed as close as possible to the inlet boundary to save computational cost. The XCDF model works well for $x_0 \geq 0.5\delta$. However, we noticed that placing the plane at the centres of the first cell from the inlet, generates higher peaks of time- and spanwise- averaged variance of the wall pressure fluctuations near the inlet. This might be due to the fixed mean velocity specified at the inlet boundary and the nature of the incompressible flow. Nevertheless, the magnitude of these pressure variance peaks are far less than those generated by the XCMC model.

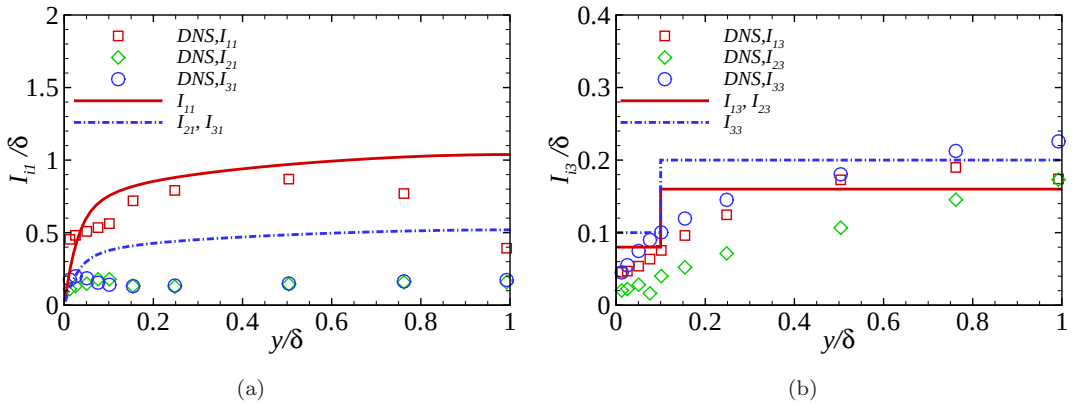

(a) (b)

FIGURE 4.3: Integral length scales in (a) the streamwise direction and (b) the spanwise direction (right). Symbols are from DNS [110], lines are specified length scales as input data of the XC, XCMC and XCDF models. The definition of I_{ij} is written in Eq. 2.52. Note $I_{21} = I_{31}$, $I_{13} = I_{23}$ and $I_{i2} = I_{i3}$.

4.3.2 Specifying input parameters

The XC, XCMC and XCDF models need first and second moment statistics and integral length scales as input parameters. These were taken from DNS data [110] and case PBC. The integral length scales were calculated by integrating two-point correlations until the value of the correlation reached 0.1. The correlations are taken from DNS data [110]. Nine integral length scales were estimated for the three components of the velocity vector (u, v, w) in all three directions (x, y, z) (see Eq. 2.52). For instance, the integral length scale in the spanwise direction $(j = 3)$ for the correlation C_i $(i = 1)$ (i.e. based on the u_1 component) is I_{13}. The channel flow in the wall-normal direction is inhomogeneous thus I_{i2} cannot be obtained by using Eq. 2.52. For simplicity, it was assumed that $I_{i2} = I_{i3}$. Fig. 4.3 shows the integral length scales used for the input data of the XC, XCMC and XCDF models. It is to be noted that we managed to use as much as possible the available reference data to have a rigorous test. In more practical applications, it is straightforward to use fewer integral length scales.

For the inflow models, the distribution of the x-direction length scales, I_{i1}, along the wall-normal direction is a function of the local mean velocity, $U_1(y)$. Only one 2-D slice of the signal is generated and convected into the domain at every time step. Thus we get $I_{i1}(y) = T_{i1} \times U_1(y)$ using Taylor's hypothesis where T_{i1} is the Lagrangian time scale. The local turbulence intensity is mostly far less than 0.3 for the test case, thus Taylor's hypothesis holds across the domain [179]. Implementations of the generated velocity by the models were performed on a virtual uniform mesh and then they were interpolated to the non-uniform mesh at the inlet.

TABLE 4.2: Resolutions and the domain size of the channel flow for $Re_\tau = 395$. The DNS data is taken from Moser et al. (1999) [110].

Case	N_x	N_y	N_z	Δx^+	Δy^+_{min}	Δy^+_{max}	Δz^+	L_x	L_z
DNS	256	193	192	10.0	·	6.5	6.5	$2\pi\delta$	$\pi\delta$
PBC	80	60	70	39.5	2	27.6	19.8	8δ	3.5δ
PBC2	160	128	140	19.8	2	10	9.88	8δ	3.5δ
PBC3	320	192	280	9.88	2	5.74	4.94	8δ	3.5δ

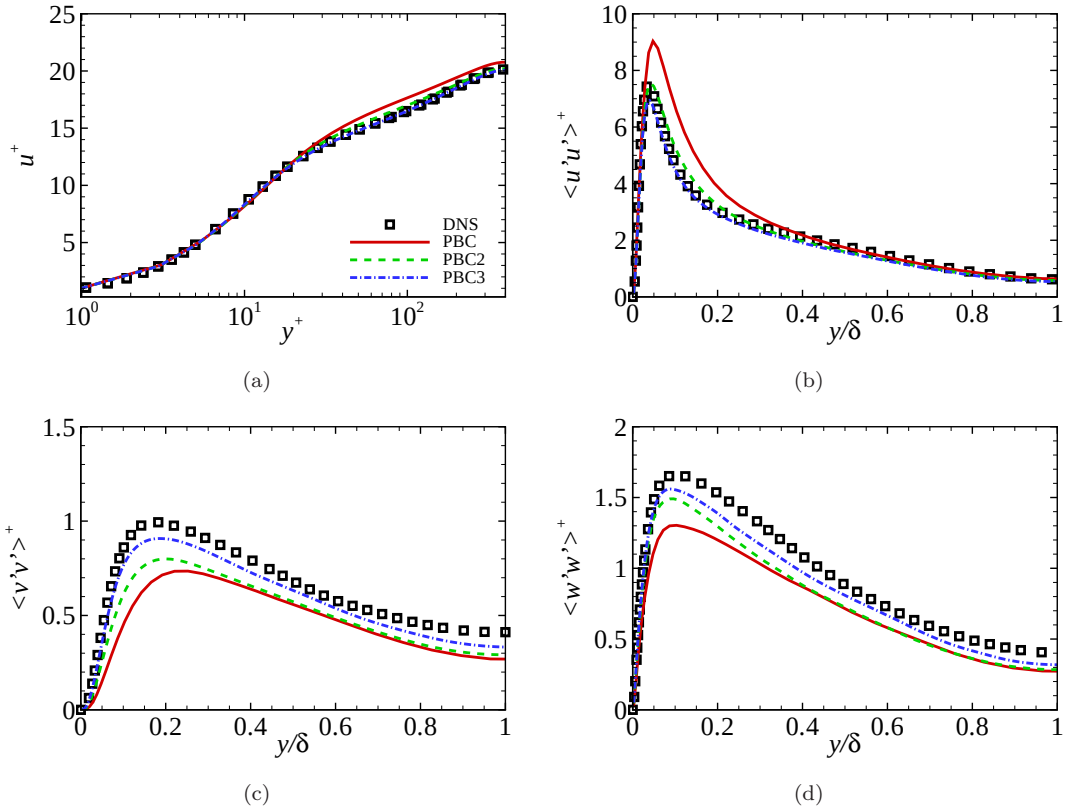

FIGURE 4.4: Profiles of (a) the mean velocity and variance in (b) streamwise, (c) wall-normal and (d) spanwise directions from the channel flow. The LES results with the periodic boundary condition are compared with DNS data [110]. Superscript + indicates that the quantities are normalized by the friction velocity u_τ and kinematic viscosity ν.

4.3.3 Baseline simulations

To serve as reference case, a plane channel flow with the periodic in-outlet boundary condition was calculated and compared with DNS data [110]. Three different resolutions were tested as summarized in Table 4.2. Note that the domain size in the streamwise direction for the baseline case (8δ) was shorter than that for the turbulent inflow case (60δ) to reduce computational costs. However this size was large enough to capture the

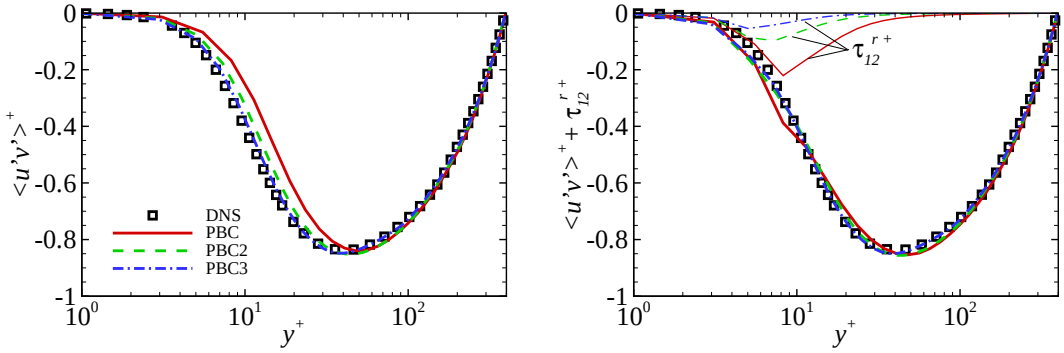

(a) (b)

FIGURE 4.5: Profiles of (a) the resolved shear stress $\langle u'v' \rangle^+$ and (b) sum of the resolved and SGS (τ_{12}^{r+}, thin-lines) shear stresses, see Eq. 2.20 for τ_{ij}^{r}. Superscript + indicates that the quantities are normalized by the friction velocity u_τ and kinematic viscosity ν.

largest structure in the channel at $Re_\tau = 395$. The largest structure can be estimated from the autocorrelation function which is available in Moser et al. (1999) [110].

Fig. 4.4 shows the mean velocity and Reynolds stress profiles in the channel flow. The mean velocity profiles show reasonably good agreement for all cases with the reference but some deviations are observed in the Reynolds stress profiles especially near the maxima ($y/\delta \approx 0.1$). As the number of grid points increases, the LES results tend to approach the DNS data. Note that the resolution for case PBC3 is nearly the same as for DNS but the results show slight differences, especially for $\langle v'v' \rangle^+$, $\langle w'w' \rangle^+$. The PBC3 calculations with and without the SGS model did not show noticeable differences in all the statistics. Therefore the difference between the cases PBC3 and the reference DNS is due to the difference in the numerical schemes for each case. A high-order finite difference method was used in Moser et al. (1999) [110] while second-order finite volume method is used in the current study. The high-order scheme would need less grid points than the low-order one to capture the same fluctuations.

The SGS contributions of the Reynolds shear stress with the different resolutions are examined in Fig. 4.5. Fig. 4.5(a) shows the resolved shear stresses and they are consistent with Fig. 4.4. The results tend to approach the reference data as the resolution increases. Total Reynolds shear stresses, i.e. $\langle u'v' \rangle^+ + \tau_{12}^{r+}$, are shown in Fig. 4.5(b). All calculations match DNS data with a good accuracy. The SGS contributions, τ_{12}^{r+}, increase as the resolution decreases. This is because the Smagorinsky model uses the grid size (Δ) as the characteristic length scale in the model, i.e. $\nu_{SGS} = (C_s\Delta)^2|\overline{S}|$, see Sec. 2.2.1. A sharp drop of τ_{12}^{r+} at $y^+ \approx 8$ for case PBC is due to the van Driest wall damping function.

Over-predictions of the mean velocity at the channel centre and $\langle u'u' \rangle^+$ near the wall, and under-predictions of $\langle v'v' \rangle^+$ and $\langle w'w' \rangle^+$near the wall for case PBC are common observations with a similar resolution of LES calculations [e.g. 9, 57]. However, case

PBC generally shows reasonable results for the first and second moments compared with DNS data. The purpose of the channel flow calculations is to serve as reference data for the assessment of the turbulent inflow condition. Thus the resolutions for case PBC are used for the turbulent inflow cases in the following section.

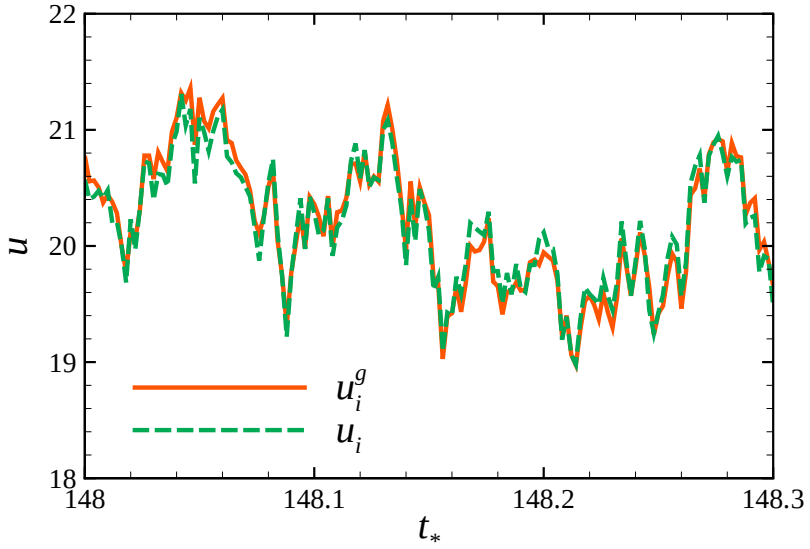

FIGURE 4.6: A typical example of the changes of the streamwise velocity before and after the continuity equation (Eq. 4.9) is satisfied. u_i^g is the XC model generated velocity before the continuity equation, and u_i is the adjusted velocity after the continuity equation.

4.3.4 Results and discussion

In the XCDF model, the synthetic turbulence is imposed on a transverse plane at $x = x_0$ and is adjusted through the velocity-pressure coupling procedure. The changes are expected to be small, otherwise the Reynolds stresses and the integral length scales used to generate the synthetic turbulence must be reconsidered. Fig. 4.6 shows a typical example of the changes of time series of the streamwise velocity before and after the continuity equation is satisfied. As expected, the difference between the two sets of velocities is very small.

An accurate prediction of the pressure fluctuations is the focus of the present work. Fig. 4.7(a) show the effects of the mass flux correction and the divergence-free modification on the dimensionless time- and spanwise-averaged variance of the normalised wall pressure fluctuations, $\langle p_w'^2 \rangle^+ = \langle p_w'^2 \rangle / (\rho^2 u_\tau^4)$. Significantly higher wall pressure fluctuations are introduced by the XC model near the inlet, and they decrease monotonically to zero at the outlet where the pressure was fixed to a constant ambient pressure. In contrast, the variances of the wall pressure fluctuations for both cases XCMC and XCDF are in good agreement with the reference data (i.e. PBC) downstream of $x/\delta = 10$. The simple mass correction in case XCMC brings a significant improvement on pressure

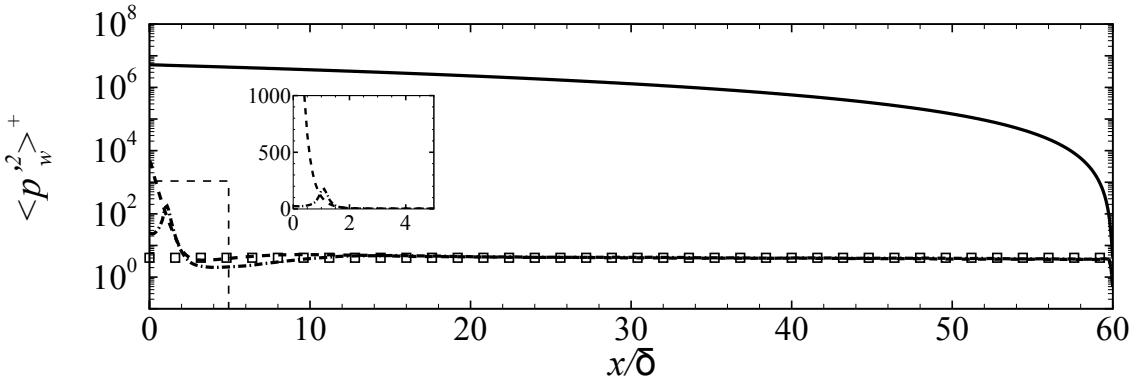

(a)

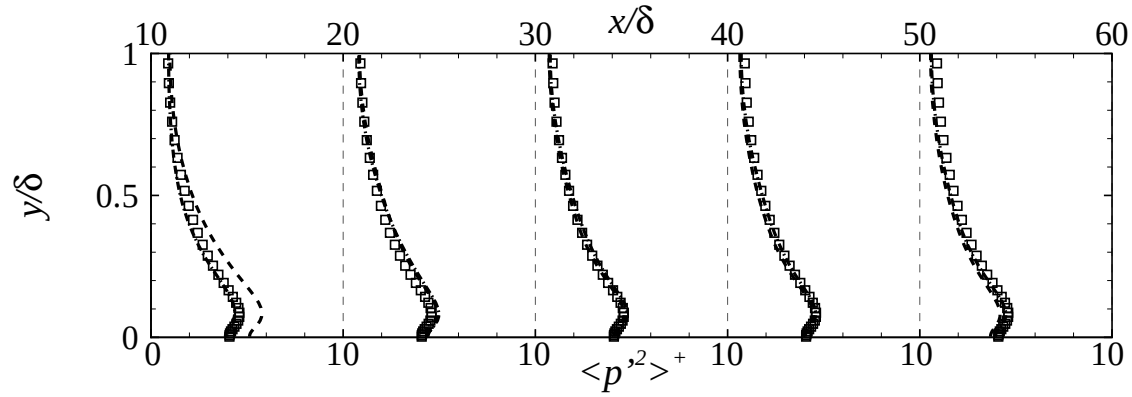

(b)

FIGURE 4.7: (a) Development of dimensionless time- and spanwise- averaged variance of the wall pressure fluctuations, $\langle p'^2_w \rangle^+$. The inset shows a zoomed view of the dashed box on the left bottom corner. (b) Profiles of dimensionless time- and spanwise-averaged variance of pressure fluctuations in the wall-normal direction at the different downstream locations, $\langle p'^2 \rangle^+$. PBC □, XC —, XCMC ––, XCDF – · –.

fluctuations and its performance in Fig. 4.7(a) seems similar to that of case XCDF. However, the generated inflow synthetic turbulence in case XCMC does not satisfy the divergence-free condition, and there must be some signature for this.

In checking the Probability Density Functions (PDFs) of the pressure fluctuations sampled at various stations at the centre of the channel (see Fig. 4.8), we observed more extreme peak pressure fluctuations in case XCMC compared to case XCDF. Fig. 4.8 shows that the occurrence of extreme peak pressure fluctuations for case XCMC can be more than twice that of case XCDF. This certainly shows an good feature of the XCDF model.

Unphysical peaks near the inlet are generated for both cases where the synthetic turbulence was imposed. Case XCMC gave an order higher pressure fluctuations near the inlet compared with case XCDF (see the inset in Fig. 4.7(a)). The XCMC model

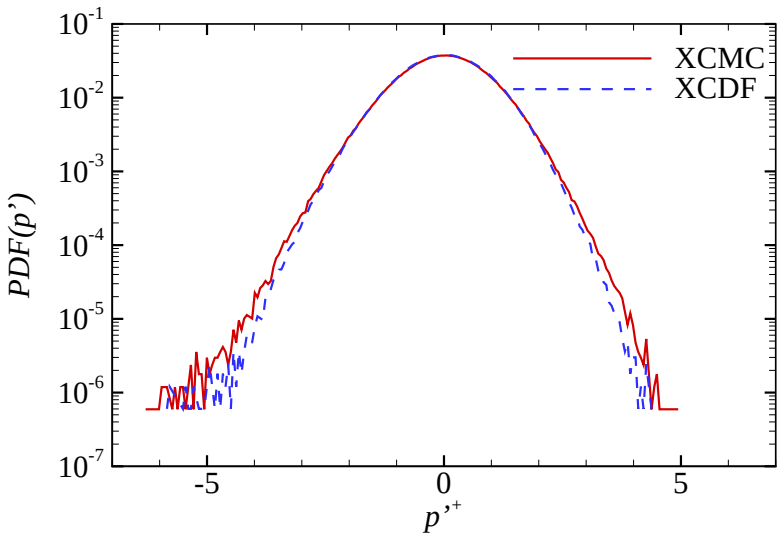

FIGURE 4.8: Probability Density Functions (PDFs) of dimensionless pressure fluctuations $p'^{+} = p'/\rho u_\tau^2$ sampled at x/δ=5, 10, 20, 30, 40, 55 and y/δ=1. The total number of samples is 2.4×10^6.

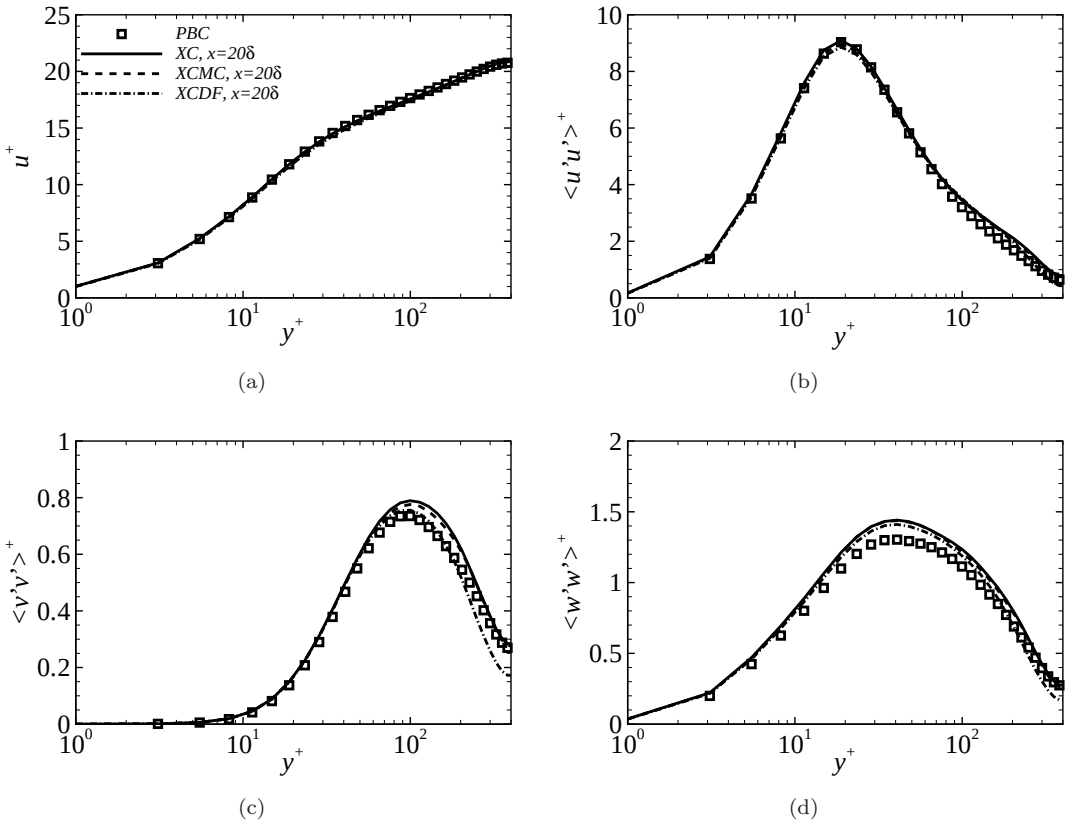

FIGURE 4.9: Profiles of statistics at $x = 20\delta$ obtained from using different inflow methods are compared with those for case PBC.

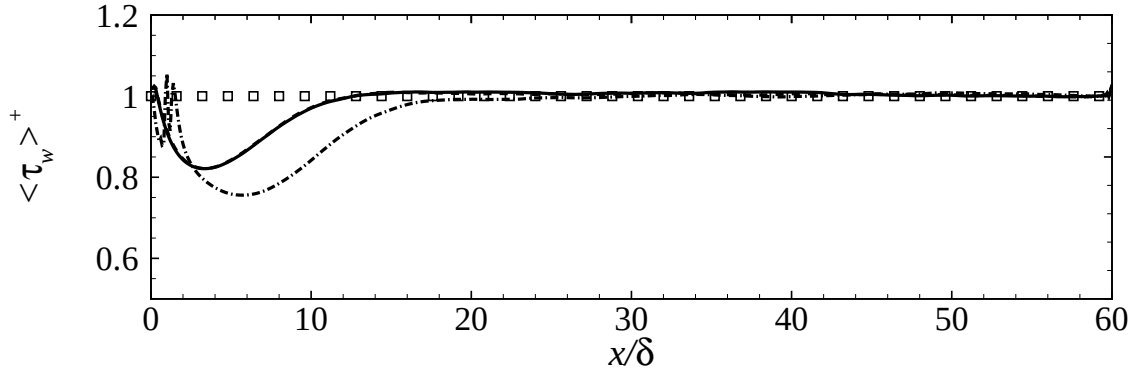

(a)

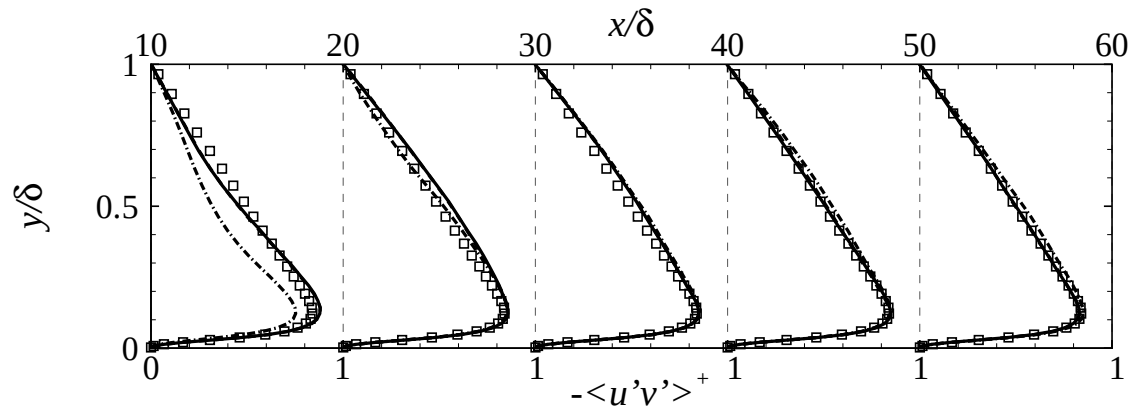

(b)

FIGURE 4.10: (a) Development of dimensionless wall shear stress τ_w^+. (b) Profiles of dimensionless time and spanwise averaged Reynolds shear stress $-\langle u'v'\rangle^+$ at different downstream locations. PBC □, XC —, XCMC –, XCDF – · –.

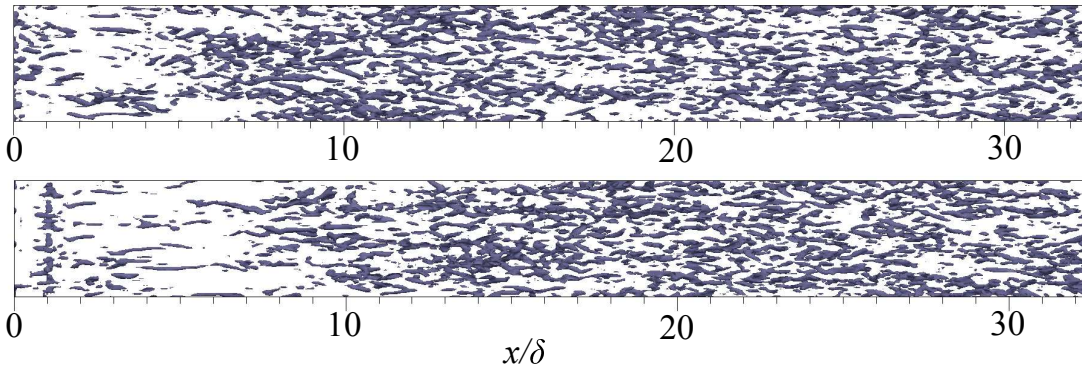

FIGURE 4.11: Iso-surface of $Q = 200$ in ($x/\delta \leq 32$, $0 < y/\delta < 0.25$). XCMC model (top), and XCDF model (bottom).

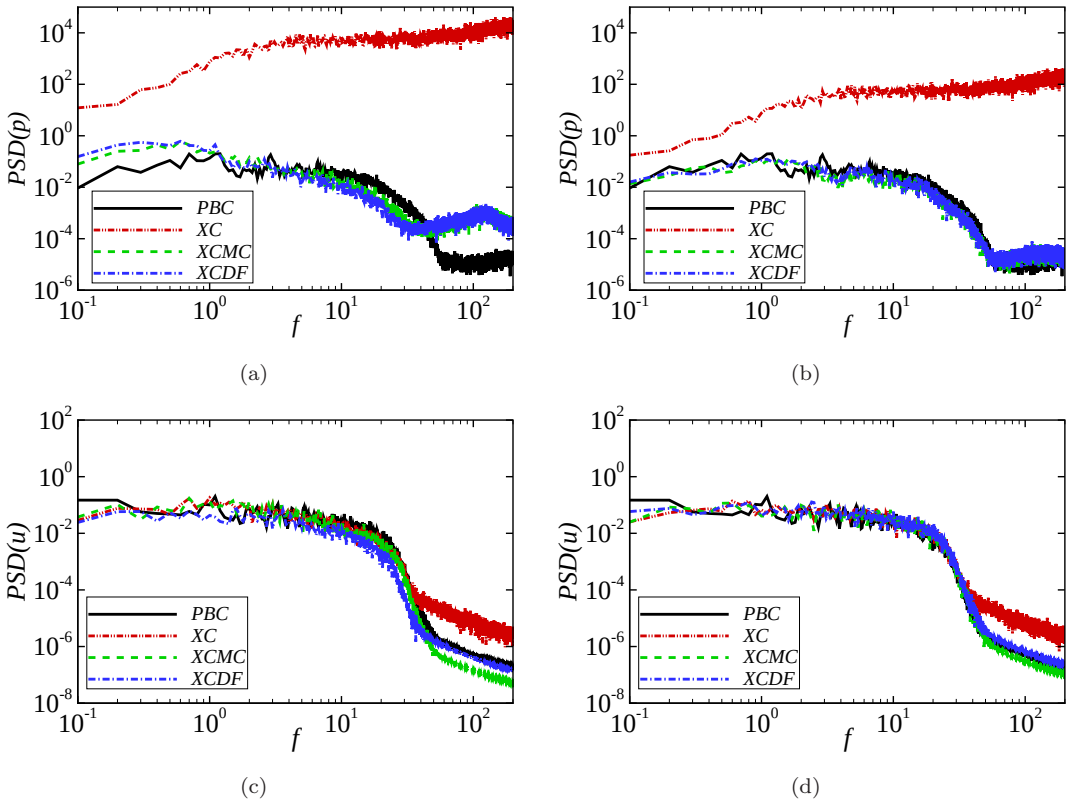

FIGURE 4.12: Power spectral density of pressure fluctuations (a,b) and the streamwise velocity fluctuations (c,d) at $y/\delta = 1$. (a,c) $x/\delta = 10$; (b,d) $x/\delta = 55$. All quantities are normalized appropriately by ρ, u_τ and δ.

may thus be less satisfactory than the XCDF model if the region of interest is close to the inlet.

Fig. 4.7(b) show profiles of the dimensionless time- and spanwise-averaged variance of the pressure fluctuations, $\langle p'^2\rangle^+ = \langle p'^2\rangle/(\rho^2 u_\tau^4)$, at different downstream locations. The pressure fluctuations for case XCDF downstream from $x/\delta = 10$ and for case XCMC from $x/\delta = 20$ are in an excellent agreement with the reference data (i.e. PBC). Note that the $\langle p'^2\rangle^+$ for case XC is far too large to be shown in Fig. 4.7(b).

It is of interest to check the turbulence statistics profiles. As a typical example, Fig. 4.9 present the time- and spanwise-averaged velocity and velocity fluctuation variances at $x = 20\delta$ obtained from using the different inflow methods. All of the quantities are normalised appropriately by friction velocity u_τ and they all show a good performance when compared with the reference - case PBC. This suggests that the three inflow models show a similar performance in this aspect.

The flow development in terms of the recovery distances of wall shear stress and Reynolds shear stress is crucial for the inflow methods. Fig. 4.10(a) shows dimensionless wall shear stress $\tau_w^+ = \tau_w/(\rho u_\tau^2)$. In spite of the significantly different pressure fluctuations between cases XC and XCMC shown in Fig. 4.7, the wall shear stress and

Reynolds shear stress profiles for both cases are almost identical as shown in Fig. 4.10. The development distance in terms of the recovery of the wall shear stress and Reynolds shear stress for the XC and XCMC models is $x/\delta \approx 10$, which is similar to those in Deck et al. (2011) [22] in which a turbulent boundary layer was simulated using a different synthetic turbulence inflow method [57]. The development distance for case XCDF is noticeably greater than those for cases XC and XCMC, partly because the effective inflow plane for case XCDF is at $x_0 = \delta$. Nevertheless, the error of wall shear stress at $x/\delta = 15$ for case XCDF is within 5%. Setting the 5% error as the criterion to define the development distance, then it is 14δ for the XCDF model counting from the plane at x_0.

Fig. 4.10(b) shows dimensionless Reynolds shear stress profiles $-\langle u'v'\rangle^+ = -\langle u'v'\rangle/u_\tau^2$. The error of Reynolds shear stress (at $x/\delta = 10, y/\delta = 0.1$) for case XCDF is within 5%. To visualize the near wall structures, the second invariant of the velocity gradient tensor can be used – often called the Q-criterion (e.g. [27]), which is written as

$$Q = \frac{1}{2}(\Omega_{ij}\Omega_{ij} - S_{ij}S_{ij}), \tag{4.27}$$

where $\Omega_{ij} = (\frac{\partial u_i}{\partial x_j} - \frac{\partial u_j}{\partial x_i})/2$ and $S_{ij} = (\frac{\partial u_i}{\partial x_j} + \frac{\partial u_j}{\partial x_i})/2$. Essentially Q is the balance between the rotation (Ω_{ij}) and strain (S_{ij}) rates. Thus a positive value of Q indicates that the strength of rotation overcomes that of the strain. Fig. 4.11 shows the isosurface $Q = 200$ in the upstream region of the domain for XCMC and XCDF models. XCMC shows a delay of development of near-wall structures, which is consistent with Fig.4.10(a). However, XCMC and XCDF models show almost the same performance downstream of $x/\delta = 10$.

Power Spectral Densities (PSD) of the pressure fluctuations and streamwise velocity fluctuations at two typical stations are shown in Fig. 4.12. These are consistent with Figs. 4.7 and 4.10. The PSD of the pressure fluctuations for case XC (in which the constant mass flux condition is not satisfied) is over-predicted by orders of magnitude through much of frequency range, whereas those for cases XCMC and XCDF show a reasonable agreement with the reference data (PBC) at $x/\delta = 10$ and even better agreement at $x/\delta = 55$. Spectra of the streamwise velocity fluctuations for all cases are in good agreement at most frequencies in Figs. 4.12(c) and 4.12(d). The maximum frequency that can be resolved by the current time step (Nyquist limit) $f = \frac{1}{2\Delta t} = 250$. The maximum frequency is further restricted by the spatial resolution. Note that CFL$<$ 0.4 at the middle of the channel.

4.3.4.1 Remarks on the XCDF model

It is a significant challenge to solve the divergence-free problem which arises in applying synthetic inflow conditions, especially since the latter should include crucial features like

turbulence integral length scales, spectra, Reynolds stresses, anisotropy and inhomogeneity, and whilst maintaining high computational efficiency. The proposed divergence-free XCDF model certainly is not free of limitations. The development distance in terms of the skin friction needs to be improved if estimation of the skin friction is of major interest. Combining the XCDF model with some up-to-date stochastic forcing methods such as Laraufie et al. (2011) [81] would improve the development distance. Imposing the synthetic turbulence on a transverse plane near the domain inlet does increase computational resources by less than 2% for these test cases, hence this overhead is negligible.

Based on the statistics from the current test cases, the divergence-free inflow method does not seem to be superior in all aspects compared to a simple mass flux correction approach. However, XCDF has distinctive features. Firstly, the mass correction factor, $U_b/U_{b,T}$, in Eq. 4.2 ranges 1 ± 0.02 for the current test case which is relatively high considering $U_b/u_\tau = 18.33$. In practical applications, a very coarse mesh at the inlet may be adopted (i.e. fewer sampling points). And subsequently the mass correction factor can be even greater which can lead to a noticeable alteration in the prescribed Reynolds stress in Eq. 2.41. In such situations, one could argue that the mass flux correction effectively modifies the input turbulence parameters. Secondly, there is an unphysical peak of pressure fluctuations near the inlet as shown in Fig. 4.7(a). It decays rapidly but may cause unphysical and unacceptably high noise levels for some aeroacoustic applications, especially when the region of interest is inevitably close to the inlet. Thirdly, we noticed that the XCMC model generated more extreme peak pressure fluctuations at the middle of the channel compared to case XCDF, though these are not clearly shown in the spectra of pressure fluctuations.

The modification to the PISO algorithm is similar in some respects to the body-force approach, e.g. [65, 67, 81]. However, there are clear differences too. For example, in Keating et al. (2006) [67], the stochastic force is isotropic. XCDF, on the other hand, can reproduce specified anisotropy by providing individual Reynolds stresses and integral length scales. Also no empirical constant is involved in the XCDF model, unlike in typical body-force approaches.

Laraufie et al. (2011) [81] suggests that the development distance decreases with increasing Reynolds number, thus applicability of the XCDF model will likely improve further for spatially developing flows at high Reynolds numbers. For example, we have used the XCDF model to simulate surface pressure fluctuations on the Commonwealth Advisory Aeronautical Council (CAARC) standard building at a Reynolds number 3×10^5 based on the free stream velocity and the height of the building [20]. The validation against wind tunnel experiments has been very promising.

The divergence-free model can be easily implemented in other CFD codes. For example, a similar method has been used in an in-house code [118]. Our method has

been tested using both PISO and PIMPLE (i.e a combination of PISO and SIMPLE, see Appendix B) solvers in OpenFOAM, which suggests the significant potential of the method.

4.4 Summary

A new divergence-free synthetic turbulence inflow technique has been developed with incompressible flow solvers. To satisfy the divergence-free criterion, the velocity-pressure coupling (PISO) procedure is modified slightly by substituting the generated synthetic turbulence for the intermediate velocities on a transverse plane near the domain inlet before the corrector steps are performed. The synthetic turbulence is mildly adjusted through the correctors and thus is divergence-free. It is to be stressed that this modification of the PISO procedure costs no additional CPU time.

The effects of the modification of the PISO algorithm on solution accuracy have been examined analytically and numerically. The maximum error (always on the transverse plane where synthetic turbulence is imposed) is, for the velocity, one order of magnitude higher than the truncation error, whereas the maximum error for the pressure is less than one order of magnitude higher than the truncation error. This is not surprising because imposing the synthetic turbulence within the domain (rather than at the inlet) is similar in some respects to a body-force approach. Maximum disturbances occur where the synthetic turbulence is imposed. Nevertheless, the errors decay downstream (e.g. $x/\delta > 5$) to the levels suggested in Issa (1985) [55].

The suggested divergence-free turbulence inflow model XCDF has been tested on a channel flow and compared with the XC model [183] and the XC model with a mass flux correction – XCMC. Both XCDF and XCMC give very significant improvements on the computed pressure fluctuations. For example, the variance and spectra of the pressure fluctuations are in good agreement with reference data obtained from a plane channel flow using axially periodic boundary conditions. In addition, the XCDF model is genuinely divergence-free and provides solution improvements in other respects too, such as more reasonable peak pressure fluctuations.

In applications where only time averaged pressure and aerodynamic forces (e.g. mean lift and drag on a wind turbine blade or mean wind loads on a building) are of interest, the XC and XCMC models are generally satisfactory. However, if instantaneous forces (e.g. peak structural wind loads in wind engineering applications) are the focus, the divergence-free method XCDF is recommended. In particular, the XCDF method can be very useful in some applications in which the turbulence motions are required to insert in the computation domain. For example, the XCDF method can be used at the interfaces of the coupling of a weather-scale model and a street-scale LES model to

provide sufficient turbulent fluctuations when nested meshes are used.

Chapter 5

The effect of freestream turbulence on the flow over a static airfoil

5.1 Introduction

The effect of turbulence on the aerodynamic characteristics of an airfoil are important in wind turbine aerodynamics because the operating condition (atmospheric boundary layer) of wind turbines are mostly turbulent. Upstream turbulence can modify transition, separation points on the turbine blade and also acoustic-noise emissions from the blade. Thus it is of great interest to understand the effects of turbulence on the aerodynamic characteristics of an airfoil. Currently, many of the prediction tools for wind turbine performance use 2-D airfoil data measured from wind tunnels for a laminar inflow condition [155].

The atmospheric boundary layer is complicated. It is anisotropic and contains wind shear and temperature gradients etc. To simplify the problem, isotropic and shear-free freestream turbulence is considered in the present study. The divergence-free turbulence inflow condition (XCDF, see Ch. 4) is applied to the flow over a NACA 0006 airfoil at $Re = 50,000$. The length of the laminar separation bubble on a thin airfoil such as NACA 0006 is shorter than that on a thick airfoil at low Reynolds number. As the Reynolds number increases, the laminar bubble tends to be avoided [91]. Then the flow topology over the thin airfoil at low Reynolds number is closer than that over the thick airfoil to the flow topology at high Reynolds number. Thus a NACA 0006 airfoil case is selected for the test case and validated using LES.

The objectives for this chapter are twofold; the first is to provide a reliable framework that can be applicable to an aerodynamic and unsteady surface pressure analysis for wind

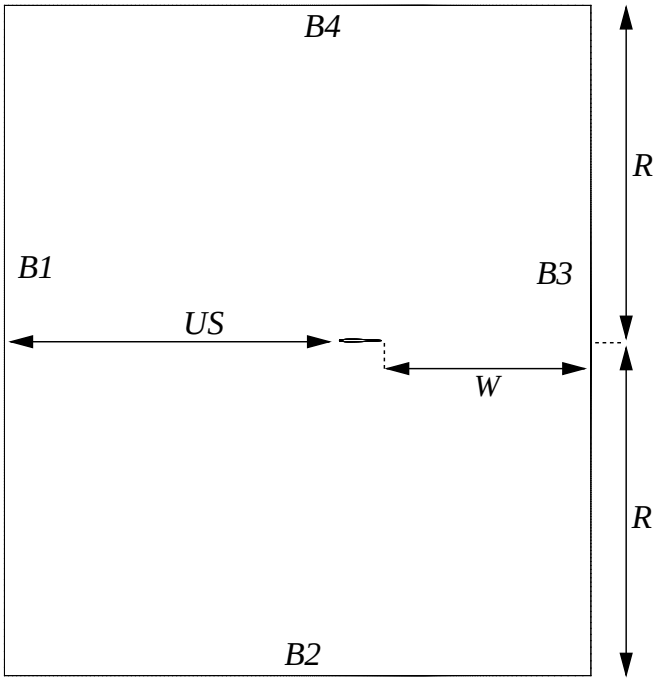

FIGURE 5.1: A sketch of the domain.

turbine blades with upstream turbulence. The second is to quantify and understand the effect of freestream turbulence on the aerodynamic loads and unsteady surface pressure on an airfoil. Sec. 5.3 presents a simulation for an airfoil flow for a laminar inflow condition as a baseline case and the results are compared with the DNS data by Jones et al. (2008) [61]. Raw data of the reference was provided by a personal communication [61, 62]. The numerical method and domain information are described in Sec. 5.2. Based on the baseline simulation, the effect of freestream turbulence on the flow over a static airfoil is examined at 0° and 7° angles of attack. This is presented in Sec. 5.4 and a summary is following in Sec. 5.5. Some results and discussions on this subject were reported in the conference paper, Kim, Xie, Castro. *UK WES conf., Southampton, UK,* 2012 [68].

5.2 Methodology

The domain shape and mesh topology around the airfoil for the baseline simulation are shown in Figs. 5.1 and 5.2. The purpose of the rectangular shape of the inlet was to resolve freestream turbulence by adopting a quasi-rectangular mesh on the upstream region. This rectangular mesh was applied from the boundary '$B1$' to a distance $2.1c$ from the leading edge. From this $2.1c$ upstream location to a $1c$ upstream distance from the leading edge, the mesh was gradually adopted to the C-type mesh as shown in Fig. 5.2(b).

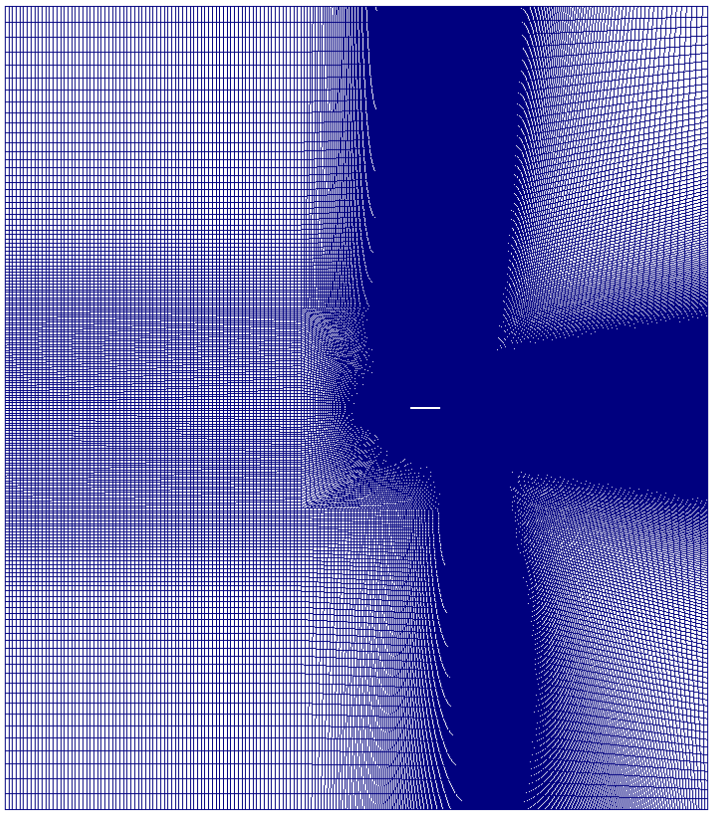

(a)

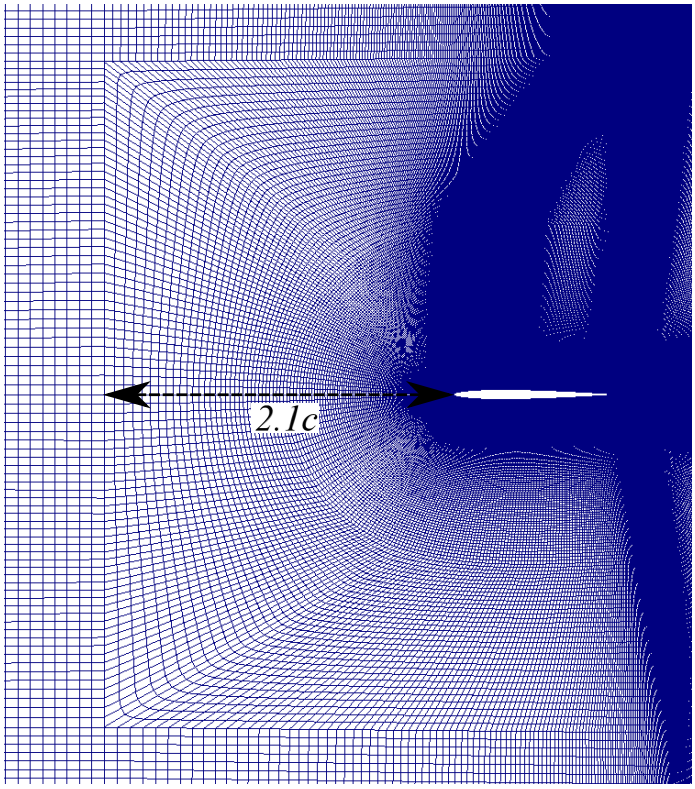

(b)

FIGURE 5.2: Mesh topology for (a) the whole domain and (b) near the leading edge.

The first grid point was placed at $2\times10^{-4}c$ away from the airfoil surface to ensure that $y_1^+ \approx 1$. Pointwise V16 was used to generate all meshes. The role of the SGS model is important for the baseline simulation because a laminar separation bubble, reattachment and transition points occur over the upper airfoil surface. These phenomena are poorly captured with the Smagorinsky model [151], while the mixed-time-scale SGS model (see Sec. 2.2.3) is adequate in such situations as the SGS contribution becomes zero in the laminar region. Thus MTS SGS model was adopted. Model constants for the MTS model were modified by Krishnan et al. (2009) [78] and were $C_{MTS} = 0.03$, $C_T = 10$. A simple top-hat filter was applied for the explicit filter in the MTS model.

Averaging started once the lift coefficient reached a statistically converged state and averaging was performed over $30T$ approximately, where $T = c/U_\infty$ and U_∞ was the freestream velocity. Spanwise averaging was also conducted for all figures for 3-D cases. The time step was $t/T = 3 \times 10^{-4}$ which satisfied the condition that the maximum CFL $\left(\frac{\Delta t U}{\Delta x}\right)$ number was less than 1.3. A second order, implicit scheme was used for the temporal discretization and a second order central difference scheme was used for the convection term. The transient incompressible flow solver from OpenFOAM 1.7.1 was used and the PISO algorithm (see Sec. 4.2.3.1) was adopted for the velocity-pressure coupling. Pointwise V16 was used to generate all meshes.

A periodic boundary condition was applied in the spanwise direction for 3-D cases and no-slip wall conditions were used on the airfoil surface for all calculations. Other boundary conditions for the baseline simulation (Base) are summarized in Table 5.1. The boundary conditions for other cases are also found in the table and details for these cases will be explained in the following sections. The freestream velocity at the boundaries was determined by the angle of attack, α, on each case, i.e. $u = U_\infty\cos(\alpha)$, $v = U_\infty\sin(\alpha)$. Note that the coordinates x, y and z represent the streamwise, cross-flow and spanwise direction respectively, with the origin at the leading edge of the airfoil throughout all simulations.

TABLE 5.1: Summary of the boundary conditions for different cases. U_∞ is the freestream velocity and d/dn is normal derivative to the boundary. The transverse plane is placed at $x_0/c = -7$ where the XCDF model (see Ch. 4) is imposed.

Case	B1	B2	B3	B4	x_0/c
Base	$u_i = U_\infty$, $dp/dn = 0$	$u_i = U_\infty$, $dp/dn = 0$	$du_i/dn = 0$, $p = p_\infty$	$du_i/dn = 0$, $p = p_\infty$	n/a
3DTA0	$u_i = U_\infty$, $dp/dn = 0$	slip-wall, $dp/dn = 0$	$du_i/dn = 0$, $p = p_\infty$	slip-wall, $dp/dn = 0$	XCDF
3DTA7	$u_i = U_\infty$, $dp/dn = 0$	$u_i = U_\infty$, $dp/dn = 0$	$du_i/dn = 0$, $p = p_\infty$	$du_i/dn = 0$, $p = p_\infty$	XCDF

5.3 Baseline simulations: laminar inflow

In order to save CPU time, tests for mesh convergence and domain size in the streamwise and cross-flow directions were conducted on a 2-D domain without the SGS model for the baseline simulations. The mesh convergence tests without the SGS model in the 2-D domain are useful as LES requires a very fine resolution, close to DNS, near the wall. The grid points around the airfoil were increased until the pressure and skin-friction coefficients converged leaving the other conditions and the mesh unchanged. Based on the tests on the 2-D mesh, a 3-D mesh was generated by extruding the 2-D mesh in the spanwise direction.

TABLE 5.2: The computational domain size in unit c and number of grid points in the 2-D domain, see Fig. 5.1. Note that N_{up} and N_{low} are the number of grid points on the upper and lower airfoil surface respectively.

	2D1	2D2	2D3	2D4	2D5
US [c]	8	8	8	8	8
R [c]	8	8	8	10	8
W [c]	5	5	5	5	5
N_{US}	363	363	363	363	363
N_R	330	330	330	340	330
N_W	150	150	150	165	150
N_{up}	533	400	266	266	393
N_{low}	533	400	266	266	150

5.3.1 Two-dimensional domain

Details of the domain size and number of grid points are tabulated in Table 5.2. The surface pressure and skin-friction coefficients are shown in Fig. 5.3 for the 2-D cases and there are no noticeable differences between cases 2D1 (the finest grid) and 2D2 (the medium grid). C_p and C_f for case 2D3 show, however, the different peak values and locations of laminar separation bubbles on the upper surface compared with those for cases 2D1 and 2D2. The peak value of the skin-friction decreases 30% for case 2D3 compared to that for case 2D1. The reattachment point is delayed from $x/c = 0.14$ for case 2D1 to $x/c = 0.25$ for case 2D3.

Jones et al. (2008) [61] investigated the requirement of the domain size on the flow over a NACA 0012 airfoil at $Re = 50,000$. In Jones et al. [61], an integral characteristic boundary condition [171] was adopted at the inlet to minimize unwanted reflection from the computational boundaries. It was reported that $R = 7.3$, $W = 5$ (see Fig. 5.1) were sufficient to capture the potential flow. For the current case, a domain size $R = 8$, $W = 5$ was used. The domain size $R = 10$, $W = 8$ (2D4) was tested to confirm that

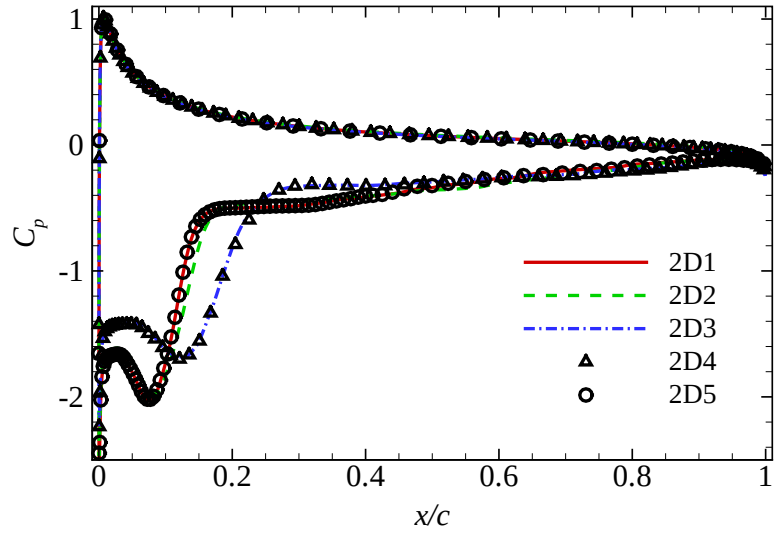

(a)

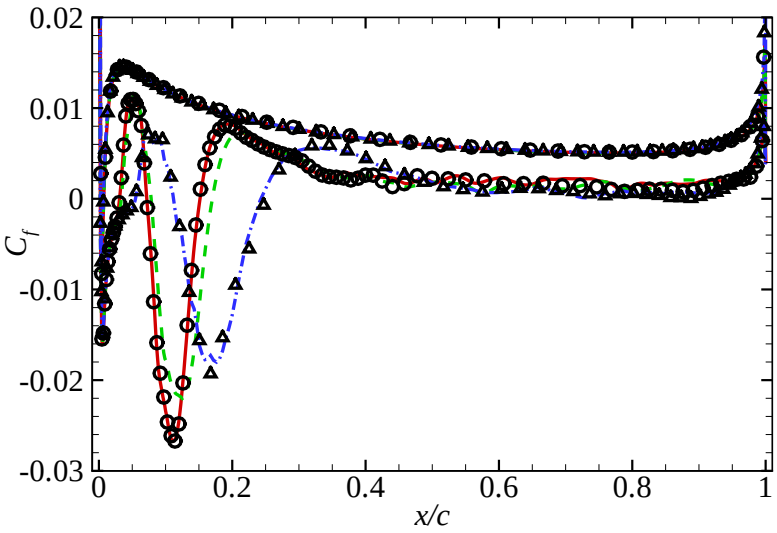

(b)

FIGURE 5.3: The effects of the domain size and grid points around the airfoil in the 2-D domain on (a) pressure coefficients, (b) skin-friction coefficients. $Re = 50,000$ and $\alpha = 7°$.

the current size of the domain is sufficiently large. The azimuthal distribution of the pressure, $p - p_\infty$, for $2c$ and $3c$ displacements from the trailing edge are shown in Fig. 5.4. Azimuthal distributions show good agreement among cases 2D1, 2D3 and 2D4 with negligible differences in the wake region. It is concluded that the domain size $R = 8$, $W = 5$ is adequate to capture the potential flow at these given conditions on the NACA 0006 airfoil. The mesh for case 2D5 was carefully designed so that it produced reasonably similar results with cases 2D1 and 2D2 by using the minimum number of grid points. The results from case 2D5 are the same as those from case 2D1 as shown in Fig. 5.3. Thus the mesh for case 2D5 was chosen and used to generate the 3-D mesh.

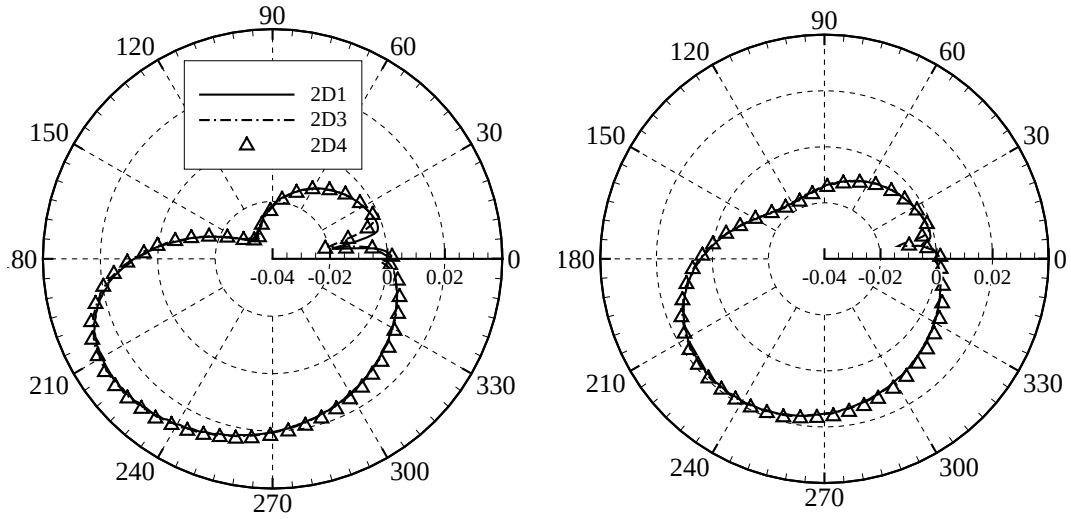

(a) (b)

FIGURE 5.4: The azimuthal distribution of the pressure, $\frac{p-p_\infty}{\rho U_\infty^2}$. The azimuthal angle [°] begins at the trailing edge in the anti-clockwise direction. The distance from the trailing edge is (a) two chord length and (b) three chord length.

TABLE 5.3: The computational domain size in unit c and number of grid points in the spanwise direction. Note that all 3-D meshes are generated based on the 2D5 mesh in Table 5.2.

	3D1	3D2	3D3	3D4
L_z [c]	0.2	0.2	0.2	0.4
N_z	64	32	16	64

5.3.2 Three-dimensional domain

The 2-D simulations without the SGS model were conducted for the mesh convergence and domain size tests. The effect of the domain size and resolution in the spanwise direction were examined and the details of mesh information are presented in Table 5.3. The effects of the resolution in the spanwise direction were tested to investigate a minimum requirement of the grid points in the span as shown in Fig. 5.5. Cases 3D1, 3D2 and 3D3 contain 64, 32 and 16 grid points in the spanwise direction while the domain width is the same which is $0.2c$. Fig. 5.6 shows the resolution in wall-units for case 3D2. The resolution in wall-unit is calculated as,

$$\Delta x_i^+ = \frac{\Delta x_i \sqrt{|\tau_w|}}{\nu}, \tag{5.1}$$

where $x_i = z,\ n,\ s$ representing the spanwise, surface-normal and surface-tangential components respectively. $\Delta z^+_{\max}$ for case 3D2 is around 20 on the suction side, thus $\Delta z^+_{\max}$ for cases 3D1 and 3D3 would be 10 and 40 respectively. Jones et al. [61] used

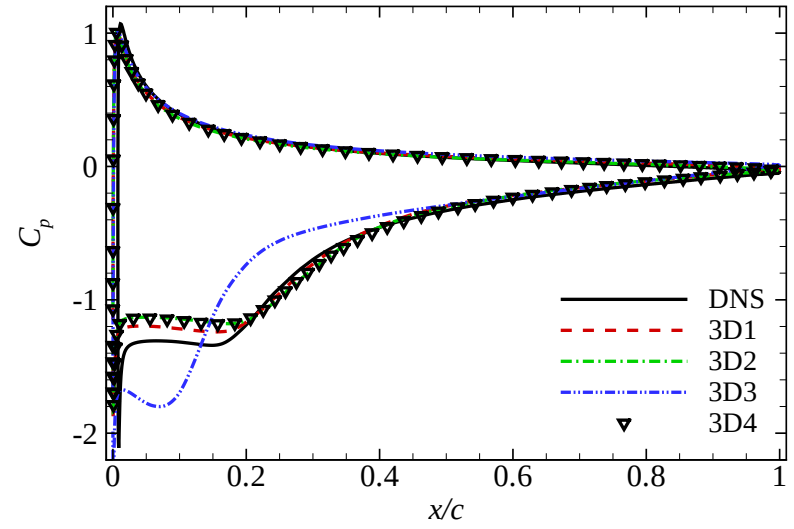

(a)

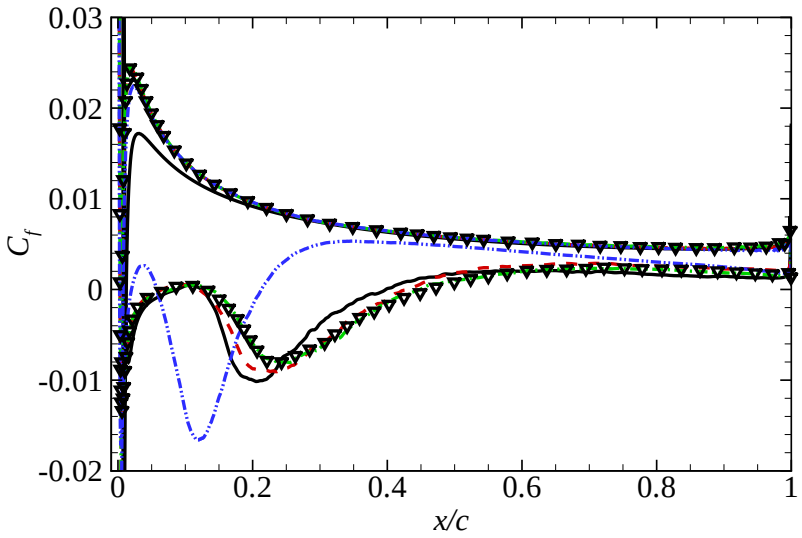

(b)

FIGURE 5.5: The effect of domain width and grid points on an airfoil in the 3-D domain. (a) Pressure and (b) skin-friction coefficients for $Re = 50,000$ and $\alpha = 7°$.

$\Delta z^+_{\max} = 6.49$ on a flow over a NACA 0012 airfoil using DNS and Sandham et al. (2002) [134] used $\Delta z^+_{\max} = 7.5$ on a turbulent plane channel flow using DNS. For LES calculations, Jarrin (2008) [57] had tested various resolutions for turbulent plane channel flow and reported that the flow was reasonably well resolved for $\Delta z^+ < 19$. Thus the flows for cases 3D1 and 3D2 are considered to be well-resolved under the criterion of the mesh requirement for the LES calculations of the turbulent plane channel flow.

In Fig. 5.5, the pressure and skin-friction coefficients show little difference between cases 3D1 and 3D2, but those for case 3D3 present significant difference especially where the laminar separation bubble exists. The profiles for the mean velocity and turbulence fluctuations over the upper airfoil surface are compared with the reference data in Fig.

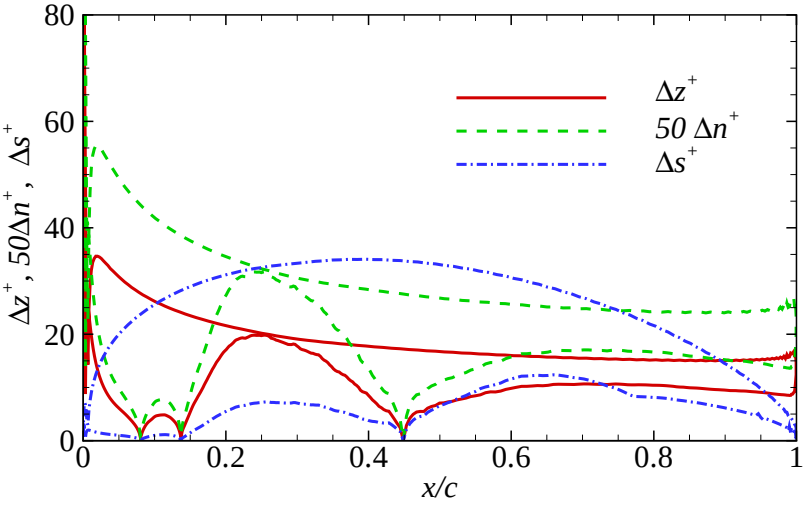

FIGURE 5.6: Wall-unit resolutions normalized by the skin-friction from case 3D2. s and n are the surface tangential and surface normal direction components respectively.

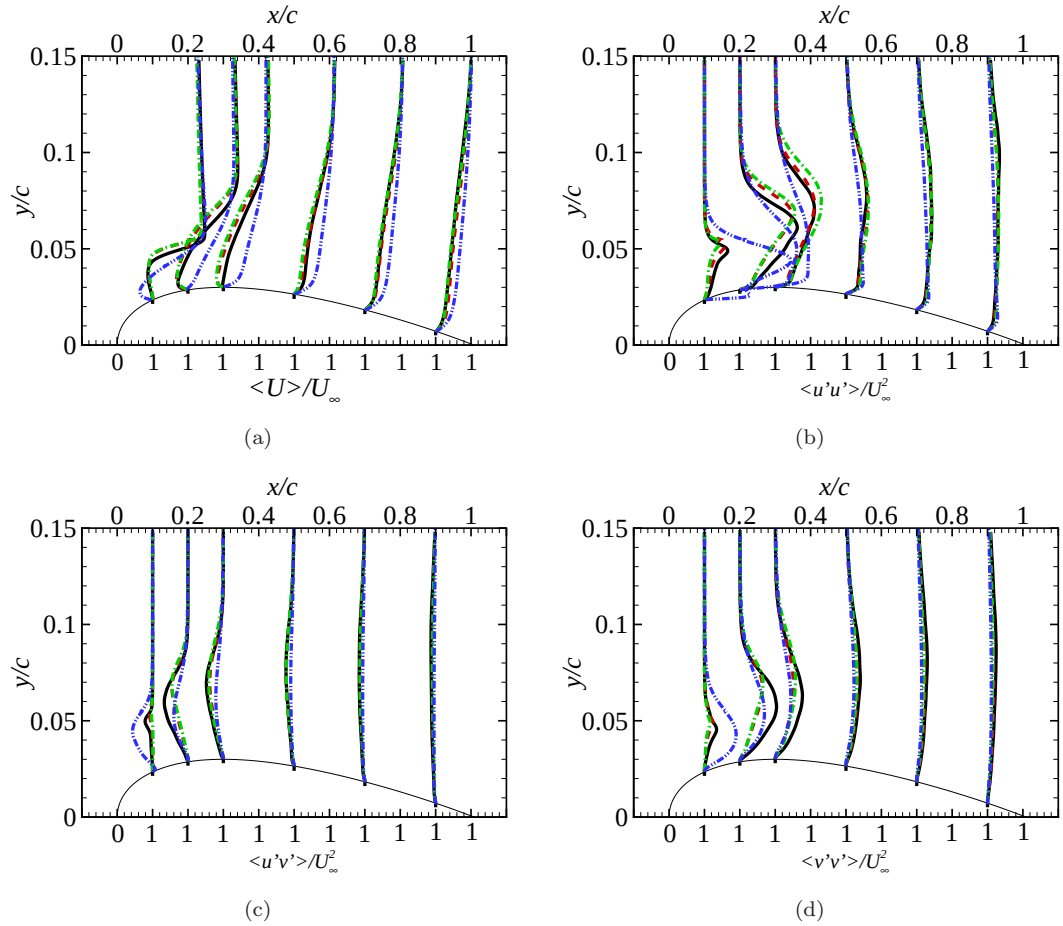

FIGURE 5.7: The profiles over the upper surface for the (a) mean streamwise velocity, (b) streamwise turbulence fluctuation, (c) Reynolds shear stress and (d) cross-flow turbulence fluctuation for $Re = 50,000$ and $\alpha = 7°$. — DNS [61], −−3D1, − · −3D2, − · ·−3D3, see Table 5.3.

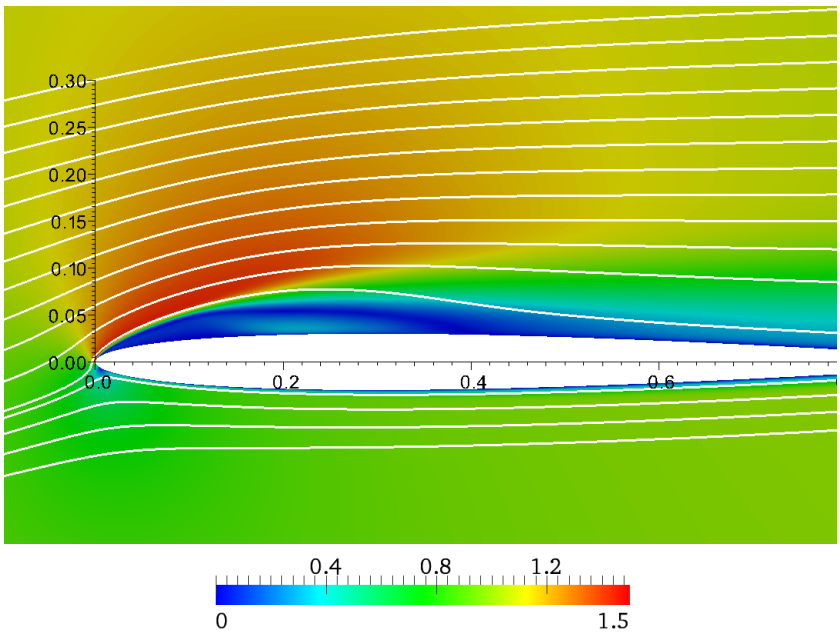

FIGURE 5.8: The mean velocity magnitude $|U|/U_\infty$ with streamlines for case 3D2, $Re = 50,000$ and $\alpha = 7°$. The coordinates are normalized by the chord.

5.7. Consistency is also found in all flow profiles above the upper airfoil surface. All turbulence fluctuations for case 3D3 are over-predicted and the mean velocity near the airfoil shows a positive value for $0.2 \leq x/c \leq 0.3$ while those for other cases show negative values. This can be interpreted as case 3D3 presents a shorter laminar separation bubble than the other cases.

The computational domain size in the spanwise direction was investigated. von Terzi (2004) [175] had simulated a backward-facing step flow and reported that a minimum of four times the step height was required for the domain width which was approximately the reattachment length in the backward-facing step flow. Jones et al. [61] applied this relation between the domain width and step height to the flow over an airfoil and set $L_z = 0.2c$ as their spanwise domain size. Fig. 5.8 shows the mean velocity magnitude with streamlines. The laminar separation bubble thickness is approximately $0.05c$ which suggests the domain width $0.2c$ is required for the current case. To confirm the analogy in Jones et al. (2008) [61], actual calculations were performed. Cases 3D2 and 3D4 were based on an identical 2-D mesh (2D5 in Sec. 5.3.1) and had the same resolution in the spanwise direction but with different domain widths. The domain width for case 3D2 was $0.2c$ and that for case 3D4 was $0.4c$. As shown in Fig. 5.5, the results for cases 3D2 and 3D4 show no evident difference and fairly good agreements with DNS data. Thus the domain width of $L_z = 0.2c$ is considered adequate for the baseline simulation.

5.4 The effect of freestream turbulence

The baseline simulation (3D2) was described in the previous section and the results showed good agreement with the DNS data. Based on the baseline simulation, the effects of freestream turbulence are investigated by using the divergence-free turbulence inflow (XCDF model, see Ch. 4) on the flow over a NACA 0006 airfoil at 0° and 7° incidence. Surface forces and pressure are analysed and compared with appropriate analytical solution and measurements.

5.4.1 Upstream turbulence

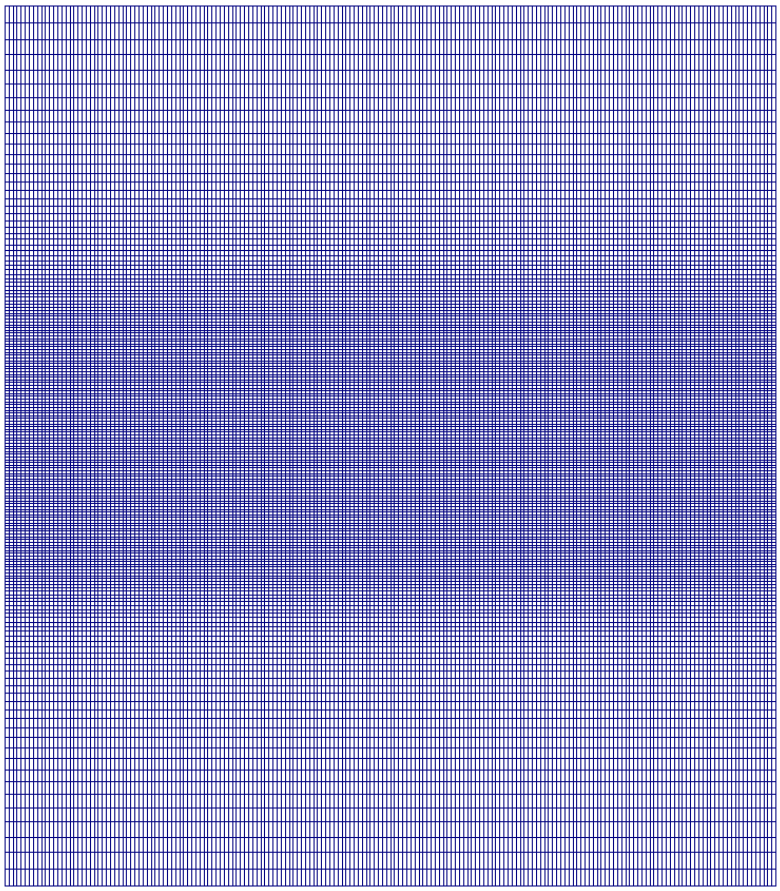

FIGURE 5.9: A box domain for homogeneous isotropic turbulence.

To characterize upstream turbulence, a new mesh was generated as shown in Fig. 5.9 in which the upstream region of the domain was the same as case 3D2, but the airfoil was removed and the downstream part of the mesh was the same as the upstream one. Two different turbulence intensities (TI_0 = 5%, 10%) were used where the subscript '0' denotes input variables. The upstream turbulence characteristics were quantified in

TABLE 5.4: Upstream turbulence characteristics: turbulence intensity (TI), integral length scales and Reynolds number on the domain without the airfoil. The inflow is generated at the origin ($x/I_{11} = 0$) and the airfoil will be placed at $x/I_{11} = 23.3$. Note that $Re_I = \frac{U_\infty I_{11}}{\nu}$ and $Re_\lambda = \left(\frac{20}{3} Re_I\right)^{1/2}$ [122]. $I_{11} = I_{21} = I_{31}$ and $I_{11} = 3I_{i2} = 3I_{i3}$ where $i = 1, 2, 3$.

x/I_{11}	TI[%]	I_{11}/c	Re_I	Re_λ
0	5	0.3	15,000	316
23.3	2.1	0.352	16,250	342
0	10	0.3	15,000	316
23.3	3.8	0.267	19,000	298

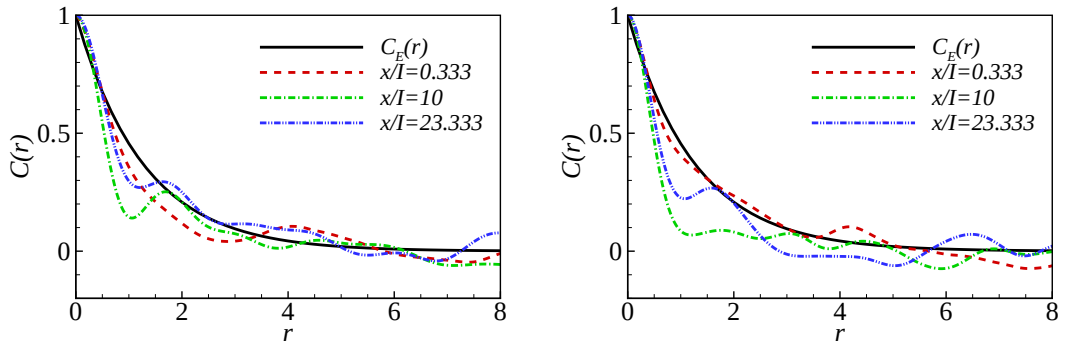

(a) $TI_0 = 5\%$ (b) $TI_0 = 10\%$

FIGURE 5.10: The autocorrelations for the streamwise component of velocity at different downstream locations. r is the normalized separation, $r = t\frac{U_\infty}{I_{11}}$ and $C_E(r)$ is the modelled correlation function which is defined as $C_E(r) = \exp\left(\frac{\pi}{4I_{11}} r\right)$ in the XCDF model, see Sec. 4.2.1.

the domain without the airfoil which is called an 'empty box case'. Then the same turbulence characteristics were used for the flow over the airfoil.

The turbulence length scales in the atmospheric boundary layer ranges from 0.001 to 500m [63]. The turbulence scales which are greater than the order of magnitude of the chord length have to be considered as an unsteady inflow condition [147]. Thus the integral length scales were set to the size which is comparable with the chord length and they were $I_{i1} = 3I_{i2} = 3I_{i3} = 0.3c$ where $i = 1, 2, 3$, see Eq. 2.52. The grid size normalized by the integral length scale (I_{11}) was $\Delta x = 0.246I_{11}$, $\Delta y = 0.167I_{11}$ and $\Delta z = 0.021I_{11}$. If it is considered that when 80% kinetic energy is resolved an LES is 'good', then the resolution $\Delta x \approx \frac{1}{6}I$ is required for LES calculations of homogeneous isotropic turbulence (HIT) [122]. The current grid size for the upstream region is a reasonable resolution in that regard.

The coordinate for the empty box case was normalized by the integral length scale, I_{11}. The boundary conditions were identical with case 3DTA0 in Table 5.1. Numerical schemes and the coordinate system were unchanged as in Sec. 5.2 but the origin was

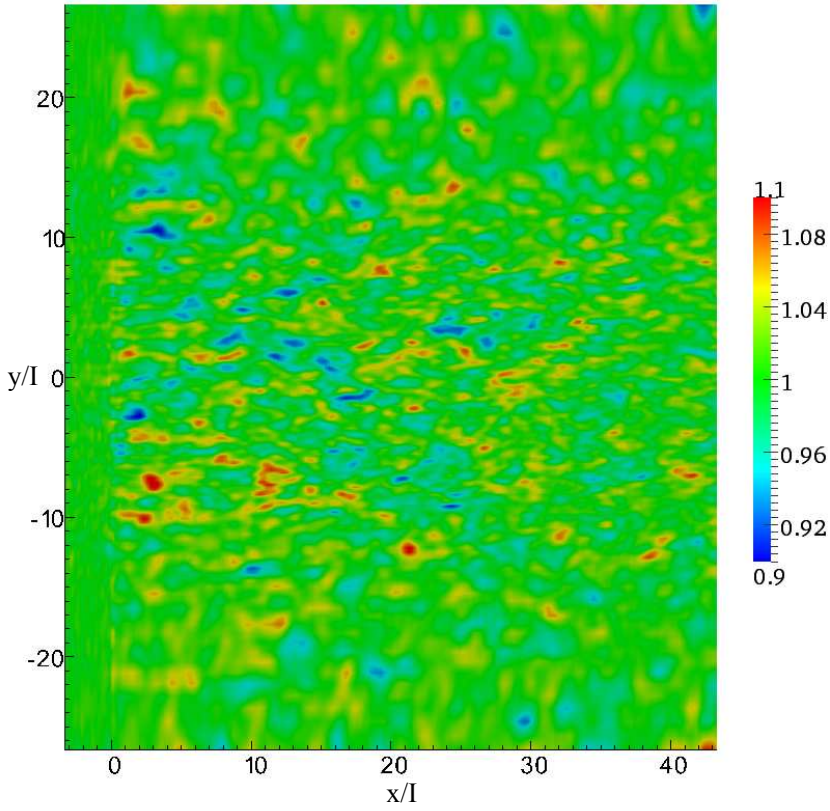

FIGURE 5.11: The streamwise component of velocity normalized by the freestream velocity at the middle of the domain for $TI_0 = 5\%$.

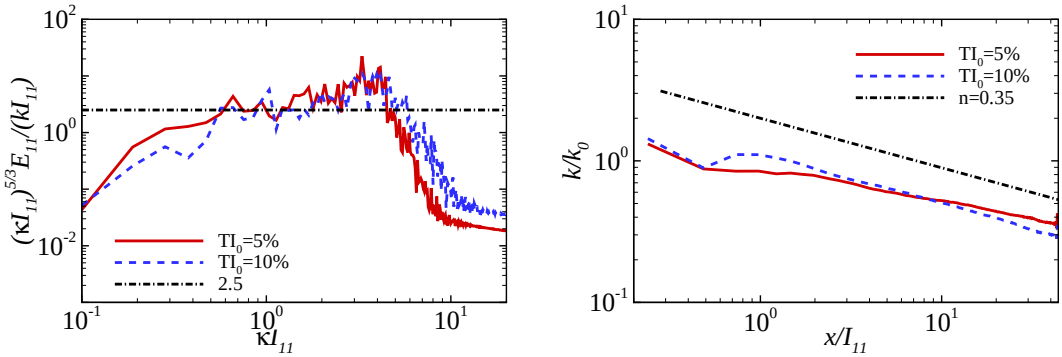

(a) (b)

FIGURE 5.12: (a) A one-dimensional energy spectrum, E_{11}, of the streamwise velocity component normalized by the local turbulent kinetic energy at $x/I_{11} = 23.3$ (see Table 5.4). The dot-dashed line is the inertial region value, 2.5. (b) The turbulent kinetic energy normalized by the input value k_0. The dot-dashed line is from $\frac{k}{k_0} \sim \left(\frac{x}{I_{11}}\right)^{-n}$. The suffix '$_0$' indicates the input variables

placed where synthetic turbulence was imposed. The distance between the inlet and the origin was $3.33I_{11}$. The time step normalized by I_{11} and U_∞ was $t \times U_\infty/I_{11} = 0.0133$. The domain width and number of grid points in the spanwise direction was the same as those in case 3D2.

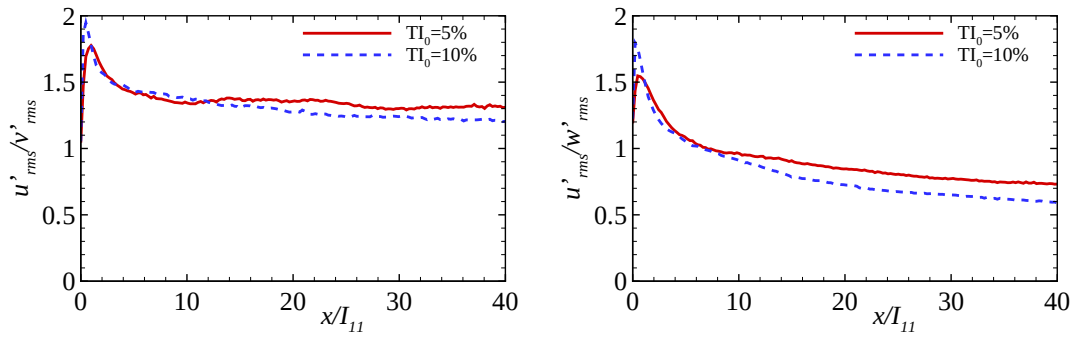

FIGURE 5.13: Anisotropy of upstream turbulence.

The turbulent characteristics at the origin and at the point where the leading edge will be placed ($x/I_{11} = 23.3$) are summarized in Table. 5.4. The integral length scale at $x/I_{11} = 23.3$ was not known *a priori*, so it was estimated by using autocorrelations after the calculations of the empty box case were finished. Time series of the streamwise component velocity was used to calculate the autocorrelations at different downstream locations and they are shown in Fig. 5.10. $C(r)$ in the vicinity of the synthetic turbulence imposition, i.e. $x/I_{i1} = 0.333$, agrees well with the target function, $C_E(r)$, for both $TI_0 = 5\%$ and 10%. As the flow convects downstream, the autocorrelations adjust to a Gaussian shape at $r \approx 0$. The calculated integral length scales at $x/I_{11} = 23.3$ are shown in Table 5.4. A snapshot of the streamwise component of the instantaneous velocity contour is shown in Fig. 5.11. Synthetic turbulence was imposed at $x/I_{11} = 0$. The airfoil will be placed at $x/I_{11} = 23.3$ in the following section thus the prime interests are focused on the region for $0 < x/I_{11} < 23.3$.

Fig. 5.12(a) shows the (compensated) one-dimensional energy spectrum of the streamwise velocity fluctuations at $x/I_{11} = 23.3$ for two turbulence intensities. The inertial subrange (constant value) can be found for both cases. The highest wavenumber that can be resolved by the current resolution (Nyquist limit) is $\kappa_{\max} I_{11} = \frac{1}{2}\frac{2\pi}{\Delta x} I_{11} = 12.8$ but E_{11} starts to drop $\kappa I_{11} \approx 5$. This phenomenon is associated with the SGS model, filtering method and numerical scheme. The top-hat filter was adopted for the explicit filter in the mixed-time-scale SGS model (Sec. 2.2.3). Piomelli (1999) [116] showed that the top-hat filter smoothed the structures which was larger than the cut-off size in spectral space, see Fig. 2.3. Xie et al. (2004) [185] also observed similar behaviours from their finite volume based LES calculations.

To calculate the Kolmogorov length scale, $\eta = (\nu^3/\varepsilon)^{1/4}$, the dissipation rate, ε, is estimated by comparing the compensated energy spectrum in Fig. 5.12(a) with the universal energy spectrum in the inertial subrange,

$$E_{11}(\kappa) = C_K \varepsilon^{2/3} \kappa^{-5/3}, \tag{5.2}$$

where $C_K = 0.49$ is the Kolmogorov constant [122]. Based on the estimated ε, the ratios between the grid size and the Kolmogorov length scale have values $\Delta x/\eta = 37.9$ and 63.4 for $TI_0 = 5\%$ and 10% respectively. It is shown that the current grid size is much larger than the Kolmogorov length scale and LES is designed for such a case.

Fig. 5.12(b) shows the rate of changes of turbulent kinetic energy normalized by the input value along the streamwise direction. Note that the suffix '$_0$' indicates the input variables. There are over-shoots at the first cells away from the origin. Then k/k_0 decreases as x/I_{11} increases. The peaks at the first cells were not observed in the channel flow in Ch. 4. These were improved as the domain width increased i.e. $k/k_0 \approx 1$ at $x/I_{11} = 0$. Thus it is concluded that the peaks are produced due to the geometrical constraints (the domain width required by the airfoil simulations) rather than the inflow generation technique. A small increase of the turbulent kinetic energy is seen at $x/I_{11} \approx 1$. This is because synthetic turbulence is adjusted to the governing equation and boundary conditions as soon as it is introduced within the domain, resulting in a temporal increase of the turbulent kinetic energy.

In homogeneous isotropic turbulence, turbulent kinetic energy decays with time or space. The rate of decay has been studied extensively and it is known that the variance of turbulence follows $\langle u'u' \rangle \sim x^{-n}$. But different values of the decay exponent n were reported from experiment [79] and DNS calculation [127] varying from 1.02 to 1.2. The decay exponent for the empty box case shown in Fig. 5.12(b) is around $n = 0.35$ which is much lower than that reported in literature. This may be due to a relatively narrow domain width ($L_z = 0.2c$) considering the integral length scale in the spanwise direction ($I_{i3} = 0.1c$). It may be also because the resolutions for the current case is relatively coarse for the turbulence kinetic energy to decay naturally. However, the focus here is to generate an isotropic turbulence field in the upstream region of the airfoil and the resolution will be much finer in the vicinity of the airfoil in the following section. The calculated turbulence intensities at which the airfoil will be placed are $TI = 2.1\%$ and 3.8% as shown in Table 5.4.

The degree of isotropy is examined along the streamwise direction by comparing the ratios of the velocity fluctuations between the streamwise and the other components as shown in Fig. 5.13. At $x/I_{11} = 23.3$, $\frac{u'_{rms}}{v'_{rms}} \approx 1.3 - 1.4$, $\frac{u'_{rms}}{w'_{rms}} \approx 0.8 - 0.9$ for both turbulence intensities. It is concluded that a relatively good isotropy is achieved with both turbulence levels considering the ratio of velocity variance differs by $10 - 30\%$ in most wind tunnel measurements [150].

Though some parts of the inertial subrange are resolved and reasonably good degree of isotropy is achieved in the empty box case, upstream turbulence does not decay with the rate for finely controlled homogeneous isotropic turbulence as in literature due to some constraints for the airfoil simulations. The aim for the empty box cases, however, is to investigate the effect of the given upstream turbulence characteristics on the flow over

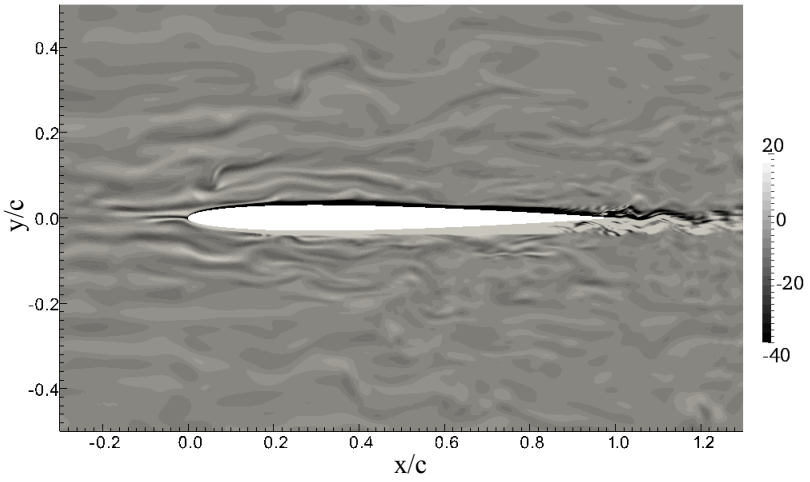

FIGURE 5.14: Instantaneous z-component of vorticity at the mid-span for case 3DTA0. The contour is normalized by U_∞ and c.

an airfoil rather than trying to achieve a high degree of an accuracy for the turbulence decay rate.

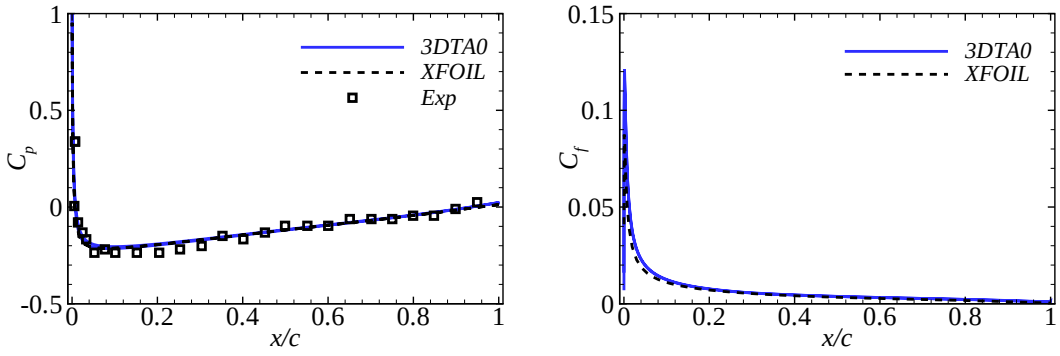

(a) (b)

FIGURE 5.15: The coefficients of (a) the surface pressure and (b) skin-friction. Exp [178]: laminar inflow for $Re = 2.4-5.1\times10^6$. XFOIL [25]: laminar inflow, $Re = 50,000$ with no boundary layer tripping.

5.4.2 Zero degree incidence

For the flow over an airfoil at 0° incidence, 5% of turbulence intensity was imposed on a transverse 2-D plane in the upstream region of the airfoil. The 2-D plane was parallel to the inlet and placed at $x/c = -7$ which was $1c$ away from the inlet. This case is called case 3DTA0. See Table 5.1 for the boundary conditions. A symmetric mesh with respect to the chord line was used and this mesh was generated by a mirror-copy of the upper part of the mesh for case 3D2 in Sec. 5.3.2, so that the upper and lower parts of the mesh were symmetric. Roughly 11.8×10^6 total grid points were needed for the case 3DTA0.

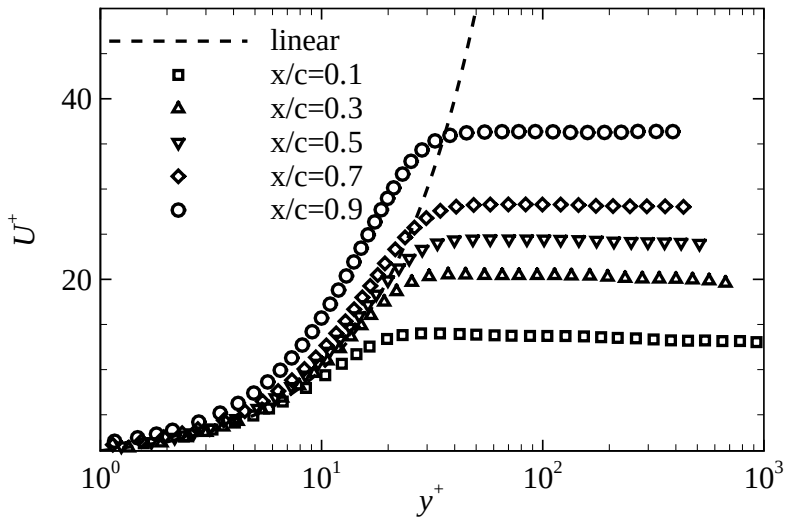

FIGURE 5.16: The profiles of the streamwise velocity components over the upper surface at different downstream locations in wall-units. The linear line indicates $U^+ = y^+$. Note $U^+ = \frac{U(x)}{u_\tau(x)}$ and $y^+ = \frac{y_0 u_\tau(x)}{\nu}$ where y_0 is the distance from the wall, $u_\tau(x) = \sqrt{\frac{\tau_w(x)}{\rho}}$ and $\tau_w(x)$ is the wall shear stress.

5.4.2.1 Aerodynamic characteristics

Synthetic turbulence from the upstream region approaches the airfoil and interacts with the boundary layer on the airfoil as shown in Fig. 5.14. The coefficients of the surface pressure and skin-friction are compared with the data from Weiberg and Dannenberg (1954) [178] and XFOIL 6.96 [25]. Both reference data were taken under laminar upstream flows but it seems that the effect of upstream turbulence on the surface forces is very weak for a symmetric airfoil at zero incidence because the surface forces show little difference between cases with and without upstream turbulence. Similar results were found in Bertagnolio (2008) [8]. Fig. 5.15 shows that all C_p agree well with each other and C_f drops continuously along the x direction indicating that transition does not occur on either surface of the airfoil.

Fig. 5.16 shows the profiles of the streamwise velocity component over the upper surface at different downstream locations. The velocity profiles are close to the linear line for $y^+ < 10$ at most locations. Note that the dashed-line indicates $U^+ = y^+$, i.e. laminar profile. The profiles become steeper as they approach the trailing edge due to the adverse pressure gradient on the airfoil surface as shown in Fig. 5.15(a) [94]. The profiles of the streamwise fluctuations have maxima at the same wall-unit distance, $y^+ \approx 15$, regardless of the x locations as shown in Fig. 5.17(a) but the magnitudes increase as x increases. Fig. 5.17(b) shows the streamwise fluctuations normalized by the corresponding fluctuations from the empty box case at $x/I_{11} = 23.3$. The streamwise fluctuations ($\frac{\langle u'u' \rangle}{\langle u'u' \rangle_0}$) approach unity for $y_0/c > 3 \times 10^{-2}$ which means

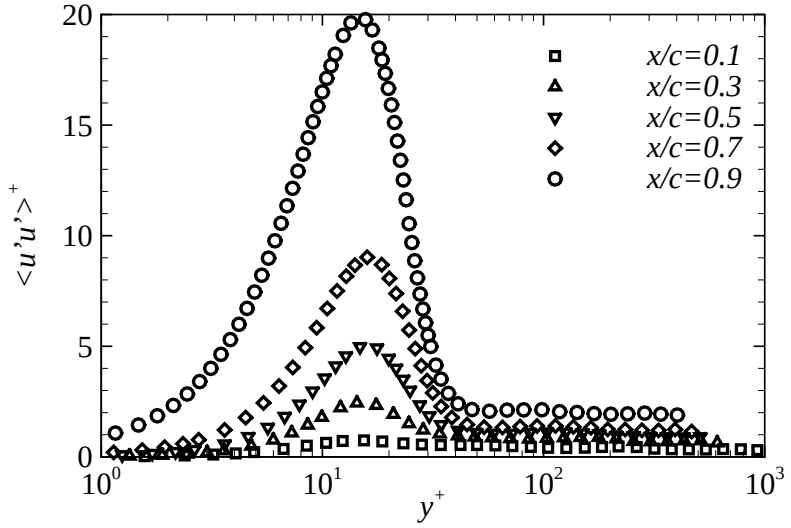

(a)

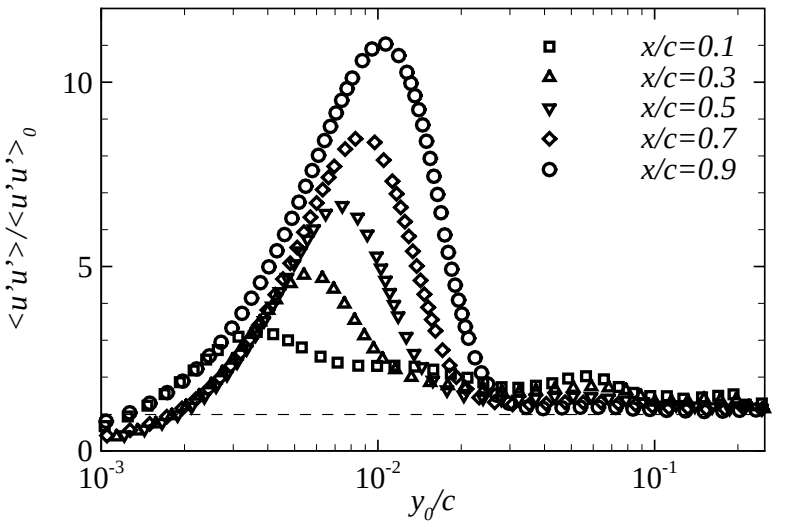

(b)

FIGURE 5.17: The profiles of the streamwise fluctuations over the upper surface at different downstream locations (a) presented in wall-units and (b) normalized by $\langle u'u' \rangle_0$ from the empty box case at $x/I_{11} = 23.3$ (equivalent to $x/c = 0$) for $TI_0 = 5\%$ in Sec. 5.4.1. y_0 is the distance from the wall and the dashed-line is unity.

that the fluctuations are recovered to the background fluctuation away from the airfoil surface.

5.4.2.2 Surface pressure characteristics

Freestream turbulence induces unsteady pressure fluctuations as it passes over a lifting surface. This unsteady surface pressure is a major source of the far field noise [105]. In aeroacoustic applications, it is important to predict the unsteady surface pressure

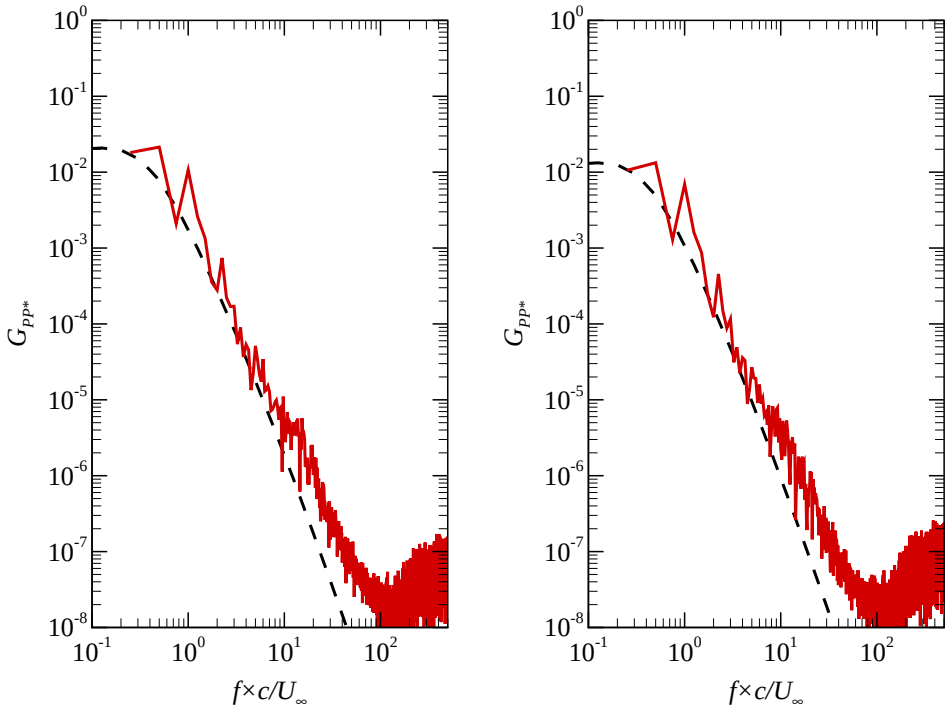

(a) $x/c = 0.04$

(b) $x/c = 0.06$

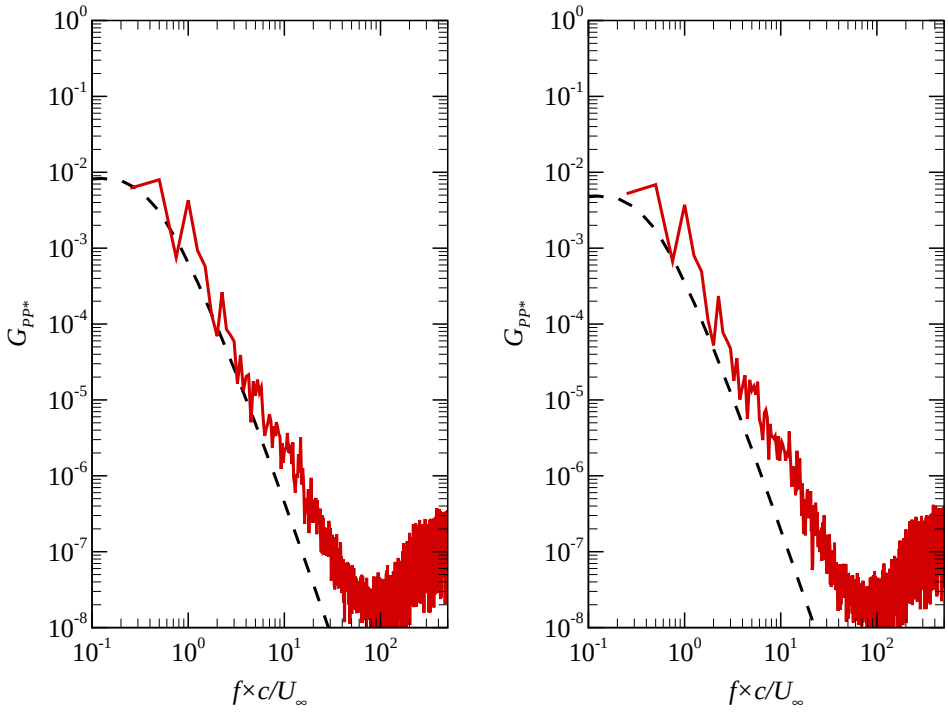

(c) $x/c = 0.09$

(d) $x/c = 0.14$

FIGURE 5.18: The spectral density of pressure difference at different chord locations. - - Amiet [2–4] (Eq. 5.7), — 3DTA0 (Eq. 5.4). Note that $G_{pp*} = G_{pp}/q^2$ where $q = 1/2\rho U_\infty^2$ is the dynamic pressure.

when the object encounters a broad range of wavenumber components in upstream turbulence. This is because the unsteady surface pressure is used for input parameters in many aeroacoustic analogies. The spectral density of the pressure difference between the upper and lower surfaces of the airfoil is analysed and compared with the analytical solution by Amiet [2–4]. At zero angle of attack, the analytical solution provides the spectral density of the pressure difference between upper and lower surfaces of a flat plate when sinusoidal upwind gusts impinge on it in inviscid flows. Mish and Devenport (2006) [105] formulated the solution and compared with their measurements. Before briefly explaining the Amiet's model, the spectral density of the pressure difference at 'x', $G_{pp}(x, f)$, is defined as,

$$\begin{aligned} G_{pp}(x,f) &= \lim_{T\to\infty} \frac{1}{2T} E\left[\Delta\hat{p}(x,f)\Delta\hat{p}(x,f)^*\right] \\ &= \lim_{T\to\infty} \frac{1}{2T} \left| \int_{-T}^{T} \Delta p(x,t) e^{-i2\pi ft} dt \right|^2 \\ &= \lim_{T\to\infty} \frac{2}{T} \left| \int_{0}^{T} \Delta p(x,t) e^{-i2\pi ft} dt \right|^2, \end{aligned} \tag{5.3}$$

where $\Delta\hat{p}(x, f)$ and $\Delta p(x, t)$ are the pressure differences between the upper and lower surfaces at x in the frequency and time domain respectively. The complex conjugate is denoted by an asterisk (*) and the expected value by $E[\ ]$. In actual calculations, measurement time, T, is finite and it is written as $T = N_s\Delta t$ in discrete signals and so $\Delta p(x, t) = \Delta p(x, n\Delta t)$. Eq. 5.3 in discretized form is,

$$\begin{aligned} G_{pp}(x,f) &= \frac{2}{N_s\Delta t} \left| \sum_{n=0}^{N_s-1} \Delta p(x,n\Delta t) e^{-i2\pi fn} \Delta t \right|^2 \\ &= \frac{2}{N_s F_s} \left| \sum_{n=0}^{N_s-1} \Delta p(x,n\Delta t) e^{-i2\pi fn} \right|^2, \end{aligned} \tag{5.4}$$

where N_s is the number of sample and F_s is the sampling rate which is $1/\Delta t$.

Amiet's [2–4] model constructs $G_{pp}(x, f)$ by adding a range of modes which have different wavenumbers in the spanwise direction. The idea behind the analytical solution is to use the transfer function, g, in Eq. 5.5 which associates the turbulent velocity with an airfoil pressure jump [2]. The pressure difference in Eq. 5.3 can be presented as a function of the turbulent velocity, i.e. $\Delta p(x, t) = f(u'(t))$ and the pre-defined energy spectrum provides the magnitude of the turbulent velocity per unit frequency. In Amiet's model, the origin is placed at the leading edge and all parameters are normalized by the half chord length, b, thus the trailing edge is placed at $x = 2$ where x is the streamwise

direction and z is the spanwise direction. Note that y was adopted as the spanwise direction in literature [3, 4, 105]. The transfer function of the model is,

$$g(x,\kappa_x,\kappa_z) = -\frac{\mathcal{E}(x,\kappa_z)}{\pi\beta}\left\{\pi x\left\{(\kappa_z^2/\beta^2-\mu^2)^{1/2}+i(\mu M+\kappa_x)\right\}\right\}^{-1/2} \times e^{-x(\kappa_z^2/\beta^2-\mu^2)^{1/2}+i\mu M x}, \tag{5.5}$$

where κ_x, κ_z are the wavenumbers in the streamwise and spanwise directions which are normalized by b. The parameters β and μ are functions of Mach number (M), $\beta=\sqrt{1-M^2}$ and $\mu = M\kappa_x/\beta^2$. The function $\mathcal{E}$ is,

$$\mathcal{E}(x,\kappa_z) = 1-(x/2)^{1/2}\left\{1-\mathrm{erf}\left[\left(2(2-x)(\kappa_z^2/\beta^2-\mu^2)^{1/2}\right)^{1/2}\right]\right\}, \tag{5.6}$$

where the error function (erf) defined as $\mathrm{erf}(\zeta) = 2/\sqrt{\pi}\int_0^\zeta \exp(-t^2)dt$ for any complex number ζ. The function $\mathcal{E}$ is used only for $\kappa_z \geq (M/\sqrt{1-M^2})\kappa_x$, otherwise it has another definition. For the current case, only Eq. 5.6 is used because only incompressible flows are considered, i.e. $M \approx 0$. The spectral density function is then,

$$G_{pp}(x,f) = 16\pi U_\infty(\pi\rho b)^2\int_0^\infty g^*(x,\kappa_x,\kappa_z)g(x,\kappa_x,\kappa_z)\times\Phi_{ww}(\kappa_x,\kappa_z)\mathrm{e}^{i\kappa_z\eta_z}d\kappa_z, \tag{5.7}$$

where U_∞ is the freestream velocity and ρ is the fluid density. Note that η_z is the spanwise separation, i.e. $\eta_z = z-z'$ and only $\eta_z = 0$ is considered for the present study. Φ_{ww} is the two-dimensional turbulence spectrum [115],

$$\Phi_{ww}(\kappa_x,\kappa_z) = \frac{4\langle u'u'\rangle}{9\pi\kappa_e^2}\frac{\hat{\kappa}_x^2+\hat{\kappa}_z^2}{(1+\hat{\kappa}_x^2+\hat{\kappa}_z^2)^{7/3}}, \tag{5.8}$$

where $\kappa_e = 0.7468/I$ and I is the integral length scale. $\hat{\kappa}_i = \kappa_i/\kappa_e$ $(i=x,z)$ and $\langle u'u'\rangle$ is the variance of the streamwise velocity fluctuation.

To apply Amiet's model [2–4] for case 3DTA0, the input length scale was estimated from the autocorrelation at $x/I_{i1} = 23.3$ as shown in Table 5.4 and the streamwise velocity fluctuation was taken at the same location which was $\langle u'u'\rangle/U_\infty^2 = 0.00102$. The analytical solutions of Amiet's model [2–4] (Eq. 5.7) by using these input parameters are shown in Fig. 5.18 and they are compared with the calculated G_{pp} (Eq. 5.4) for case 3DTA0. The calculations show very good agreement with Amiet's model [2–4] for all locations. The tendency of G_{pp} for case 3DTA0 follows the analytical solution as well. The decrease rate of G_{pp} for $f\frac{c}{U_\infty} > 0.3$ matches well with the analytical solution and the magnitude of G_{pp} decreases as x increases. The lowest frequency, $f\frac{c}{U_\infty} = 0.25$ corresponds to 4 flow passes over the airfoil. High frequency bumps are observed for

$f\frac{c}{U_\infty} > 10^2$ which are also found in channel flows with the XCDF model, see Fig. 4.12(a). The bumps tend to diminish as the tolerance for the implicit linear solver decreases indicating that these are numerical errors. Also, their magnitudes are very small and occur in a very high frequency range thus they are negligible.

The magnitude of G_{pp} would decrease as the turbulence intensity decreases. For the laminar inflow case, G_{pp} approaches zero and Amiet's model, Eq. 5.7, also shows the same phenomenon. The turbulence spectrum decreases as the turbulence level decreases as in Eq. 5.8. The reduction would be proportional to the variance of turbulence fluctuations, $\langle u'u' \rangle$. In this section, the calculated G_{pp} subjected to the specified turbulence characteristics, showed good agreement with the reference [2–4]. Thus it is shown that the current framework is a reliable approach for an unsteady surface pressure analysis and the same framework is now applied on the flow over an airfoil with non-zero incidence. This is important because the analytical solution by Amiet [2–4] is valid at 0° incidence only and there is no reliable analytical solution for non-zero incidence to date. By using LES, one can simulate an airfoil flow for any angle of attack.

5.4.3 Non-zero degree incidence

The XCDF model was applied to the flow over an airfoil at 0° incidence in the previous section. Two different turbulence levels ($TI_0 = 5\%$, $TI_0 = 10\%$) were imposed in the upstream region of the airfoil at 7° incidence by using the mesh for case 3D2. This case is called case 3DTA7. Tables 5.1 - 5.3 show the details of the mesh and boundary conditions for case 3DTA7.

TABLE 5.5: The effect of freestream turbulence on the lift and drag coefficients.

Case	C_L	C_D	C_L/C_D
3D2	0.638	0.0665	9.59
3DTA7 ($TI_0 = 5\%$)	0.648	0.0523	12.4
3DTA7 ($TI_0 = 10\%$)	0.635	0.0478	13.3

5.4.3.1 Aerodynamic characteristics

Fig. 5.19 shows snapshots of the spanwise vorticity component for cases 3D2 and 3DTA7 for two turbulence intensities. Some numerical oscillations in the vorticity fields are observed near the boundary layer edge regardless of the inflow conditions. This may indicate that the flow is slightly under-resolved in that region. For the laminar inflow, a clean free shear layer develops from the leading edge. Also leading edge separation is observed and the flow breaks down to turbulence due to Kelvin-Helmholtz instability. For the turbulent inflow, the vortical structure near the leading edge shows a clear difference compared to that for the laminar inflow. The free shear layer is disturbed by freestream

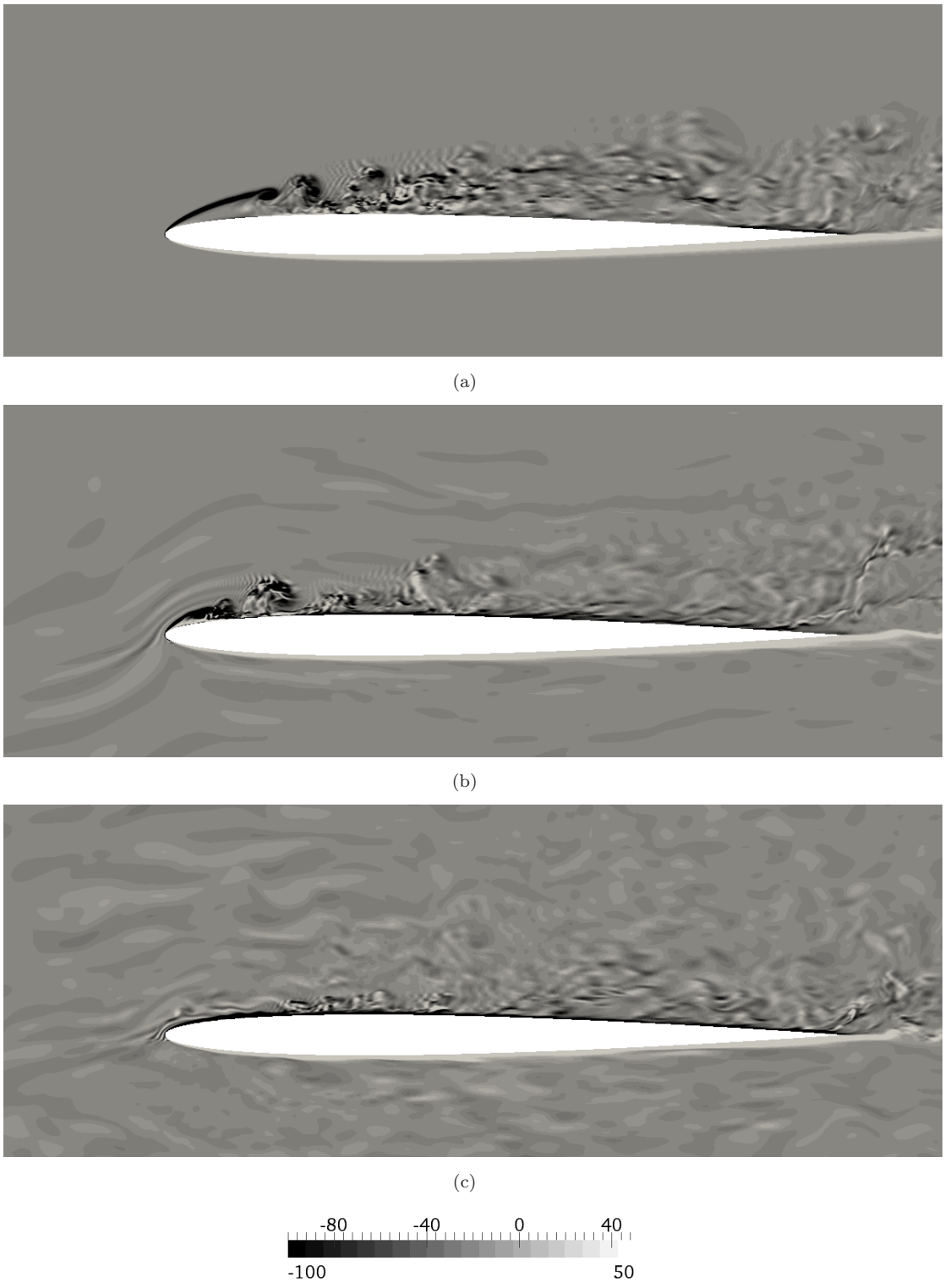

FIGURE 5.19: Instantaneous z-component of vorticity at mid-span for (a) case 3D2 ($TI = 0\%$), (b) case 3DTA7 for $TI_0 = 5\%$ and (c) $TI_0 = 10\%$. The contours are normalized by U_∞ and c.

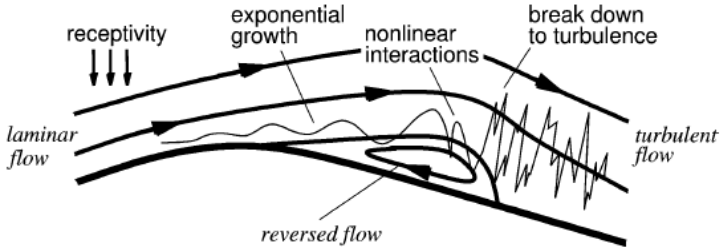

FIGURE 5.20: A structure of a mean laminar separation bubble with the mechanism for instability and transition [180].

turbulence and the size of the separation bubble significantly decreases for $TI_0 = 5\%$ and it is hard to discern the separation bubble for $TI_0 = 10\%$. This is because the size of separation bubbles is very sensitive to the upstream disturbances [42]. Fig. 5.20 shows a sketch of the mechanism for instability and transition in a laminar separation bubble [180] with laminar inflow. When the upstream flow is turbulent, the nonlinear interaction may be significant prior to the laminar separation bubble. It increases momentum transport normal to the shear layer and leads to an early reattachment compared with that for the laminar inflow case.

The pressure and skin-friction coefficients for all cases are shown in Fig. 5.21. A pressure plateau on the upper surface in cases 3DTA7 for different turbulence levels clearly illustrates the decrease of the bubble size due to freestream turbulence. The negative peaks of the skin-friction for cases 3DTA7 approach the leading edge as the turbulence intensity increases. The reattachment point can be identified as the station where the sign changes of the skin-friction on the upper surface. It changes from $x/c = 0.445$ for the laminar inflow case to $x/c = 0.139$ and $x/c = 0.089$ for $TI_0 = 5\%$ and $TI_0 = 10\%$, respectively.

Freestream turbulence from the upstream region interacts with the boundary layer on the airfoil surface and it expedites the transition. It is reasonable to speculate that the boundary layer with the upstream turbulence at low Reynolds number would be similar to that with a laminar inflow at high Reynolds number in some aspects. In Fig. 5.21(a), the pressure coefficients for the current cases are compared with the XFOIL data [25] which was conducted with a laminar inflow at $\alpha = 7^\circ$ and Reynolds number varying from 0.1×10^6 to 2×10^6. A rapid development of the pressure peak near the leading edge is observed as Reynolds number increases, which is typical of thin airfoils [178]. The shape of C_p from the calculations tends to approach that of the highest Reynolds number case for XFOIL as the turbulence level increases. Thus it can be concluded that the boundary layer at low Reynolds number for the turbulent inflow shows similar characteristics to that at high Reynolds number with laminar inflow in terms of the mean surface pressure.

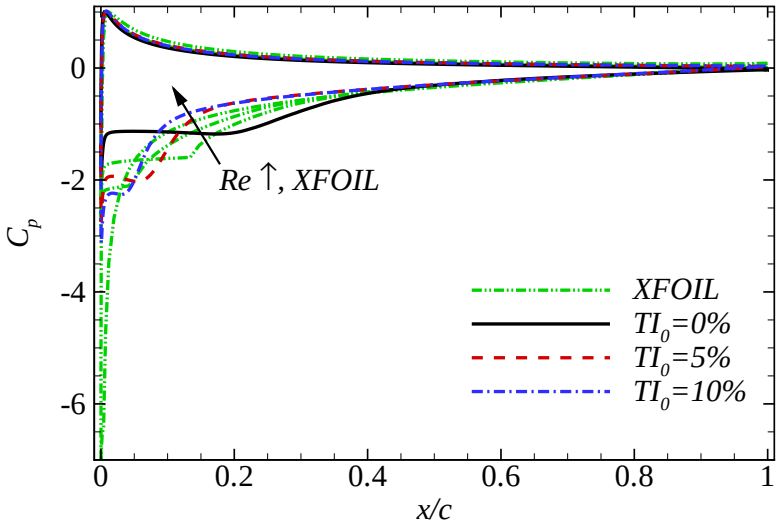

(a)

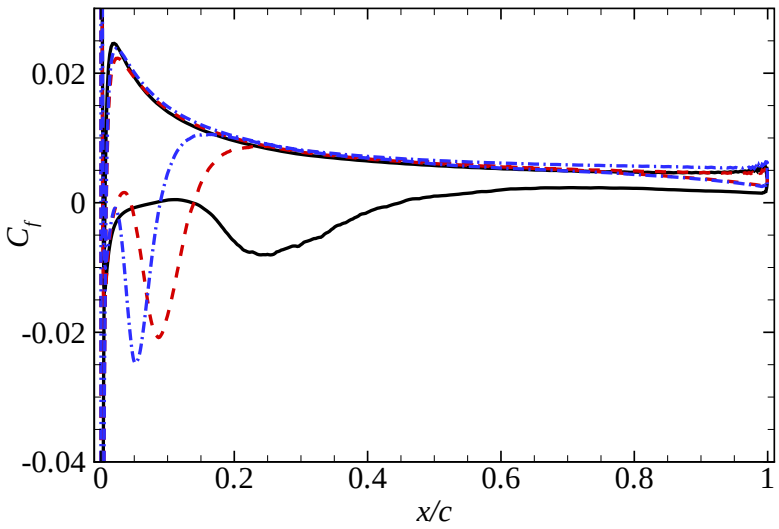

(b)

FIGURE 5.21: The effect of freestream turbulence on the (a) pressure coefficients and (b) skin-friction coefficients at $Re = 50,000$ and $\alpha = 7°$. The effective turbulence intensities at the leading edge are 3.2% and 6.1% respectively, see Table 5.4. Note that $TI_0 = 0\%$ corresponds to case 3D2. The same airfoil and angle of attack were adopted for the XFOIL data [25]. The upstream condition was laminar and Reynolds number varied; 1×10^5, 2×10^5 and 2×10^6.

Fig. 5.22 shows the effect of freestream turbulence on the mean streamwise velocity profiles near the separation bubble. The boundary layer for the laminar inflow case are separated (negative streamwise velocity) near the wall for all locations. The thickness of the bubble decreases and the reattachment point approaches the leading edge as the turbulence intensity increases due to a higher momentum mixing. The flows are attached for both $TI_0 = 5\%$ and 10% at $x/c = 0.14$. This is consistent with the skin-friction as shown in Fig. 5.21(b).

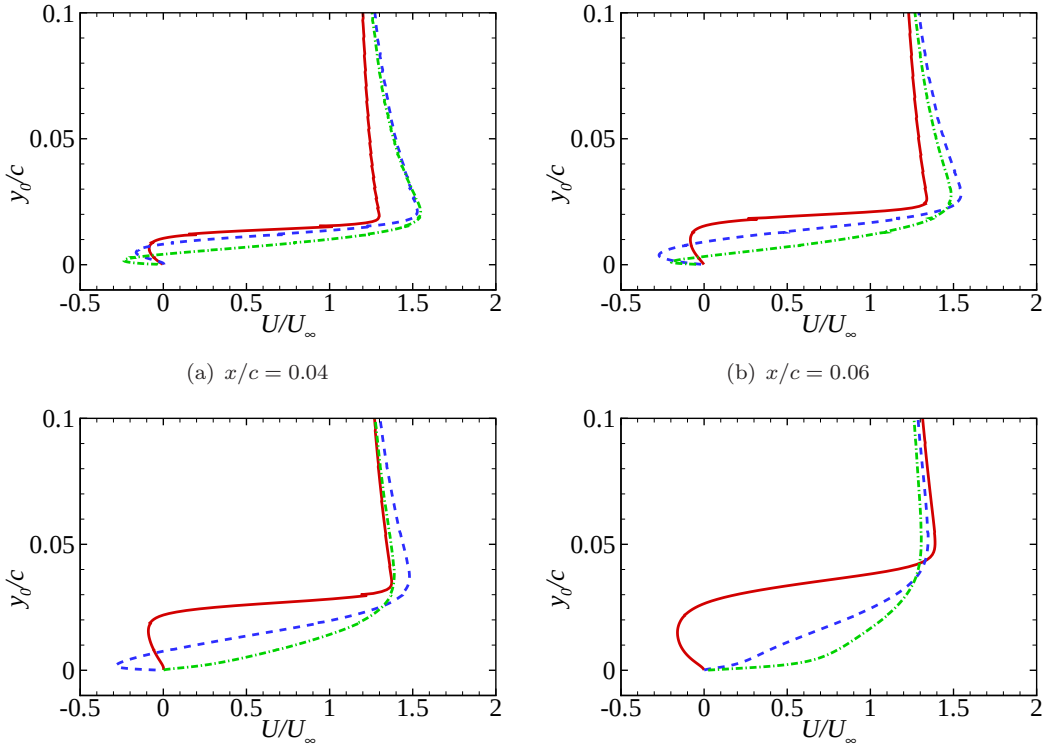

(a) $x/c = 0.04$ (b) $x/c = 0.06$

(c) $x/c = 0.09$ (d) $x/c = 0.14$

FIGURE 5.22: The effect of freestream turbulence on the streamwise component of the mean velocity profiles near the separation bubble for $\alpha = 7°$. — $TI_0 = 0\%$ (3D2), - - $TI_0 = 5\%$, -·- $TI_0 = 10\%$. Note y_0 is the distance from the wall.

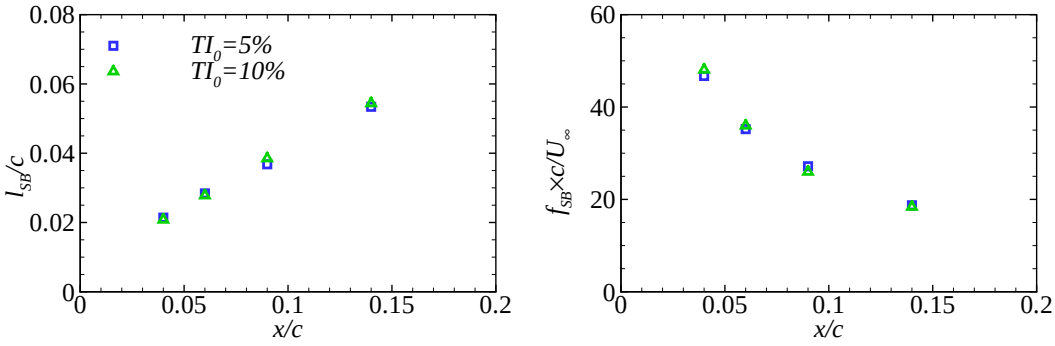

(a) (b)

FIGURE 5.23: (a) The thickness of the separation bubble, l_{SB}, at different chord locations and (b) the corresponding frequency, $f_{SB} = U_\infty / l_{SB}$.

The integrated lift and drag coefficients and their ratios are shown in Table 5.5. The lift coefficients change non-monotonically as the turbulence intensity increases and this depends on the length and magnitude of the pressure plateau as shown in Fig. 5.21. The drag coefficients decrease monotonically as the inflow turbulence increases. These changes compared with the laminar inflow case, are mainly due to the decrease of the separation bubble size. Though the lift decreases for $TI_0 = 10\%$ compared to that for $TI_0 = 5\%$, the drag decreases as the turbulence level increases resulting in an

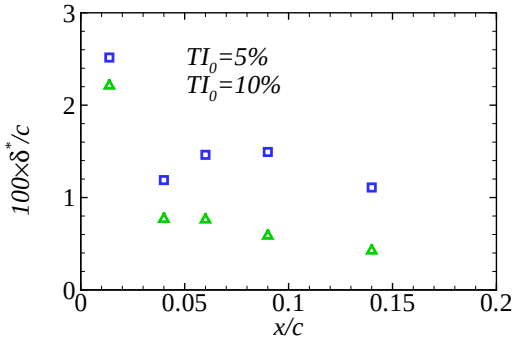

FIGURE 5.24: The displacement thickness, $\delta^* = \int_0^{\delta_{99}} (1 - u(y)/U_\infty)dy$, for cases 3DTA7 for $TI_0 = 5\%$, 10% at different x locations. Note that δ_{99} is the thickness of the 99% freestream velocity.

increase of the lift-drag ratio. Thus freestream turbulence gives a favourable effect on the aerodynamic performance in the current study.

5.4.3.2 Surface pressure characteristics

The effects of freestream turbulence on the surface pressure characteristics at 7° incidence are examined in this section. Fig. 5.25 shows the spectral density of the pressure difference (Eq. 5.4) for cases 3DTA0 and 3DTA7 at different downstream locations. At $f\frac{c}{U_\infty} = O(10)$, two order of magnitudes higher of G_{pp} is predicted for case 3DTA7 at $TI_0 = 5\%$ than that for case 3DTA0 for all x locations. It is reasonable to estimate the characteristic size of the separation bubble, l_{SB}, for cases 3DTA7 as the distance from the airfoil surface to the point of the maximum streamwise velocity (i.e. thickness of the bubble) [42]. Then the size (l_{SB}) and frequency ($f_{SB} = U_\infty/l_{SB}$) of separation bubbles are estimated from Fig. 5.22 and they are shown in Fig. 5.23. It should be noted that the bubble thickness shows little difference between cases for two different turbulence intensities based on the current definition of the thickness. But the shapes of the boundary layer are noticeably different as shown in Fig. 5.22. The gradient of boundary layer is steeper for $TI_0 = 10\%$ than that for $TI_0 = 5\%$. This difference in the boundary layers is shown clearly in the displacement thickness, see Fig. 5.24.

In Fig. 5.23, the characteristic size (bubble thickness) increases and frequency decreases as x increases for $0.04 < x/c < 0.14$. The estimated frequency (Fig. 5.23(b)) at each x location shows a similar (approximately doubled) value with the secondary peak frequency for G_{PP} in Fig. 5.25 at each corresponding x location. Note that the secondary peak frequencies are marked with the bars in Fig. 5.25. This shows that the bubble thickness is a reasonable approximation for the characteristic size of the separation bubble. The secondary peak frequency tends to decreases as x increases and this is consistent with Fig. 5.23(b). Therefore the increment of the G_{pp} magnitude near the

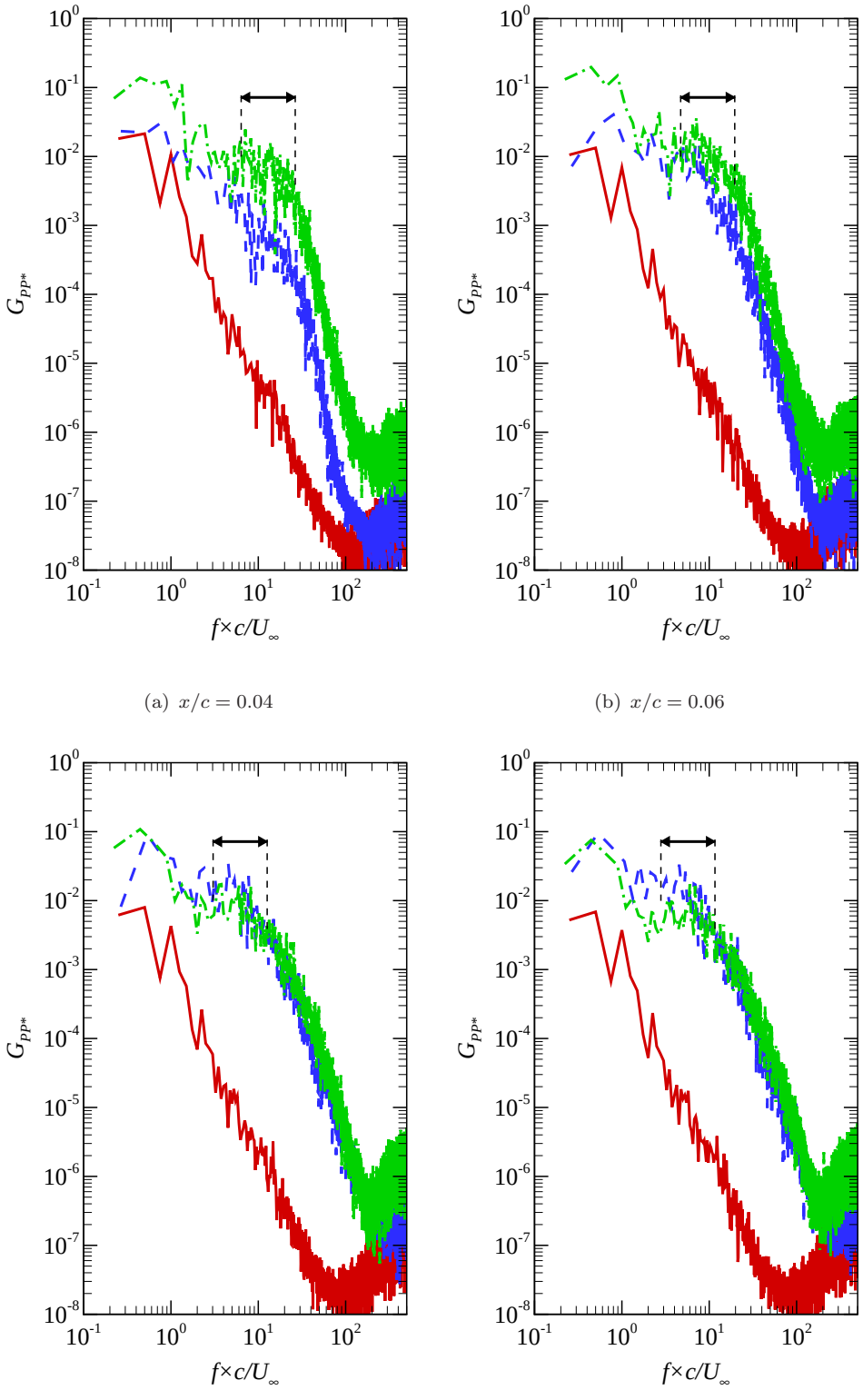

(a) $x/c = 0.04$

(b) $x/c = 0.06$

(c) $x/c = 0.09$

(d) $x/c = 0.14$

FIGURE 5.25: The effect of freestream turbulence and incidence on the spectral density of pressure difference (Eq. 5.4) at different chord locations. — TI_0 = 5% 3DTA0, - - TI_0 = 5% 3DTA7, -·- TI_0 = 10% 3DTA7. Note that $G_{PP*} = G_{PP}/q^2$ where $q = 1/2\rho U_\infty^2$ is the dynamic pressure.

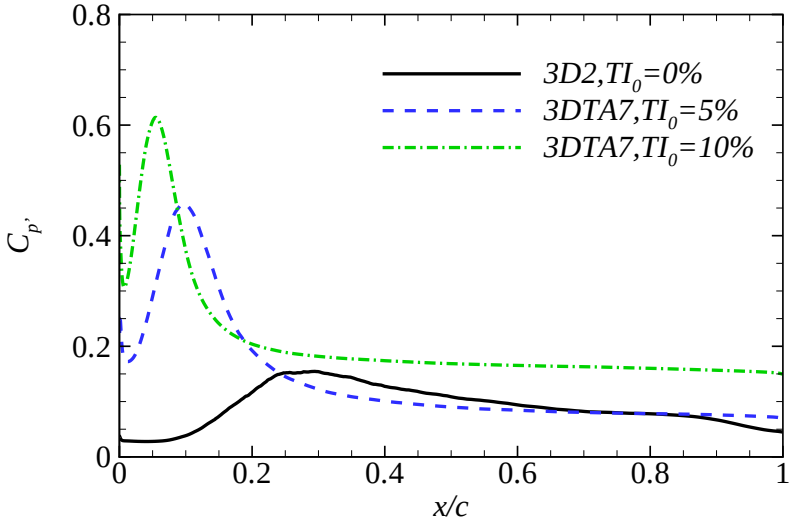

FIGURE 5.26: The effect of freestream turbulence on the pressure fluctuations on the upper airfoil surface at 7° incidence.

secondary peak for cases 3DTA7 is attributed to the separation bubble which is absent at zero incidence.

The spectral density increases as the entry upstream turbulence level increases at 7° for $x/c < 0.09$. However, at $x = 0.14$, the G_{pp} magnitude for case 3DTA7 for $TI_0 = 5\%$ is similar or somewhat larger than that for $TI_0 = 10\%$ as shown in Fig. 5.25(d). This is interesting since higher pressure fluctuations are expected with higher upstream turbulence. To understand this, the surface pressure fluctuations are shown in Fig. 5.26. The surface pressure fluctuation is defined as,

$$C_{p'} = \frac{p_{rms}}{\frac{1}{2}\rho U_\infty}, \tag{5.9}$$

where p_{rms} is the *root-mean-square* of the pressure fluctuations. $C_{p'}$ for case 3DTA7 for $TI_0 = 10\%$ shows higher magnitudes over most of the chord than those for $TI_0 = 5\%$ except for $0.09 < x/c < 0.19$. This is because the peak pressure fluctuations occur further away from the leading edge at lower turbulence intensity than those at higher one which is consistent with Figs. 5.21(b) and 5.25. In the region $0.09 < x/c < 0.19$, Cp' for $TI_0 = 5\%$ is greater.

5.5 Summary

The effect of freestream turbulence on the flow over a NACA 0006 airfoil is examined. As a baseline simulation, the flow over the airfoil at 7° incidence with a laminar inflow condition is simulated and the results are compared with DNS data [61]. The surface forces, reattachment points and flow profiles over the airfoil surface are well predicted. Thus

it is demonstrated that the LES calculations with the mixed-time scale SGS model are able to simulate the flow with a laminar/turbulent transition. The baseline simulation provides the reference case for the turbulent inflow cases.

To quantify the characteristics of upstream turbulence, a box domain without the airfoil was set up and the turbulent inflow was imposed on the 2-D transverse plane near the inlet. An inertial subrange in the energy spectrum is captured and a reasonable degree of isotropy is achieved at the point where the airfoil is placed. The decay rate of turbulence is under-predicted compared to that reported in literature due to a relatively small domain width and a coarse mesh. However, the focus is to provide "reasonable turbulence" immediately upstream of the leading edge.

The divergence-free version of Xie and Castro's inflow method (Ch. 4) is applied on the flow over the airfoil. The effects are examined using both aerodynamic and surface pressure characteristics. The spectral density of pressure difference (G_{pp} in Eq. 5.4) on the airfoil surface at 0° incidence shows good agreement with the analytical solution [2–4]. This would be challenging with other synthetic turbulence inflow techniques which do not satisfy the divergence-free condition as the computed pressure fluctuations from non-divergence-free turbulence generator are generally huge (see Ch. 4), i.e. the magnitude of spectral density of pressure difference would be much higher. Thus the current approach provides a reliable framework for aerodynamics and unsteady surface pressure analysis of airfoil flows in a general situation.

The impact of freestream turbulence at 7° angle of attack is investigated as an example. The separation bubble is diminished as the turbulence level increases resulting in an increase of the lift to drag ratio. Overall magnitudes of G_{pp} increase with the angle of attack and also an increase of the turbulence level. A footprint for the separation bubble is observed in G_{pp} near the secondary peak frequency. The characteristic frequency of the separation bubble is estimated by using the bubble thickness, l_{SB}, i.e. $f_{SB} = U_\infty / l_{SB}$. It is shown that the secondary peak frequency for G_{pp} corresponds to the estimated frequency of the separation bubble. The spectral density of the pressure difference, G_{pp}, varies at different x locations and its magnitude is proportional to the local surface pressure fluctuations.

Chapter 6

Dynamic stall

6.1 Introduction

At yaw, wind turbine blades operate in a periodically oscillating condition and dynamic stall appears frequently [138]. The generated forces lead to accumulating fatigue within the blades reducing their expected service life. Ekaterinaris and Menter (1994) [29] reported that the predicted load hysteresis using Reynolds Averaged Navier-Stokes (RANS) approaches tended to deviate from the experimental data, especially for the deep stall case. For the better prediction on the flow over a pitching airfoil, an LES approach is adopted. The methodology used for the present work is summarized in Sec. 6.2. For a baseline simulation, static and pitching NACA 0012 airfoils are simulated and the results are validated against experimental data by Lee and Gerontakos (2004) [85] and Rinoie and Takemura (2004) [128]. These are presented in Sec. 6.3. The Reynolds number based on the chord, c, and freestream velocity, U_∞, is $Re = 135,000$ for both the static and pitching airfoils. The angle of attack is 10° for the static airfoil and $\alpha(t) = 10^\circ + 15^\circ \sin(\omega t)$ for the pitching airfoil. The pitching frequency is presented as the reduced frequency, $k_{\text{red}} = \frac{\omega c}{2U_\infty}$ (Eq. 1.1) and $k_{\text{red}} = 0.025 - 0.1$ for this study. The pitching axis is at the quarter chord point from the leading edge.

This chapter is mainly composed of two parts. Firstly, significant features of dynamic stall such as stall delay and leading edge vortices (LEV) are characterized by the aerodynamic forces and flow visualizations (Sec. 6.4). Secondly, the effect of freestream turbulence on the flow over a pitching airfoil are investigated (Sec. 6.5). The summary of the chapter is presented in Sec. 6.6. Part of this work was presented in a conference paper by Kim, Castro, Xie. *DLES9, Dresden, Germany,* 2013 [70].

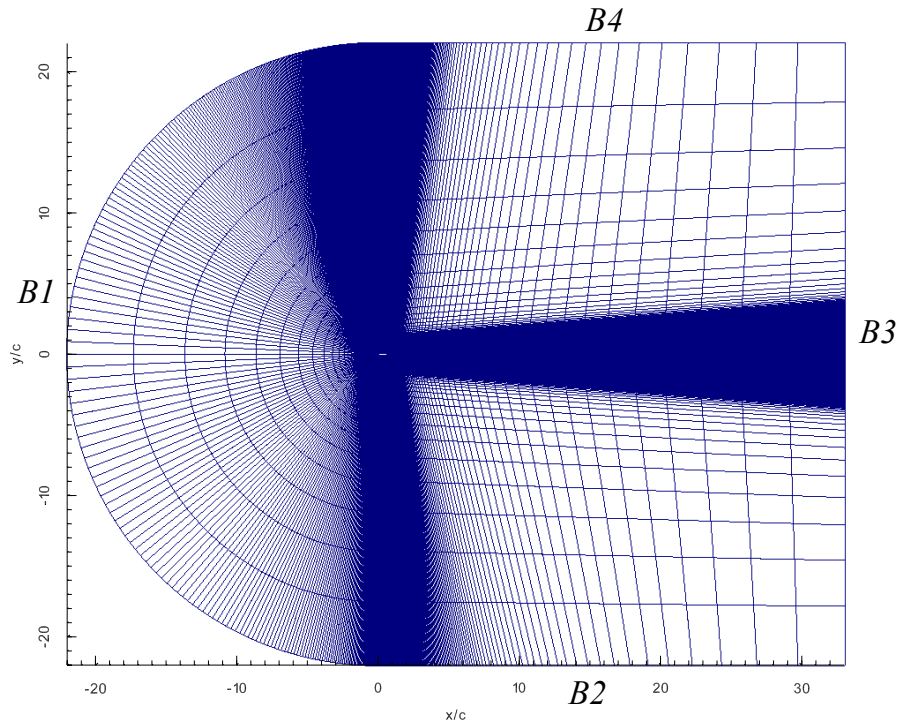

(a) C-type

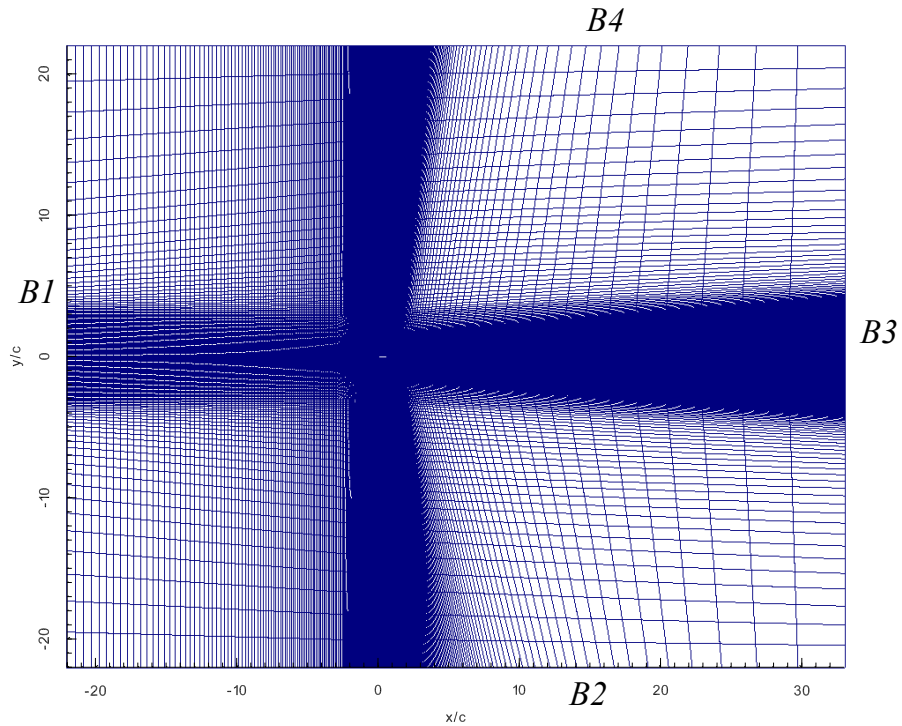

(b) Modified

FIGURE 6.1: Mesh topology for (a) case PC5 as in Table 6.4 and (b) the modified version of case PC5.

6.2 Methodology

Two independent methodologies were adopted for the static and pitching airfoils. A common methodology for both cases is described first, then details will be explained in the following sections. For the common set-ups, a typical C-type mesh was applied as shown in Fig. 6.1(a). The mixed-time-scale (MTS) SGS model [54] was used with $C_{MTS} = 0.03$ and $C_T = 10$ as model constants [78] and a simple top-hat filter was applied for the explicit filter. A second order, implicit scheme was used for the temporal discretization and the bounded second order (Gamma) scheme [59] was used for the convection term. The time step was $t/T = 1.5 \times 10^{-4}$ and the maximum CFL ≈ 2. The transient incompressible flow solver from OpenFOAM was used and the PIMPLE algorithm (see Appendix B) was adopted for the velocity-pressure coupling. The number of outer correctors was set to two and the number of pressure correctors was set to three. Pointwise V16 was used to generate all meshes.

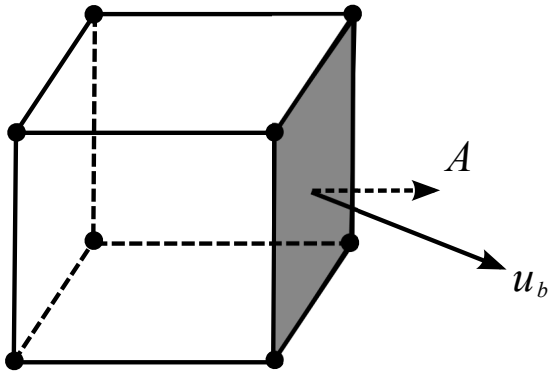

FIGURE 6.2: The surface area vector $\boldsymbol{A}$ and boundary velocity vector $\boldsymbol{u}_b$ on the control volume for the dynamic mesh. Dots are cell vertices.

6.2.1 Dynamic mesh

The pitching motion of the airfoil was predefined and the dynamic mesh approach was adopted for the internal mesh to accommodate the deformation of the domain due to the airfoil motion. The term "dynamic mesh" refers to the relative distances among grid points changing in time to adjust to an unsteady motion of the subject through squeezing and stretching cells. The pimpleDyMFoam solver in OpenFOAM was used for the dynamic mesh. For the finite volume method, the conservation equation of property, ϕ, over an arbitrary moving control volume, V_C, in integral form is (cf. Eq. 3.3),

$$\frac{d}{dt}\int_{V_C} \phi dV_C + \int_A d\boldsymbol{A} \cdot (\boldsymbol{u} - \boldsymbol{u}_b)\phi = \int_{V_C} \boldsymbol{\nabla} \cdot (\Gamma \boldsymbol{\nabla}\phi) dV_C, \tag{6.1}$$

where $\boldsymbol{u}$ is the fluid velocity vector, $\boldsymbol{A}$ is the outward pointing surface area vector and $\boldsymbol{u}_b$ is the boundary velocity vector of the cell-face, see Fig. 6.2. Note that Γ is the

diffusivity coefficient. The local boundary velocity, $\boldsymbol{u}_b$, is interpolated from the point velocity, $\boldsymbol{u}_p$, which is imposed at each vertex of the control volume. To govern the vertex motion, the Laplacian operator with a diffusivity, γ, is adopted [60],

$$\boldsymbol{\nabla} \cdot (\gamma \boldsymbol{\nabla} \boldsymbol{u}_p) = 0. \tag{6.2}$$

The boundary conditions for Eq. 6.2 are enforced from the known boundary motion, e.g. a symmetric or moving wall. Then the vertex position at the time level $n+1$ is calculated by using $\boldsymbol{u}_p$,

$$\boldsymbol{x}^{n+1} = \boldsymbol{x}^n + \boldsymbol{u}_p \Delta t. \tag{6.3}$$

The mesh quality around moving object is important while the mesh away from the boundaries has more freedom to deform. The diffusivity, γ, in Eq. 6.2 has an influence on the mesh deformation and several types of the diffusivity were examined by [60] such as,

- Constant : γ =constant,
- Linear : $\gamma = \frac{1}{l}$,
- Quadratic : $\gamma = \frac{1}{l^2}$,
- Exponential : $\gamma = e^{-l}$,

where l is the cell centre distance to the nearest selected boundary. Fig. 6.3 shows the effect of the diffusivity on the mesh quality for the trailing edge of the moving airfoil demonstrated by [60]. For the quadratic diffusivity, the mesh quality is superior to that

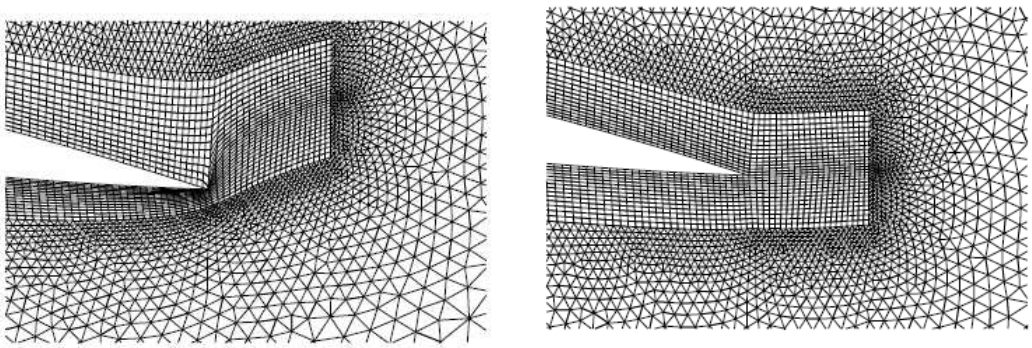

(a) γ =constant (b) $\gamma = \frac{1}{l^2}$

FIGURE 6.3: The effect of diffusivity, γ, on the mesh quality around the moving airfoil trailing edge [60].

for the constant diffusivity. Thus the quadratic diffusivity was adopted for the current study. As all grid points move based on Eq. 6.3, an explicit interface between the static and dynamic mesh region is not required. Further demonstrations of the dynamic mesh in OpenFOAM can be found in Kassiotis (2008) [64] and Moradnia (2008) [108].

TABLE 6.1: Summary of the boundary conditions for a static (ST) and pitching (PC) airfoils. U_∞ is the freestream velocity and d/dn is a normal derivative to the boundary. The transverse plane is placed at $x = x_0$ where the synthetic turbulence (XCDF) is imposed. See Fig. 6.1 for the mesh type.

Mesh type	B1	B2	B3	B4	$x_0/c = -7$
C-type (ST, PC)	$u_i = U_\infty$, $dp/dn = 0$	$u_i = U_\infty$, $dp/dn = 0$	$du_i/dn = 0$, $p = p_\infty$	$du_i/dn = 0$, $p = p_\infty$	n/a
Modified (PC)	$u_i = U_\infty$, $dp/dn = 0$	$u_i = U_\infty$, $dp/dn = 0$	$du_i/dn = 0$, $p = p_\infty$	$du_i/dn = 0$, $p = p_\infty$	XCDF

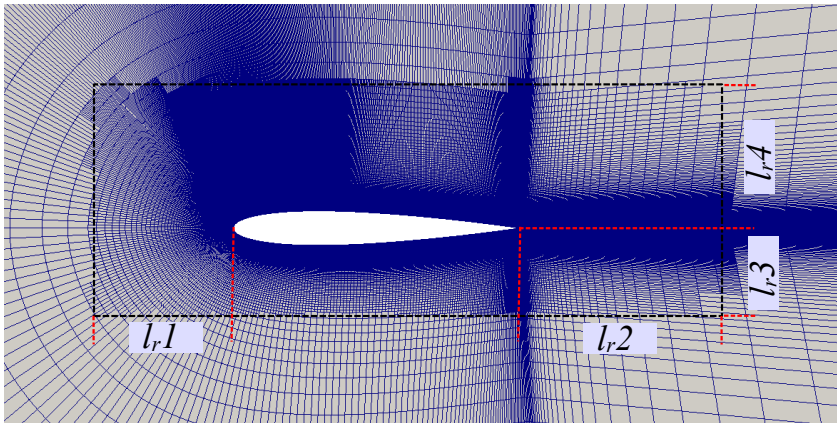

FIGURE 6.4: A local refined mesh for the static airfoil case. The size of refined region (RR) is characterized by the lengths, l_r1, l_r2, l_r3 and l_r4 , see Table 6.2.

TABLE 6.2: Types of the refined regions (RR) and their sizes (l_r), the directions to refine (Dir). Different refinement regions are applied for different cases, see Table 6.3. $l_r1 - l_r4$ are depicted in Fig. 6.4.

RR	l_r1	l_r2	l_r3	l_r4	Dir	Cases
*RR*1	$0.5c$	$0.7c$	$0.3c$	$0.5c$	x, y	$ST_{2D1,2}$
*RR*1	$0.5c$	$0.7c$	$0.3c$	$0.5c$	x, y, z	$ST_{3D1,2,3}$
*RR*2	$0.25c$	$0.4c$	$0.2c$	$0.35c$	z	$ST_{3D2,3}$
*RR*3	$0.1c$	$0.2c$	$0.1c$	$0.2c$	z	ST_{3D3}

6.3 Baseline simulations

The mesh convergence tests were conducted for the static and pitching airfoils as baseline simulations. A local refinement mesh was used for the static airfoil and a structured mesh

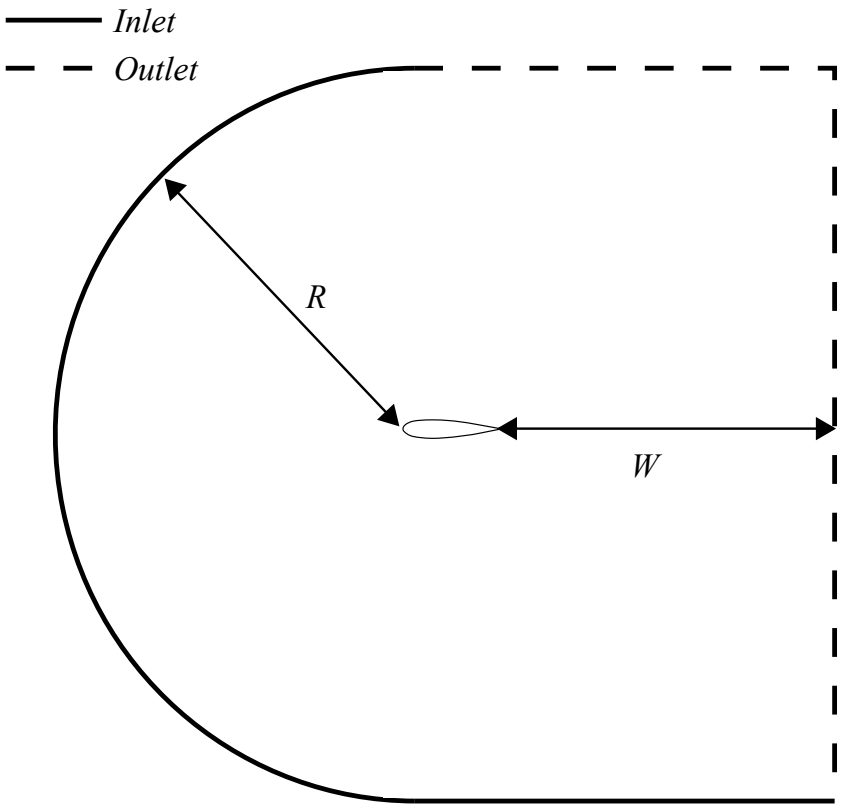

FIGURE 6.5: A sketch of the domain (not to scale) and the boundary conditions.

TABLE 6.3: The computational domain size for the static airfoil and number of grid points before the refined mesh is applied. N_{up} and N_{low} are the number of grid points on the upper and lower airfoil surfaces respectively. Note that N_z is the number of grid points in the spanwise direction. The refinement ratio is 2 and N_z' is the final number of grid points in the spanwise direction after the refinement is applied. See Fig 6.5 for R and W.

	ST_{2D1}	ST_{2D2}	ST_{3D1}	ST_{3D2}	ST_{3D3}
R [c]	22	22	22	22	22
W [c]	33	33	33	33	33
L_z [c]	n/a	n/a	0.25	0.25	0.25
N_R	70	200	70	70	70
N_W	66	66	66	66	66
N_{up}	367	733	367	367	367
N_{low}	106	211	106	106	106
N_z	n/a	n/a	16	16	16
N_z'	n/a	n/a	32	64	128

was used for the pitching airfoil cases. For the local refinement mesh, 'refineMesh' utility in OpenFOAM [112] was used based on structured mesh generated by using Pointwise. The purpose of the static airfoil case is to compare the results for the pitching airfoil case to those for the static airfoil case at a given angle of attack.

6.3.1 Mesh convergence tests for the static airfoil

For the static airfoil case, 10° incidence was applied at $Re = 135,000$. To obtain the mean aerodynamic forces, averaging started once the lift coefficient reached a statistically converged state and averaging was conducted over $10T$ where $T = c/U_\infty$. Spanwise averaging was also conducted for all figures for 3-D cases. The boundary conditions for the static airfoil case (ST) are summarized in Table 6.1 and periodic boundary conditions were used in the spanwise direction for 3-D cases. The coordinates x, y and z with the origin at the leading edge of the airfoil represented the streamwise, cross-flow and spanwise direction respectively.

In order to save CPU time, the mesh convergence tests in the streamwise and cross-flow directions were conducted on the 2-D domain without an SGS model. The number of grid points was increased until the surface forces for the 2-D simulations did not change. The first off-wall grid point was placed at $y_1 \approx 1 \times 10^{-4}c$ near the leading edge and $y_1 \approx 3 \times 10^{-4}c$ for the trailing edge before the refined mesh was applied.

A local refined mesh was applied for the static airfoil case to reduce the computational costs as shown in Fig. 6.4. The size of the refined region is characterized with l_r1, l_r2, l_r3 and l_r4 and the details of the refined regions are summarized in Table 6.2. The number of grid points and domain sizes for the mesh convergence tests before the local refinement was applied, are summarized in Table 6.3. The refinement ratio was 2, i.e. the grid size was halved in any direction where the refinement was applied.

Fig. 6.6 shows the surface pressure and skin-friction coefficients for cases $\mathrm{ST}_{\mathrm{2D1}}$ and $\mathrm{ST}_{\mathrm{2D2}}$ and they match very well with each other. Thus the mesh for case $\mathrm{ST}_{\mathrm{2D1}}$ was used to generate the 3-D mesh. The 3-D mesh was generated by extruding the $\mathrm{ST}_{\mathrm{2D1}}$ mesh into the spanwise direction with 16 grid points. Then the local refinement was applied, see Tables 6.2 and 6.3. The number of grid points in the spanwise direction after the local refinements is N_z' as shown in Table 6.3. The total number of grid points for case $\mathrm{ST}_{\mathrm{3D3}}$ is about 21×10^6. In contrast, a structured mesh without the local refinement would require 33×10^6 grid points approximately, for the same resolution around the airfoil.

Fig. 6.7(a) shows the pressure coefficients for the 3-D cases and they show reasonably good agreement with the experimental data [128] in spite of the different spanwise resolutions. In contrast, the skin-friction coefficient more closely approaches the measured

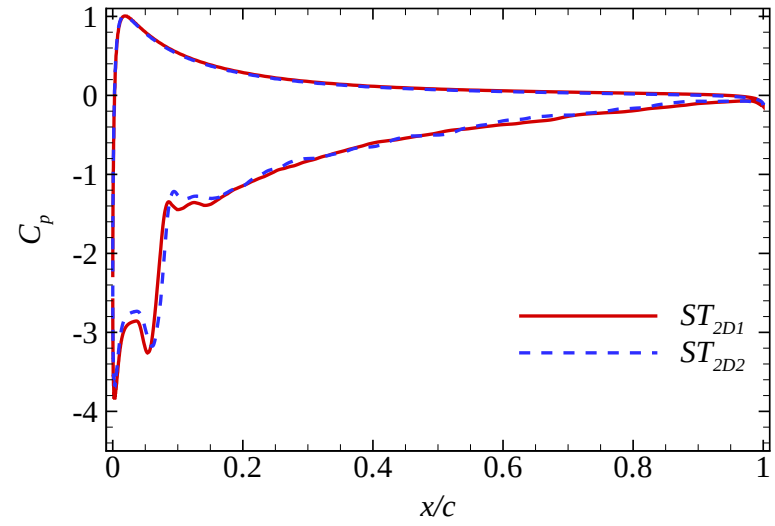

(a)

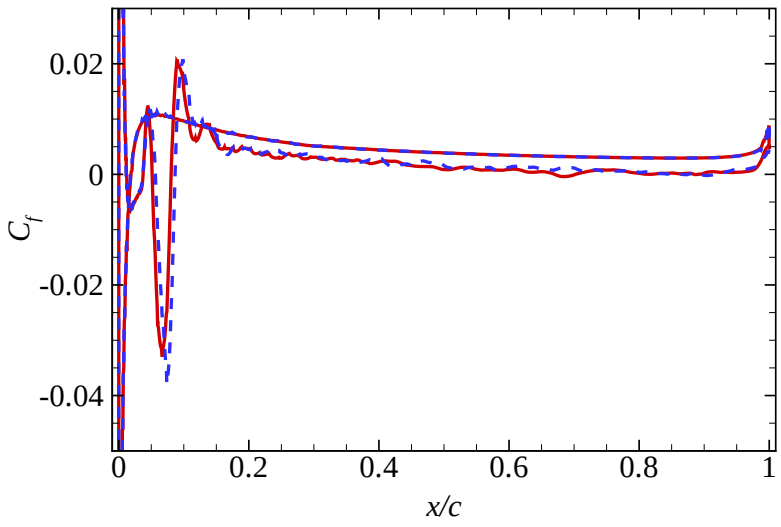

(b)

FIGURE 6.6: The effect of resolution on the (a) pressure and (b) skin-friction coefficients for the 2-D static airfoil at $\alpha = 10°$.

values as the number of grid points increases in the spanwise direction. The reattachment points are at $x/c = 0.1$ for the experiment [128], $x/c = 0.18$ for case ST_{3D1}, $x/c = 0.14$ for case ST_{3D2} and $x/c = 0.09$ for case $3\mathrm{ST}_{3D3}$. Also the magnitudes of the peaks in C_f near the leading edge due to the laminar separation bubble increases as the number of grid points increases in the spanwise direction. Case ST_{3D3} shows good agreement with the reference data in terms of C_p and C_f, thus this case is considered as the baseline simulation for the static airfoil flow in the following sections.

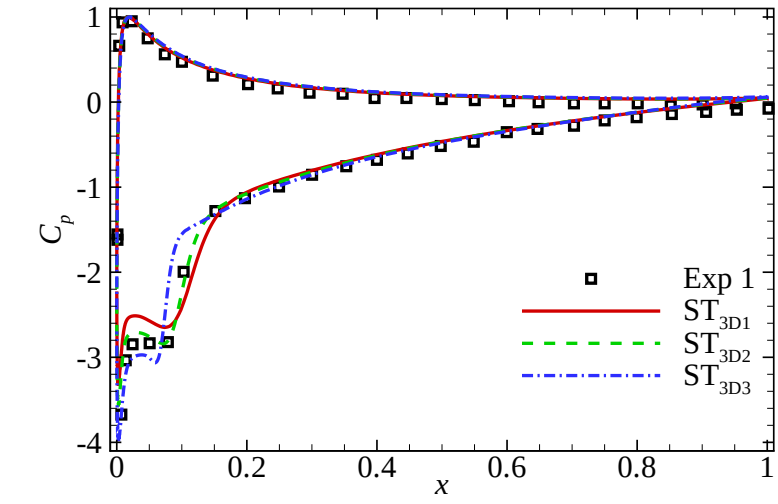

(a)

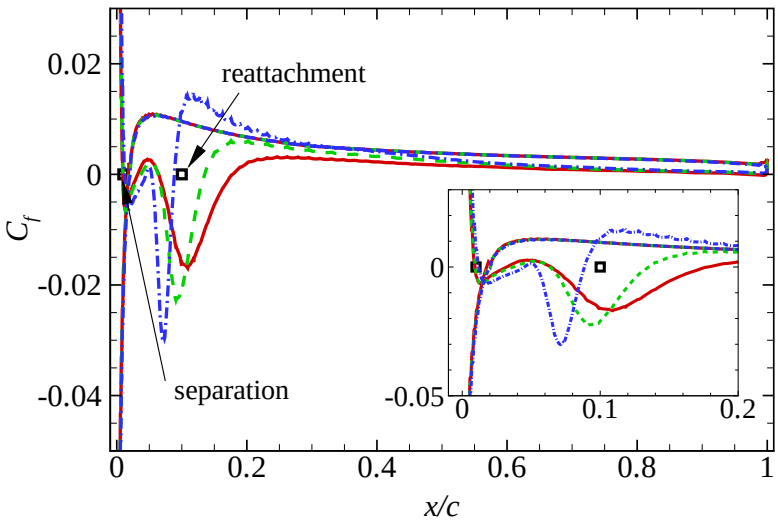

(b)

FIGURE 6.7: The effect of resolution in the spanwise direction on the (a) pressure and (b) skin-friction coefficient for the 3-D static airfoil at $\alpha = 10°$. The inset shows a zoomed view near the leading edge. Data for Exp1 is taken from Rinoie and Takemura (2004) [128].

6.3.2 Mesh convergence tests for the pitching airfoil

The pitching motion was described by the angle of attack, $\alpha = 10° + 15° \sin(\omega t)$ where ω was the pitching frequency and the reduced frequency is $k_{\text{red}} = \frac{\omega c}{2U_\infty}$, see Eq. 1.1. For the mesh convergence tests, $k_{\text{red}} = 0.1$ was adopted. The initial angle of attack was set to $10° \downarrow$. Note that '$\uparrow$' indicates pitch-up and '$\downarrow$' indicates pitch-down. Pitch-up motion has a negative sign for the pitching moment. The mean angle of attack,

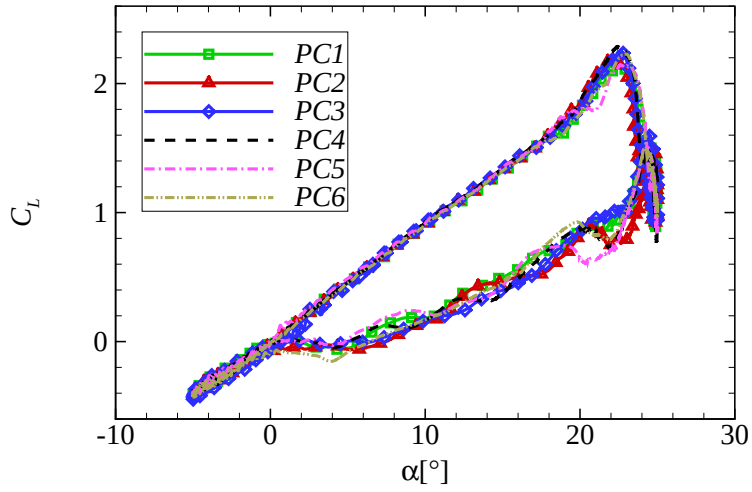

(a)

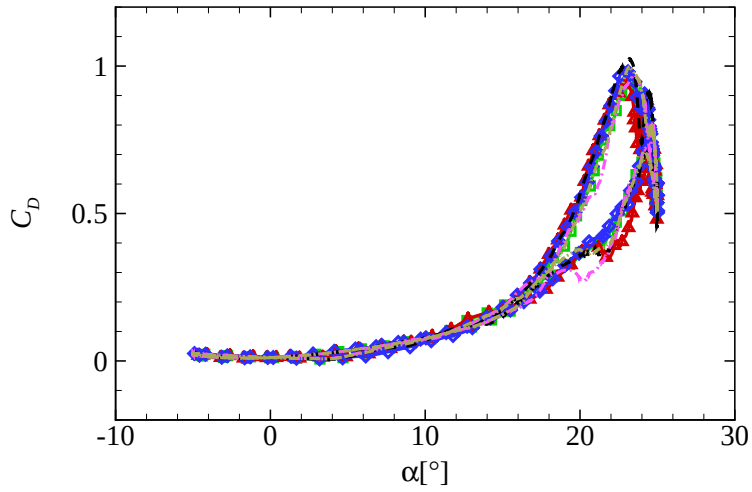

(b)

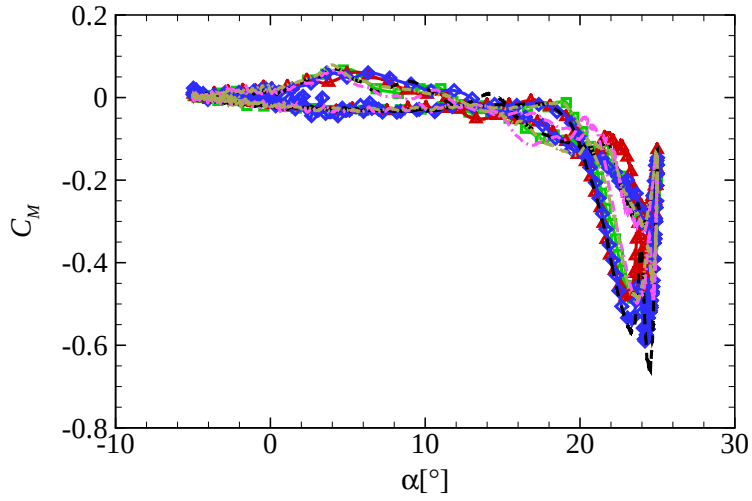

(c)

FIGURE 6.8: The effect of resolution and domain size on the lift, drag and moment coefficients for the pitching airfoil at $k_{\text{red}} = 0.1$ and $\alpha = 10° + 15°\sin(\omega t)$.

TABLE 6.4: The computational domain size in unit c and number of grid points for pitching (PC) airfoils. Note that the domain size in the upstream direction is the same as that in radial direction, R, for the modified mesh as shown in Fig. 6.1. See Fig 6.5 for R and W.

	PC1	PC2	PC3	PC4	PC5	PC6
R [c]	22	22	22	22	22	22
W [c]	33	33	33	33	33	33
L_z [c]	0.5	0.5	0.5	0.5	0.5	1
N_R	206	323	206	206	206	206
N_W	66	66	81	81	81	81
N_{up}	386	386	700	386	386	386
N_{low}	193	193	193	193	193	193
N_z	40	40	40	80	20	80

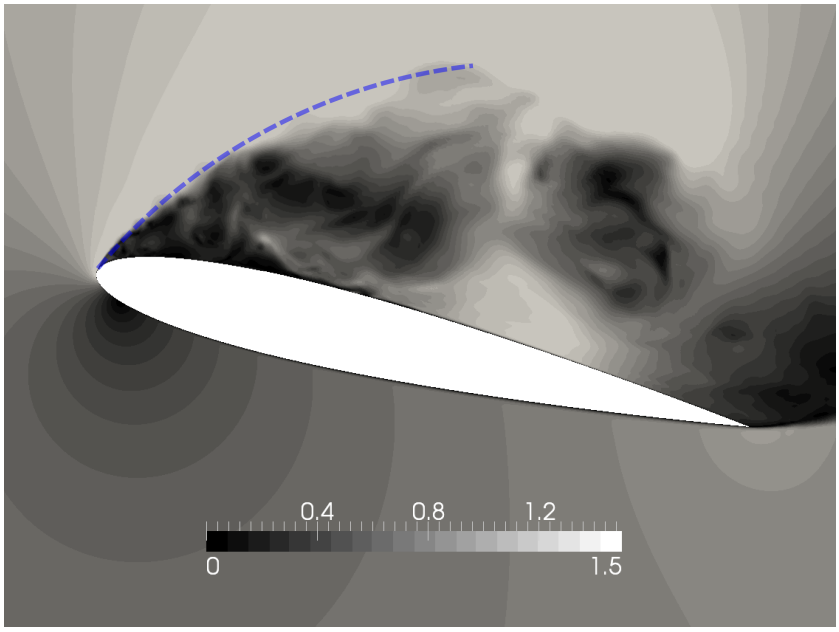

FIGURE 6.9: A snapshot of the velocity magnitude normalized by U_∞ for case PC5 at $k_{\text{red}} = 0.1$ and $\alpha = 22.9° \uparrow$. A dashed-line is drawn along the shear layer near the leading edge.

10°, was presented by the velocity components at the boundaries, $u = U_\infty \cos(10°)$ and $v = U_\infty \sin(10°)$. The Reynolds number for all pitching cases was $Re = 135,000$.

Two types of mesh topology were used for the pitching airfoil cases; the C-type mesh was adopted for the laminar inflow and the modified mesh (Fig. 6.1(b)) was used for the turbulent inflow. The mesh around the airfoil was identical for both meshes. The quarter chord point was placed at $x = 0.25c$ where x, y and z were the streamwise, cross-flow and spanwise directions. The first grid point from the airfoil was located at a distance $1 \times 10^{-4}c$ near the leading edge and $3 \times 10^{-4}c$ near the trailing edge. Aspect

ratios were 15 at the leading edge and 2.3 at the trailing edge. Symmetric boundary conditions were applied in the spanwise directions and other boundary conditions for the pitching airfoil case (PC) are tabulated in Table 6.1. The mesh convergence tests for the pitching airfoil were conducted and the domain size and number of grid points are summarized in Table 6.4.

Fig. 6.8 shows the lift, drag and moment hysteresis from the mesh convergence tests. Data in Fig. 6.8 is taken after the first $\alpha = 0^\circ \uparrow$ which corresponds to 12 flow passes over the chord (tU_∞/c) after the initial condition. Only the first cycle after the first $\alpha = 0^\circ \uparrow$ for all cases is shown in Fig. 6.8 because the hysteresis from successive cycles matches together with only small deviations.

A strong shear layer is developed near the leading edge as shown in Fig. 6.9. It is important that the mesh is fine enough to capture the shear layer. Thus the effects of the resolution in the cross-flow direction (PC1 and PC2) and chordwise direction (PC1 and PC3) were tested. The effect of the resolution in the spanwise direction was of interest because the transition and reattachment points were sensitive to the spanwise resolution for the flow over a static airfoil (see Sec. 6.3.1). Thus the effect of the spanwise resolution was tested in cases PC1, PC4 and PC5. Cases PC3 and PC6 were set to investigate the domain width effect on the hysteresis for the pitching airfoil. The results from all these cases agree reasonably well with each other. The angles where the maximum lift occurs, are around $23^\circ \uparrow$ and the size of hysteresis loops is very similar for all cases. Thus the mesh for case PC5 is used as the baseline simulation for the pitching airfoil in following works. It is noted that about 700 CPU hours were required to simulate a few cycles of pitching motion using 96 processors for case PC5.

6.4 Dynamic stall events

TABLE 6.5: The effect of the reduced frequency on important unsteady aerodynamic values. $\alpha_{L,\max}$ is the angle of attack where the maximum lift occurs.

Case	k_{red}	$C_{L,\max}$	$C_{M,\min}$	$C_{D,\max}$	$\alpha_{L,\max}$
Exp [85]	0.025	1.47	-0.143	0.425	17.5°
Exp [85]	0.05	1.87	-0.211	0.66	21.1°
Exp [85]	0.1	2.44	-0.263	0.91	24.7°
LES2	0.025	1.49	-0.159	0.412	16.4°
LES2	0.05	1.74	-0.287	0.629	19.5°
LES2	0.1	2.01	-0.345	0.856	22.8°

Dynamic stall is a phenomenon associated with an unsteady airfoil (or lifting surface) motion that presents large hysteresis on the lift, drag and pitching moment while incidence is beyond its static stall angle [15]. At a certain pitching angle which exceeds

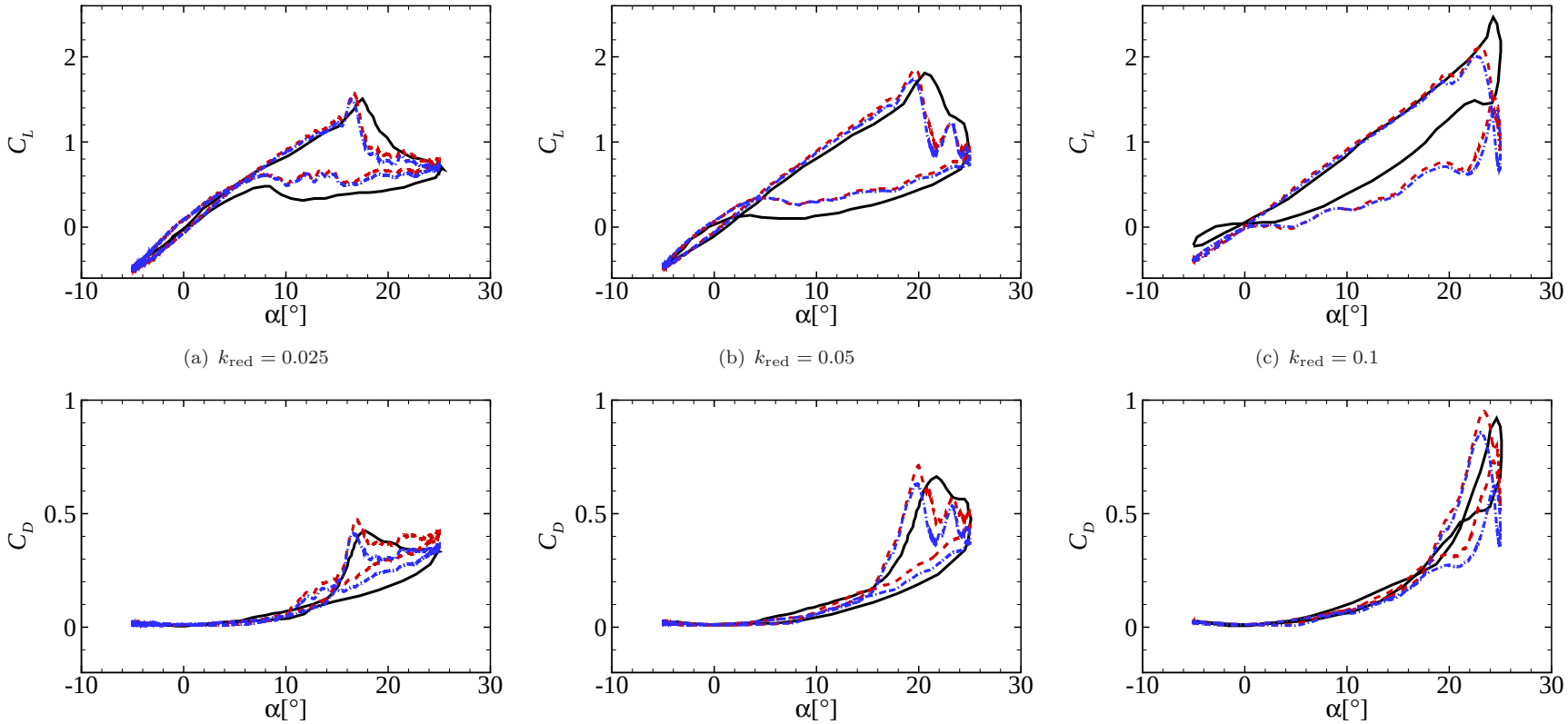

(a) $k_{\mathrm{red}} = 0.025$ (b) $k_{\mathrm{red}} = 0.05$ (c) $k_{\mathrm{red}} = 0.1$

(d) $k_{\mathrm{red}} = 0.025$ (e) $k_{\mathrm{red}} = 0.05$ (f) $k_{\mathrm{red}} = 0.1$

FIGURE 6.10: The effect of the reduced frequency on the lift, drag and moment coefficients. — Exp [85], - - LES1, -·- LES2. The results for cases LES1 and LES2 are calculated with the mesh for case PC5 and 3 cycles were used for the phase average. Note that forces for LES2 are taken from only part of the airfoil surface, $0 < x/c < 0.8$.

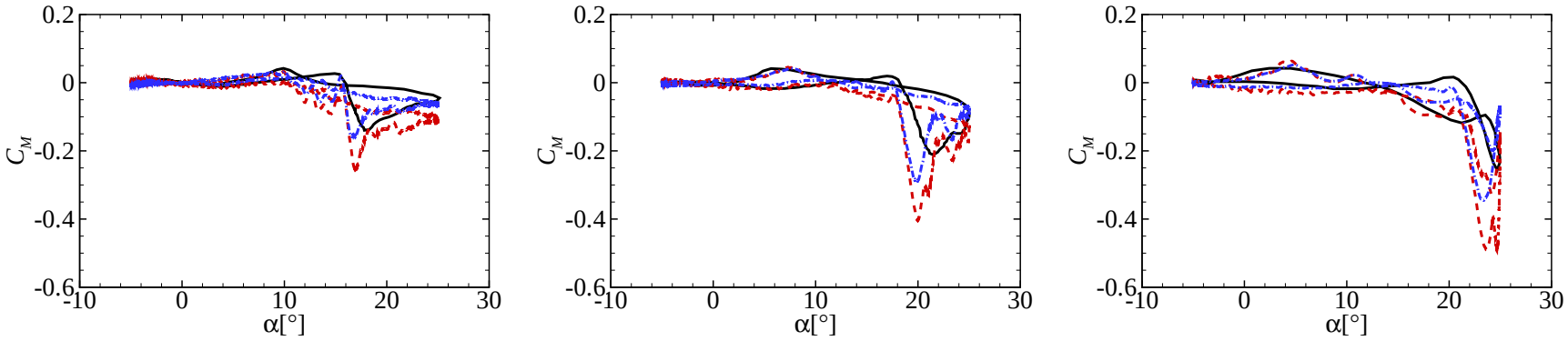

(a) $k_{\mathrm{red}} = 0.025$ (b) $k_{\mathrm{red}} = 0.05$ (c) $k_{\mathrm{red}} = 0.1$

FIGURE 6.11: See Fig. 6.10 for caption.

the static stall point, the flow on the airfoil is still attached, i.e. stall is delayed. As the pitching angle increases, the lift and moment change rapidly as the flow starts to detach, i.e. dynamic stall occurs. Complex flow phenomena are investigated by analysing surface forces, pitching moments and flow fields.

Based on the mesh used for case PC5, the effect of the reduced frequencies, $k = 0.025$, 0.05 and 0.1, on the forces and moments hysteresis is investigated as shown in Figs. 6.10 and 6.11. From the first $\alpha = 0^\circ \uparrow$, three cycles were used for the phase average. The results are compared with experimental data [85] that were averaged over 100 cycles. Though the phase-averaged data from the LES calculations in Figs. 6.10 and 6.11 were not fully converged, the stall angle and size of hysteresis were nearly the same at each cycle. Therefore, a longer phase average would not be expected to improve agreement between the simulation and experimental data. The load hysteresis from the simulations are integrated over the airfoil surface while those from the experiment were integrated over a line along the pressure tabs. It is also noted that adopting $1c$ domain width (PC6) did not present noticeable differences in force and moment hysteresis compared to $0.5c$ (PC3).

In the experiment [85], C_L, C_D and C_M were calculated from pressure tab measurements and these tabs were placed at $0 < x/c < 0.8$ over the airfoil surface. For an accurate comparison, two sets of airfoil surfaces were used to calculate the surface forces; the first set used the entire airfoil surface (LES1) and the second one used a part of the airfoil surface which covered $0 \leq x/c \leq 0.8$ (LES2). In consequence, case LES2 shows better agreement with the reference data than case LES1 for all predictions as shown in Figs. 6.10 and 6.11. Important unsteady aerodynamic values are summarized in Table 6.5 and compared with the experimental data.

Generally, all aerodynamic coefficients match well with the measurements. As the reduced frequency increases, the magnitudes of the peaks for C_L, C_D and C_M increase and the angle for the maximum lift increases. The same trend was also reported in literature [15, 98]. Note that the moment coefficients for the experimental data [85] was divided by 0.15 because the chord length ($c = 0.15$m) was not taken into account when C_M was calculated in their original works. This was confirmed by Prof. Timothy Lee [85] *via* a personal communication.

The lift coefficients for $k_{\text{red}} = 0.025$, 0.05 show very good agreement while those for $k_{\text{red}} = 0.1$ show somewhat different behaviours; the C_L loop has a larger area and maximum lift is lower for the calculations than those for the experiments. Uncertainties on the aerodynamic loads and pitching moment in the measurements were discussed in Lee and Gerontakos (2004) [85] and it is quoted here,

"*The effect of the length of the Tygon tubing was a simple time constant delay on all pressure signals with frequency above 2.95 Hz, which rendered a limited reduced frequency* k_{red} *of 0.0993 at* $U_\infty = 14ms^{-1}$ *or* $Re = 1.35 \times 10^5$ *in the present experiment.*

Therefore, as a result of the difficulties encountered with the inevitable lag in the transducer's response, the curves of lift and pressure drag coefficients, C_L and C_D, and the pitching-moment coefficient, C_M, for $k_{red} > 0.1$ can only be considered qualitatively, but large hysteresis effects are apparent nevertheless."

If the measurement data can only be considered qualitatively for $k_{\text{red}} > 0.1$, then the question is whether the deviations between the calculations and measurements for $k_{\text{red}} = 0.1$ in Figs. 6.10 and 6.11 are derived from the response lag in using the Tygon tubing. This question was sent to Prof. Timothy Lee [85] and the response is quoted below,

"*The tubing length did not seem to be problematic; we did try with half the length (at certain orifices) and did not see any disparity. I guess that it would also be difficult to compute the C_L during downstroke before the reattachment. As far as the accuracy of $k_{red} = 0.09$ case (especially during downstroke), the jury is still out there.*

The downstroke data could be tricky due to the massive leading edge vortex induced separated flow. The corresponding surface pressure measurements could therefore be debatable. But again at this low Re, the experimental data could vary between researchers due to different flow qualities/facilities and the experimental setups. Your simulation results however seem to agree with the experimental data quite nicely at $k_{red} = 0.05$ and 0.025; I can only say that the leading edge vortex disruption/bursting maybe less rigorous (for $k_{red} = 0.025$, 0.05)."

It would be challenging to measure the surface pressure when the leading edge vortex is very strong during the downstroke in experiments. LES, in contrast, does not suffer with a technical limit to measure the surface pressure as long as the large structures are resolved accurately. A reasonable phase-average was conducted to obtain the statistical data and the mesh convergence tests showed that a wider domain width (PC6 in Table 6.4) did not show noticeable difference on the hysteresis loop. Therefore, the current calculations are reliable for $k_{\text{red}} = 0.1$.

Laminar separation bubble diminishing

During the pitch-up process, the boundary layer on the suction side of the airfoil is suppressed and the size of the laminar separation bubbles significantly diminishes or disappears. Fig. 6.12 shows comparisons between the static and pitching airfoils at a similar incidence. For the pitching airfoil for $k_{\text{red}} = 0.05$, the pressure coefficient and vorticity field at $\alpha = 5.9^\circ \uparrow$ do not show any indication of laminar separation bubbles. In contrast, a negative pressure plateau on C_p due to the laminar separation bubble was observed from the measurement [85] of the static airfoil flow as shown in Fig. 6.12(a). This indicates the diminishing or disappearance of the laminar separation bubble on the pitching airfoil. The instantaneous spanwise component of vorticity at the middle section confirms that the boundary layer is attached on the pitching airfoil at this incidence.

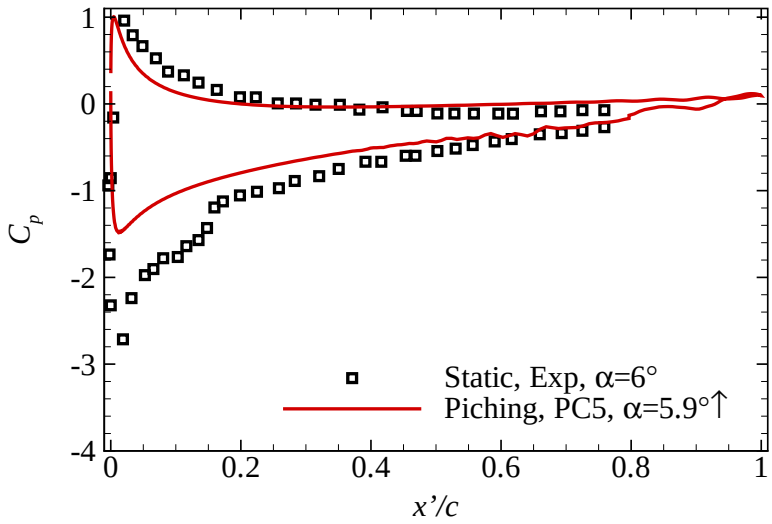

(a)

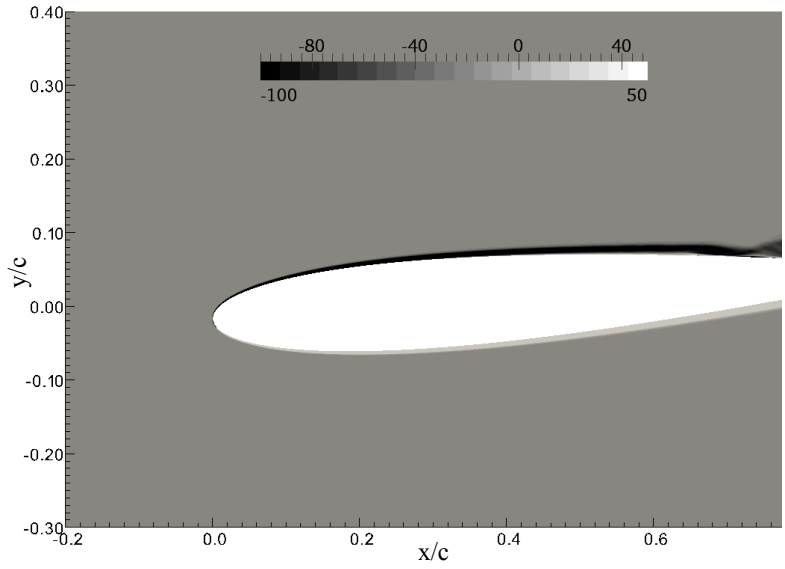

(b)

FIGURE 6.12: (a) The pressure coefficient and (b) instantaneous z-vorticity at the middle section for case PC5 at $\alpha = 5.9° \uparrow$ and $k_{\text{red}} = 0.05$. The vorticity contour is normalized by c and U_∞. The experimental data [85] was conducted on a static airfoil at $\alpha = 6°$ with the same airfoil and Reynolds number.

Boundary layer suppression

The boundary layer suppression is observed at a relatively high angle of attack (yet lower than the dynamic stall angle). Note that the static stall occurs at around 13° [85] at the given conditions. Fig. 6.13 shows the contours of instantaneous velocity magnitude for the static and pitching airfoils at $\alpha \approx 10°$. The boundary layer thickness for the pitching airfoil is thinner than that for the static airfoil near the trailing edge. Thus the boundary layer for the pitching airfoil is suppressed compared with that for the static airfoil at similar incidence.

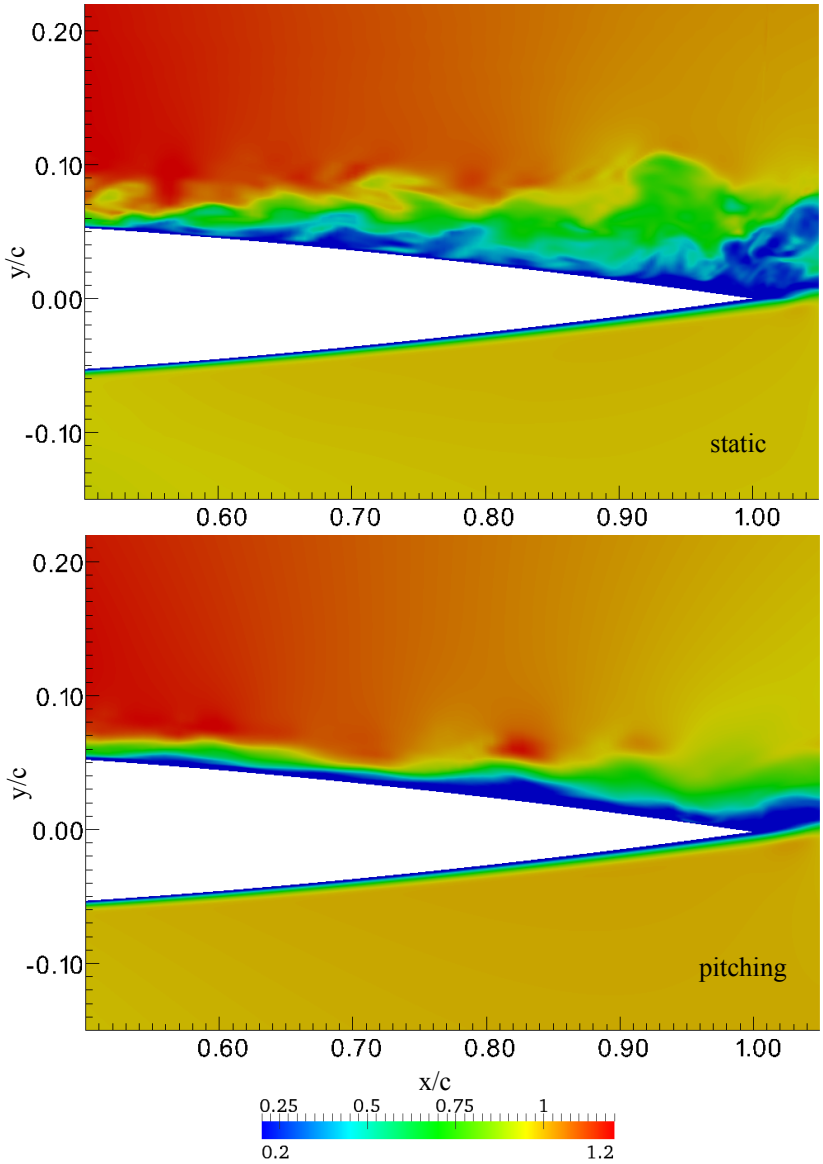

FIGURE 6.13: Instantaneous velocity magnitude contour near the trailing edge for the static (top: ST_{3D3}, $\alpha = 10°$) and pitching (bottom: PC5, $\alpha = 10.1° \uparrow$, $k_{red} = 0.05$) airfoils at the middle section of the span. The velocity contour is normalized by U_∞.

This boundary layer suppression is mainly due to the time lag of the boundary layer development on moving subjects [82, 86]. When the airfoil is pitching, the flow around it at a given geometric angle of attack (angle between the freestream velocity direction and chord line) does not 'see' the same flow topology as that around the static airfoil at the same geometric angle of attack. This is because the flow over the pitching airfoil 'remembers' its history. During the upstroke, the boundary layer of the pitching airfoil looks suppressed because it 'remembers' the previous (in time) flow topology which is produced at lower incidence.

The pitching airfoil passes the static stall angle, $\alpha \approx 13° \uparrow$ [85], without any discernible change in the lift coefficient slope for all reduced frequency ranges as shown

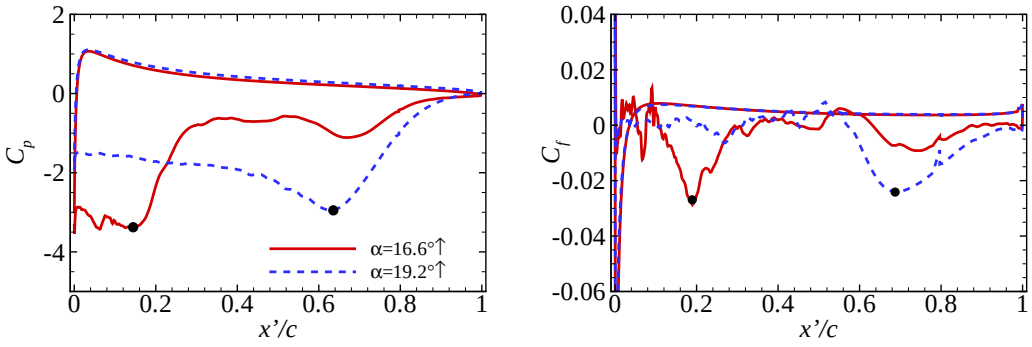

(a) (b)

FIGURE 6.14: (a) The pressure and (b) skin-friction coefficients at two different states during the upstroke, $\alpha = 16.6° \uparrow$ and $19.2° \uparrow$. The reduced frequency is $k_{\text{red}} = 0.05$ and the mesh for case PC5 is used. A spanwise average is applied to calculate the data and x' is the local coordinate which is aligned to the chord line.

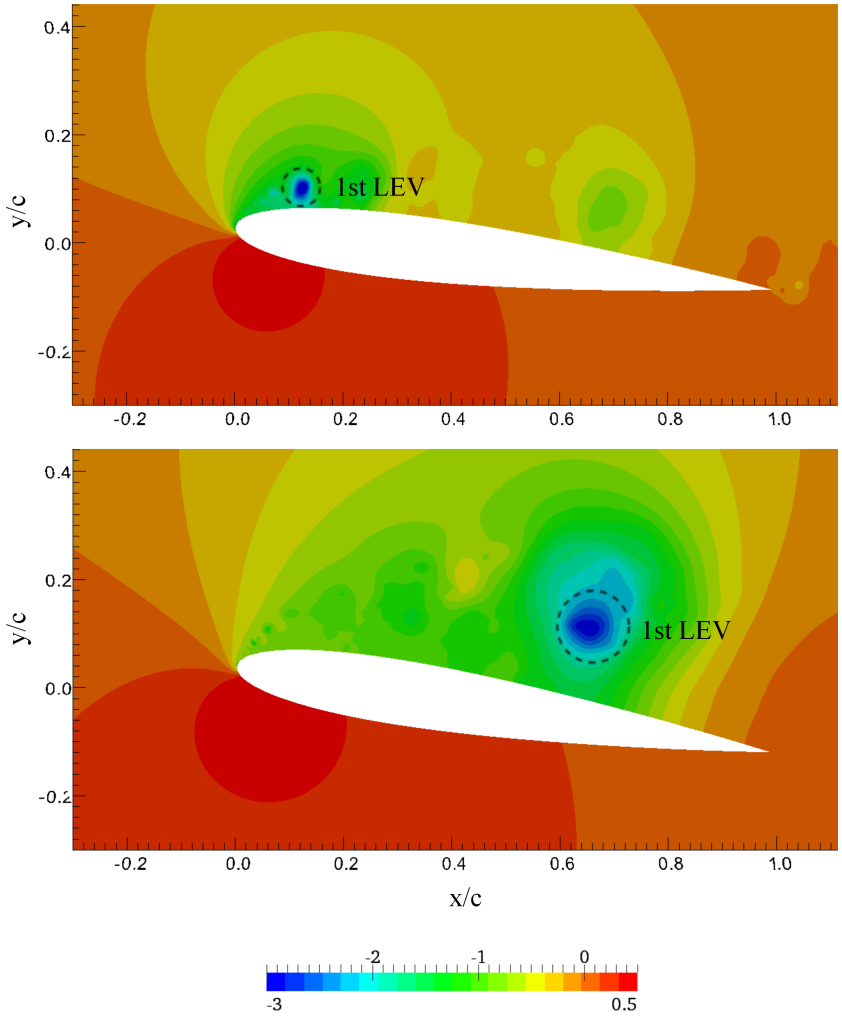

FIGURE 6.15: Negative pressure peaks over the airfoil for $k_{\text{red}} = 0.05$ by using the PC5 mesh, $\alpha = 16.6° \uparrow$ (top), $19.2° \uparrow$ (bottom). The pressure fields are normalized by ρU_∞^2.

in Fig. 6.10, i.e. stall is delayed. Stall delay phenomena are due to a combination of the aforementioned laminar separation bubble diminishing and the lag of the boundary layer development (BL suppression). For the rigorous understanding for stall delay on a pitching airfoil, unsteady boundary layers have to be well understood but this has not yet been accomplished [86].

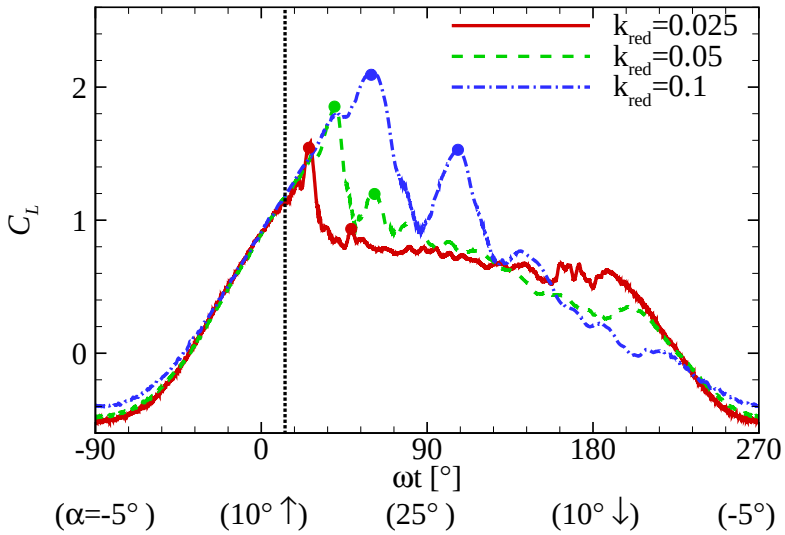

FIGURE 6.16: The lift coefficients (from LES2 in Fig. 6.10) versus period at different k_{red}. The dots indicate the lift peaks due to the shedding of the leading edge vortices. The vertical dot-line indicates the static stall angle, i.e. $\alpha = 13°$ [85].

Leading edge vortex

As angle of attack increases, the 1st leading edge vortex (LEV) is initiated. When each LEV is generated and convects downstream, a lift increase follows. The reason for this increment was well commented by Dickinson and Götz (1993) [24]. They mentioned that "*attached bubble (LEV) greatly enlarges the effective camber of the wing, and thus increase the production of conventional potential lift, which results from potential flow around the airfoil and application of the Kutta condition at the trailing edge*". The LEV initiation, convection and its influence to the lift, drag and pitching moment are the most important phenomena in dynamic stall events. Thus, the characteristics of the 1st LEV are quantified for $k_{\text{red}} = 0.025 - 0.1$.

The convection speed of the leading edge vortex (U_{LEV}) with respect to the chord line at $\alpha = 0°$, can be quantified by measuring the travelling time of the pressure peaks on the suction side of the airfoil [38]. Fig. 6.14 shows the pressure and skin-friction coefficients at two different angles of attack. A strong leading edge vortex presents peaks of C_p and C_f which are marked in the figure. Then U_{LEV} is estimated by using the time interval between the two incidences and the distance between the peak points. The negative peaks on the pressure contours at the same incidence in Fig. 6.15 (dashed circles) confirm the correlation between the LEV and the surface forces.

By using this estimation, it is shown that $U_{LEV} \approx 0.25U_\infty$ for $k_{\text{red}} = 0.025 - 0.1$. It is noticed that the LEV convection speed is independent of k_{red}. Green et al. (1992) [38] measured the LEV convection speed with various types of airfoils. They concluded that the LEV convection speed was independent of the airfoil motion, and also reported that $U_{LEV} \approx 0.26U_\infty - 0.31U_\infty$ at the maximum pitch angle $\alpha_{\max} \approx 25°$ for the NACA 0012 airfoil. A similar LEV convection velocity, $U_{LEV} \approx 0.3U_\infty$, was also reported by other group [16]. Considering uncertainties in determining vortex cores, the difference in the LEV convection speed between the current case and those in literature is relatively small.

Fig. 6.16 shows C_L versus period for a better reading. The bullet points represent the peaks due to the leading edge vortex convection over the upper airfoil surface. The magnitudes of the first and second peaks decrease as the reduced frequency decreases. The maximum-lift angle approaches the static stall angle as the reduced frequency decreases. At very small pitching frequency, a quasi-steady state would be achieved and the coefficients for the pitching airfoil would show no difference from those for the static case at the corresponding incidence. McAlister et al. (1978) [96] reported that the aerodynamic forces are quasi-steady for $k_{\text{red}} < 0.004$. The shedding frequency between the first and second leading edge vortices are characterized by the Strouhal number,

$$St = \frac{f_s c \sin\alpha_{LEV}}{U_\infty}, \tag{6.4}$$

where f_s is the shedding frequency and α_{LEV} is the mean angle of attack between the first and second LEV peaks. Then the Strouhal number for the present study ($k_{\text{red}} = 0.025 - 0.1$) is $St \approx 0.1$. This Strouhal number is lower than the well-known bluff-body shedding frequency, $St \approx 0.2$ [130]. Zaman et al. (1989) [187] reported that the Strouhal number of the flow over a static airfoil varies depending on angle of attack. They showed that $St \approx 0.2$ when $\alpha > 18°$ (post-stall) and $St \approx 0.02$ when $\alpha < 15°$ (pre-stall) for the flow over the airfoil. The shedding frequency for the current case lies between these two regimes. This is because the pitching angle passes across both pre- and post-stall regimes and the shedding frequency shows the combined characteristics of both regimes.

Figs. 6.17 and 6.18 show important features for dynamic stall by using snapshots of the spanwise component of vorticity and pressure field at $k_{\text{red}} = 0.05$. Each snapshot of the flow is marked on the lift and moment coefficients in Fig. 6.19 and it is summarized as,

1. $\alpha = 10° \uparrow$: Laminar separation bubble and boundary layer are suppressed compared to that on a static airfoil at the same angle of attack.

2. $\alpha = 13° \uparrow$: The lift keeps increasing above the static stall angle without discernible changes of the lift coefficient slope.

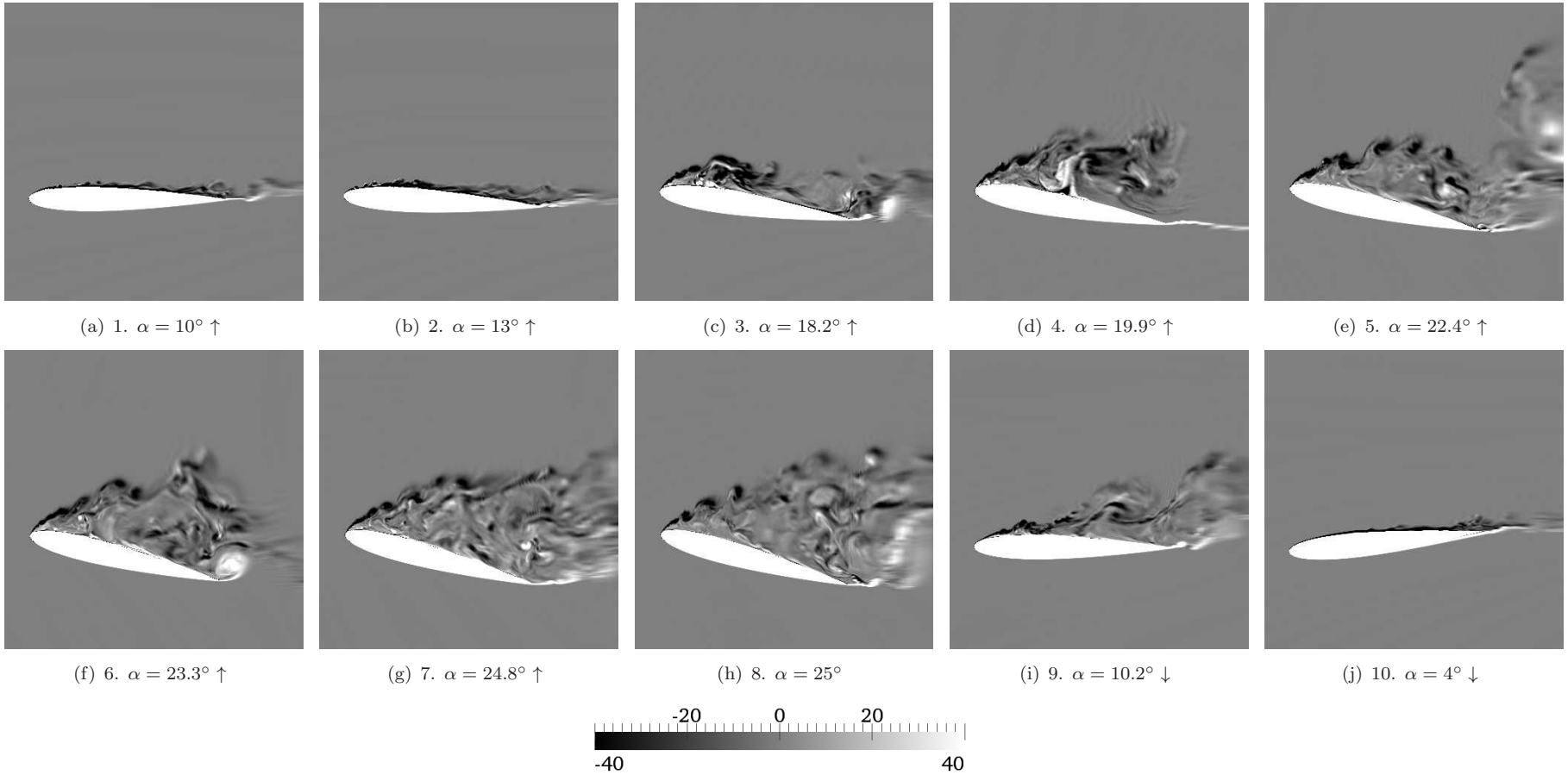

(a) 1. $\alpha = 10° \uparrow$ (b) 2. $\alpha = 13° \uparrow$ (c) 3. $\alpha = 18.2° \uparrow$ (d) 4. $\alpha = 19.9° \uparrow$ (e) 5. $\alpha = 22.4° \uparrow$

(f) 6. $\alpha = 23.3° \uparrow$ (g) 7. $\alpha = 24.8° \uparrow$ (h) 8. $\alpha = 25°$ (i) 9. $\alpha = 10.2° \downarrow$ (j) 10. $\alpha = 4° \downarrow$

FIGURE 6.17: The instantaneous z-component of vorticity normalized by c and U_∞ for $k_{\text{red}} = 0.05$ at the middle section of the span. Note that the chord line is aligned to the x-axis at $\alpha = 10°$ as the mean angle of attack is presented by the velocity components at the boundaries, $u = U_\infty \cos(10°)$ and $v = U_\infty \sin(10°)$.

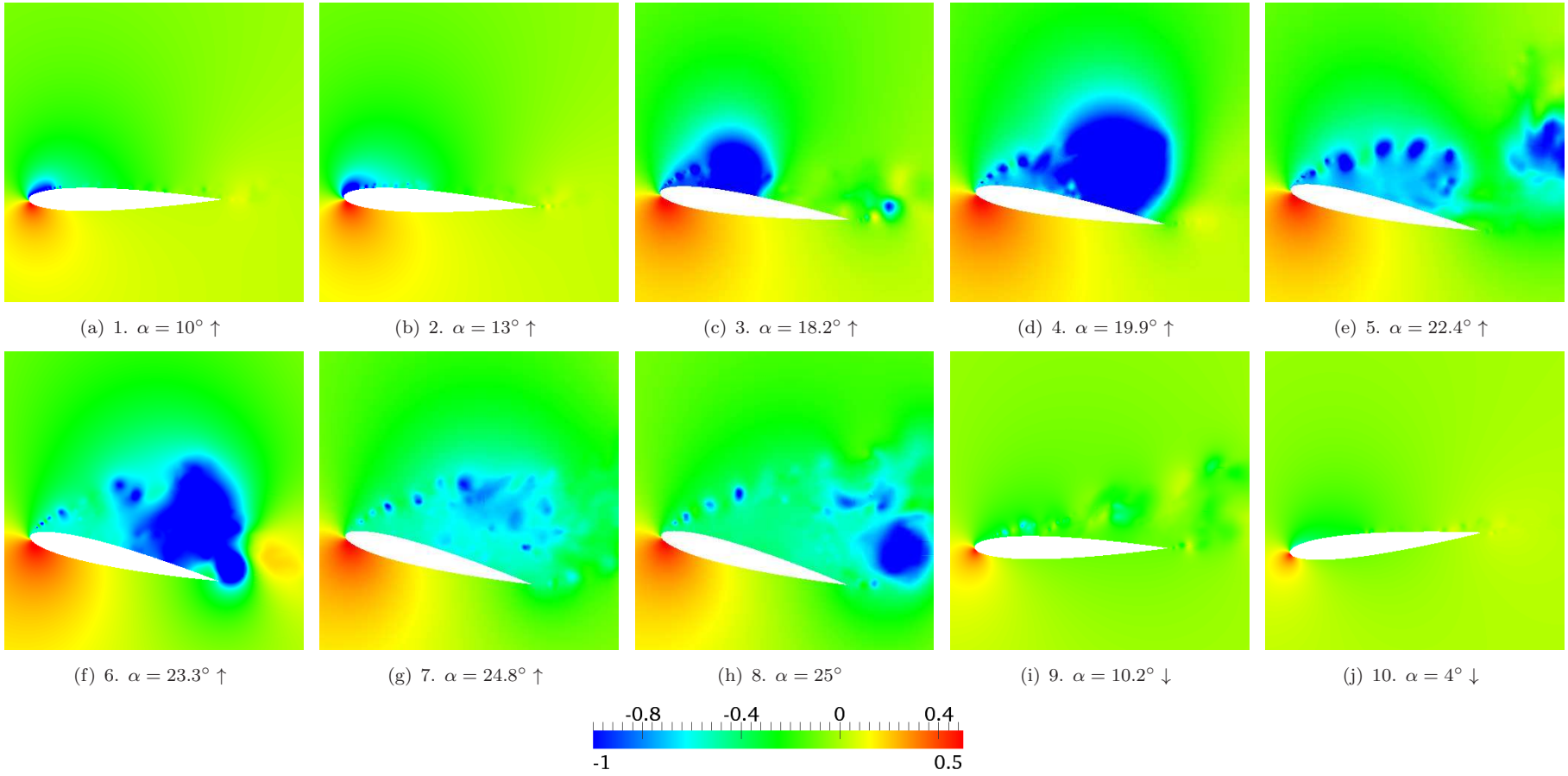

(a) 1. $\alpha = 10° \uparrow$ (b) 2. $\alpha = 13° \uparrow$ (c) 3. $\alpha = 18.2° \uparrow$ (d) 4. $\alpha = 19.9° \uparrow$ (e) 5. $\alpha = 22.4° \uparrow$

(f) 6. $\alpha = 23.3° \uparrow$ (g) 7. $\alpha = 24.8° \uparrow$ (h) 8. $\alpha = 25°$ (i) 9. $\alpha = 10.2° \downarrow$ (j) 10. $\alpha = 4° \downarrow$

FIGURE 6.18: The instantaneous pressure normalized by ρU_∞^2 for $k_{\text{red}} = 0.05$ at the middle section of the span.

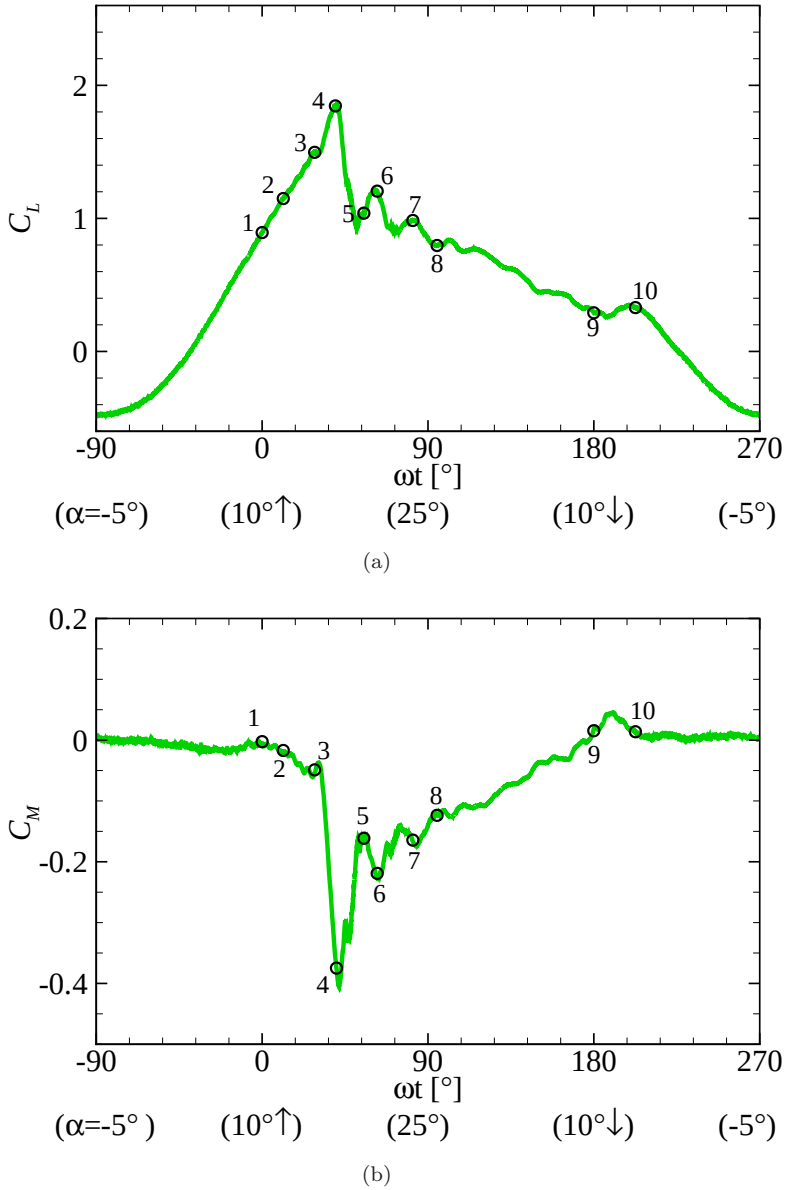

FIGURE 6.19: (a) The lift and (b) moment coefficients (from LES2 in Fig. 6.10) versus period at $k_{\text{red}} = 0.05$. The numbers correspond with the snapshots in Figs. 6.17 and 6.18. 1: $\alpha = 10° \uparrow$, 2: $\alpha = 13° \uparrow$, 3: $\alpha = 18.2° \uparrow$, 4: $\alpha = 19.9° \uparrow$, 5: $\alpha = 22.4° \uparrow$, 6: $\alpha = 23.3° \uparrow$, 7: $\alpha = 24.8° \uparrow$, 8: $\alpha = 25°$, 9: $\alpha = 10.2° \downarrow$, 10: $\alpha = 4° \downarrow$.

3. $\alpha = 18.2° \uparrow$: The moment coefficient starts to drop rapidly, i.e. moment stall. The lift coefficient slope increases rapidly and low pressure is formed at the suction side as the first leading-edge vortex is initiated.

4. $\alpha = 19.9° \uparrow$: The lift coefficient reaches the maximum and starts to decrease. The moment coefficient reaches the minimum. A large area of low pressure at the suction side is observed while the first leading-edge vortex keeps convecting downstream.

5. $\alpha = 22.4° \uparrow$: The lift coefficient increases again as the second leading-edge vortex is generated and convected downstream.

6. $\alpha = 23.3° \uparrow$: The lift coefficient passes the second peak as the second leading-edge vortex passes over the half chord. The moment coefficient reaches its second minimum. An evident tip vortex is formed which is entrained by the leading-edge vortex as it passes over the trailing edge.

7. $\alpha = 24.8° \uparrow$: A small increase of the lift is observed due to the third leading-edge vortex.

8. $\alpha = 25°$: The maximum angle of attack is reached and a large vortex is shedded.

9. $\alpha = 10.2° \downarrow$: The flow begins to be attached.

10. $\alpha = 4° \downarrow$: The flow is fully attached.

A dynamic stall event for $k_{\text{red}} = 0.025 - 0.1$, $\alpha = 10° + 15° \sin(\omega t)$ at $Re = 135,000$ has been presented. Distinctive features of dynamic stall such as laminar separation bubble diminishing, boundary layer suppression and leading edge vortex, are explained and quantified for an example reduced frequency, $k_{\text{red}} = 0.05$.

Qualitative comparisons of the flow field with measurements and RANS calculations are depicted in Fig. 6.20. Instantaneous streamlines and spanwise vorticity component show similarities with those from the experimental data by Raffel et al. (1995) [123]. The spanwise vorticity component in the current simulation reveals random-like distributions within the leading edge vortex which were also observed in the experiment, see Figs. 6.20(a) and 6.20(c). However these details were not found in the RANS calculations by Wang et al. (2010) [177], as shown in Fig. 6.20(e), which is not surprising. This demonstrates the potential of the LES techniques, which can be used to acquire a deep insight for wind turbine flows and to improve RANS models for such flows.

6.5 The effect of freestream turbulence

The developed synthetic turbulence model (XCDF in Ch. 4) was adopted to investigate the effect of freestream turbulence on the pitching airfoil by using the PC5 mesh in Table 6.4 for $k_{\text{red}} = 0.05$. Two different turbulence intensities, $TI_0 = 5\%$ and 10%, were used where suffix '0' denotes the input variable. The upstream turbulence characteristics were quantified in the domain without the airfoil and this case is called the 'empty box case'. Then the same turbulence characteristics were used for the flow over the pitching airfoil.

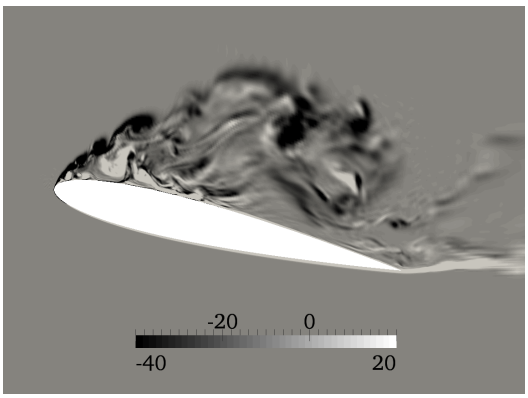

(a) z-vorticity

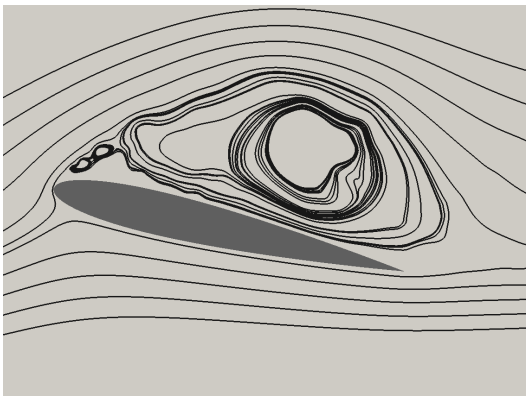

(b) Streamlines

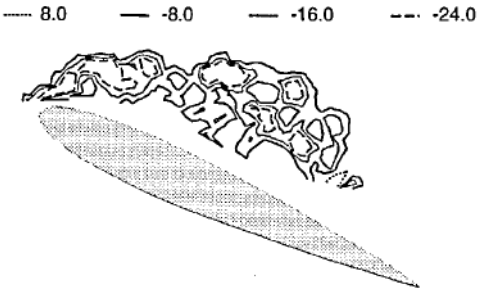

(c) z-vorticity

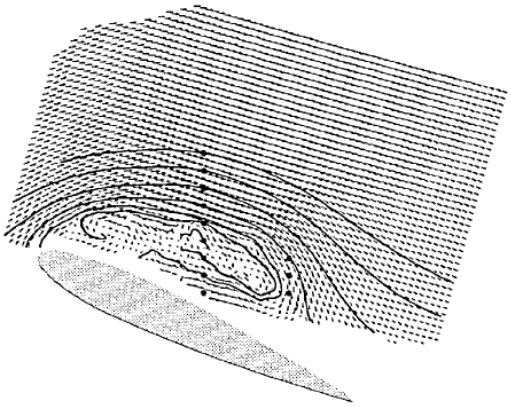

(d) velocity vector and streamline

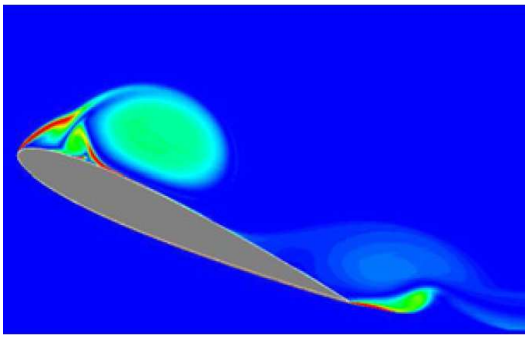

(e) z-vorticity

FIGURE 6.20: Qualitative comparisons of the flows over a pitching NACA 0012 airfoil. (a) and (b): LES calculations by using the PC5 mesh at the middle section of the airfoil at $\alpha = 23.3° \uparrow$ ($Re = 135,000$, $\alpha(t) = 10° + 15°\sin(\omega t)$, $k_{\text{red}} = 0.1$); (c) and (d): experiment by Raffel et al. (1995) [123] at $\alpha = 24° \uparrow$ ($Re = 373,000$, $\alpha(t) = 15° + 10°\sin(\omega t)$, $k_{\text{red}} = 0.15$); (e): RANS calculations by Wang et al. (2010) [177] at $\alpha = 23.7° \uparrow$ ($Re = 373,000$, $\alpha(t) = 15° + 10°\sin(\omega t)$, $k_{\text{red}} = 0.15$). Note that all figures are instantaneous snapshots.

6.5.1 Upstream turbulence

Upstream turbulence was assessed with a similar approach as in Sec. 5.4. To characterize upstream turbulence, a new mesh was generated in which the upstream region of the domain was the same as the modified mesh as shown in Fig. 6.1(b) but the airfoil was removed and the downstream part of the mesh was the same as the upstream one. The boundary conditions, numerical schemes and domain size were the same as those for case PC5. The time step, normalized by I_{11} and U_∞, was $\Delta t \times U_\infty / I_{11} = 0.0133$.

Two different turbulence intensities, $TI_0 = 5\%$ and 10%, were imposed on a 2-D transverse plane at $x/c = -7$ in the coordinate system for case PC5. The integral length scales for the XCDF model were $I_{i1} = 0.3c$, $I_{i2} = 0.15c$ and $I_{i3} = 0.15c$ in the streamwise, cross-flow and spanwise directions, respectively, where i indicates the velocity components, see Eq. 2.52. The grid size normalized by the integral length scale was $\Delta x = 0.333 I_{11}$, $\Delta y = 0.252 I_{11}$ and $\Delta z = 0.083 I_{11}$. The coordinate for the empty box case was normalized by the integral length scale (I_{11}) and the origin was placed where the synthetic turbulence was imposed. The position where the airfoil, would then, be placed was at $x/I_{11} = 23.3$. The turbulent characteristics at these two points, $x/I_{11} = 0$ and $x/I_{11} = 23.3$, are summarized in Table. 6.6. The integral length scale and Reynolds numbers at $x/I_{11} = 23.3$ were estimated after the calculations for the empty box case were finished. Note that Eq. 2.52 was used to estimate the integral length scale at $x/I_{11} = 23.3$.

TABLE 6.6: Upstream turbulence characteristics: turbulence intensity (TI), integral length scales and Reynolds number on the domain without the airfoil. The inflow is generated at the origin ($x/I_{11} = 0$) and the airfoil will be placed at $x/I_{11} = 23.3$. Note that $Re_I = \frac{U_\infty I_{11}}{\nu}$ and $Re_\lambda = \left(\frac{20}{3} Re_I\right)^{1/2}$ [122]. $I_{11} = I_{21} = I_{31}$ and $I_{11} = 2I_{i2} = 2I_{i3}$ where $i = 1, 2, 3$.

x/I_{11}	TI[%]	I_{11}/c	Re_I	Re_λ
0	5	0.3	40,500	520
23.3	4.5	0.43	58,050	622
0	10	0.3	40,500	520
23.3	6.3	0.47	64,350	650

Fig. 6.21(a) shows the (compensated) one-dimensional energy spectrum of the streamwise velocity fluctuations normalized by the local turbulent kinetic energies at $x/I_{11} = 23.3$. The inertial subrange (a plateau value) is visible for both cases. The highest wavenumber that can be resolved by the current resolution (Nyquist limit) is $\kappa_{\max} I_{11} = \frac{1}{2}\frac{2\pi}{\Delta x} I_{11} = 9.42$ but E_{11} starts to drop $\kappa I_{11} \approx 2.5$. This phenomenon is associated with the SGS model, resolution, filtering method and numerical scheme. Firstly, the top-hat filter would smooth the large structure in spectral space as discussed in Sec. 5.4.1, see also Fig. 2.3. Secondly, the numerical scheme has an effect on the early

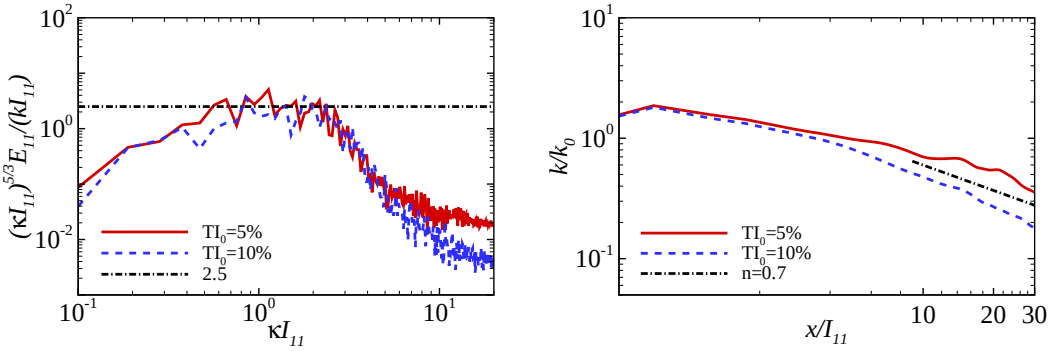

(a) (b)

FIGURE 6.21: (a) A one-dimensional energy spectrum, E_{11}, of the streamwise velocity component normalized by the local turbulent kinetic energy at $x/I_{11} = 23.3$ (see Table 6.6). The dot-dashed line is the inertial region value, 2.5. (b) The turbulent kinetic energy which is normalized by the input value k_0. The dot-dashed line is from $\frac{k}{k_0} \sim \left(\frac{x}{I_{11}}\right)^{-n}$. Note that the suffix '$_0$' indicates the input variables.

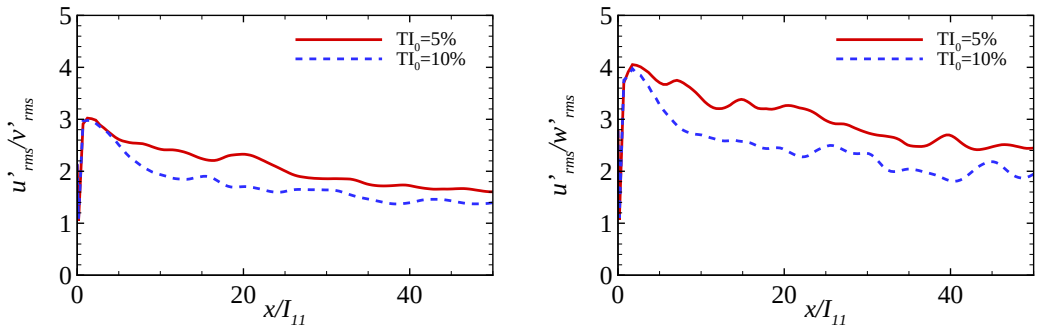

(a) (b)

FIGURE 6.22: Anisotropy of upstream turbulence.

drop of E_{11}. The Gamma scheme [59] (Sec. 3.3) was used for the current study. This scheme is a bounded second order scheme and inherently more diffusive than the central differencing scheme. It leads to a further drop in the high wavenumber range as shown in Fig. 6.21(a). The ratios between the grid size and estimated Kolmogorov length scale are calculated in the same method as in Sec. 5.4.1 and they are $\Delta x/\eta = 199$ and 257 for $TI_0 = 5\%$ and 10% respectively. It shows that the current grid size is placed substantially above the dissipation range.

The effect of the Gamma scheme is also found in the decay rate of turbulence. Fig. 6.21(b) shows the rate of changes of the turbulent kinetic energy normalized by the input values k_0 along the x direction. The estimated exponent is larger, $n = 0.7$, than that with the central differencing scheme as in Sec. 5.4.1 which was $n = 0.35$. This is mainly due to the bounded numerical scheme in the present study. Although the Gamma scheme is diffusive, it guarantees the boundedness. Thus numerical oscillations

are avoided near the strong shear layer or in the deep stall regions owing to the dynamic mesh.

Although some discrepancies from the turbulence characteristics reported in literature are observed in the present study, the focus of the work here is to generate reasonable freestream turbulence and quantify its characteristics immediately upstream of the leading edge which are the integral length scales and turbulence intensities. It is also to be noted that the mesh is the region where the airfoil is placed will be refined in Sec. 6.5.2. This will improve the simulation of the turbulence decay.

The degree of isotropy is shown in Fig. 6.22. The ratios of turbulence fluctuations are $\frac{u'_{rms}}{v'_{rms}} \approx 2$ and $\frac{u'_{rms}}{w'_{rms}} \approx 3$ at $x/I_{11} = 23.3$ where the airfoil will be placed and they approach unity as x increases. It should be noted that a better degree of isotropy is achieved when periodic boundary conditions were applied in the spanwise direction. Again the purpose of this study is to investigate the effect of the given freestream turbulence characteristics on the flow over a pitching airfoil rather than to predict an accurate decay of homogeneous isotropic turbulence. Therefore turbulence intensities 5% and 10% with current configurations are applied to the pitching airfoil flow and the turbulence characteristics at $x/I_{11} = 23.3$ are considered as effective freestream turbulence at the leading edge.

6.5.2 The effect of turbulence intensities

Two different turbulence intensities, $TI_0 = 5\%$, 10%, were imposed on the transverse plane at $x/c = -7$ in the upstream region of the pitching airfoil for $k_{\text{red}} = 0.05$. Fig. 6.23 shows the effect of freestream turbulence on aerodynamic characteristics. Generally freestream turbulence does not significantly change the force and moment hysteresis at the given conditions. The angles for the maximum lift, drag and minimum moment are nearly the same as those for case $TI_0 = 0\%$. The magnitudes for maximum drag and minimum moment decrease for the turbulent inflow cases. The drag coefficients in the pre-stall regime show no difference between laminar and turbulent inflow cases. This indicates that most of the drag is contributed by the pressure difference rather than the skin-friction. Thus the maximum drag reduction at $\alpha \approx 20^\circ \uparrow$ for the turbulent inflow cases is because the pressure drag contribution is reduced by freestream turbulence. The moment stall is when the first leading edge vortex passes the half chord, see $\alpha = 19.9^\circ \uparrow$ in Figs. 6.18 - 6.19 for more details. Freestream turbulence disturbs the leading edge vortex and it may affect the minimum pitching moment. Figs. 6.24(a) and 6.24(e) show snapshots of the spanwise vorticity component near the angle for the minimum moment, $\alpha = 20.3^\circ \uparrow$. Strong vortices on the latter half chord are observed for the laminar inflow case but these are scattered and relatively weak at a similar location for the turbulent inflow case.

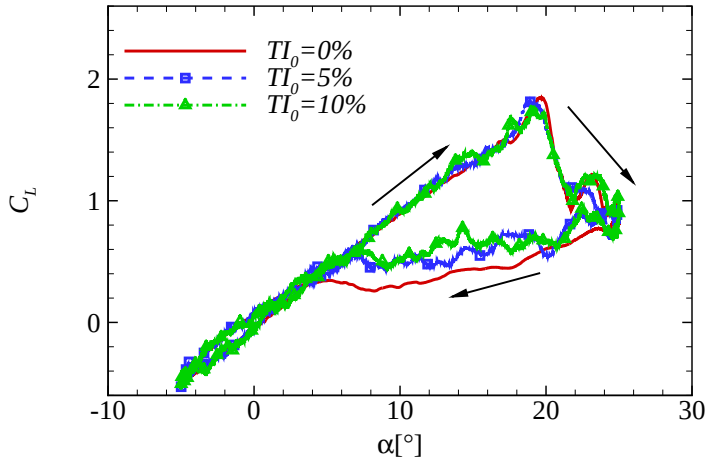

(a)

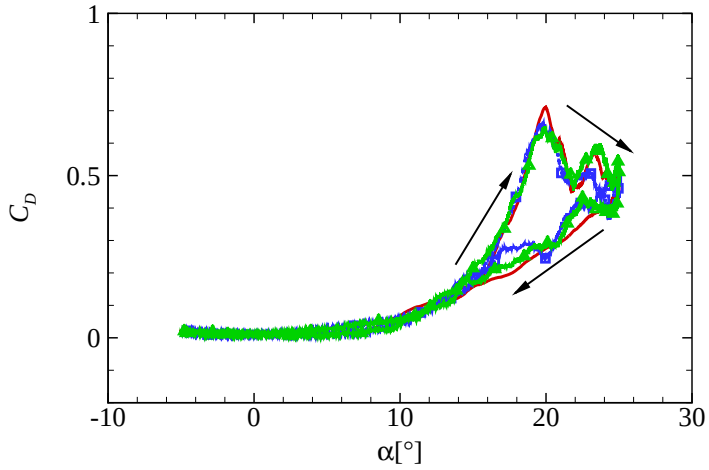

(b)

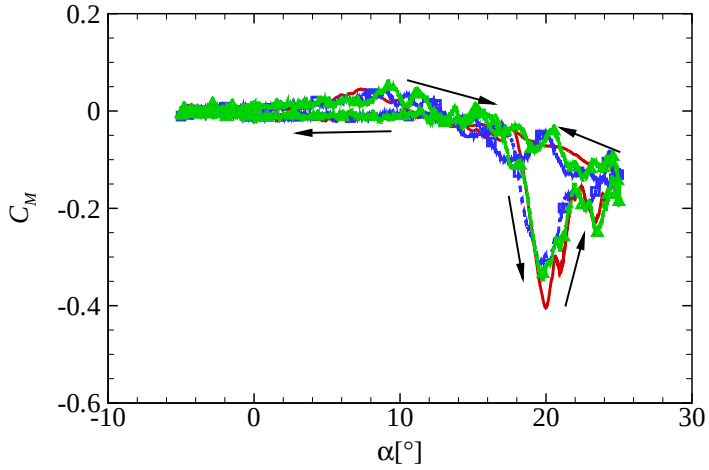

(c)

FIGURE 6.23: The effect of freestream turbulence on the lift, drag and moment coefficients. Case $TI_0 = 0\%$ used the mesh for PC5 and the same mesh was used for the turbulent inflow cases. The effective turbulence intensities at the leading edge are 4.5% ($TI_0 = 5\%$) and 6.3% ($TI_0 = 10\%$), see Table 6.6. For all cases, $k_{\text{red}} = 0.05$.

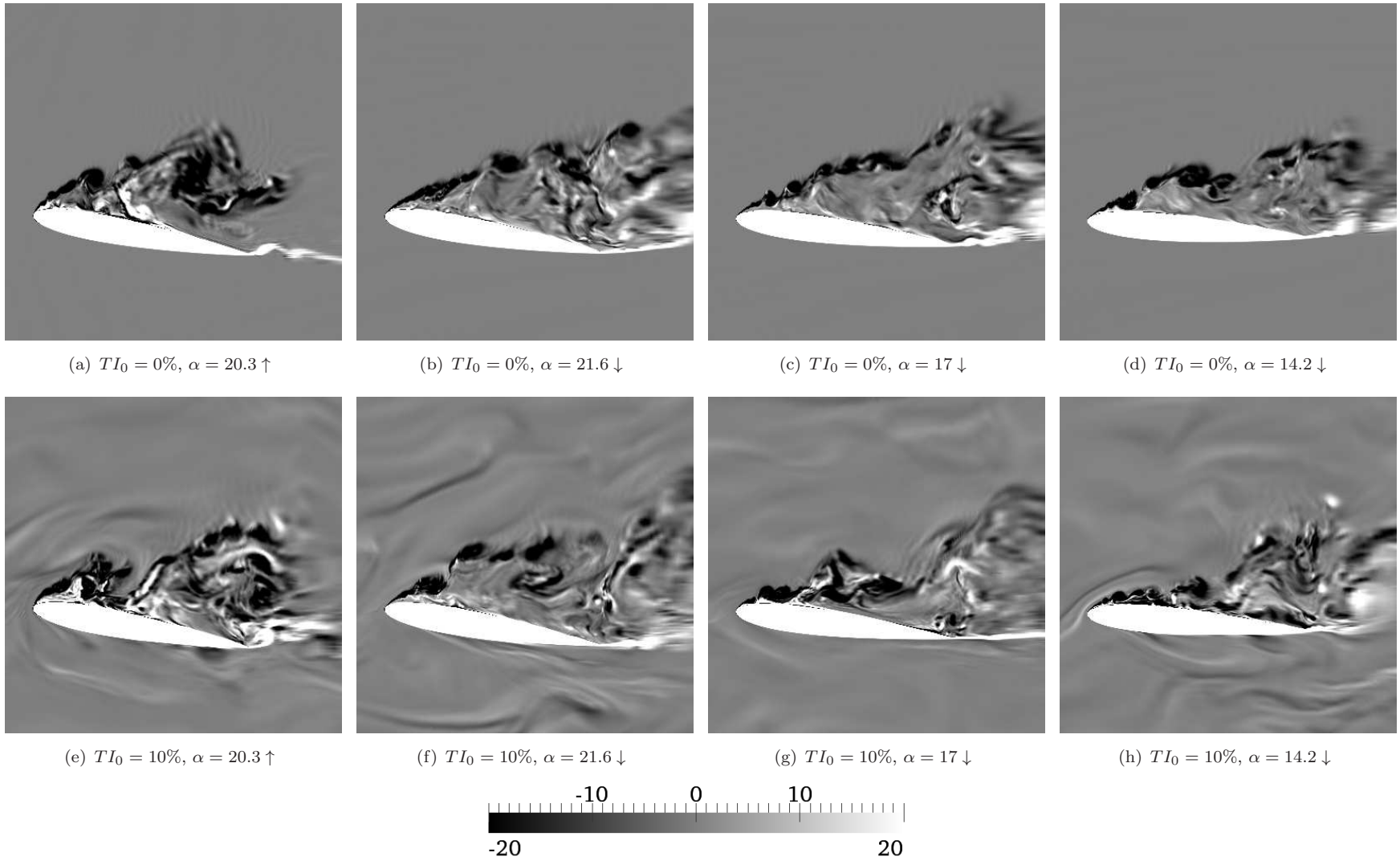

(a) $TI_0 = 0\%$, $\alpha = 20.3 \uparrow$ (b) $TI_0 = 0\%$, $\alpha = 21.6 \downarrow$ (c) $TI_0 = 0\%$, $\alpha = 17 \downarrow$ (d) $TI_0 = 0\%$, $\alpha = 14.2 \downarrow$

(e) $TI_0 = 10\%$, $\alpha = 20.3 \uparrow$ (f) $TI_0 = 10\%$, $\alpha = 21.6 \downarrow$ (g) $TI_0 = 10\%$, $\alpha = 17 \downarrow$ (h) $TI_0 = 10\%$, $\alpha = 14.2 \downarrow$

FIGURE 6.24: The instantaneous z-vorticity at the mid-span for $TI_0 = 0\%$ (top-row) and $TI_0 = 10\%$ (bottom-row). Vorticity fields are normalized by U_∞ and c.

The most evident impact of freestream turbulence occurs on the lift coefficient during the downstroke. The lift increases for the turbulent inflow case compared with that for the laminar inflow case. The average increment is $\Delta C_L \approx 0.2$ during the downstroke. Similar results were reported by Amandolèse and Széchényi (2004) [1]. They measured the upstream turbulence effects on the flow over a pitching airfoil (see Fig. 1.7 [1]). In their work, the maximum lift angles showed little change while the lift increments were observed during the downstroke as the turbulence intensity increased. For the current study, the lift increment from case $TI_0 = 5\%$ to 10% is noticeable for $18^\circ \downarrow < \alpha < 16^\circ \downarrow$ but the difference during the rest of the downstroke is within the uncertainties of the coefficient. This can be due to several reasons. First, the difference of the effective turbulence intensities at the leading edge, $TI = 4.5\%$ and 6.3%, is small between two cases so that their effects on the lift hysteresis are not significant (see Table 6.6). The ratio of the turbulence intensities between $TI_0 = 10\%$ and 5% should be, ideally, two in the downstream region, but $\frac{6.3\%}{4.5\%} = 1.4$ at $x/I_{11} = 23.3$. This discrepancy is due to the symmetry boundary condition in the spanwise direction. If only the streamwise fluctuation, $\langle u'u' \rangle$, in which the effect of the boundary condition in the spanwise direction is minimal, is considered, $\langle u'u' \rangle$ at the leading edge for $TI_0 = 10\%$ is nearly doubled compared to that for $TI_0 = 5\%$. Note that the periodic boundary condition in the spanwise direction could not be used due to the dynamic mesh. The mesh convergence tests were conducted with the symmetric boundary condition and adopting $1c$ domain width showed no noticeable difference in the load hysteresis compared with $0.5c$. Second, the stall mechanism is different between the two airfoils. The NACA 0012 airfoil for the current study is the leading edge separation type while a NACA 64_4-421 airfoil which is the trailing edge type was used in Amandolèse and Széchényi (2004) [1]. The geometry effect may be stronger than the turbulence effect for the NACA 0012 airfoil.

Fig. 6.24 shows some typical snapshots of the instantaneous spanwise component of vorticity on the pitching airfoil with laminar and turbulent inflows. The flows are fully detached and Kelvin-Helmholtz shedding is observed along with the shear layer from the leading edge for the laminar inflow case. For the turbulent inflow, upstream turbulence of which length scales are comparable with the chord length (e.g. Fig. 6.24(f)) interacts with the separated flow and makes the flow more chaotic compared with that for the laminar inflow case. The separated flows are suppressed by freestream turbulence though the impact varies with incidence. These interactions lead to a decrease of the separated region and an increase of the lift during the downstroke. Especially the influence of freestream turbulence is evident at $\alpha = 14.2^\circ \downarrow$ near the leading edge as shown in Fig. 6.24(h).

6.6 Summary

The dynamic stall events on a pitching airfoil have been investigated. The lift, drag and moment hysteresis show good agreement with the experimental data [85] at three different reduced frequency, $k_{\mathrm{red}} = 0.025$, 0.05 and 0.1. The laminar separation bubble diminishing and boundary layer suppression on the pitching airfoil are illustrated through the surface forces and flow contours. The leading edge vortex is quantified in terms of its convective speed and shedding frequency and compared with those in literature. The capability of LES is demonstrated for highly separated flows at deep stall.

The effect of freestream turbulence on the flow over a pitching airfoil is examined based on the baseline case which is simulated for the laminar inflow. The empty box simulations have been conducted to quantify upstream turbulence. Some deviations in the turbulence characteristics are observed compared with those in literature due to the SGS modelling, numerical scheme, filtering method and resolution. However, the focus here is to provide reasonable turbulence characteristics in the upstream region of the leading edge, which are turbulence intensities and integral length scales.

The lift, drag and moment coefficients for the pitching airfoil flow show the effect of upstream turbulence. The magnitudes for maximum drag and minimum moment decrease with the turbulent inflows which are mainly attributed to the suppression of separated flows by freestream turbulence. The most evident impact of freestream turbulence occurs on the lift coefficient, i.e. the lift increasing by $\Delta C_L \approx 0.2$ with freestream turbulence during the downstroke. A similar trend is found from experimental works [1]. The snapshots of the vorticity fields at different incidence also confirms that freestream turbulence has an impact on the flow around the pitching airfoil. The separated flows during the downstroke are disturbed and suppressed by freestream turbulence resulting in the lift increase.

This is the first attempt for applying an LES calculation on the flow over a pitching airfoil with the moderate Reynolds number, $Re = 135,000$, to the author's knowledge. The required massive computational resources make these tasks even more difficult. About 700 CPU hours were required to simulate a few cycles of pitching motion using 96 processors.

Chapter 7

Rotational augmentation

7.1 Introduction

The boundary layer on a wind turbine blade is different from that on a static airfoil. It is essentially a three-dimensional flow due to the rotation. The fluid particle near the rotating blade is pushed away from the rotating axis such that a spanwise flow occurs towards to the blade tip when it is seen from a rotating frame of reference. This is due to the centrifugal force. The difference between the boundary layers on the rotating blade and the stationary blade is conjectured to be the main reason for the deviations between the predicted and measured aerodynamic loads for wind turbines [149]. On a rotating blade, stall occurs at a higher angle of attack than on a static airfoil [44]. This phenomenon is referred to as rotational augmentation. Wind turbine design tools which use a static airfoil data tend to underestimate the power output at a given velocity, due to rotational augmentation.

There are two main explanations of the mechanisms for rotational augmentation; (a) mass depletion: the centrifugal force pushes the air in the radial direction and the mass depletion due to the radial flow reduces the boundary layer thickness resulting in a lower pressure on the suction side. (b) Coriolis effect: the radial flow to the blade tip provides Coriolis acceleration toward the trailing edge. This acceleration acts as favourable pressure gradient and thus suppresses the separation and increases the lift. In order to identify the Coriolis effect on rotational augmentation, the mass depletion is not considered [39] and a NACA 0012 airfoil is used. This airfoil is a leading edge separation type and the transition point is very close to the leading edge. Thus it is expected that the effect of the early transition by the radial-flow instability (see Sec. 1.2.4) would be minor for this airfoil. Therefore the aim of this study is to exclusively identify whether the Coriolis force is one mechanism of rotational augmentation.

In this chapter, the idealized model derived by Gross et al. (2012) [39] which is presented in Sec. 7.2, is adopted to investigate the rotational effect on an airfoil under

pre- and post- stall regimes. Then, Gross et al.'s model [39] is applied to a rotating laminar boundary layer and the results are compared with the analytical solution derived by Fogarty [33]. In Sec. 7.3, the flow over a static NACA 0012 airfoil is simulated as a baseline simulation at $Re_c = U_{\text{eff}} c/\nu = 135,000$ where U_{eff} is the effective velocity (see Fig. 7.1). The validated model in Sec. 7.2 is applied to the sectional rotating blade in a rotating reference frame at two angles of attack ($\alpha = 10°$, $14°$) and two radius-chord ratios ($\frac{r}{c} = 2.5$, 10). This is presented in Sec. 7.4 and the summary follows in Sec. 7.5. Part of this work was presented in a conference paper by Kim, Castro, Xie. *DLES9, Dresden, Germany*, 2013 [70].

7.2 Methodology

As the baseline simulations, the flow over a static airfoil under pre- ($\alpha = 10°$) and post- ($\alpha = 14°$) stall regimes were simulated and they were validated with experimental data [85, 128]. The same methodology as the static airfoil case in Sec. 6.3.1 was adopted for the baseline simulations, unless otherwise mentioned. The Reynolds number was defined as $Re_c = \frac{U_{\text{eff}} c}{\nu}$ where U_{eff} was the effective velocity which was determined by the rotational and freestream velocities as shown in Fig. 7.1. A new variable, Rotation number, was introduced and defined as,

$$Ro = \frac{\Omega c}{U_\infty}, \tag{7.1}$$

where Ω was the angular velocity. OpenFOAM-2.1.0 was used for the flow solver.

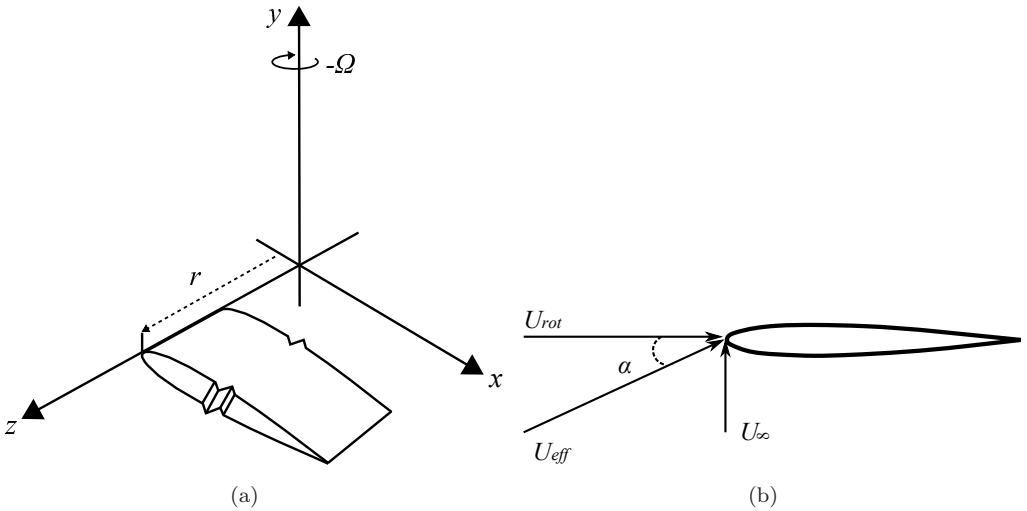

FIGURE 7.1: (a) The coordinate system for the rotating blade and (b) definition of the effective velocity, U_{eff}, where α is angle of attack, $U_{\text{rot}} = \Omega r$ and U_∞ is the freestream velocity. Note that the angular velocity vector, $\mathbf{\Omega} = [0, -\Omega, 0]^T$.

7.2.1 The model for the rotational effect

The general governing equations for the mass and momentum conservations of incompressible flow in an arbitrary non-inertial frame of reference are [162],

$$\boldsymbol{\nabla} \cdot \boldsymbol{u} = 0, \tag{7.2}$$

$$\frac{\partial \boldsymbol{u}}{\partial t} + \boldsymbol{u} \cdot \boldsymbol{\nabla} \boldsymbol{u} = -\frac{1}{\rho}\boldsymbol{\nabla} p + \nu \boldsymbol{\nabla}^2 \boldsymbol{u} - \dot{\boldsymbol{U}}_{\boldsymbol{0}} - \dot{\boldsymbol{\Omega}} \times \boldsymbol{r} - \boldsymbol{\Omega} \times (\boldsymbol{\Omega} \times \boldsymbol{r}) - 2(\boldsymbol{\Omega} \times \boldsymbol{u}), \tag{7.3}$$

where $\boldsymbol{u}$ and $\boldsymbol{r}$ are the relative velocity and position vectors respectively, with respect to the arbitrary non-inertial reference frame. $\boldsymbol{\Omega}$ and $\boldsymbol{U_0}$ are the angular velocity and translational velocity of the origin of the non-inertial reference frame relative to an inertial frame. Note that it is a common momentum conservation equation up to the second term on the right-hand side of Eq. 7.3 and the rest of the terms are due to the non-inertial frame of reference.

For the current study, the rotating axis is fixed in time and the angular velocity is constant. Thus the third and fourth terms on the right-hand side of Eq. 7.3 vanish. Gross et al. [39] developed a model for the rotational effects on a sectional blade and this model was applied for the current study. They derived the model equations by using an order-of-magnitude analysis on the Navier-Stokes equations in the cylindrical coordinate system. In the order-of-magnitude analysis, the boundary layer thickness and the velocities are scaled with

$$\delta \sim \sqrt{\frac{\nu c}{\Omega r}}, \tag{7.4}$$

$$u_\theta, u_y, u_r \sim \Omega r, \tag{7.5}$$

where Ω is the magnitude of the angular velocity. Then the stress tensor τ_{ij} is scaled with $\rho\nu\frac{\Omega r}{\delta}$, pressure with $\rho(\Omega r)^2$ and the differentials are scaled with $(r\partial\theta, \partial y, \partial r, \partial t) \sim (\delta, \delta, \delta, \delta/(\Omega r))$.

Considering $\dot{\boldsymbol{\Omega}} = 0$, $\dot{\boldsymbol{U}}_{\boldsymbol{0}} = 0$, the additional term in the right-hand side of Eq. 7.3 is reduced to $\boldsymbol{f}_r = -\boldsymbol{\Omega} \times (\boldsymbol{\Omega} \times \boldsymbol{r}) - 2(\boldsymbol{\Omega} \times \boldsymbol{u})$. The order-of-magnitudes for the governing equations in Eqs. 7.2 - 7.3 are obtained in a cylindrical coordinate system with the scaling properties, see Eqs. 7.6 - 7.9.

$$\underbrace{\underbrace{\frac{\partial u_\theta}{r\partial\theta}}_{\sim\frac{\Omega r}{\delta}} + \underbrace{\frac{\partial u_y}{\partial y}}_{\sim\frac{\Omega r}{\delta}} + \underbrace{\frac{\partial u_r}{\partial r}}_{\sim\frac{\Omega r}{\delta}}}_{(\Omega r)^{1.5}(\nu c)^{-0.5}} = -\underbrace{\frac{u_r}{r}}_{\sim\Omega}, \tag{7.6}$$

$$\underbrace{\underbrace{\frac{\partial u_\theta}{\partial t}}_{\sim\frac{(\Omega r)^2}{\delta}} + \underbrace{(\boldsymbol{u}\cdot\boldsymbol{\nabla})u_\theta}_{\sim\frac{(\Omega r)^2}{\delta}} = -\underbrace{\frac{1}{\rho}\frac{\partial p}{r\partial\theta}}_{\sim\frac{(\Omega r)^2}{\delta}} + \underbrace{\boldsymbol{\nabla}\cdot\nu\boldsymbol{\nabla}u_\theta}_{\sim\nu\frac{\Omega r}{\delta^2}} - \underbrace{\nu\frac{u_\theta}{r^2}}_{\sim\nu\frac{\Omega}{r}} + \underbrace{\nu\frac{2}{r^2}\frac{\partial u_r}{\partial\theta}}_{\sim\nu\frac{\Omega}{\delta}} - \underbrace{\frac{u_r u_\theta}{r}}_{\sim\Omega^2 r} + \underbrace{f_{r,1}}_{\sim\Omega^2 r},}_{(\Omega r)^{2.5}(\nu c)^{-0.5}} \quad \underbrace{}_{(\Omega r)^{2.5}(\nu c)^{-0.5}} \quad \underbrace{}_{\frac{\Omega^2 r^2}{c}} \quad \underbrace{}_{\Omega^{1.5}(r\nu)^{0.5}c^{-0.5}} \tag{7.7}$$

$$\underbrace{\underbrace{\frac{\partial u_y}{\partial t}}_{\sim\frac{(\Omega r)^2}{\delta}} + \underbrace{(\boldsymbol{u}\cdot\boldsymbol{\nabla})u_y}_{\sim\frac{(\Omega r)^2}{\delta}} = -\underbrace{\frac{1}{\rho}\frac{\partial p}{\partial y}}_{\sim\frac{(\Omega r)^2}{\delta}} + \underbrace{\boldsymbol{\nabla}\cdot\nu\boldsymbol{\nabla}u_y}_{\sim\nu\frac{\Omega r}{\delta^2}} - \underbrace{f_{r,2}}_{\sim\Omega^2 r},}_{(\Omega r)^{2.5}(\nu c)^{-0.5}} \quad \underbrace{}_{(\Omega r)^{2.5}(\nu c)^{-0.5}} \quad \underbrace{}_{\frac{\Omega^2 r^2}{c}} \tag{7.8}$$

$$\underbrace{\underbrace{\frac{\partial u_r}{\partial t}}_{\sim\frac{(\Omega r)^2}{\delta}} + \underbrace{(\boldsymbol{u}\cdot\boldsymbol{\nabla})u_r}_{\sim\frac{(\Omega r)^2}{\delta}} = -\underbrace{\frac{1}{\rho}\frac{\partial p}{\partial r}}_{\sim\frac{(\Omega r)^2}{\delta}} + \underbrace{\boldsymbol{\nabla}\cdot\nu\boldsymbol{\nabla}u_r}_{\sim\nu\frac{\Omega r}{\delta^2}} - \underbrace{\nu\frac{u_r}{r^2}}_{\sim\nu\frac{\Omega}{r}} - \underbrace{\nu\frac{2}{r^2}\frac{\partial u_\theta}{\partial\theta}}_{\sim\nu\frac{\Omega}{\delta}} + \underbrace{\frac{{u_\theta}^2}{r}}_{\sim\Omega^2 r} + \underbrace{f_{r,3}}_{\sim\Omega^2 r},}_{(\Omega r)^{2.5}(\nu c)^{-0.5}} \quad \underbrace{}_{(\Omega r)^{2.5}(\nu c)^{-0.5}} \quad \underbrace{}_{\frac{\Omega^2 r^2}{c}} \quad \underbrace{}_{\Omega^{1.5}(r\nu)^{0.5}c^{-0.5}} \tag{7.9}$$

where the convective derivative is

$$\boldsymbol{u}\cdot\boldsymbol{\nabla} = \frac{1}{r}u_\theta\frac{\partial}{\partial\theta} + u_y\frac{\partial}{\partial y} + u_r\frac{\partial}{\partial r}, \tag{7.10}$$

and the Laplacian operator is

$$\boldsymbol{\nabla}\cdot\boldsymbol{\nabla}(=\boldsymbol{\nabla}^2) = \frac{1}{r^2}\frac{\partial^2}{\partial\theta^2} + \frac{\partial^2}{\partial y^2} + \frac{1}{r}\frac{\partial}{\partial r}\left(r\frac{\partial}{\partial r}\right). \tag{7.11}$$

The method intends to simulate the small sectional part of an infinitely long blade at the radius, r, from the rotating axis as shown in Fig. 7.1(a). Assuming that the radius, r, is large compared to the chord length, the high order terms of r are retained, i.e. $r^{1.5}$ in the continuity and $r^{2.5}$, r^2, $r^{1.5}$, r in the momentum equations. Therefore the highlighted terms with the red colour are neglected, i.e. r^0 in Eq. 7.6 and r^{-1}, $r^{0.5}$ in Eqs. 7.7 - 7.9. When the radius is sufficiently larger than the domain width, it is assumed that the radial variation is small and periodic boundary conditions in the spanwise direction are used. Under these assumptions, the governing equations can be written in Cartesian coordinates by using $x, y, z = r\theta, y, r$ and $u, v, w = u_\theta, u_y, u_r$. As shown in Fig. 7.1(a), the blade rotates around the y-axis, $\boldsymbol{\Omega} = [0, -\Omega, 0]^T$ and the radius vector is aligned with the z-axis, $\boldsymbol{r} = [0, 0, r]^T$, in the rotating frame of reference. In such situations, the source term f_r' on the right-hand-side of the Cartesian coordinates system is,

$$
\begin{aligned}
f_r' &= -\boldsymbol{\Omega} \times (\boldsymbol{\Omega} \times \boldsymbol{r}) - 2(\boldsymbol{\Omega} \times \boldsymbol{u}) + \begin{bmatrix} -\frac{wu}{z} \\ 0 \\ \frac{uu}{z} \end{bmatrix} \\
&= \begin{bmatrix} 0 \\ 0 \\ z\Omega^2 \end{bmatrix} + \begin{bmatrix} 2w\Omega \\ 0 \\ -2u\Omega \end{bmatrix} + \begin{bmatrix} -\frac{wu}{z} \\ 0 \\ \frac{uu}{z} \end{bmatrix} \\
&= \begin{bmatrix} 2w\Omega - \frac{wu}{z} \\ 0 \\ z\Omega^2 - 2u\Omega + \frac{uu}{z} \end{bmatrix}.
\end{aligned}
\tag{7.12}
$$

This source term is essentially the same as case "C" in Gross et al. (2012) [39] which was derived under the same assumptions as Eq. 7.12. Note that this source term in the Cartesian coordinates vanishes far away from the airfoil because $w = 0$ and $u = z\Omega$, i.e. the potential flow is recovered.

The SGS model is not shown explicitly in Eqs. 7.6 - 7.12. The mixed-time scale model (MTS) [54] was used for the current study which was based on the eddy viscosity model. This model is a function of the rate of strain tensor and estimated SGS kinetic energy (see Sec. 2.2.3) which are frame-indifferent. Also, the angular velocity Ω is constant for the current study thus the MTS model is frame-indifferent at the given conditions. The model, therefore, satisfies the basic constraints for an SGS model in a non-inertial reference frame suggested by Speziale (1989) [162]. From a practical point of view, the rotational effect on the SGS model would be very small as LES requires a very fine mesh. Thus the SGS model is not shown explicitly in Eqs. 7.6 - 7.9 but it is taken into account in the actual calculations.

7.2.2 Validations for the rotational effect model

It is straightforward to implement Gross et al.'s [39] model; adding a source term (Eq. 7.12) on the right-hand-side of the momentum equations of the source code OpenFOAM in the Cartesian coordinate. Gross et al. qualitatively compared their model with a full blade simulation at low Reynolds number. In this section, this model is quantitatively validated with an analytical solution developed by Fogarty (1951) [33]. The source term in Eq. 7.12 was applied for a rotating laminar boundary layer. It was assumed that the radial changes are small within the domain, thus the periodic boundary condition was applied in the radial direction as shown in Fig. 7.2. An infinitely thin wall of length X_0 was placed in the middle of the computational domain and its leading edge was located at the origin, as shown in Fig. 7.2(b). The domain width in the spanwise direction was $0.025X_0$ and the number of grid points in this direction was 4. A uniform velocity

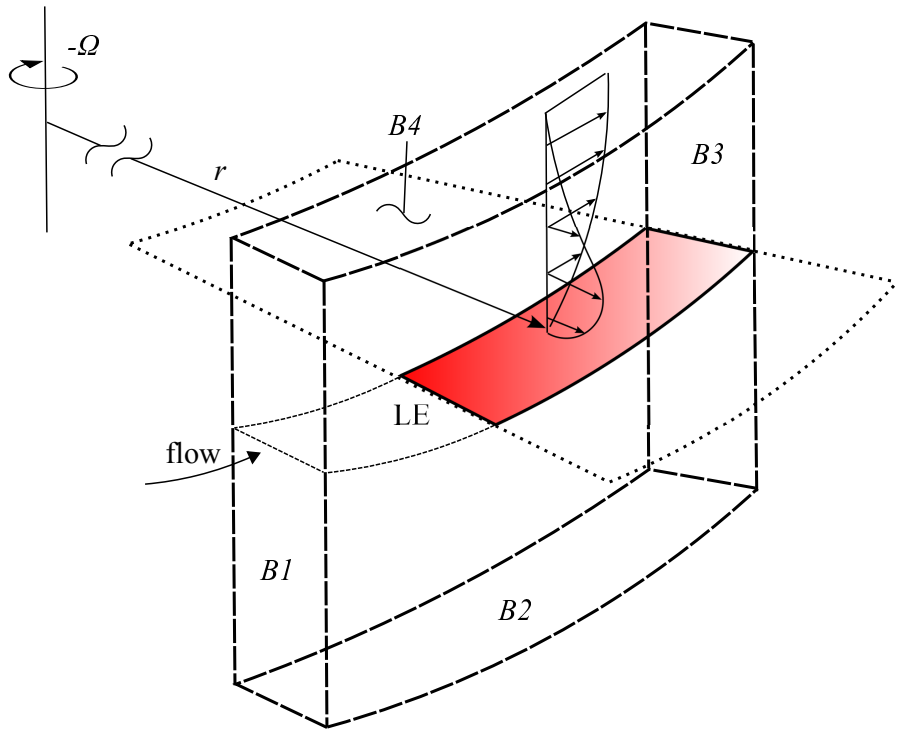

(a)

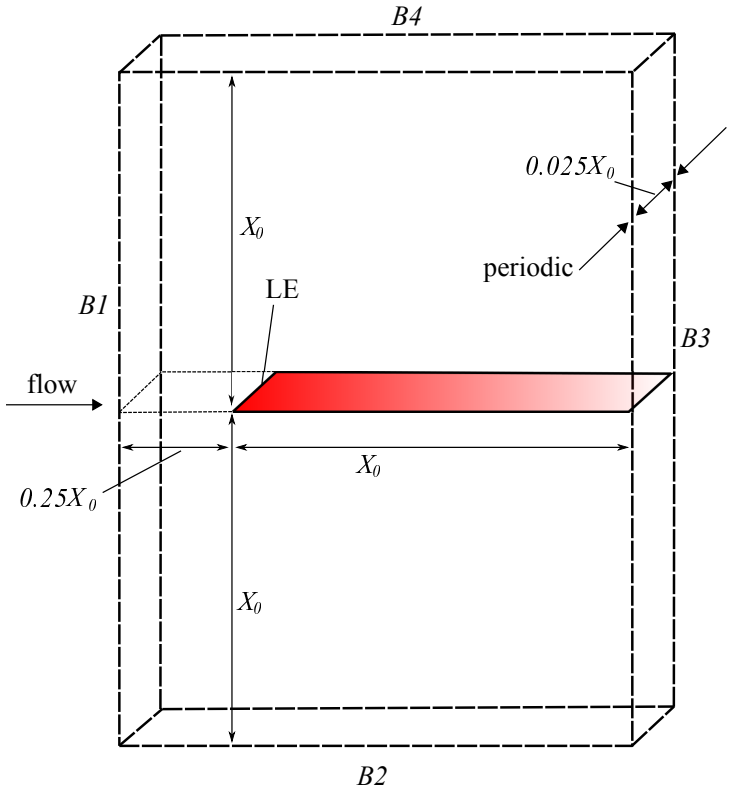

(b)

FIGURE 7.2: A sketch of (a) a boundary layer on a rotating plate and a domain (thick dashed-line) in cylindrical coordinates and (b) the approximated domain in Cartesian coordinates to apply the model for rotation, Eq. 7.12. Note that the shaded area represents an infinitely thin plate and the leading edge (LE) is placed at the origin.

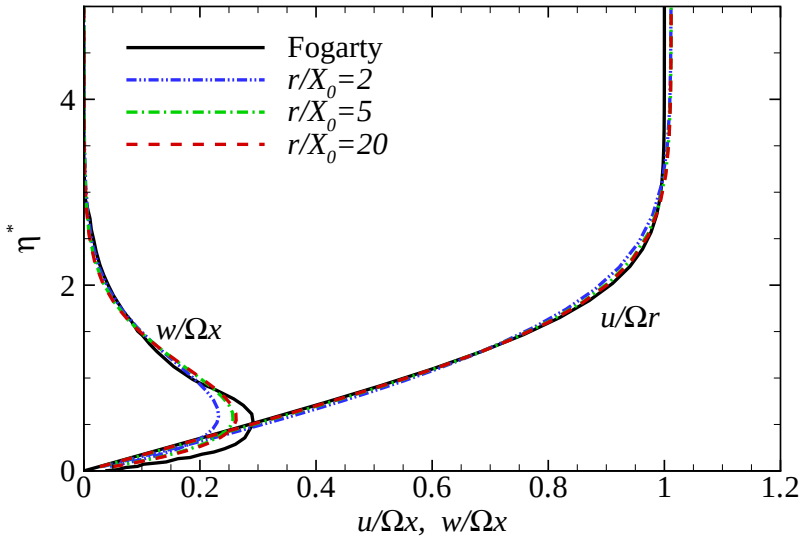

FIGURE 7.3: The velocity profiles for the flow on the rotating laminar boundary layer. Computed data were collected at $x = 0.875X_0$. The reference data (solid line) is taken from Fogarty [33]. Note that positive w means radial flow away from the rotating axis.

U_∞ was imposed at the inlet boundary ($B1$) and $Re_X = \frac{U_\infty X_0}{\nu} = 40,000$. The inlet boundary condition was set to a fixed velocity and zero pressure gradient. The outlet boundary conditions ($B2$, $B2$, $B3$) were set to zero velocity gradients and a constant value of pressure. A uniform mesh was used in the steamwise direction on the plate and the grid size in this direction was $\Delta x = 0.005X_0$. The first wall-off grid point was placed at $y_1 = 2.5 \times 10^{-4}X_0$. 60 grid points were placed in the cross-flow direction on each side of the wall and they were gradually stretched out to the boundaries. A second order scheme was used for both temporal and convective terms and the time step was $0.0025t\frac{U_\infty}{X_0}$.

To verify the 'large r' assumption for the current model, three different $\frac{r}{X_0}$ values were tested which were 2, 5 and 20. The streamwise and spanwise velocity profiles are shown in Fig. 7.3. η^* is the wall normal distance normalized by the displacement thickness, $\delta^* = \int_0^\infty \left(1 - \frac{u(y)}{U_\infty}\right) dy$ at the measured point. The angular velocity, Ω, for each case was determined by the relation, $\Omega = \frac{U_\infty}{r}$, and x was the distance from the leading edge. The streamwise velocity profile from Fogarty [33] was essentially the Blasius boundary layer profile. All velocity profiles were collected at $x = 0.875X_0$ and the profiles taken from other positions also agreed with each other when they were normalized with appropriate properties. The magnitude for the calculated freestream velocities in Fig. 7.3 is over-predicted by 1% but it asymptotes to unity as η^* increases. Cases for the doubled domain size and number of grid points in the y-direction were also simulated but no noticeable difference was found.

The radial velocity profiles, w, for $\frac{r}{X_0} = 5, 20$ are in agreement with each other and they underestimate by about 10% the maximum w compared with the reference profile.

However the shape of the profiles are similar with the reference's. It is hard to expect a perfect match for the radial velocity profiles between Fogarty [33] and Gross et al.'s [39] methods since Fogarty [33] is based on simpler assumptions. For $\frac{r}{X_0} = 2$, the radial velocity profile is slightly under-predicted (approximately 10%) compared with those for $\frac{r}{X_0} = 5, 10$. This may be because the 'large r' assumption starts to be less appropriate at some point for $\frac{r}{X_0} < 5$. But the general shape and peak radial velocity point for $\frac{r}{X_0} = 2$ still show reasonable agreement with the profiles for $\frac{r}{X_0} = 5, 20$. The corresponding parameters of $\frac{r}{X_0}$ is $\frac{r}{c}$ for the airfoil case and it ranges from $\frac{r}{c} = 2.5$ to 10 for the current study. Thus the source term, Eq. 7.12, is applied to the airfoil flow cases in the following section.

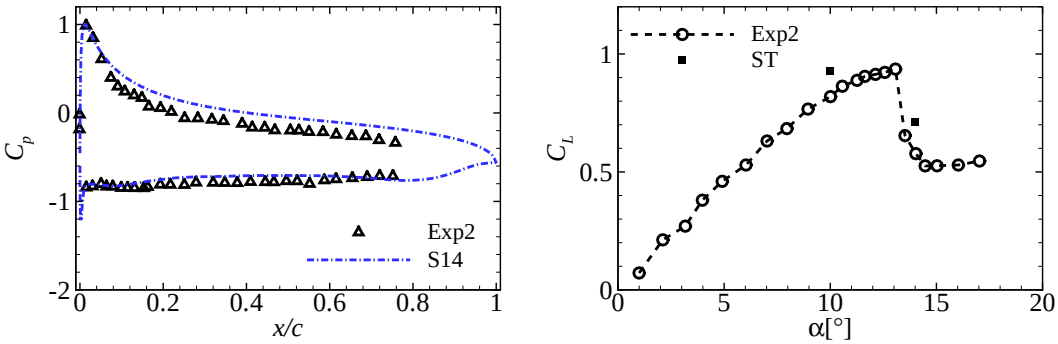

FIGURE 7.4: The pressure coefficients on the 3-D static airfoil at $\alpha = 14°$ (left) and lift coefficients (right). Data for Exp2 is taken from Lee and Gerontakos (2004) [85].

7.3 Mesh convergence tests and validations

The baseline simulation for the pre-stall regime ($\alpha = 10°$) was examined and validated in Sec. 6.3.1. This case is called case S10 hereafter. With the same configurations for case S10, the post-stall regime case of a stationary airfoil was simulated at an incidence angle 14°, which is called case S14.

Fig. 7.4 shows the pressure coefficient for case S14 and lift coefficients for cases S10 and S14. The pressure coefficient on the upper airfoil surface for case S14 is flat indicating that the flow is fully separated. Lift coefficients for cases S10 and S14 are plotted and compared with the experimental data [85]. The lift coefficients are slightly over-predicted for both angles of attack but the stall point lies between the two angles as in the experiment. The trend and magnitude of the pressure coefficients for the calculations agree very well with the experimental data, thus these two stationary cases are considered as the baseline simulations.

7.4 The effect of the rotation

Based on the simulations of stationary cases, the rotational effect was applied by using the source term in Eq. 7.12. The rotational effect was characterized by the Rotation number as in Eq. 7.1. Reynolds number, angle of attack and radius were set an input variables, and the other variables were determined as,

$$\begin{aligned} U_{\text{eff}} &= Re_c \frac{\nu}{c}, \\ U_{\text{rot}} &= U_{\text{eff}} \cos\alpha, \\ \Omega &= \frac{U_{\text{rot}}}{r}, \\ U_{\infty} &= U_{\text{eff}} \sin\alpha, \\ Ro &= \frac{\Omega c}{U_{\infty}}. \end{aligned} \tag{7.13}$$

The variables are summarized in Table 7.1. The radius to chord ratios, $r/c = 2.5$, 10, represent the inner (i) and outer (o) regions of the blade respectively.

TABLE 7.1: Summary of the variables. For all cases, $Re_c = 135,000$.

Case	α	r/c	Ro
S10	10°	n/a	0
S14	14°	n/a	0
R10o	10°	10	0.567
R10i	10°	2.5	2.27
R14o	14°	10	0.401
R14i	14°	2.5	1.6

Fig. 7.5 shows the surface pressure and skin-friction for all cases. At $\alpha = 10°$, the boundary layer on the upper airfoil surface is mostly attached and there is little difference in the surface forces regardless of the radius-chord ratios. Some oscillations are observed in C_f for $0.1 < x/c < 0.3$ in Fig. 7.5(b). These may be due to a relatively short averaging period, i.e. $10\frac{c}{U_{\text{eff}}}$. These may due to At $\alpha = 14°$, the rotational effect is still weak at $r/c = 10$ but a significant negative pressure coefficient on the upper airfoil surface is found at $r/c = 2.5$ (R14i) which corresponds to an inner region of the blade. Further discussions on the negative pressure coefficient on the upper airfoil surface for case R14i will be followed later in this section.

Fig. 7.6 presents the velocity profiles to investigate the boundary layer developments on the upper airfoil surface. All velocity profiles are almost identical when the flow is attached ($\alpha = 10°$) regardless of r/c. The pressure and skin-friction coefficients in Fig. 7.5 confirms this. However, a different phenomenon is found when the boundary layer is

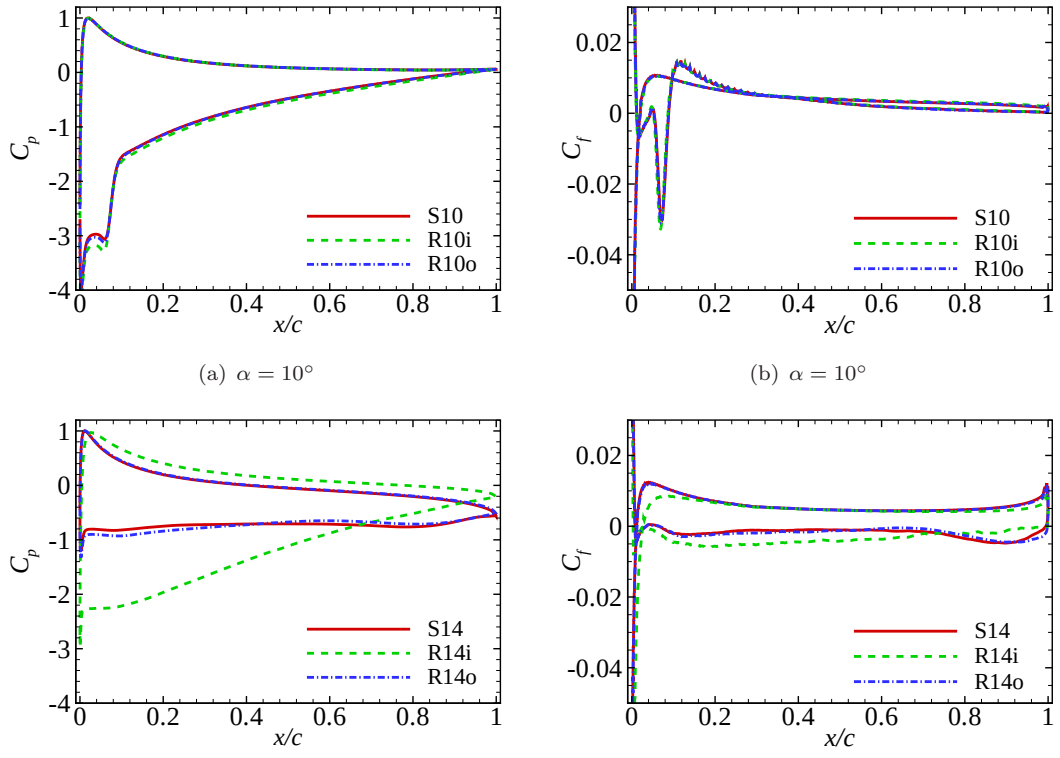

(a) $\alpha = 10°$ (b) $\alpha = 10°$

(c) $\alpha = 14°$ (d) $\alpha = 14°$

FIGURE 7.5: The effect of rotation on the surface pressure (left) and skin-friction coefficients (right).

separated ($\alpha = 14°$). The streamwise velocity profiles for cases S14 and R14o are nearly the same but there are noticeable spanwise velocities observed for case R14o. Note that the positive spanwise velocity represents the flow away from the rotating axis, see Fig. 7.1. The impact of this spanwise flow is hardly seen in the surface forces as shown in Figs. 7.5(c) and 7.5(d). For case R14i, the thickness of the boundary layer is mostly smaller than in cases S14 and R14o (see Fig. 7.6(c)). Also the peak spanwise velocity for case R14i is larger than the magnitude of the freestream velocity for $x/c < 0.5$.

Schreck and Robinson (2002) [138] conducted a full-scale horizontal axis wind turbine experiment and a similar tendency was reported. They compared the surface pressure distributions on the turbine blade when the turbine was parked (stationary) and rotating. A significant negative pressure along the chord was found on the suction side of the rotating blade while the pressure distribution was nearly flat for the stationary case especially near the hub, i.e. $R = 0.3$, see Fig. 7.7.

Fig. 7.8 shows snapshots of spanwise velocity fields. At $\alpha = 10°$ (left column), the boundary layer is very thin which corresponds with Fig. 7.6(a) and little of the rotational effect is observed. In contrast, the spanwise velocity increases as Rotation number increases at $\alpha = 14°$ (right column). The boundary layer becomes thinner case R14i than that for case S14 due to the rotation effect.

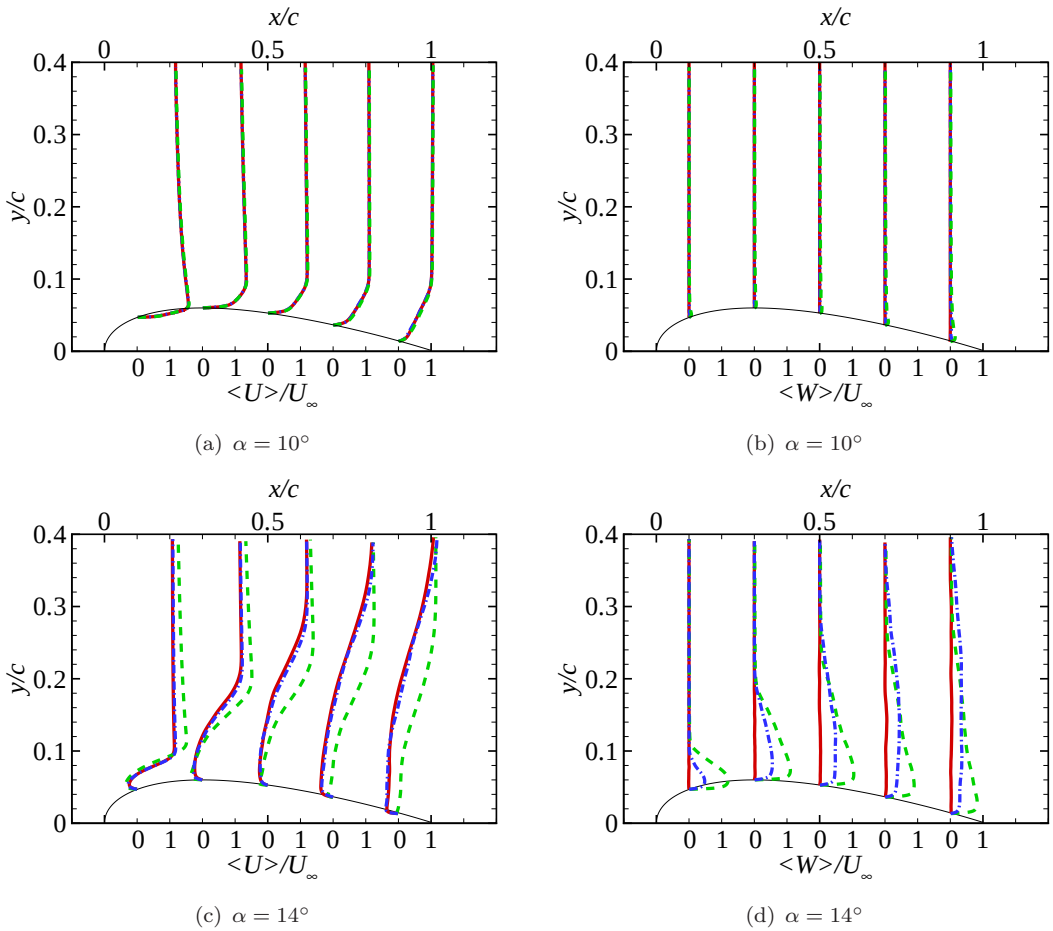

(a) $\alpha = 10°$ (b) $\alpha = 10°$

(c) $\alpha = 14°$ (d) $\alpha = 14°$

FIGURE 7.6: The effect of rotation on the profiles for the streamwise (left) and spanwise (right) velocity components. Legend is the same as in Fig. 7.5.

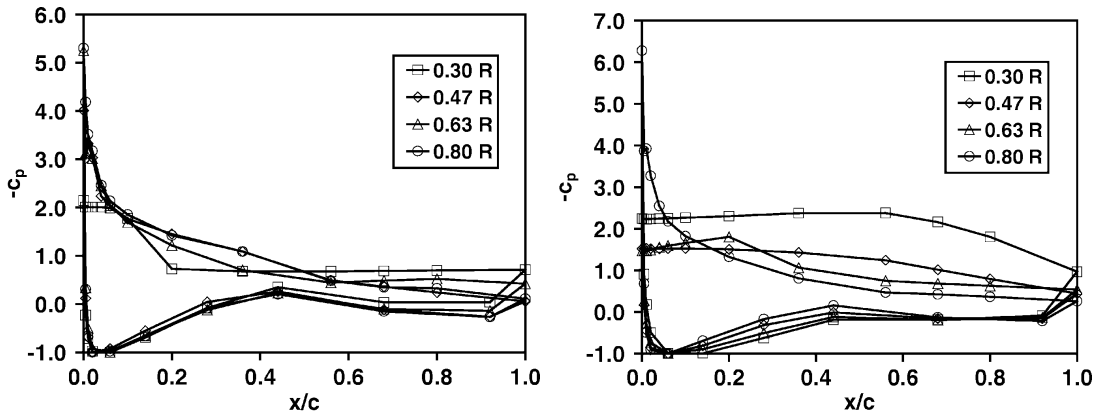

(a) (b)

FIGURE 7.7: The surface pressure distributions on the (a) stationary and (b) rotating blades from a horizontal axis wind turbine blade at zero yaw by Schreck and Robinson (2002) [138]. R is the distance from the hub normalized by the rotor radius.

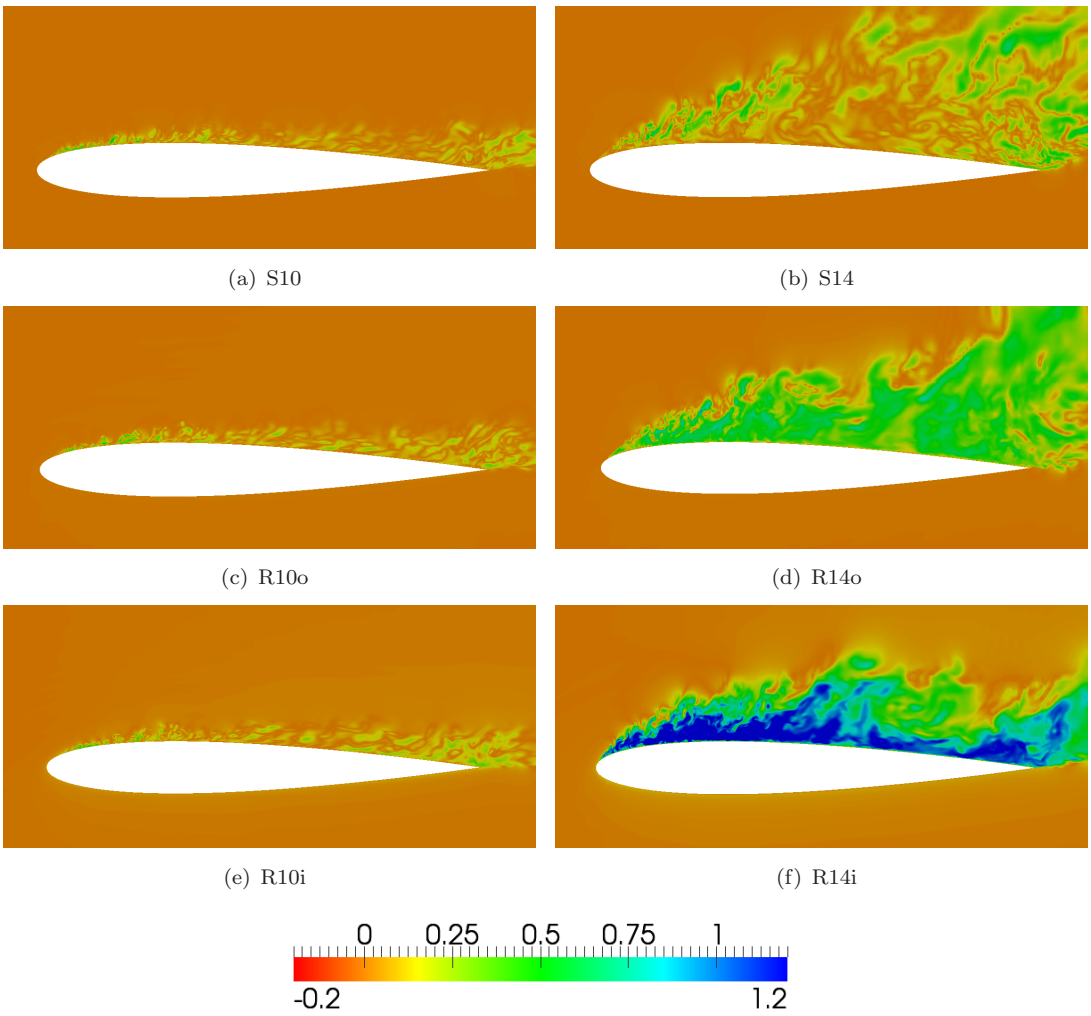

(a) S10 (b) S14

(c) R10o (d) R14o

(e) R10i (f) R14i

FIGURE 7.8: Instantaneous spanwise velocity components normalized by U_{eff}. Positive values represent the outward direction from the rotating axis.

Similar trends can be found in the spanwise and streamwise vortices in Figs. 7.9 and 7.10 respectively. The Kelvin-Helmholtz instability is clearly found near the leading edge for all cases. The effect of the rotation is small in the pre-stall regime (left column) and becomes apparent in the post-stall regime (right column). At $\alpha = 14°$, the point of the transition onset seems to approach the leading edge, albeit small, and the angle between the airfoil surface and shear layer decreases as the Rotation number increases, see Fig. 7.9. The streamwise vorticity is also of interest because the spanwise velocity presents a boundary layer (shear flow) in this direction as shown in Fig. 7.8. Again, a weak dependency of the rotation is found when the flow is attached, while the streamwise vortex near the leading edge, see Figs. 7.10(d) and 7.10(f), become apparent as Rotation number increases when the flow is detached, i.e. $\alpha = 14°$. Especially strong streamwise vortices are formed from the leading edge for case R14i as shown in Fig. 7.10(f).

An idealized test case is adopted for this study that allows a periodic boundary condition in the spanwise direction, i.e. the spanwise flow is well developed and statistically

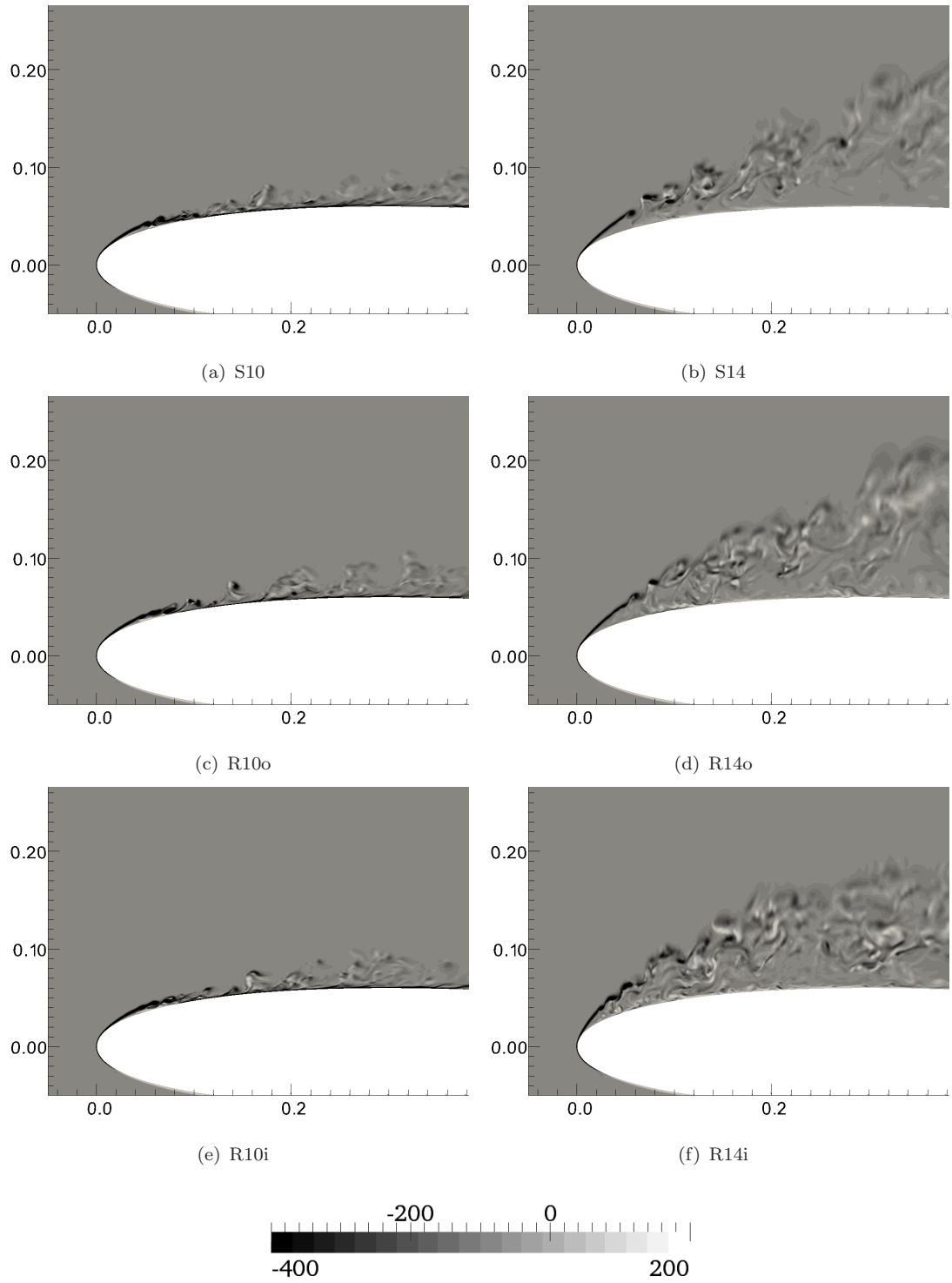

(a) S10 (b) S14

(c) R10o (d) R14o

(e) R10i (f) R14i

FIGURE 7.9: Instantaneous spanwise vorticity fields near the leading edge. The contours and coordinates are normalized by U_{eff} and c.

steady. In this configuration, the reduction of boundary layer thickness by the mass depletion due to the centrifugal pumping is excluded, which was explained as one of the primary mechanisms of rotational augmentation [46]. Without this mass depletion on the boundary layer, Gross et al. [39] still observed the boundary layer suppression and rotational augmentation from their calculations. They concluded that the spanwise

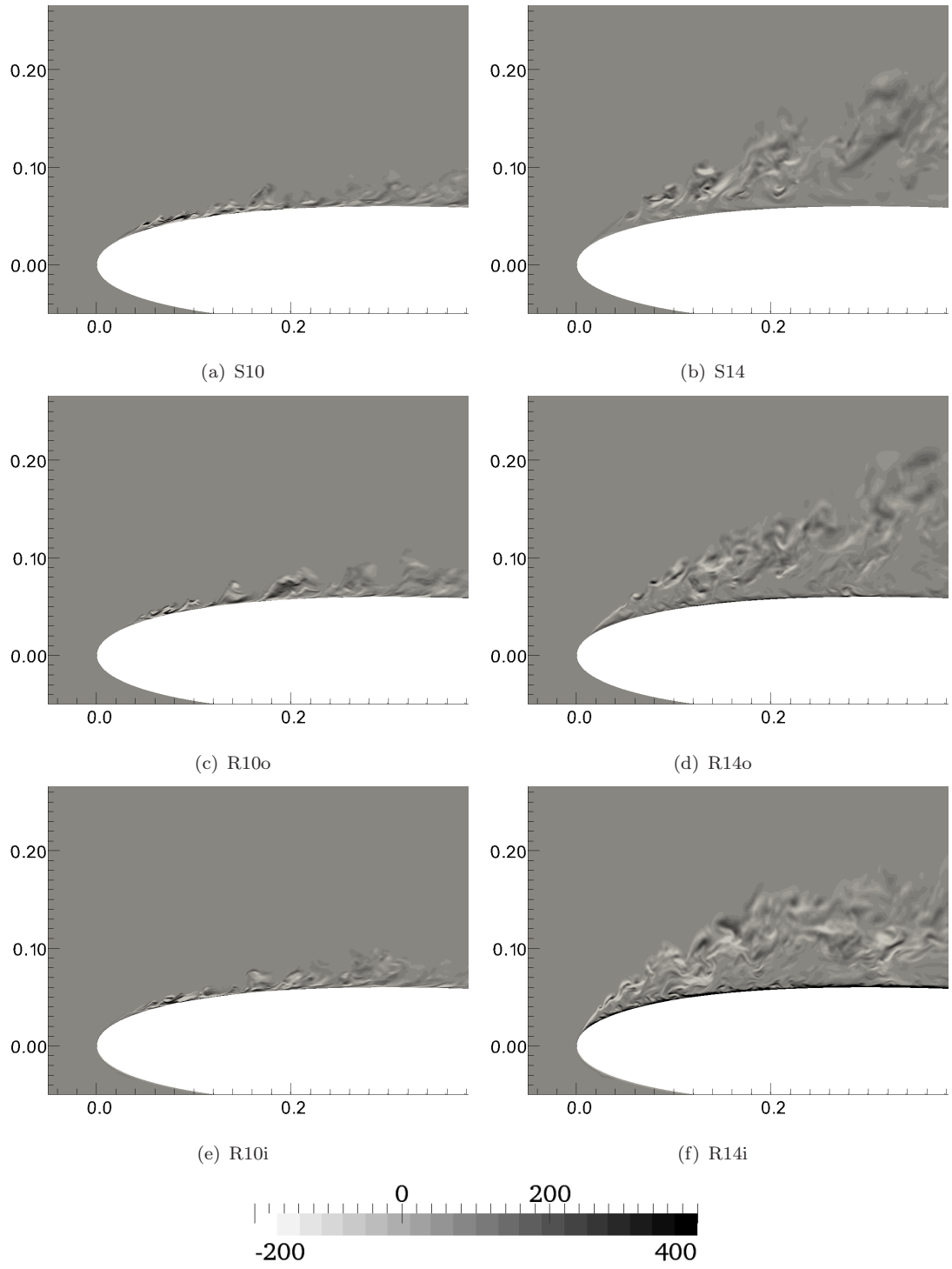

(a) S10 (b) S14

(c) R10o (d) R14o

(e) R10i (f) R14i

FIGURE 7.10: Instantaneous streamwise vorticity fields near the leading edge. The contours and coordinates are normalized by U_{eff} and c.

flow provided the cross-flow instability which triggered the early transition [135] thus it delayed the separation and suppressed the boundary layer.

The airfoil in Gross et al. (2012) [39] was S809 and this airfoil was a trailing edge

separation type while a NACA 0012 used for the current study is a leading edge separation type. The transition point on the leading edge separation type airfoil is very close to the leading edge for $Re > 70,000$ [91]. The transition occurs $x/c < 0.1$ for the stationary cases as shown in Figs. 7.5 and 7.9. Thus it is expected that the effect of the early transition by the cross-flow instability on the aerodynamic forces would be minimal for the current case. Then it can be concluded that the Coriolis acceleration in the chordwise direction is a primary mechanism for rotational augmentation for the current study.

7.5 Summary

Rotational effects are examined for the flow over an airfoil under pre- and post-stall regimes to understand the Coriolis effect on rotational augmentation. The model for the rotational effect derived by Gross et al. [39] in the rotating reference frame is adopted. This model is applied on the rotating laminar boundary layer and validated with the analytical solution by Fogarty [33]. The calculated radial velocity for the boundary layer shows reasonable agreement with the analytical solution for the radius to plate length ratio, $2 \leq \frac{r}{X_0} \leq 20$.

The stationary airfoil flows are calculated as baseline simulations and the results show good agreement with the experimental data. Based on these calculations, the rotational effect for the different radius-chord ratios (i.e. Rotation number) is examined. The rotational effect is evident only when the flow is detached at the small radius-chord ratio, i.e. $r/c = 2.5$. A small radius-chord ratio corresponds to the inner part of the rotating blade and a similar trend was found in the full scale wind turbine measurements [138]. This implies that the Coriolis effect is a primary mechanism for rotational augmentation, because the mass depletion and early transition are absent for the current configuration. The surface pressure, skin-friction and the snapshots of the contours such as the spanwise velocity and vorticity are all consistent, and collectively confirm that the rotational effect is evident on the separated flow at the small radius-chord ratio. Thus it is exclusively identified that the Coriolis effect is a primary factor in rotational augmentation with a leading edge separation type of an airfoil.

Chapter 8

Conclusions and suggestions

Research key points are drawn for wind turbine aerodynamics in which large-eddy simulations are used. The studies are focused on the effects of freestream turbulence on a wind turbine blade. The primary results are summarized and suggestions are given for future work.

8.1 Conclusions

For an efficient and realistic turbulent inflow condition for large-eddy simulation, a new divergence-free synthetic turbulence inflow technique is developed for incompressible flow solvers. The divergence-free condition is critical to the unsteady load and aeroacoustic noise predictions for wind turbines. To satisfy the divergence-free condition, the velocity-pressure coupling procedure (PISO) is modified slightly by substituting the generated synthetic turbulence before the corrector steps are performed. It is easy to implement the new model into other velocity-pressure algorithms such as PIMPLE. The impact of the modification for the velocity-pressure coupling algorithm is examined analytically and numerically. The maximum disturbances occur where synthetic turbulence is imposed and the errors decay to sufficiently small values downstream where the object of interest would be placed. The suggested divergence-free turbulence inflow model (XCDF) has been tested for a channel flow and compared with the XC model [183]. XCDF provides significant improvements on the computed statistics of the pressure fluctuations, such as the variance and spectra. A simple mass flux correction on the XC model also brings a similar improvement with XCDF, but the XCDF model is genuinely divergence-free and provides more reasonable peak pressure fluctuations.

The XCDF model is applied to the flow over a NACA 0006 airfoil. The effects of freestream turbulence on the aerodynamic characteristics and unsteady surface pressure are examined. The spectral density of the pressure difference on the airfoil surface, G_{pp},

at zero incidence shows good agreement with the analytical solution [2–4]. Thus the current methodology can be applied on an airfoil flow subjected to freestream turbulence for both aerodynamic and aeroacoustic analyses. This is important because no reliable analytical solution is available for the flow over an airfoil at non-zero incidence so far. By using large-eddy simulation, one can simulate an airfoil flow at any given angle of attack. As an example, the turbulence impacts on the flow over an airfoil at 7° incidence is examined. The separation bubble is diminished as turbulence level increases resulting in the increase of the lift-drag ratio. The secondary peak in G_{pp} is observed at the frequency which corresponds to the characteristic frequency for the separation bubble.

The dynamic stall events on a pitching airfoil are investigated by using large-eddy simulation. Generally, aerodynamic hysteresis shows good agreement with the experimental data [85] for the reduced frequency $k_{\mathrm{red}} = 0.025 - 0.1$. These frequencies are typical of operating conditions for wind turbines (see Fig. 1.6 and Table 1.1). The laminar separation bubble diminishing and boundary layer suppression on the pitching airfoil are illustrated by the surface forces and flow contours. The leading edge vortex is quantified in terms of its convective speed and shedding frequency. The results are comparable with those in literature. It is demonstrated that the LES calculation is capable to capture a strong unsteady 3-D phenomenon at deep stall. Based on the simulations for the pitching airfoil with the laminar inflow, the XCDF model is applied to investigate the turbulence effects on dynamic stall. The magnitudes of the maximum drag and minimum moment decrease for the turbulent inflow cases. These are mainly attributed to the suppression of the separated flow by freestream turbulence. The most evident impact of freestream turbulence occurs on the lift coefficient, i.e. the lift increasing, $\Delta C_L \approx 0.2$, during the downstroke. A similar trend is found in the experimental works for a different airfoil [1]. The snapshots of the vorticity fields at different incidence confirm that freestream turbulence affects the flow around the pitching airfoil.

Rotational effects are examined for the flow over an airfoil under pre- and post-stall regimes to identify the Coriolis effect on rotational augmentation. By using the rotational model by Gross et al. [39], a periodic boundary condition is applied in the spanwise direction on the sectional blade simulation. The rotational effect is evident only when the flow is separated at the small radius-chord ratio which corresponds to the near hub region. The surface pressure, skin-friction and the snapshots for the contours such as the spanwise velocity and vorticity are all consistent, i.e. an evident rotational effect on the separated flow at the small radius-chord ratio. For the current configuration, the mass depletion due the centrifugal pumping and early transition by the cross-flow instability are absent. Therefore, the Coriolis effect is exclusively identified as a primary factor for rotational augmentation for a leading edge separation type airfoil.

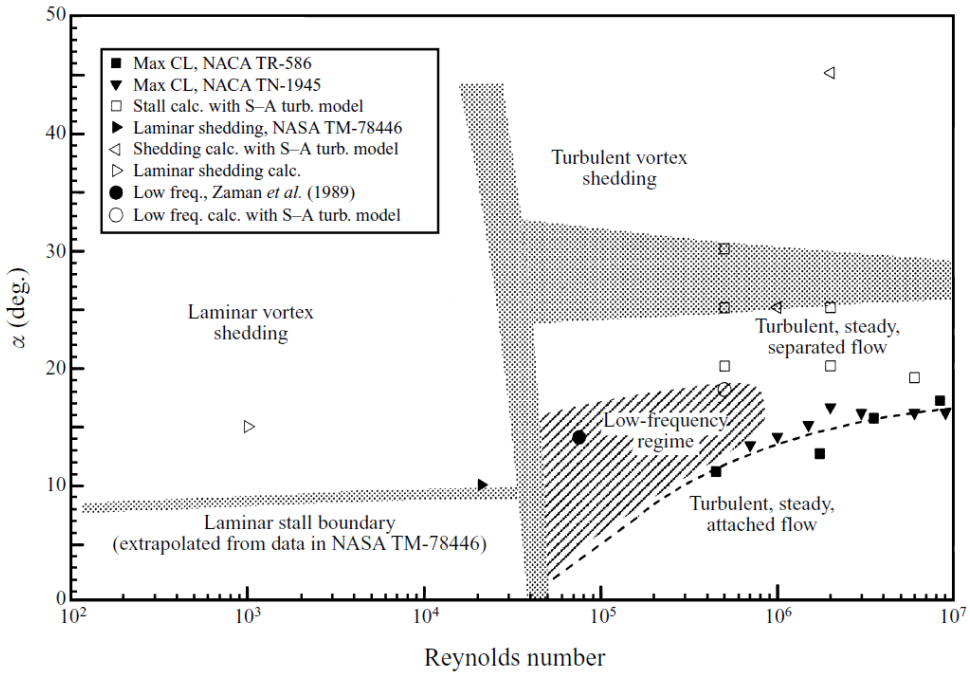

FIGURE 8.1: A contour of flow regimes for a NACA0012 airfoil at angles of attack versus Reynolds number. Shadded regions denote tentative approximate boundaries for the regimes [182].

8.2 Suggestions

A few points which are not covered in the current study are included here as a guideline to future works.

- The XCDF model is developed in grounds of incompressible fluids and an extension of this model to compressible flow solvers would be very useful. The divergence-free condition in the XCDF model is not available in compressible flows, thus other constraint needs to be considered. It would be relatively easy to extend the XCDF model to an *implicit* compressible flow solver, e.g. the PISO method for compressible flows by Issa (1985) [55]. This is because the continuity equation, with the equation of state, is constructed in the form of a Poisson equation and the system of algebraic equations need to be solved iteratively. Thus the algorithm for the *implicit* compressible flow solvers would be similar to that used in Sec. 4.2.3. However, it will probably need a further constraint or an advanced technique such as the energy conservation, to extend the XCDF model to *explicit* compressible flow solvers.

- NACA 0006 and NACA 0012 airfoils are used in the present study because many details of reference data are available on these airfoils and the fundamentals (the effect of turbulence, dynamic stall behaviours and mechanisms for the rotational

effects etc.) behind the airfoil aerodynamics are, in principle, similar. A study with airfoils which are widely used in the wind energy community such as S809, NACA 44xx or NACA 63-4xx [155] would have a more direct impact on wind turbine design.

- Fig. 8.1 shows the regimes of flow patterns over a NACA 0012 airfoil [182]. Due to the limit of the computational power, the Reynolds number for the current study ranges from $50,000$ to $135,000$ which is in the lower limit of the turbulence regime. For a large wind turbine, the Reynolds number is usually over 10^6. Therefore it is desirable to increase the Reynolds number in future works. Adopting a wall-modelling method (see Sec. 2.4) would be an alternative approach but clarifying the uncertainty in the method is a challenging task.

- Additionally, the effect of more realistic atmospheric turbulence on wind turbine blades is also of great interest. This includes the wind shear, gust and anisotropic turbulence effects.

Appendix A

Forward stepwise method

The forward-stepwise method (FSM) follows the ideas from Xie and Castro (2008) [183] (the model by Xie and Castro is called XC). The exponential correlation procedure is applied to all three directions while the XC model used it only in the streamwise direction as in Eq. 2.51. The FSM method is consistent in imposing correlations and simplifies the code compared with the XC model.

A.1 Mathematical formulation

The formulations for generating the unscaled velocity fluctuation ($u_{*,j}$ in Eq. 2.40) in FSM are shown in Eqs. A.1 - A.3. For the first step, a 2-D random number slice, $\boldsymbol{r}(t,j,k)$, with a zero mean and unit variance is generated. Based on $\boldsymbol{r}(t,j,k)$, the correlations in each direction are successively imposed by using the exponential function. The variables, $\boldsymbol{\phi}(t,j,k)$, $\boldsymbol{\psi}(t,j,k)$ and $\boldsymbol{u}_*(t,j,k)$, are intermediate 2-D vector fields and the last is correlated in the t, j, k directions where t corresponds to the streamwise direction. Only one 2-D vector slice of random numbers is generated at each time step.

$$\boldsymbol{\phi}(t,j+1,k) = \boldsymbol{\phi}(t,j,k)\exp\left(-\frac{C_w}{n_y}\right) + \boldsymbol{r}(t,j,k)\left[1-\exp\left(-\frac{2C_w}{n_y}\right)\right]^{0.5}, \tag{A.1}$$

$$\boldsymbol{\psi}(t,j,k+1) = \boldsymbol{\psi}(t,j,k)\exp\left(-\frac{C_w}{n_z}\right) + \boldsymbol{\phi}(t,j,k)\left[1-\exp\left(-\frac{2C_w}{n_z}\right)\right]^{0.5}, \tag{A.2}$$

$$\boldsymbol{u}_*(t+\Delta t,j,k) = \boldsymbol{u}_*(t,j,k)\exp\left(-\frac{C_w}{n_t}\right) + \boldsymbol{\psi}(t,j,k)\left[1-\exp\left(-\frac{2C_w}{n_t}\right)\right]^{0.5}, \tag{A.3}$$

where n_i is defined in Eq. A.4 for the computational grid size, Δx, and time step, Δt.

$$n_i = \begin{cases} \frac{I_i}{\Delta x_i}, & (i = y, z) \\ \frac{T}{\Delta t}, & (i = t) \end{cases}, \tag{A.4}$$

where I is the integral length scale and T is the Lagrangian time scale. T is determined by using Taylor's hypothesis, i.e. $T = I/U$. The integral length scale in the streamwise direction (t) does not appear explicitly in the model. C_w is a model constant in the present work and tests showed that $C_w = 0.41$ produces the best results with the given length scales and Reynolds stresses.

The variables, $\boldsymbol{\phi}$, $\boldsymbol{\psi}$ and $\boldsymbol{u}_*$, are all vectors and each vector component needs the same procedure as in Eqs. A.1 - A.3. $\boldsymbol{u}_*$ has unit variance but does not contain cross-correlation. Lund et al. [92] suggested Eqs. 2.40 and 2.41 to provide cross-correlations to $\boldsymbol{u}_*$. Therefore the mean velocity, Reynolds stresses and integral length scales are input parameters for the FSM model as in the XC model.

A.1.1 Proof A

It is important for the FSM model to prove that, A. the intermediate variables in Eqs. A.1 - A.3 satisfy the target correlation function, e.g. $\overline{u_*(x+r)u_*(x)} = C(r) = \exp(-C_w \frac{r}{I})$ where $(\bar{})$ is an assembly average operator; B. the later correlation imposing process in one direction does not affect the former in an other direction. For the proofs, two conditions and one property are introduced by using a random number X.

- Zero mean condition : $\overline{X} = 0$,
- Unit variance condition : $\overline{X_i X_i} = 1$,
- Zero covariance property : $\overline{X_i X_j} = 0$, $i \neq j$.

In proof A, it is shown that the intermediate variables have the target correlation. For example, Eq. A.3 is used and the same proof can obviously be applied to Eqs. A.1, A.2. For the sake of simplicity, the intermediate vectors ($\boldsymbol{\phi}$, $\boldsymbol{\psi}$, $\boldsymbol{u}_*$) are treated as scalar and model constant is assumed to be unity $C_w = 1$. Also $\exp(-1/n_i) = A_{ni}$ and $\exp(-2/n_i) = A_{ni}^2$ for neatness. Then Eq. A.3 is re-written as,

$$u_*(t + \Delta t, j, k) = u_*(t, j, k)A_{nt} + \psi(t, j, k)[1 - A_{nt}^2]^{0.5}. \tag{A.5}$$

The autocorrelation, $\overline{u_*(t+\tau, j, k)u_*(t, j, k)}$, with the separation of $\tau = l\Delta t$ (l is a positive integer) is then,

$$
\begin{aligned}
&\overline{u_*(t+l\Delta t,j,k)u_*(t,j,k)} \\
&= \overline{\left\{u_*(t+(l-1)\Delta t,j,k)A_{nt}+\psi(t,j,k)[1-A_{nt}^2]^{0.5}\right\}u_*(t,j,k)} \\
&= \overline{u_*(t+(l-1)\Delta t,j,k)u_*(t,j,k)}A_{nt}+\overline{\psi(t,j,k)u_*(t,j,k)}[1-A_{nt}^2]^{0.5} \\
&= \overline{u_*(t+(l-1)\Delta t,j,k)u_*(t,j,k)}A_{nt} \\
&= \overline{u_*(t+(l-2)\Delta t,j,k)u_*(t,j,k)}A_{nt}^2 \\
&\cdots \\
&= \overline{u_*(t,j,k)u_*(t,j,k)}A_{nt}^l \\
&= A_{nt}^l = \exp\left(-\frac{l}{n_t}\right).
\end{aligned}
\tag{A.6}
$$

Note that,

$$
\begin{aligned}
&\overline{u_*(t,j,k)u_*(t,j,k)} = 1, \\
&\overline{\psi(t,j,k)u_*(t,j,k)} = 0.
\end{aligned}
\tag{A.7}
$$

By using the same approach, it can be shown for $\boldsymbol{\phi}$ and $\boldsymbol{\psi}$ as,

$$
\overline{\phi(t,j+m\Delta y,k)\phi(t,j,k)} = \exp\left(-\frac{m}{n_y}\right), \tag{A.8}
$$

$$
\overline{\psi(t,j,k+n\Delta z)\psi(t,j,k)} = \exp\left(-\frac{n}{n_z}\right). \tag{A.9}
$$

Therefore the proof A shows that the Eqs. A.1 - A.3 have statistically correct correlation functions as they are imposed.

A.1.2 Proof B

In proof B, it is shown that each correlation procedure does not modify the formal procedure. For simplicity,

$$
\begin{aligned}
&u_*(t+l\Delta t,m_1,n_1) = u_l', \quad u_*(t+l\Delta t,m_2,n_2) = u_l'', \\
&\psi(t+l\Delta t,m_1,n_1) = \psi_l', \quad \psi(t+l\Delta t,m_2,n_2) = \psi_l'',
\end{aligned}
\tag{A.10}
$$

where $m_1 \neq m_2$ and $n_1 \neq n_2$. The two point correlation for $u_*(t,m_1,n_1)$ and $u_*(t,m_2,n_2)$ leads to,

$$
\begin{aligned}
\overline{u'_l u''_l} &= \overline{\left(u'_{l-1}A_{nt} + \psi'_{l-1}[1-A_{nt}^2]^{0.5}\right)\left(u''_{l-1}A_{nt} + \psi''_{l-1}[1-A_{nt}^2]^{0.5}\right)} \\
&= \overline{u'_{l-1}u''_{l-1}}A_{nt}^2 + \overline{\psi'_{l-1}\psi''_{l-1}}[1-A_{nt}^2]^{0.5\times 2} + \left(\overline{u'_{l-1}\psi''_{l-1}} + \overline{u''_{l-1}\psi'_{l-1}}\right)A_{nt}[1-A_{nt}^2]^{0.5} \\
&= \overline{u'_{l-1}u''_{l-1}}A_{nt}^2 + \overline{\psi'_{l-1}\psi''_{l-1}}[1-A_{nt}^2]^{0.5\times 2} \\
&= \left(\overline{u'_{l-2}u''_{l-2}}A_{nt}^2 + \overline{\psi'_{l-2}\psi''_{l-2}}[1-A_{nt}^2]^{0.5\times 2}\right)A_{nt}^2 + \overline{\psi'_{l-1}\psi''_{l-1}}[1-A_{nt}^2]^{0.5\times 2} \\
&= \overline{u'_{l-2}u''_{l-2}}A_{nt}^{2\times 2} + \overline{\psi'_{l-2}\psi''_{l-2}}[1-A_{nt}^2]^{0.5\times 2}\left[1+A_{nt}^2\right] \\
&= \overline{u'_{l-2}u''_{l-2}}A_{nt}^{2\times 2} + \overline{\psi'_{l-2}\psi''_{l-2}}[1-A_{nt}^{2\times 2}] \\
&... \\
&= \overline{u'_0 u''_0}A_{nt}^{2\times l} + \overline{\psi'_0\psi''_0}[1-A_{nt}^{2\times l}] \\
&\approx \overline{\psi'_0\psi''_0}.
\end{aligned}
\tag{A.11}
$$

It should be noted that l is large enough to neglect $A_{nt}^{2\times l}$ in Eq. A.11. n_t is constant in time and,

$$
\begin{aligned}
&\overline{\psi'_{l-1}\psi''_{l-1}} = \overline{\psi'_{l-2}\psi''_{l-2}} = \ ... \ = \overline{\psi'_0\psi''_0}, \\
&\overline{u'_{l-l}\psi''_{l-l}} = \overline{u''_{l-l}\psi'_{l-l}} = 0.
\end{aligned}
\tag{A.12}
$$

Eq. A.11 shows that the two point correlation on the u_* field is the same as that in the ψ field. This means the latter correlation procedure does not affect the former. In the same approach, the two point correlation for $\psi(t, j+m\Delta y, k)$ and $\psi(t, j, k)$ leads,

$$
\begin{aligned}
\overline{\psi(t,j+m\Delta y,k)\psi(t,j,k)} &= \overline{\{\psi(t,j+m\Delta y,k-1)A_{nz} + \phi(t,j+m\Delta y,k-1)[1-A_{nz}^2]^{0.5}\}} \\
&\times \overline{\{\psi(t,j,k-1)A_{nz} + \phi(t,j,k-1)[1-A_{nz}^2]^{0.5}\}} \\
&= ... \\
&= \overline{\psi(t,j+m\Delta y,0)\psi(t,j,0)}A_{nz}^{2\times k} \\
&+ \overline{\phi(t,j+m\Delta y,0)\phi(t,j,0)}\left[1-A_{nz}^{2\times k}\right] \\
&\approx \overline{\phi(t,j+m\Delta y,0)\phi(t,j,0)} \\
&= \exp\left(-\frac{m}{n_y}\right).
\end{aligned}
\tag{A.13}
$$

In Eq. A.13, k should be large enough so that $A_{nz}^{2\times k}(=\exp(-\frac{2k}{n_z}))$ is negligible. The proof B shows that the later correlation procedure in one direction does not affect the

former in an other direction, i.e. the correlation functions are statistically independent.

A.2 A comparison between the XC and FSM models

The formulations for the FSM model are shown in the previous section. Its performance is assessed here and comparisons with the XC model are presented. The XC and FSM models are applied at the inlet of a plane channel flow and the results are compared with those by using periodic in-outlet boundary conditions (PBC). The purpose of using periodic simulation data is simply to provide a straightforward validation for the inflow method. All numerical conditions for the XC and FSM models are identical with those in Ch. 4 unless otherwise mentioned. For the XC model, the revised model coefficient was adopted here, see Sec. 4.2.1.

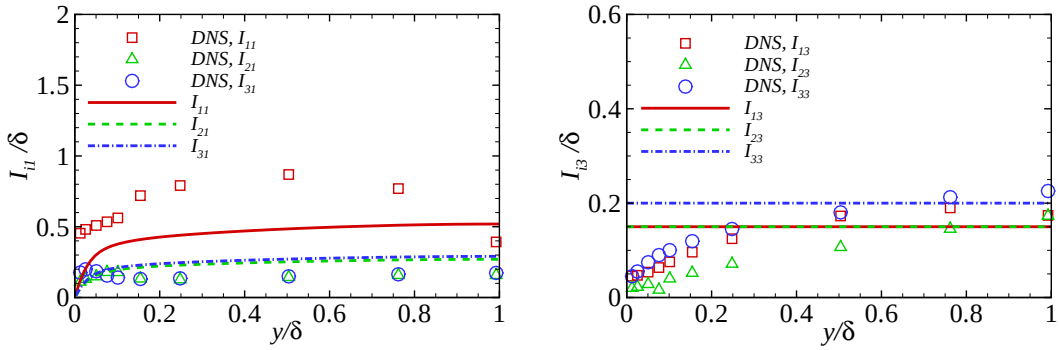

(a) (b)

FIGURE A.1: Integral length scales in (a) the streamwise direction and (b) the spanwise direction. Symbols are from DNS [110], lines are specified length scales as input data for cases XC1 and FSM1. The definition of I_{ij} is shown in Eq. 2.52. Note $I_{21} = I_{31}$, $I_{13} = I_{23}$ and $I_{i2} = I_{i3}$.

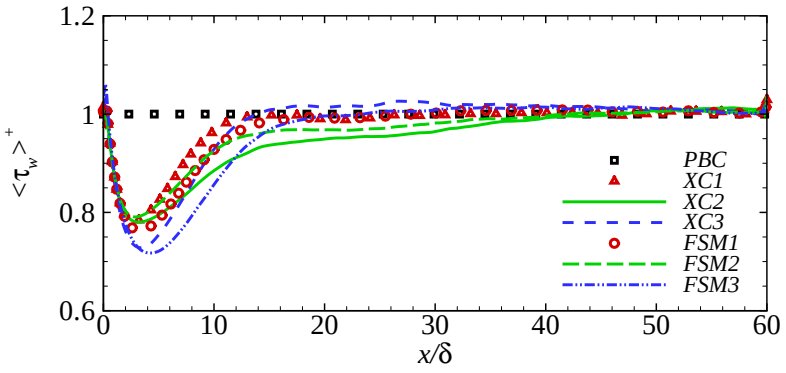

FIGURE A.2: Developments of the wall shear stress, $\tau_w^+ = \frac{\tau_w}{\rho u_\tau^2}$.

The XC and FSM models need the first and second moment statistics as input parameters. These statistics were taken from case PBC in Sec. 4. The length scales which are used for the current case are shown in Fig. A.1. The cases with these length

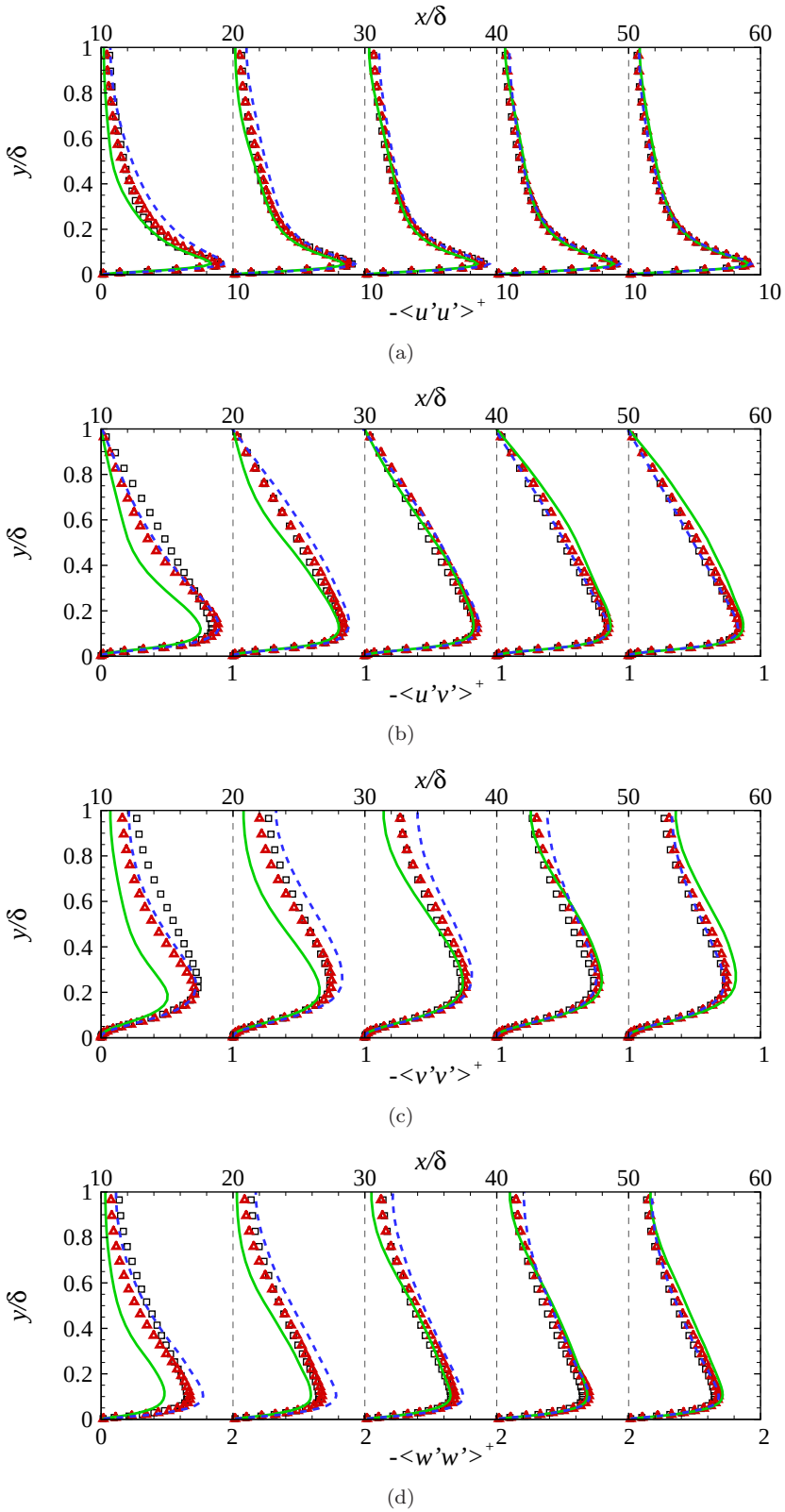

FIGURE A.3: The effect of the input length scales on developments of Reynolds stresses for the XC model. □ PBC, △ XC1, — XC2, - - XC3.

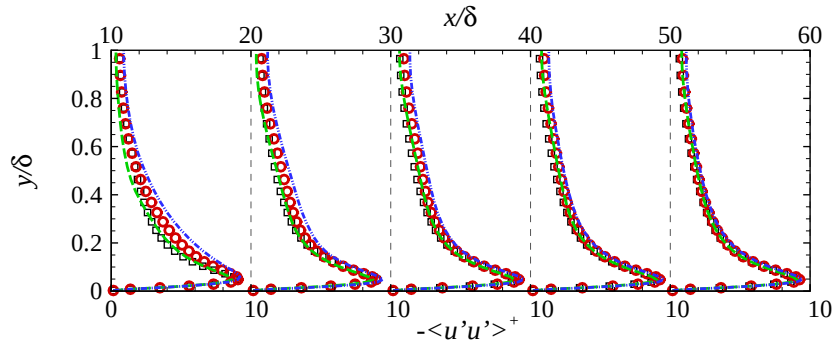

(a)

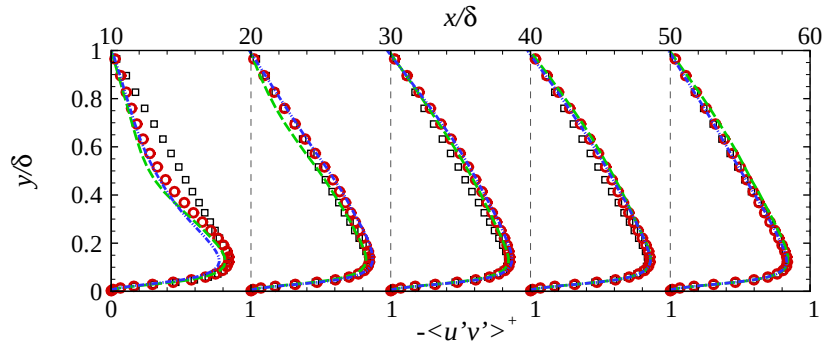

(b)

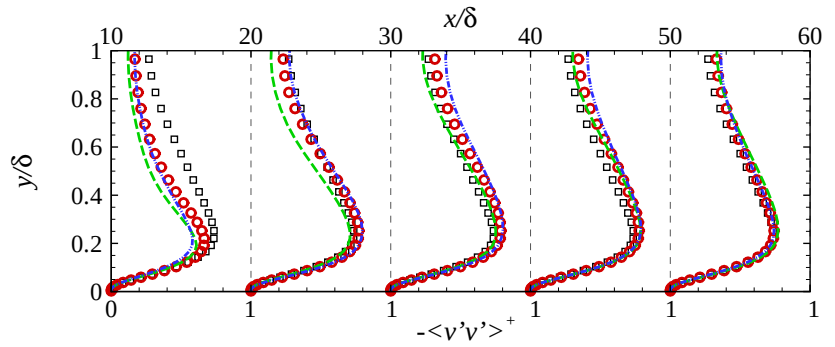

(c)

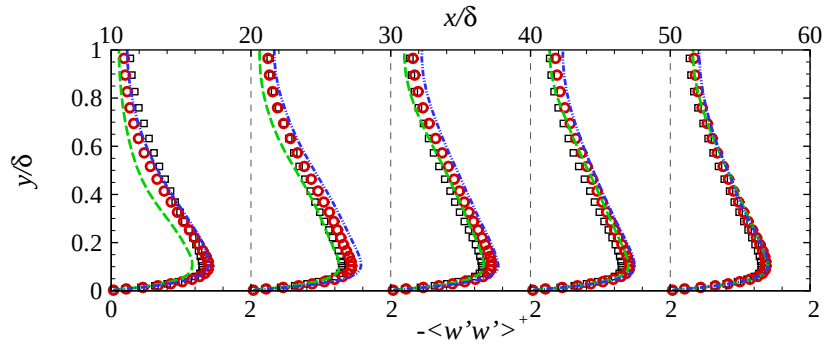

(d)

FIGURE A.4: The effect of the input length scales on developments of Reynolds stresses for the FSM model. □ PBC, ◯ FSM1, - - FSM2, — · · — FSM3.

scales are called XC1 and FSM1 respectively. For the sensitivity tests of input length scales, a halved (cases XC2 and FSM2) and doubled (cases XC3 and FSM3) values of the length scales used for cases XC1 and FSM1, were adopted.

A certain axial distance is required before the turbulence becomes fully developed with a turbulence inflow. Thus a key assessment criterion is the development distance. For this purpose, the wall shear stress and Reynolds stress profiles are compared with those from case PBC in Sec. 4. Fig. A.2 shows development of the wall shear stress. The $\langle\tau_w\rangle^+$ for case XC1 converges by $x/\delta \approx 12$ and that for case FSM1 does so a little later, at $x/\delta \approx 14$. These convergence distances based on the wall shear stress are similar to or slightly shorter than those reported in literature using synthetic methods [58, 66]. After the wall shear stress is converged, it stays at the target value, unity, until the outlet.

The Reynolds stress profiles for all cases are presented in Figs A.3 and A.4. Note that the profiles for case PBC are target values. All profiles for cases XC1 and FSM1 show good agreement with those for case PBC for $x/\delta \geq 20$. It is found that $\langle u'u'\rangle^+$ and $\langle w'w'\rangle^+$ are developed earlier than the other profiles; their profiles match well with the reference data at $x/\delta = 10$. It seems to be more difficult to predict the $\langle v'v'\rangle^+$ profile compared with other profiles at $x/\delta = 10$ and this leads to a slow development in the Reynolds shear stress $\langle u'v'\rangle^+$. The Reynolds-stress equation is shown in Eq. A.14 and the first term on the right-hand-side is the rate of production. When $i = 1$ and $j = 2$, Eq. A.14 is reduced to the Reynolds shear stress equation and the production term becomes $-\langle v'v'\rangle\frac{\partial U}{\partial y}$ for $k = 2$. Note that the wall-normal ($k = 2$) gradient is only non-zero for the channel flow. Thus $\langle v'v'\rangle^+$ plays an important role in the Reynolds shear stress development and an accurate prediction of $\langle v'v'\rangle^+$ helps early flow developments. Jarrin et al. (2006) [58] reported that a higher $\langle v'v'\rangle^+$ at the inlet helps the momentum mixing near the wall resulting in faster flow developments.

$$\begin{aligned}\frac{\partial\langle u_i'u_j'\rangle}{\partial t} + U_k\frac{\partial\langle u_i'u_j'\rangle}{\partial x_k} = &-\left(\langle u_i'u_k'\rangle\frac{\partial U_j}{\partial x_k} + \langle u_j'u_k'\rangle\frac{\partial U_i}{\partial x_k}\right)\\ &+\left\langle\frac{p'}{\rho}\left(\frac{\partial u_i'}{\partial x_j} + \frac{\partial u_j'}{\partial x_i}\right)\right\rangle\\ &-\frac{\partial}{\partial x_k}\left(\langle u_i'u_j'u_k'\rangle + \frac{\langle p'u_j\rangle}{\rho}\delta_{ik} + \frac{\langle p'u_i\rangle}{\rho}\delta_{jk} - \nu\frac{\partial\langle u_i'u_j'\rangle}{\partial x_k}\right)\\ &-2\nu\left\langle\frac{\partial u_i'}{\partial x_k}\frac{\partial u_j'}{\partial x_k}\right\rangle.\end{aligned} \tag{A.14}$$

The sensitivity tests for the input length scales have been conducted to observe their effects on the performance of the XC and FSM models. Nine components of the length scale are required as input data. The test considers only halved (cases XC2 and FSM2) and doubled (cases XC3 and FSM3) values of those in cases XC1 and FSM1. Developments of the wall shear stress along the channel for each case are shown in Fig.

A.2. Cases which adopt the halved and doubled length scales tend to slow down the flow development. Cases with the original length scales (XC1 and FSM1) reach the target value earlier than the other cases but eventually all cases approach the target value. Though case FSM1 reaches the target value earlier than case FSM2, it shows a slightly greater initial drop than case FSM2. Since one of the main objectives of the inflow condition is to minimize the development distance, the initial drop is not a crucial issue in the assessments.

Figs A.3 and A.4 show the profiles of Reynolds stresses. Cases with the original length scales (XC1 and FSM1) generally show better agreement with case PBC than the other cases at most of locations. The $\langle v'v' \rangle^+$ for the XC model tends to be over-predicted as the input length scales increase for $x/\delta < 30$. Case XC2 presents a curved $\langle u'v' \rangle^+$ profile in the region for $y/\delta > 0.1$ and $x/\delta > 40$ in Fig. A.3. As the length scale increases (e.g. XC1, XC3), the $\langle u'v' \rangle^+$ profile is improved (straightened). The Reynolds stress profiles for the FSM model, however, are less sensitive to the input length scales, as shown in Fig. A.4(b).

A.3 Summary

Overall, the XC model shows marginally better performance (i.e. a shorter distance of flow developments) than the FSM model. However, there are still advantages of the FSM model; the procedure for imposing the correlations is consistent in all three directions which makes the FSM method easy to implement and slightly less expensive. Potentially the FSM model is also more flexible for using spatially varying length scales whereas the XC model becomes quite complicated if varying length scales are to be used (see also [173]). However, the XC model is mainly adopted for the the current study, i.e. Chs. 4 - 6 since it is considered that the flow development distance is the first criteria of the inflow condition assessment.

Appendix B

Velocity and pressure coupling with incompressible solvers

A succinct explanation for the difficulty of calculating the pressure field in the Navier-Stokes equations and an idea for the velocity-pressure coupling was given by Ferziger and Perić (2002) [32] and it is quoted here,

"Solution of the Navier-Stokes equations is complicated by the lack of an independent equation for the pressure, whose gradient contributes to each of the three momentum equations. Furthermore, the continuity equation does not have a dominant variable in incompressible flows. Mass conservation is a kinematic constraint on the velocity field rather than a dynamic equation. One way out of this difficulty is to construct the pressure field so as to guarantee satisfaction of the continuity equation. "

The pressure can be associated with the velocity via the continuity equation. The most widely used coupling algorithm for a transient solver is PISO [55] which is explained in Sec. 4.2.3.1. This algorithm can be summarized by the following steps,

1. The momentum equation is solved by using the values of flux and pressure from the previous time. This step is called the *momentum predictor*, Eq. 4.10, because the velocity field is solved with the previous pressure and flux.

2. The pressure is corrected by solving the continuity equation, Eq. 4.13. This step is called the *pressure corrector*.

3. The velocity is then corrected (Eq. 4.11) by using the corrected pressure field from the pressure corrector step. This is known as a *projection method* because the divergence-producing part is projected out [32].

4. Steps 2-3 are repeated for a pre-specified number of pressure correctors. This non-iterative calculation (i.e. the momentum predictor is not repeated within one

time step) presumes that the final velocity and pressure fields are correct after the specified number of corrector steps [174].

For the steady-state problem, the system of algebraic equations, Eqs. 4.8 and 4.9 are solved iteratively as the effective time step is much larger than that for unsteady problems. In such case, the SIMPLE algorithm by Patankar [114] is used. The main difference with the PISO algorithms is that the momentum and continuity equations are solved iteratively with some relaxation factors in the SIMPLE algorithm. It is summarized by the following procedure,

1. The momentum equation is solved with the under-relaxation factor, α_U [59], by using values of the flux and pressure from the previous time level.
2. The pressure is corrected by solving the continuity equation but a fraction of the correction is updated by using the relaxation factor, α_p,

$$p^* = p^n + \alpha_p p', \tag{B.1}$$

   where $0 < \alpha_p < 1$. Note that $p^* = p^n + p'$ in PISO.
3. The velocity is corrected (Eq. 4.11) by the corrected pressure in step 2.
4. Go to step 1 and repeat steps 1-3 until the predefined tolerance is met.

A combination of the SIMPLE and PISO algorithms is possible for a large time-step transient solver [112] which is called PIMPLE. In the PIMPLE algorithm, the momentum equation is solved repeatedly as in SIMPLE but multiple corrector steps are performed (as in PISO) within the SIMPLE iteration.

Appendix C

Consistency in the PISO algorithm

Notations for the PISO algorithm in literature and some source codes may be confusing for whom is not fully aware of the method. Therefore consistency among the equations used in this study, OpenFOAM code v1.7.1 (OF) [112] and Ferziger and Perić [32] are shown here for the reader's convenience.

C.1 A note on notations in Ferziger and Perić

Taking the divergence, Eqs. 4.11 and 4.10 are rewritten respectively as,

$$\frac{\partial}{\partial x_i}\left[\frac{1}{A_P}\frac{\partial}{\partial x_i}(p^n + p')\right]_P = \left[\frac{\partial}{\partial x_i}\left(\tilde{u}_i^* + \tilde{u}_i'\right)\right]_P - \left[\frac{\partial u_i^{**}}{\partial x_i}\right]_P, \tag{C.1}$$

and

$$\frac{\partial}{\partial x_i}\left(\frac{1}{A_P}\frac{\partial p^n}{\partial x_i}\right)_P = \left[\frac{\partial \tilde{u}_i^*}{\partial x_i}\right]_P - \left[\frac{\partial u_{i,P}^*}{\partial x_i}\right]_P. \tag{C.2}$$

Subtracting Eq. C.2 from Eq. C.1, neglecting $\tilde{u}_i'$ and requiring $\partial u_i^{**}/\partial x_i = 0$ yields,

$$\frac{\partial}{\partial x_i}\left(\frac{1}{A_P}\frac{\partial p'}{\partial x_i}\right)_P = \left[\frac{\partial u_i^*}{\partial x_i}\right]_P. \tag{C.3}$$

This equation is identical to Eq. *7.39* in [32].Neglecting $\tilde{u}_i'$ in Eq. 4.11 and subtracting the equation from Eq. 4.14 leads,

$$u''_{i,P} = \tilde{u}'_{i,P} - \frac{1}{A_P}\left(\frac{\partial p''}{\partial x_i}\right)_P ,, \tag{C.4}$$

which is identical to Eq. *7.43* in [32]. Taking divergence and requiring $\partial u''_i/\partial x_i = 0$ (note u_i^{**} and u_i^{***} are divergence free), Eq. C.4 is written as,

$$\frac{\partial}{\partial x_i}\left[\frac{1}{A_P}\frac{\partial p''}{\partial x_i}\right]_P = \left[\frac{\partial \tilde{u}'_i}{\partial x_i}\right]_P . \tag{C.5}$$

This is identical as Eq. *7.44* in [32].

C.2 A note on notations in the OpenFOAM code

Again for the reader's convenience, a brief description and the PISO source code in OF are respectively presented here and in C.3.

- The prediction equation Eq. 4.10, corresponds to line 75 in the OF code in C.3.
- The corrector steps Eqs. 4.11 and 4.14 (with $\tilde{u}'_{i,P}$ neglected) correspond to line 123 in the OF code in C.3. Note that $\tilde{u}^*_{i,P}$ in Eq. 4.11 is temporally saved as U in line 123 in the OF code. Similarly the flux of $\tilde{u}^*_{i,P}$ is temporally saved as *phi* in line 97 in the OF code in C.3.
- Poisson equations, Eqs. 4.13 and 4.15, correspond to line 97 in the OF code in C.3.

The generated velocity by the XCDF model is substituted after the predictor step but before the flux of $\tilde{u}^*_{i,P}$ is constructed, i.e. between the lines 84 and 85 in the original OF code in C.3.

C.3 pisoFOAM.C in OpenFOAM v.1.7.1

```
00032 \*---------------------------------------------------------------------------*/
00033
00034 #include "fvCFD.H"
00035 #include "singlePhaseTransportModel.H"
00036 #include "turbulenceModel.H"
00037
00038 // * * * * * * * * * * * * * * * * * * * * * * * * * * * * * * * * * * * * * //
00039
00040 int main(int argc, char *argv[])
00041 {
00042     #include "setRootCase.H"
00043
```

```
00044     #include "createTime.H"
00045     #include "createMesh.H"
00046     #include "createFields.H"
00047     #include "initContinuityErrs.H"
00048
00049     // * * * * * * * * * * * * * * * * * * * * * * * * * * * * * * * * * * * * * //
00050
00051     Info<< "\nStarting time loop\n" << endl;
00052
00053     while (runTime.loop())
00054     {
00055         Info<< "Time = " << runTime.timeName() << nl << endl;
00056
00057         #include "readPISOControls.H"
00058         #include "CourantNo.H"
00059
00060         // Pressure-velocity PISO corrector
00061         {
00062             // Momentum predictor
00063
00064             fvVectorMatrix UEqn
00065             (
00066                 fvm::ddt(U)
00067               + fvm::div(phi, U)
00068               + turbulence->divDevReff(U)
00069             );
00070
00071             UEqn.relax();
00072
00073             if (momentumPredictor)
00074             {
00075                 solve(UEqn == -fvc::grad(p));
00076             }
00077
00078             // --- PISO loop
00079
00080             for (int corr=0; corr<nCorr; corr++)
00081             {
00082                 volScalarField rAU(1.0/UEqn.A());
00083
00084                 U = rAU*UEqn.H();
00085                 phi = (fvc::interpolate(U) & mesh.Sf())
00086                     + fvc::ddtPhiCorr(rAU, U, phi);
00087
00088                 adjustPhi(phi, U, p);
00089
00090                 // Non-orthogonal pressure corrector loop
00091                 for (int nonOrth=0; nonOrth<=nNonOrthCorr; nonOrth++)
00092                 {
00093                     // Pressure corrector
00094
00095                     fvScalarMatrix pEqn
00096                     (
00097                         fvm::laplacian(rAU, p) == fvc::div(phi)
00098                     );
00099
00100                     pEqn.setReference(pRefCell, pRefValue);
00101
00102                     if
```

```
00103                     (
00104                         corr == nCorr-1
00105                      && nonOrth == nNonOrthCorr
00106                     )
00107                     {
00108                         pEqn.solve(mesh.solver("pFinal"));
00109                     }
00110                     else
00111                     {
00112                         pEqn.solve();
00113                     }
00114
00115                     if (nonOrth == nNonOrthCorr)
00116                     {
00117                         phi -= pEqn.flux();
00118                     }
00119                 }
00120
00121                 #include "continuityErrs.H"
00122
00123                 U -= rAU*fvc::grad(p);
00124                 U.correctBoundaryConditions();
00125             }
00126         }
00127
00128         turbulence->correct();
00129
00130         runTime.write();
00131
00132         Info<< "ExecutionTime = " << runTime.elapsedCpuTime() << " s"
00133             << "  ClockTime = " << runTime.elapsedClockTime() << " s"
00134             << nl << endl;
00135     }
00136
00137     Info<< "End\n" << endl;
00138
00139     return 0;
00140 }
00141
00142
00143 // ************************************************************************* //
```

Bibliography

[1] Amandolèse X, Széchényl E. Experimental study of the effect of turbulence on a section model blade oscillating in stall. *Wind Energy*, 7:267–282, 2004.

[2] Amiet RK. Acoustic radiation from an airfoil in a turbulent stream. *J. Sound Vib.*, 41:407–420, 1975.

[3] Amiet RK. High frequency thin-airfoil theory for subsonic flow. *AIAA J.*, 14: 1076–1082, 1976.

[4] Amiet RK. Airfoil response to an incompressible skewed gust of small spanwise wave-number. *AIAA J.*, 14:541–542, 1976.

[5] Barakos GN, Drikakis D. Unsteady separated flows over maneuvering lifting surfaces. *Phil. Trans. R. Soc. Lond. A*, 358:3279–3291, 2000.

[6] Bardina J. *Improved turbulence models based on large eddy simulation of homogeneous, incompressible turbulent flows.* PhD thesis, Stanford University, 1983.

[7] Batten P, Goldberg U, Chakravarthy S. Interfacing statistical turbulence closures with large-eddy simulation. *AIAA J.*, 42:485–492, 2004.

[8] Bertagnolio F. NACA0015 measurements in LM wind tunnel and turbulence generated noise. Technical Report Risø-R-1657, RisøDTU National Laboratory for Sustainable energy, 2008.

[9] Boppana VBL, Xie ZT, Castro IP. Large-Eddy Simulation of dispersion from line sources in a turbulent channel flow. *Flow Turb. Combust.*, 88:311–342, 2012.

[10] Bougeault P, Lacarrére P. Parameterization of Orography-induced turbulence in a Mesobeta-scale model. *Mon. Wea. Rev.*, 117:1872–1890, 1989.

[11] Breton SP. *Study of the stall delay phenomenon and of wind turbine blade dynamics using numerical approaches and NREL's wind tunnel tests.* PhD thesis, Norwegian University of Science and Technology, 2008.

[12] Butterfield CP, Hansen AC, Simms D, Scott G. Dynamic stall on wind turbine blades. Technical Report TP-257-4510, NREL, 1991.

[13] Butterfield CP, Simms DA, Musial WP, Scott GN. Spanwise aerodynamic loads on a rotating wind turbine blade. Technical Report SERI TP-257-3983, Solar Energy Research Institute, 1990.

[14] Buxton ORH. *Fine scale features of turbulent shear flows.* PhD thesis, Imperial College Science, Department of Aeronautics, 2011.

[15] Carr LW, McAlister W, McCroskey WJ. Analysis of the development of dynamic stall based on oscillating airfoil experiments. Technical Report TN D-8382, NASA, 1977.

[16] Chandrasekhara M, Carr LW. Flow visualization studies of the Mach number effects on dynamic stall of an oscillating airfoil. *J. Aircraft*, 27:516–522, 1990.

[17] Chaviaropoulos PK, Hansen MOL. Investigating three-dimensional and rotational effects on wind turbine blades by means of a quasi-3D Navier-Stokes solver. *J. Fluids Eng.*, 122:330–336, 2000.

[18] Corten GP. *Flow separation on wind turbine blades.* PhD thesis, Universiteit Utrecht, 2001.

[19] Counihan J. An improved method of simulating an atmospheric boundary layer in a wind tunnel. *Atmos. Environ.*, 3:197–214, 1969.

[20] Daniels SJ, Castro IP, Xie ZT. Peak loading and surface pressure fluctuations of a tall model building. *J. Wind Eng. Ind. Aerodyn.*, in press, 2013.

[21] de Villier E. *The potential of large eddy simulation for the modeling of wall bounded flows.* PhD thesis, Imperial College Science, Technology and Medicine, 2006.

[22] Deck S, Weiss PÉ, Pamiès M, Garnier E. Zonal detached eddy simulation of a spatially developing flat plate turbulent boundary layer. *Comput. Fluids*, 48:1–15, 2011.

[23] Devinant Ph, Laverne T, Hureau J. Experimental study of wind-turbine airfoil aerodynamics in high turbulence. *J. Wind Eng. Ind. Aerodyn.*, 90:689–707, 2002.

[24] Dickinson MH, Götz KG. Unsteady aerodynamic performance of model wings at low Reynolds numbers. *J. Exp. Biol.*, 174:45–64, 1993.

[25] Drela M, Giles MB. Viscous-inviscid analysis of transonic and low Reynolds number airfoils. *AIAA J.*, 25(10):1347–1355, 1987.

[26] Du Z, Selig MS. The effect of rotation on the boundary layer of a wind turbine blade. *Renewable Energy*, 20:167–181, 2000.

[27] Dubief Y, Delcayre F. On coherent-vortex identification in turbulence. *J. Turb.*, 1:1–22, 2000.

[28] Economist. Getting warmer. A special report on climate change and the carbon economy. Technical report, Economist, December 2009.

[29] Ekaterinaris JA, Menter FR. Computation of oscillating airfoil flows with one- and two-equation turbulence models. *AIAA J.*, 32(12):2359–2365, 1994.

[30] Ekaterinaris JA, Platzer MF. Computational prediction of airfoil dynamic stall. *Prog. Aerospace Sci.*, 33:759–846, 1997.

[31] Fan TC, Tian M, Edwards JR, Hassan HA, Baurle RA. Validation of a hybrid Reynolds-averaged/large-eddy simulation method for simulating cavity flameholder configurations. *AIAA*, pages 2001–2929, 2001.

[32] Ferziger JH, Perić M. *Computational Methods for Fluid Dynamics*. Springer, 2002.

[33] Fogarty LE. The laminar boundary layer on a rotating blade. *J. Aeronaut. Sci.*, 18(4):247–252, 1951.

[34] Fröhlich J, von Terzi D. Hybrid LES/RANS methods for the simulation of turbulent flows. *Prog. Aerospace Sci.*, 44:349–377, 2008.

[35] Germano M, Piomelli U, Moin P, Cabot WH. A dynamic subgrid-scale eddy viscosity model. *Phys. Fluids*, 3:1760–1765, 1991.

[36] Ghosal S, Moin P. The basic equation of the large eddy simulation of turbulent flows in complex geometry. *J. Comput. Phys.*, 118:24–37, 1995.

[37] Gilling L. *Airfoils in turbulent inflow*. PhD thesis, Aalborg University, 2009.

[38] Green RB, Galbraith RAM, Niven AJ. Measurements of the dynamic stall vortex convection speed. *Aeronaut. J.*, pages 319–325, 1992.

[39] Gross A, Fasel HF, Friederich T, Kloker MJ. Numerical investigation of rotational augmentation for S822 wind turbine airfoil. *Wind Energy*, 15:983–1007, 2012.

[40] Grötzbach G. in Encyclopedia of Fluid Mechanics. *N.P. Chereminisoff editor*, 6, 1987.

[41] Gungor AG, Sillero JA, Jiménez J. Pressure statistics from direct simulation of turbulent boundary layer. *Seventh Int. Conf. Comput. Fluid Dyn. (Hawaii)*, 2012.

[42] Hain R, Kähler CJ, Radespiel R. Dynamics of laminar separation bubbles at low-Reynolds-number aerofoils. *J. Fluid Mech.*, 630:129–153, 2009.

[43] Hanna SR, Tehranian S, Carissimo B, Macdonald RW, Lohner R . Comparisons of model simulations with observations of mean flow and turbulence within simple obstacle arrays. *Atmos. Environ.*, 36:5067–5079, 2002.

[44] Hansen AC, Butterfield CP. Aerodynamics of horizontal-axis wind turbines. *Annu. Rev. Fluid Mech.*, 25:115–149, 1993.

[45] Hansen MOL, Sørensen JN, Voutsinas S, Sørensen N, Madsen HA. State of the art in wind turbine aerodynamics and aeroelasticity. *Prog. Aerospace Sci.*, 42: 285–330, 2006.

[46] Harris FD. Preliminary study of radial flow effects on rotor blades. *J. American Helicopt. Soc.*, 11(3):1–21, 1966.

[47] Himmelskamp H. *Profile investigations on a rotating airscrew.* PhD thesis, Mit. Max-Planck-Institut für Strömungsforschung Göttingen Nr. 2, 1945.

[48] Hinze JO. *Turbulence 2nd Ed.* McGraw-Hill, 1975.

[49] Hoffmann JA. Effects of freestream turbulence on the performance characteristics of an airfoil. *AIAA J.*, 29(9):1353–1354, 1991.

[50] Horlock JH, Wordsworth J. The three-dimensional laminar boundary layer on a rotating helical blade. *J. Fluid Mech.*, 23:305–314, 1965.

[51] Hu D, Hua O, Du Z. A study on stall-delay for horizontal axis wind turbine. *Renewable Energy*, 31:821–836, 2006.

[52] Huang RF, Lee HW. Effects of freestream turbulence on wing-surface flow and aerodynamic performance. *J. Aircraft*, 36(6):965–972, 1999.

[53] Huang SH, Li QS, Wu JR. A general inflow turbulence generator for large eddy simulation. *J. Wind Eng. Ind. Aerodyn.*, 98:600–617, 2010.

[54] Inagaki M, Kondoh T, Nagano Y. A Mixed-Time-Scale SGS model with fixed model-parameters for practical LES. *J. Fluids Eng.*, 127:1–13, 2005.

[55] Issa RI. Solution of the implicitly discretised fluid flow equations by operator-splitting. *J. Comput. Phys.*, 62:40–65, 1985.

[56] Iwamoto, K. Databased for fully developed channel flow. Technical report, Dept. Mech. Eng., Univ. Tokyo, 2002. URL `http://www.thtlab.t.u-tokyo.ac.jp/`.

[57] Jarrin N. *Synthetic inflow boundary conditions for the numerical simulation of turbulence.* PhD thesis, University of Manchester, 2008.

[58] Jarrin N, Benhamadouche S, Laurence D, Prosser R. A synthetic-eddy-method for generating inflow conditions for large-eddy simulations. *Int. J. Heat Fluid Flow*, 27:585–593, 2006.

[59] Jasak H. *Error analysis and estimation for the finite volume method with application to fluid flows.* PhD thesis, Imperial College of Science, Technology and Medicine, 1996.

[60] Jasak H, Tuković Ž. Automatic mesh motion for the unstructured finite volume method. *Transactions of FAMENA*, 30:1–18, 2004.

[61] Jones LE, Sandberg RD, Sandham ND. Direct numerical simulations of forced and unforced separation bubbles on an airfoil at incidence. *J. Fluid Mech.*, 602: 175–207, 2008.

[62] Jones LE, Sandham ND, Sandberg RD. Acoustic source identification for transitional airfoil flows using cross correlations. *AIAA J.*, 48(10):2299–2312, 2010.

[63] Kaimal JC, Finnigan JJ. *Atmospheric boundary layer flows - their structure and measurement*. Oxford University Press, 1994.

[64] Kassiotis C. Which strategy to move the mesh in the computational fluid dynamic code OpenFOAM. Technical report, École Normale Supérieure de Cachan, Laboratoire de Mécanique et Technologies, 2008.

[65] Keating A, Piomelli U. A dynamic stochastic forcing method as a wall-layer model for large-eddy simulation. *J. Turb.*, 7, 2006.

[66] Keating A, Piomelli U, Balaras E, Kaltenbach HJ. *a priori* and *a posteriori* tests of inflow conditions for large-eddy simulation. *Phys. Fluids*, 16:4696–4712, 2004.

[67] Keating A, Prisco GD, Piomelli U. Interface conditions for hybrid RANS/LES calculations. *Int. J. Heat Fluid Flow*, 27:777–788, 2006.

[68] Kim Y, Castro IP, Xie ZT. Divergence-free turbulence inflow conditions for large-eddy simulations of flows around an airfoil. *UK WES conf., Southampton, UK*, 2012.

[69] Kim Y, Castro IP, Xie ZT. Divergence-free turbulence inflow condition for large-eddy simulations with incompressible flow solvers. *Comput. Fluids*, 84:56–68, 2013.

[70] Kim Y, Castro IP, Xie ZT. Large-eddy simulations for wind turbine blade: rotational augmentation and dynamic stall. *Direct Large Eddy Simulation 9, Dresden, Germany*, 2013.

[71] Kim Y, Xie ZT, Castro IP. A forward stepwise method of inflow generation for LES. *Sixth Int. Conf. Fluid Mech., Guangzhou, China*, 2011.

[72] Kim Y, Xie ZT, Castro IP. Numerical study of 3-D effects on dynamic stall of a wind turbine blade. *13th Int. Conf. Wind Eng.*, 2011.

[73] Klein M, Sadiki A, Janicka J. A digital filter based generation of inflow data for spatially developing direct numerical or large eddy simulations. *J. Comput. Phys.*, 186:652–665, 2003.

[74] Kolmogorov AN. The local structure of turbulence in incompressible viscous fluid for very large Reynolds numbers. *Proc. R. Soc. Lond. A*, 434(1890):9–13, 1991.

[75] Kondo K, Murakami S, Mochida A. Generation of velocity fluctuations for inflow boundary condition of LES. *J. Wind Eng. Ind. Aerodyn.*, 67-68:51–64, 1997.

[76] Kornev N, Hassel E. Synthesis of homogeneous anisotropic divergence-free turbulent fields with prescribed second-order statistics by vortex dipoles. *Phys. Fluids*, 19, 2007.

[77] Kraichnan R. Diffusion by a random velocity field. *Phys. Fluids*, 13:22–31, 1969.

[78] Krishnan L, Sandham ND, Steelant J. Shock-wave/boundary-layer interactions in a model scramjet intake. *AIAA J.*, 47:1680–1691, 2009.

[79] Krogstad PÅ, Davidson PA. Is grid turbulence Saffman turbulence? *J. Fluid Mech.*, 642:373–394, 2010.

[80] Lakshminarayana B, Jabbari A, Yamaoka H. Turbulent boundary layer on a rotating helical blade. *J. Fluid Mech.*, 51:545–569, 1972.

[81] Laraufie R, Deck S, Sagaut P. A dynamic forcing method for unsteady turbulent inflow conditions. *J. Comput. Phys.*, 230:8647–8663, 2011.

[82] Larsen JW, Nielsen SRK, Krenk S. Dynamic stall model for wind turbine airfoils. *J. Fluids Struct.*, 23:959–982, 2007.

[83] Le H, Moin P, Kim J. Direct numerical simulation of turbulent flow over a backward-facing step. *J. Fluid Mech.*, 330:349–374, 1997.

[84] Lee S, Lele SK, Moin P. Simulation of spatially evolving turbulence and the applicability of Taylor's hypothesis in compressible flow. *Phys. Fluids*, 4:1521–1530, 1992.

[85] Lee T, Gerontakos P. Investigation of flow over an oscillating airfoil. *J. Fluid Mech.*, 512:313–341, 2004.

[86] Leishman JG. *Principles of helicopter aerodynamics*. CAMBRIDGE UNIVERSITY PRESS, 2000.

[87] Leonard A. Energy cascade in large-eddy simulation of turbulent fluid flows. *Adv. Geophys.*, 18:237–248, 1974.

[88] Leonard BP. Simple high-accuracy resolution program for convective modelling of discontinuities. *Int. J. Num. Meth. Fluids*, 8:1291–1318, 1988.

[89] Leonard S, Terracol M, Sagaut P. Commutation error in LES with time-dependent filter width. *Comput. Fluids*, 36:513–519, 2007.

[90] Leschziner M, Li N, Tessicini F. Simulating flow separation from continuous surfaces: routes to overcoming the Reynolds number barrier. *Phil. Trans. R. Soc. A*, 367:2885–2903, 2009.

[91] Lissaman PBS. Low-Reynolds-number airfoils. *Ann. Rev. Fluid Mech.*, 15:223–239, 1983.

[92] Lund TS, Wu X, Squires KD. Generation of turbulent inflow data for spatially-developing boundary layer simulations. *J. Comput. Phys.*, 140:233–258, 1998.

[93] Manwell JF, McCowan JG, Rogers AL. *Wind energy explained*. WILEY, 2002.

[94] Marsden O, Bogey C, Bailly C. Direct noise computation of the turbulent flow around a zero-incidence airfoil. *AIAA J.*, 46(4):847–883, 2008.

[95] McAlister KW, Carr LW. Water-tunnel visualizations of dynamic stall. *J. Fluids Eng.*, 101:376–380, 1979.

[96] McAlister KW, Carr LW, McCroskey WJ. Dynamic stall experiments on the NACA 0012 airfoil. Technical Report Technical Paper 1100, NASA, 1978.

[97] McAlister KW, Pucci SL, McCroskey WJ, Carr LW. An experimental study of dynamic stall on advanced airfoil sections volume 2. Pressure and force data. Technical Report TR-82-A-8, NASA, 1982.

[98] McCroskey WJ. The phenomenon of dynamic stall. Technical Report TR 81-A-6, NASA, 1981.

[99] McCroskey WJ, McAlister KW, Carr LW, Pucci SL. An experimental study of dynamic stall on advanced airfoil sections volume 1. Summary of the experiment. Technical Report TR-82-A-8, NASA, 1982.

[100] McCroskey WJ, Yaggy PF. Laminar boundary layers on helicopter rotors in forward flight. *AIAA J.*, 6(10):1919–1926, 1968.

[101] McMillan OJ, Ferziger JH. Direct testing of subgrid-scale models. *AIAA J.*, 17 (12):1340–1346, 1979.

[102] Meneveau C, Katz J. Scale-invariance and turbulence models for large-eddy simulation. *Ann. Rev. Fluid Mech.*, 32:1–32, 2000.

[103] Menter, FR. Two-equation eddy viscosity turbulence models for engineering applications. *AIAA J.*, 32:1598–1605, 1994.

[104] Menter FR, Kuntz M. Adaptation of eddy-viscosity turbulence models to unsteady separated flow behind vehicles. *In:McCallen R, Browand F, Ross J (eds.) Symposium on the aerodynamics of heavy vehicles: trucks, buses and trains. Monterey, USA, 26 Dec 2002, Springer, Berlin Heidelberg New York*, 2004.

[105] Mish PF, Devenport WJ. An experimental investigation of unsteady surface pressure on an airfoil in turbulence - part 1: effects of mean loading. *J. Sound Vib.*, 296:417–446, 2006.

[106] Miyake Y, Fujita S. A laminar boundary layer on a rotating three-dimensional blade. *J. Fluid Mech.*, 65:481–498, 1974.

[107] Moin P, Kim J. Numerical investigation of turbulent channel flow. *J. Fluid Mech.*, 118:341–377, 1982.

[108] Moradnia P. Project work for the PhD course in OpenFOAM, A tutorial on how to use dynamic mesh solver IsoDyMFOAM. Technical report, Lunds Universitet, 2008.

[109] Mordant N, Metz P, Michel O, Pinton JF. Measurement of lagrangian velocity in fully developed turbulence. *Physical Review Letters*, 57:2145011–2145014, 2001.

[110] Moser R, Kim J, Mansour NN. Direct numerical simulation of turbulent channel flow up to $\mathrm{Re}_\tau = 590$. *Phys. Fluids*, 11:943–945, 1999.

[111] Nikitin NV, Nicoud F, Wasistho B, Squires KD, Spalart PR. An approach to wall modeling in large-eddy simulations. *Phys. Fluids*, 12:1629–1632, 2000.

[112] OpenFOAM. User guide. Technical report, OpenFOAM®, 2010.

[113] Pamiès M, Weiss PÉ, Garnier E, Deck S, Sagaut P. Generation of synthetic turbulent inflow data for large eddy simulation of spatially evolving wall-bounded flows. *Phys. Fluids*, 21, 2009.

[114] Patankar SV. Numerical heat transfer and fluid flow. *Hemisphere Publishing Corporation*, 1981.

[115] Paterson RW, Amiet RK. Acoustic radiation and surface pressure characteristics of an airfoil due to incident turbulence. Technical Report CR 2733, NASA, 1976.

[116] Piomelli U. Large-eddy simulation: achievements and challenges. *Prog. Aero. Sci.*, 35:335–362, 1999.

[117] Piomelli U, Balaras E. Wall-layer models for large-eddy simulations. *Annu. Rev. Fluid Mech.*, 34:349–374, 2002.

[118] Piomelli U, Balaras E, Pasinato H, Squires KD, Spalart PR. The inner-outer layer interface in large-eddy simulations with wall-layer models. *Int. J. Heat Fluid Flow*, 24:538–550, 2003.

[119] Piomelli U, Ferziger J, Moin P, Kim J. New approximate boundary conditions for large eddy simulations of wall-bounded flows. *Phys. Fluids*, 1:1061–1068, 1989.

[120] Piziali RA. 2-D and 3-D oscillating wing aerodynamics for a range of angles of attack including stall. Technical Report TR 94-A001, NASA, 1994.

[121] Poletto R, Revell A, Craft T, Jarrin N. Divergence free synthetic eddy method for embedded LES inflow boundary conditions. *Seventh Int. Symp. Turb. Shear Flow Phenom. (Ottawa)*, 2011.

[122] Pope SB. *Turbulent flows.* Cambridge, 2000.

[123] Raffel M, Kompenhans J, Wernert P. Investigation of the unsteady flow velocity field above an airfoil pitching under deep dynamic stall conditions. *Exp. Fluids*, 19:103–111, 1995.

[124] Rai MM, Moin P. Direct numerical simulation of transition and turbulence in a spatially evolving boundary layer. *J. Comput. Phys*, 109:169–192, 1993.

[125] Rajagopalan S, Antonia RA. Some properties of the large structure in a fully developed turbulent duct flow. *Phys. Fluids*, 22:614–622, 1979.

[126] Ramsay RR, Hoffmann MJ, Gregorek GM. Effects of grit roughness and pitch oscillations on the S809 airfoil. Technical Report TP-442-7817, NREL, 1995.

[127] Rind E, Castro IP. Direct numerical simulation of axisymmetric wakes embedded in turbulence. *J. Fluid Mech.*, 710:482–504, 2012.

[128] Rinoie K, Takemura N. Oscillating behaviour of laminar separation bubble formed on an aerofoil near stall. *The Aeronaut. J.*, 108:153–163, 2004.

[129] Ronsten G. Static pressure measurements on a rotating and a non-rotating 2.375 m wind turbine blade. Comparison with 2D calculations. *J. Wind Eng. Ind. Aerodyn.*, 39:105–118, 1992.

[130] Roshko A. On the drag and shedding frequency of two-dimensional bluff bodies. Technical Report TN-3169, NACA, 1954.

[131] Rott N, Smith WE. Some examples of laminar boundary-layer flow on rotating blades. *J. Aeronaut. Sci.*, 23(11):991–996, 1956.

[132] Rumsey, C. Turbulence modeling resource. *Langley Research Center, NASA*, June 2010. URL `http://turbmodels.larc.nasa.gov/index.html`.

[133] Sagaut P. *Large eddy simulation for incompressible flows, Third ed.* Springer, 2006.

[134] Sandham ND, Li Q, Yee HC. Entropy splitting for high-order numerical simulation of compressible turbulence. *J. Comput. Phys.*, 178:307–322, 2002.

[135] Saric WS, Reed HL, White EB. Stability and transition of three-dimensional boundary layers. *Annu. Rev. Fluid Mech.*, 35:413–440, 2003.

[136] Schmidt H, Schumann U. Coherent structure of the convective boundary layer derived from large-eddy simulations. *J. Fluid Mech.*, 200:511–562, 1989.

[137] Schreck S. Rotationally augmented flow structures and time varying loads on turbine blades. Technical Report CP-500-40982, NREL, 2007.

[138] Schreck S, Robinson M. Rotational augmentation of horizontal axis wind turbine blade aerodynamic response. *Wind Energy*, 5:133–150, 2002.

[139] Schreck S, Robinson M. Boundary layer state and flow field structure underlying rotational augmentation of blade aerodynamic response. *J. Sol. Energy Eng.*, 125: 448–456, 2003.

[140] Schreck S, Robinson M. Tip speed ratio influences on rotationally augmented boundary layer topology and aerodynamic force generation. *J. Sol. Energy Eng.*, 126:1025–1033, 2004.

[141] Schreck S, Robinson M. Blade three-dimensional dynamic stall response to wind turbine operating condition. *J. Sol. Energy Eng.*, 127:488–495, 2005.

[142] Schreck S, Sørensen NN, Robinson MC. Aerodynamic structures and processes in rotationally augmented flow fields. *Wind Energy*, 10:159–178, 2007.

[143] Schumann U. Subgrid scale model for finite difference simulations of turbulent flows in plane channels and annuli. *J. Comput. Phys.*, 18:376–404, 1975.

[144] Shen WZ, Sørensen JN. Quasi-3D Navier - Stokes model for a rotating airfoil. *J. Comput. Phys.*, 150:518–548, 1999.

[145] Shipley DE, Miller MS, Robinson MC. Dynamic stall occurrence on a horizontal axis wind turbine blade. Technical Report TP-442-6912, NREL, 1995.

[146] Shur ML, Spalart PR, Strelets MK, Travin AK. A hybrid RANS-LES approach with delayed-DES and wall-modelled LES capabilities. *Int. J. Heat Fluid Flow*, 29:1638–1649, 2008.

[147] Sicot C, Aubrun S, Loyer S, Devinant P. Unsteady characteristics of the static stall of an airfoil subjected to freestream turbulence level up to 16%. *Exp. Fluids*, 41:641–648, 2006.

[148] Sicot C, Devinant P, Loyer S, Hureau J. Rotational and turbulence effects on a wind turbine blade. Investigation of the stall mechanisms. *J. Wind Eng. Ind. Aerodyn.*, 96:1320–1331, 2008.

[149] Simms D, Schreck S, Hand M, Fingersh LJ. NREL Unsteady aerodynamics experiment in the NASA-Ames wind tunnel : A comparison of predictions to measurements. Technical Report TP-500-29494, NREL, 2001.

[150] Skrbek L, Stalp SR. On the decay of homogeneous isotropic turbulence. *Phys. Fluids*, 12:1997–2019, 2000.

[151] Smagorinsky J. General circulation experiments with the primitive equations. *Mon. Wea. Rev.*, 91:99–164, 1963.

[152] Smirnov A, Shi S, Celik I. Random flow generation technique for large eddy simulations and particle-dynamics modeling. *J. Fluids Eng.*, 123:359–371, 2001.

[153] Snel H. Review of aerodynamics for wind turbines. *Wind Energy*, 6:203–211, 2003.

[154] Snel H, Houwink R, Bosschers J. Sectional prediction of lift coefficients on rotating wind turbine blades in stall. Technical Report ECN-C-93-052, ECN, 1993.

[155] Sørensen JN. Aerodynamic aspects of wind energy conversion. *Annu. Rev. Fluid Mech.*, 43:427–448, 2011.

[156] Sørensen NN, Michelsen JA, Schreck S. Navier - Stokes predictions of the NREL Phase VI rotor in the NASA Ames 80 ft × 120 ft wind tunnel. *Wind Energy*, 5: 151–169, 2002.

[157] Spalart PR. Detached-eddy simulation. *Annu. Rev. Fluid Mech.*, 41:181–202, 2008.

[158] Spalart PR, Deck S, Shur ML, Squires KD, Strelets MK, Travin A. A new version of detached-eddy simulation, resistant to ambiguous grid densities. *Theor. Comput. Fluid Dyn.*, 20:181–195, 2006.

[159] Spalart PR, Jou WH, Strelet M, Allmaras SR. Comments on the feasibility of LES for wings, and on a hybrid RANS/LES approach. *Advances in DNS/LES*, 1997.

[160] Spalart PR, Leonard A. Direct numerical simulation of equilibrium turbulent boundary layers. *Proc. 5th Symp. on Turbulence shear Flows*, 234-252, 1987.

[161] Spalart PR, Strelets M, Travin A. Direct numerical simulation of large-eddy-break-up devices in a boundary layer. *Int. J. Heat Fluid Flow*, 27:902–910, 2006.

[162] Speziale CG. Turbulence modeling in noninertial frames of reference. *Theo. Comput. Fluid Dyn.*, 1:3–19, 1989.

[163] Sreenivasan KR, Antonia RA. The phenomenology of small-scale turbulence. *Ann. Rev. Fluid Mech.*, 29:435–472, 1997.

[164] Stack J. Tests in the variable density wind tunnel to investigate the effects of scale and turbulence on airfoil characteristics. Technical Report NACA-TN-364, Langley Memorial Aeronautical Laboratory, 1931.

[165] Stull RB. *An introduction to boundary layer meteorology.* Springer, 1988.

[166] Süli E, Mayers. *An Introduction to Numerical Analysis.* Cambridge, 2003.

[167] Tabor GR, Baba-Ahmadi MH. Inlet conditions for large eddy simulation: A review. *Comput. Fluids*, 39:553–567, 2010.

[168] Tan HS. On laminar boundary layer over a rotating blade. *J. Aeronaut. Sci.*, 20: 780–781, 1953.

[169] Tangler JL, Selig MS. An evaluation of an empirical model for stall delay due to rotation for HAWTs. Technical Report CP-440-23258, NREL, 1997.

[170] Tanner WH, Yaggy PF. Experimental boundary layer study on hovering rotors. *J. American Helicopt. Soc.*, 11(3):22–37, 1966.

[171] Thompson KW. Time dependent boundary conditions for hyperbolic system. *J. Comput. Phys.*, 68:1–24, 1987.

[172] van Driest ER. On turbulent flow near a wall. *AIAA J.*, 23(11):1007–1011, 1956.

[173] Veloudis I, Yang Z, McGuirk JJ, Page GJ, Spencer A. Novel implementation and assessment of a digital filter based approach for the generation of LES inlet conditions. *Flow Turb. Combust.*, 79:1–24, 2007.

[174] Versteeg HK, Malalasekera W. *An introduction to computational fluid dynamics, The finite volume method, 2nd ed.* PEARSON, 2007.

[175] von Terzi, DA. *Numerical investigation of transitional and turbulent backward-facing step flows.* PhD thesis, University of Arizona, 2004.

[176] Wang M, Moin P. Dynamic wall modeling for large-eddy simulation of complex turbulent flow. *Phys. Fluids*, 14:2043–2051, 2002.

[177] Wang S, Ingham DB, Ma L, Pourkashanian M, Tao Z. Numerical investigations on dynamic stall of low Reynolds number flow around oscillating airfoils. *Comput. Fluids*, 39:1529–1541, 2010.

[178] Weiberg JA, Dannenberg RE. Section characteristics of a NACA 0006 airfoil with area suction near the leading edge. Technical Report TN 3285, National advisory committee for aeronautics, 1954.

[179] Willis GE, Deardorff JW. On the use of Taylor's translation hypothesis for diffusion in the mixed layer. *Quart. J. Roy. Meteor. Soc.*, 102:817–822, 1976.

[180] Windte J, Scholz U, Radespiel R. Validation of the RANS-simulation of laminar separation bubbles on airfoils. *Aero. Sci. Tech.*, 10:484–494, 2006.

[181] Wood DH. A three-dimensional analysis of stall-delay on a horizontal-axis wind turbine. *J. Wind Eng. Ind. Aerodyn.*, 37:1–14, 1991.

[182] Wu JZ, Lu XY, Danny AG, Fan M, Wu JM. Post-stall flow control on an airfoil by local unsteady forcing. *J. Fluid Mech.*, 371:21–58, 1998.

[183] Xie ZT, Castro IP. Efficient generation of inflow conditions for large eddy simulation of street-scale flow. *Flow Turb. Comb.*, 81:449–470, 2008.

[184] Xie ZT, Castro IP. Large-eddy simulation for flow and dispersion in urban streets. *Atmos. Environ.*, 43:2174–2185, 2009.

[185] Xie ZT, Voke PR, Hayden P, Robins AG. Large-eddy simulation of turbulent flow over a rough surface. *Bound. Layer Meteo.*, 111:417–440, 2004.

[186] Yeung PK, Brasseur JG, Wang Q. Dynamics of direct large-small scale couplings in coherently forced turbulence: concurrent physical- and Fourier-space views. *J. Fluid Mech.*, 283:43–95, 1995.

[187] Zaman KBMQ, McKinzie DJ, Rumsey CL. A natural low-frequency oscillation of the flow over an airfoil near stalling conditions. *J. Fluid Mech.*, 202:403–442, 1989.